FORCED GRANULAR FLOW

C.J. Coetzee

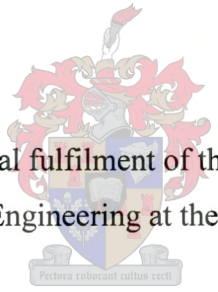

Thesis presented in partial fulfilment of the requirements for the degree
Master of Science in Engineering at the University of Stellenbosch

Thesis Supervisor: Mr. D.N.J. Els

December 2000

Stellenbosch University http://scholar.sun.ac.za

DECLARATION

I the undersigned hereby declare that the work contained in this thesis is my own original work and that I have not previously in its entirety or in part submitted it at any university for a degree.

Stellenbosch University http://scholar.sun.ac.za

ABSTRACT

The main goal of the thesis is to validate the ability of discrete element methods (DEM) to predict forced granular flow. Granular flow occurs in a broad spectrum of industrial applications. The thesis focuses on earthmoving processes typical of the mining and agricultural industries. Existing soil mechanics soil-tool models are also investigated and general flow behaviour in and around blades and buckets are established.

Soil mechanics theories are used to predict the draft forces on a flat blade moving through granular material. Corn and wheat grains are used as material. The rupture (slip) lines in front of the blade are predicted by soil mechanics and compared to experimental results. A two-dimensional test bench is used to visualise the flow of the granular material. Forces and moments that act on the tools are measured.

DEM can be used to model industrial granular flow with large displacements. Two types of earthmoving equipment are simulated. The first is a flat blade and the second is a bucket. The forces on these tools are determined using DEM and compared to experimental results. The ability of DEM to predict material compressibility, the flow of material in and around the tools, the rupture lines and the bucket fill rate are investigated. A particle relative displacement method is used to determine the rupture lines.

Stellenbosch University http://scholar.sun.ac.za

OPSOMMING

Die hoofdoel van die tesis is om die vermoë van diskrete-element-metodes (DEM) om geforseerde partikelvloei te voorspel, te ondersoek. Partikelvloei word aangetref in 'n breë spektrum van industriële toepassings. Die tesis fokus op grondverskuiwing soos aangetref in myn- en landbouprosesse. Bestaande grondmeganika-modelle word ook ondersoek, asook die algemene gedrag van partikelvloei in en rondom lemme en bakke.

Die grondmeganika-modelle word hoofsaaklik gebruik om die kragte op lemme te voorspel. Glip (skuif)-vlakke word ondersoek en vergelyk met eksperimentele resultate. 'n Twee-dimensionele toetsbank word gebruik om die vloei waar te neem. Die kragte en momente op die toerusting word ook gemeet. Mielie- en koringpitte word as materiaal gebruik.

DEM kan gebruik word om industriële partikelvloei met groot verplasings te modelleer. Twee tipes toerusting word gesimuleer. Die eerste is 'n plat lem en die tweede 'n bak. Die kragte en momente op dié toerusting word bepaal m.b.v. DEM en dan vergelyk met die eksperimentele resultate. Die vermoë van DEM om materiaalsamedrukking, vloeipatrone, glipvlakke en bakvul-tempo's te voorspel word ondersoek. 'n Partikel-relatiewe-verplasings-metode word gebruik om die glipvlakke te voorspel.

Stellenbosch University http://scholar.sun.ac.za

TABLE OF CONTENTS

Stellenbosch University http://scholar.sun.ac.za

Stellenbosch University http://scholar.sun.ac.za

Stellenbosch University http://scholar.sun.ac.za

LIST OF FIGURES

Stellenbosch University http://scholar.sun.ac.za

Stellenbosch University http://scholar.sun.ac.za

UNIVERSITEITSBIBLIOTEEK U.S.

Stellenbosch University http://scholar.sun.ac.za

Stellenbosch University http://scholar.sun.ac.za

Stellenbosch University http://scholar.sun.ac.za

LIST OF TABLES

Stellenbosch University http://scholar.sun.ac.za

NOMENCLATURE

Tensors and Vectors

$\underline{\overline{\mathbf{E}}}$	Transformation matrix
$\overline{\mathbf{e}}$	Base vector
$\overline{\mathbf{F}}$	Force vector
$\overline{\mathbf{g}}$	Gravitational acceleration vector
$\overline{\mathbf{h}}$	Angular momentum vector
$\underline{\overline{\mathbf{J}}}$	Inertia Tensor
$\overline{\mathbf{n}}$	Unit vector
$\overline{\mathbf{P}}$	Linear momentum vector
$\overline{\mathbf{r}}$	Body position vector
$\overline{\mathbf{V}}$	Velocity vector
$\overline{\mathbf{U}}$	Contact displacement vector
$\overline{\theta}$	Orientation coordinate vector (non-orthogonal)
$\overline{\rho}$	Vector pointing from the centre of mass of a body to a contacting point with an outboard body
$\overline{\omega}$	Angular velocity vector

Scalars

A	Area [m^2]
a	Force application point measured from the blade's bottom edge [m]
B	Tool width [m]
c_a	Adhesion coefficient [Nm^{-2}]
c_o	Cohesion coefficient [Nm^{-2}]
D	Rig fill depth [m]
d	Immersion ratio, particle centre distance
E	Energy [J], Young's modulus [Nm^{-2}]
e	Contact restitution coefficient

Stellenbosch University http://scholar.sun.ac.za

G	Heave height at blade [m], shear modulus [Nm^{-2}]
H	Total height of tool [m]
h	Immersion depth of tool [m]
K	Coefficient of lateral stress or lateral stress ratio, strain gauge factor
k	Particle contact stiffness [Nm^{-1}]
L	Length, moment arms [m]
M	Moment [Nm]
N_ϕ	Flow factor
O	Coordinate origin
p	Average stress [Nm^{-2}]
q	Surcharge pressure [Nm^{-2}]
R	Sphere/disk radius [m]
r	Radius [m]
t	Time [s]
u	Particle overlap [m]
W	Force acting on body due to material weight [N]
Z	Cross section modulus [m^3]
α	Blade rake angle, damping constant
β	Drag angle
Δ	Difference
δ	Material-tool friction angle
ε	Strain, Dynamic force ratio
ϕ	Material internal friction angle
γ	Unit weight [Nm^{-3}]
η	Characteristic line
μ	Particle-particle friction coefficient, angle that slip lines make with free surface
ν	*Poisson's ratio*
θ	Angle
ϑ	Angle that x-axis makes with tangent to oblique plane
ρ	Density [kg m^{-3}]
σ	Shear stress [Nm^{-2}]

Stellenbosch University http://scholar.sun.ac.za

τ	Normal stress [Nm^{-2}]
ξ	Characteristic line
ψ	Compressibility factor

Subscripts and Superscripts

a	Acceleration
b	Name of Cartesian base, conditions at blade
c	Cohesional, critical state conditions, contact point
f	Properties at failure, friction
h	Horizontal
i	Index
j	Body/Particle number
n	Normal to surface
o	Origin of coordinate system
p	Particle force
r	Properties at rupture surface
s	Shear direction, name of Cartesian base
t	Tangential direction
v	Vertical
w	Forces acting on failure wedge

Stellenbosch University http://scholar.sun.ac.za

CHAPTER 1

INTRODUCTION

Granular flows are the motion of particulate solids, where the individual grains move independently and the interactions are predominantly collisional. These flows can be driven by gravity, physical boundaries, interstitial fluids, or external body forces such as electro-magnetic fields.

1.1 A Brief Historical Review

In the past, the physics of granular materials received far less attention from researchers than, for example, hydrodynamics. Yet, it is remarkable that a few notable scientists managed in those days to marvel at some fascinating aspects of the behaviour of these types of materials.

The first recorded mention of granular flows is due to Lucretius (98-55 B.C.), the famous poet and natural philosopher in ancient Rome. He wrote: "One can scoop up poppy seeds with a ladle as easily as if they were water and, when dipping the ladle, the seeds flow in a continuous stream." Leonardo da Vinci (1452-1519) was the first to devise a simple and convincing experiment demonstrating the laws of dry friction. He was even able to make a few pertinent statements concerning piles of sand. It was not until the end of the eighteenth century, though, that Charles de Coulomb (1736-1806) wrote a definitive paper entitled "Essay on the rules of Maximis and Minimis applied to some problems of equilibrium related to architecture". It ultimately led to the Coulomb laws of friction between solids, which in time would be extended to granular materials.

Michael Faraday (1791-1867) was another scientist who, against the backdrop of his primary work on hydrodynamic instabilities, also had a strong interest in how vibrations induce the formation of sand piles.

Stellenbosch University http://scholar.sun.ac.za

William Rankine (1820-1872) examined the theoretical implications of friction in granular materials. Starting from Coulomb's ideas, he established a number of principles, which remain fully valid to this day. He defined what is now called Rankine's *passive* and *active states*.

By the latter part of the nineteenth century, Osborne Reynolds (1842-1912) had already distinguished himself in the field of hydrodynamics. He also made some fundamental contributions to the theory of granulars around the year 1885. Some concepts he developed (notably that of dilatancy) and his analysis of embankments remain high on the list of modern topics of investigation.

1.2 Economic Implication and Industrial Problems

Granular flow occurs in a broad spectrum of industrial applications. These range from separation and mixing in the pharmaceutical industry, to grinding and crushing, blasting, stockpile construction, generic flows in and from hoppers, silos, bins, conveyer belts and many more. The worldwide annual production of grains and aggregates of various kinds is gigantic, reaching approximately ten billion metric tons. Coal accounts for about 3.5 billion tons of that total and cements and ordinary construction materials for one billion tons. The processing of granular material consumes roughly 10% of all the energy produced on this planet and on the scale of priorities of human activity it ranks second, immediately behind the supplying of water. As such, any advance in understanding the physics of granular material is bound to have a major economic impact. Not much has been optimised, despite the fact that methods of transport, storage and mixing figure in all stages of the industrial processing of granules. At best, only primitive solutions were found for existing problems.

Draglines are used to remove blasted overburden from open cut mines. Its removal exposes the coal deposits beneath for mining. A dragline, as depicted in Fig. 1.1, is a crane-like structure from which hangs a huge bucket of up to 100 m^3 in volume. Draglines are an expensive and essential part of mine operations and play an important role in the competitiveness of South African mines.

Stellenbosch University http://scholar.sun.ac.za

Figure 1.1 – *A typical walking dragline*

In the coal mining industry it is generally accepted that a 1% improvement in the efficiency of a dragline will result in a R 1 million increase in annual production per dragline (Esterhuyse, 1997).

Earthmoving equipment is not only used for mining, it also plays an important role in the agricultural and earthmoving industries. The equipment is highly diverse in shape and function, but most of the soil cutting machines can be categorised into one of three principal classes, namely blade, ripper or bucket (shovel). Tools that resemble blades include bulldozer front blades, road graders, hauling scrapers, snowplows and other straight-edged blades. These instruments cut and push soil or other granular material at a depth that is generally less than their width. Ripper type tools are narrower compared to their working depth and are often attached to bulldozers and graders when it is necessary to cut and loosen hard soil. Buckets are blades equipped with sides that form a space in which soil or other materials can be cut and lifted up.

The basic shape of earthmoving tools has not changed a great deal since antiquity, although most are operated today by mechanical power sources and their construction benefits from modern metallurgical engineering. For the purpose of this thesis, we

Stellenbosch University http://scholar.sun.ac.za

make use of a flat blade and a bucket. The bucket has a general shape and does not represent that of specific equipment.

1.3 Numerical Modelling

The filling of a bucket is a complex granular flow. Instrumentation of equipment for measuring the operation is difficult and expensive. It is possible to use small-scale (usually $1/10^{th}$ scale) experimental rigs to evaluate bucket designs (Rowlands, 1991 and Esterhuyse, 1997) but they are expensive and there are questions regarding the validity of the scaling. To scale-up results from model experiments is problematic since there are no general scaling laws for granular flows as there are for fluid dynamics (Cleary, 1998).

Although numerical simulations seldom totally replace experiments, they allow designers to investigate a far wider range of options in a relatively short time and usually at much lower cost than using experimental investigations. A sensitivity analysis can be done more easily and comprehensively. Expensive experiments can then be used after numerical investigations to "fine tune" the design.

According to Mühlhaus (2000), the main obstruction in modelling geomechanics and solving geotechnical problems has been the lack of appropriate numerical tools to handle the difficulties arising from material inhomogeneity, brittle fracture, and associated complex damage patterns. The application of grid based discretisation procedures such as the Finite Element Method (FEM) can be problematic even if the material is macroscopically homogenous if, for instance, large deformations are involved. Remeshing is problematic if fracturing occurs on more then one scale, or where history dependence is involved. Meshless methods (Belytshko et al., 1994) are not yet extensively used. For these reasons, particle based methods for solid mechanics seem to be increasing in popularity.

The numerical methods for the modelling of granular flow may be grouped into two groups: continuum mechanics models and discrete element methods (DEM).

Stellenbosch University http://scholar.sun.ac.za

The continuum mechanics approach is used very successfully in the static applications in the civil and mining engineering fields such as tunnelling, foundation stability, embankment stability, etc. However, numerical difficulties arise when motion and subsequent large deformation of the material occur. The biggest problem with continuum models is that the constitutive models for dynamic flows are not well defined, because they vary for every type of granular material. The main benefit is the better understanding of the fundamentals of the material behaviour. Large systems can also be modelled in this way.

The discrete element methods are based on the simulation of the motion of granular material as separate particles. It involves following the trajectories, spins and orientations of all the particles and predicting their interactions with other particles and with their environment. This method can be used for the simulation of granular flow with large displacements as well as for discrete materials such as broken rock. The main problem with the discrete element methods is how to specify the micro-properties so that the flow on macro-level of thousands of particles behaves in the same way as real granular flow.

Cleary (2000, 1998, 1997) and Cleary and Sawley (1999) are some of the researchers that successfully modelled industrial granular flows with large displacements using DEM. They have modelled ore segregation on conveyer belts, the functioning of ball mills and dragline bucket filling.

1.4 Material Classification and Definitions

The physics of granular material deals primarily with macroscopic objects; i.e. objects making up such materials must at the very least be visible to the naked eye. These materials can be classified as follows.

- Frictional material – dry sands possess no cohesion but derive their shear strength entirely from intergranular friction (ϕ materials).
- Cohesive materials – saturated clay exhibit cohesion, but with no change in water content they appear to possess no friction (c_o materials)
- Intermediate materials which possess both cohesion and friction (c_o-ϕ materials)

Stellenbosch University http://scholar.sun.ac.za

Half to two thirds of all material handled by draglines and other equipment is relatively dry and its behaviour is dominated by friction. For the purpose of this thesis we only use frictional materials. Most of the theoretical and DEM models, however, include cohesion but due to experimental difficulties cohesive materials are not used.

The terms grains, granules, particles and granular material will be used interchangeably throughout the thesis.

1.5 Thesis Goals

Soil mechanics and earthmoving are two of the historic research areas where much work was done in the past. The empirical behaviour of soils and rocks is well documented and various numerical models were developed. However, the interface phenomena between granular materials and mechanical equipment are very poorly understood. This includes the flow of granular material in and around the buckets or blades of earthmoving, mining and agricultural equipment. Fundamental flow aspects of this type of flow are not established yet and industry can benefit substantially from this type of research. Direct contributions to industry include the optimisation of buckets and blades of materials handling equipment for energy efficiency and size, prediction and minimising of wear on tools, the development and optimisation of ore handling equipment such as ore shutes and conveyers and the addition of vibration to loaders and diggers, ore bins, silos, ploughs, etc. to reduce the size of the equipment and to ease the handling of the material.

According to Cleary (1998), the filling of buckets, in the absence of very large rocks, is observed to be relatively two-dimensional with little motion in the transverse direction. The flow pattern along a cross-section of the bucket in the drag direction is the most important aspect of filling and can be analysed satisfactorily using two-dimensional simulations. Rowlands (1991) made similar observations. All the simulations are performed in a two-dimensional environment.

Stellenbosch University http://scholar.sun.ac.za

The goals of this thesis can be summarised as follows:

1. A literature search for existing soil-tool interaction models and the validation of these models by means of experiments.
2. The evaluation of the ability of DEM to model earthmoving processes and to give some idea of the range of useful predictions that can be made.
3. The establishing of general flow behaviour in and around blades and buckets.

Most of the existing soil-tool models are based on soil mechanics principles. These models were developed for the analysis of retaining walls and later modified and applied to ground engagement tools. These models are presented in Chapter 2.

To accomplish the second goal, it is necessary first to create a numeric or synthetic material that has the same macro-properties than that of the intended natural material. This is done through a calibration procedure and presented in Chapter 4. This calibrated material is then used to evaluate the ability of DEM to model earthmoving processes.

The blade and bucket results are presented in Chapter 5 and Chapter 6 respectively. The results focus on the forces and moments acting on the tools as well as the flow of material and the formation of rupture or slip lines.

Stellenbosch University http://scholar.sun.ac.za

CHAPTER 2

SOIL MECHANICS

Basically all soil cutting, moving and tillage instruments transfer soil from its original location. Thus the mechanical failure of the soil material is involved in the sense that the mass of soil being moved does not retain its original geometric shape. The design of effective and efficient implements begins with the analysis of this soil failure in order to predict the forces and energy required by the implements. The design process proceeds subsequently to the description of soil manipulation and structural changes that result from tool action, depending upon the special application of interest. This chapter treats the basics of soil mechanics necessary for these calculations, and the analytical and numerical techniques that are available for the prediction of forces acting on straight blades.

The classical soil mechanics theory was founded in 1776 by Coulomb, who introduced most of the basic concepts and assumptions. He stated the so-called Coulomb law of shearing resistance and introduced the principle of determining the active earth pressure as a maximum value. Rankine, in 1857, approached the problem in an entirely different way. He started by investigating the conditions of equilibrium and failure for an infinitely small soil element in a semi-infinite earth mass. Whereas Coulomb and Rankine were only able to deal with straight rupture surfaces, Kötter succeeded in 1903 in deriving the differential equation governing the stress in a curved rupture-line. Hansen (1961) divides soil mechanic methods into four groups:

- Extreme methods (e.g. Coulomb, Fellenius, Rendulic)
- Theories of plasticity (e.g. Rankine, Prandtl, Kötter, Ohde)
- Theories of elasticity (e.g. Bousinesq, Bretting)
- Empirical methods (e.g. Christiani, Rowe)

Extreme methods and theories of plasticity are discussed in further detail.

Stellenbosch University http://scholar.sun.ac.za

2.1 Extreme Methods

Extreme methods are ways to solve the problem by means of a single condition of equilibrium in connection with a maximum (active) or minimum (passive) condition. It is necessary to choose the shape of the rupture surfaces so that an equation of equilibrium can be developed in which the unknown stresses in the rupture surface do not enter. The principle of the extreme method is to choose from all possible rupture-lines, the one for which the material pressure resultant attains an extreme value. Only passive conditions are examined, so we concentrate on finding an absolute minimum. This minimum value postulate seems logical because, if one imagines the blade being slowly forced forward into the soil, the force on it will steadily increase until it reaches the required minimum value at which failure can occur. It could not occur on any other surface because the force applied was never large enough. Two extreme methods are presented: Coulomb's and Perumpral's method.

2.1.1 Coulomb's Method

Coulomb noted that there appeared to be two mechanical processes in action, which determine the ultimate shearing strength of soil. One process he called friction, and the other cohesion. In the first case, a portion of the shear strength is proportional to the pressure acting perpendicular on the shearing surface. In the second, part of the strength resisting shear movement is a constant, regardless of the normal pressure acting. The total shear strength is the sum of these two components,

$$\tau = c_o + \sigma \tan(\phi) \tag{2.1}$$

where τ is the shear stress (strength), c_o = cohesion [Nm^{-2}], σ = normal stress acting on shear surface and ϕ the angle of internal friction. This is known as *Coulomb's law*.

The non-rigorous part of the extreme method approach is involved in the choice of failure surface shape. Coulomb chose a straight line because it was the simplest choice and yielded an analytical result that seemed in good agreement with experiments

Stellenbosch University http://scholar.sun.ac.za

involving smooth vertical walls and sand. Consider a wedge of material bounded by the free surface, the blade and a straight rupture surface through the foot of the blade (Fig. 2.1). The blade force makes an angle δ (material-blade friction angle) with the normal to the blade and the force on the rupture surface an angle ϕ with the normal on the rupture surface, i.e. Coulomb's law without cohesion is assumed. For a given rupture angle θ_r, the only unknowns are the total force on the blade F and the force acting on the rupture surface F_{fr}. These two unknowns can be solved, as a function of θ_r, by equating equilibrium in the x- and y-direction respectively. The minimum of this function can be solved numerically or by setting the differential of the function equal to zero, an analytical result can be obtained.

$$F = \tfrac{1}{2}\gamma B h^2 \left[\frac{\operatorname{cosec}(180° - \alpha)\sin(180° - \alpha + \phi)}{\sqrt{\sin(180° - \alpha - \delta)} - \sqrt{\dfrac{\sin(\phi + \delta)\sin(\phi + \theta_f)}{\sin(180° - \alpha - \theta_f)}}} \right]^2 \tag{2.2}$$

where B is the blade width and the other variables are defined in Fig. 2.1.

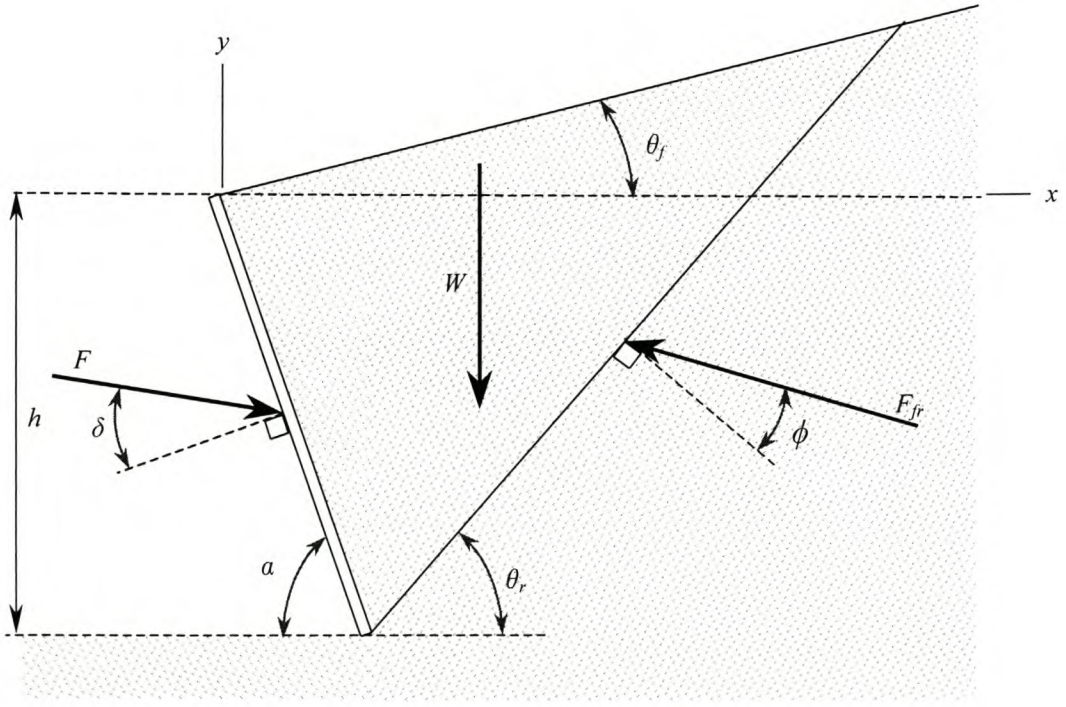

Figure 2.1 – *Coulomb's method*

Stellenbosch University http://scholar.sun.ac.za

2.1.2 Perumpral's Method

Coulomb did not include cohesion and adhesion in his analysis. He also assumed static 2-D conditions. Several authors improved on Coulomb's method by introducing cohesion, dynamic forces and 3-D effects. The method introduced by Perumpral et al. (1983) is explained in further detail.

The method is based on the following assumptions:

- The soil has cohesional and frictional characteristics, and is isotropic and homogeneous.
- The rupture surface is plane (the same as assumed by Coulomb)
- The frictional and cohesional forces are uniformly distributed on the surfaces of the wedge.
- The blade face is frictional
- Mohr-Coulomb failure criterion describes the soil failure.
- The soil density is not affected by the blade displacement.
- Acceleration forces on the tool are zero.
- Width of the centre wedge is the same as the blade width.

First we define what is known as the *geostatic stress state*. Stresses in soil are caused by the weight of the material and externally applied loads. Stress patterns can be very complicated; however, there is a situation in which the weight of soil gives rise to a very simple pattern of stress. When the ground surface is horizontal and when the nature of the soil varies little in the horizontal direction, the stresses in the soil are called geostatic stresses. There are no shear stresses on the vertical and horizontal planes within the material. This means that the vertical geostatic stress at any depth can be computed simply by considering the weight of the soil above that depth. This is similar to the concept of hydrostatic stress or pressure in a fluid. With the unit weight of the soil constant, the vertical stress is

$$\sigma_v = y\gamma \tag{2.3}$$

Stellenbosch University http://scholar.sun.ac.za

where y is the depth and γ the unit weight of the soil. In practise the unit weight of soil is seldom constant; usually the unit weight varies continuously with depth. The vertical geostatic stress can then be calculated by means of the following integral

$$\sigma_v = \int_0^y \gamma \, dy \tag{2.4}$$

The ratio of horizontal to vertical stress is expressed by a factor called the *coefficient of lateral stress* or *lateral stress ratio* and is denoted by the symbol K

$$K = \frac{\sigma_h}{\sigma_v} \tag{2.5}$$

This definition is also used whether the stresses are geostatic or not but are still principal stresses.

The method proposed by Perumpral et al. (1983), from here on called Perumpral's method, is shown in Fig. 2.2.

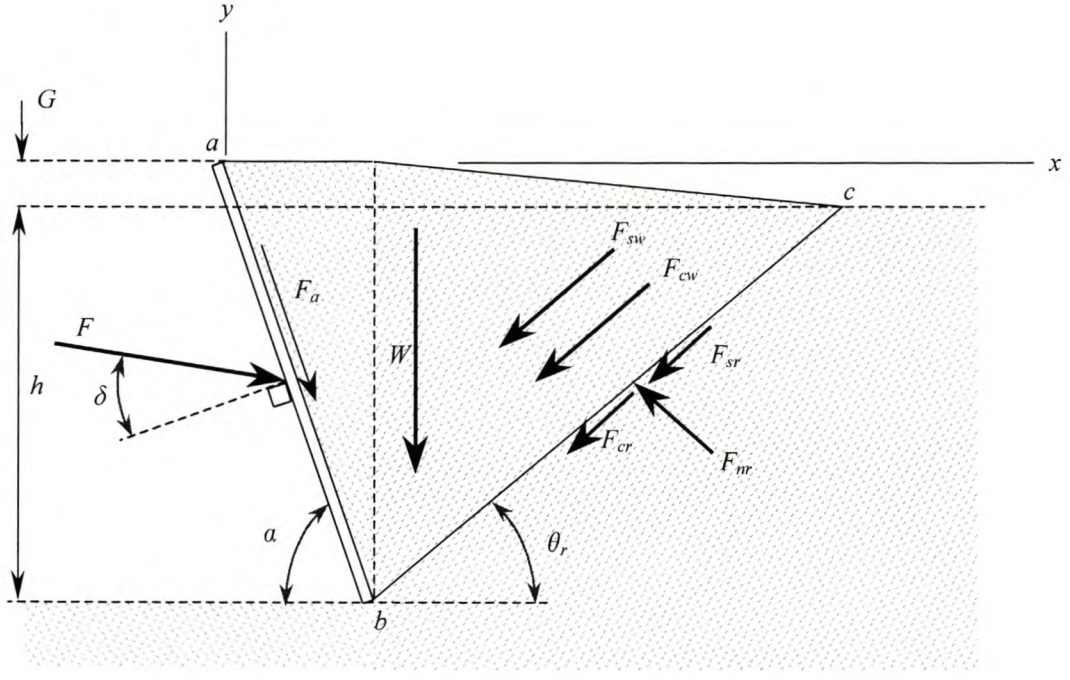

Figure 2.2 – *Perumpral's method*

Stellenbosch University http://scholar.sun.ac.za

An adhesion force F_a that acts on the blade has been introduced as well as a cohesion force F_{cr} on the rupture surface. The total rupture surface force F_{fr} has been broken up in two components: a shear component F_{sr} and a normal component F_{nr}. F_{sw} and F_{cw} are the shear and cohesion forces respectively, acting on the two wedges *abc*. A soil heave with height G has also been added. Assuming that the soil just outside of the wedge is not affected by the blade or the movement of the failure wedge, e.g. it is in a geostatic state, the force normal to the side *abc* can be written as

$$R = \rho g KZA \tag{2.6}$$

where K is the coefficient of lateral pressure at rest, $Z = 1/3(h+G)$ is the average depth at which the centroid of the wedge is located from the soil surface and A is the area of each surface *abc*. The area can be written in terms of known parameters

$$A = \tfrac{1}{2} h^2 \left(1 + G/h\right)\left[\left(1 + G/h\right)\cot(\alpha) + \cot(\theta_r)\right] \tag{2.7}$$

The forces on the two sides of the wedge can be written as

$$F_{sw} = R\tan(\phi) \tag{2.8}$$

$$F_{cw} = c_o A \tag{2.9}$$

The forces on the rupture plane are

$$F_{cr} = \frac{c_o B h}{\sin(\theta_r)} \tag{2.10}$$

$$F_{sr} = F_{nr}\tan(\phi) \tag{2.11}$$

where B is the width of the blade. Two forces exist on the soil-blade interface: the adhesion force and the force exerted by the blade in the direction of movement. The expression for the adhesion force is

$$F_a = c_a B h\left(1 + G/h\right)\sin(\alpha) \tag{2.12}$$

Stellenbosch University http://scholar.sun.ac.za

where c_a is the adhesion factor between the soil and the blade. The weight of the soil is

$$W = \rho g B A \tag{2.13}$$

With all the forces acting on the wedge known, expressions for the x- and y-components of the blade force F can be written as

$$F_x = -F_a \cos(\alpha) + 2F_{sw} \cos(\theta_r) + F_{nr} \sin(\theta_r) + (F_{sr} + 2F_{cw} + F_{cr}) \cos(\theta_r) \tag{2.14}$$

$$F_y = W + (2F_{sw} + F_{sr} + 2F_{cw} + F_{cr}) \sin(\theta_r) + F_a \sin(\alpha) - F_{nr} \cos(\theta_r) \tag{2.15}$$

Solving for the total blade force

$$F = \left[\frac{1}{\sin(\alpha + \phi + \theta_r + \delta)}\right][-F_a \cos(\alpha + \phi + \theta_r) + 2F_{sw} \cos(\phi) + W \sin(\phi + \theta_r) + (2F_{cw} + F_{cr}) \cos(\phi)] \tag{2.16}$$

All the terms on the right hand side of Eq. 2.16 can be calculated if both the rupture angle θ_r and the heave height G are known. The same procedure followed by Coulomb can be used to determine the minimum of this function, i.e. by setting the derivative equal to zero and solving for θ_r. It is, however, a complex expression and a numerical procedure can easily be employed to minimise the function.

2.1.3 Dynamic Effects

At times, soil tools may be operated at relatively high forward speeds, whether they are employed in tillage or in earthmoving activities. Two mechanisms cause the principal effects on forces required to move soil, namely the need to continuously accelerate new masses of soil as the tool travels, and the alteration of soil strength at high rates of shear. The strength of purely frictional soils does not vary a great deal with shear rate, according to McKyes (1985). For such a soil, it is the inertial forces involved in the accelerating soil, which are the most important when operating speed increases. On the

Stellenbosch University http://scholar.sun.ac.za

other hand, clay soils can show an increase in shear strength with increasing shear rate, which outweigh inertial forces nearly completely at high velocity. The inertial forces can be calculated by assuming a wedge rupture zone (Fig. 2.3).

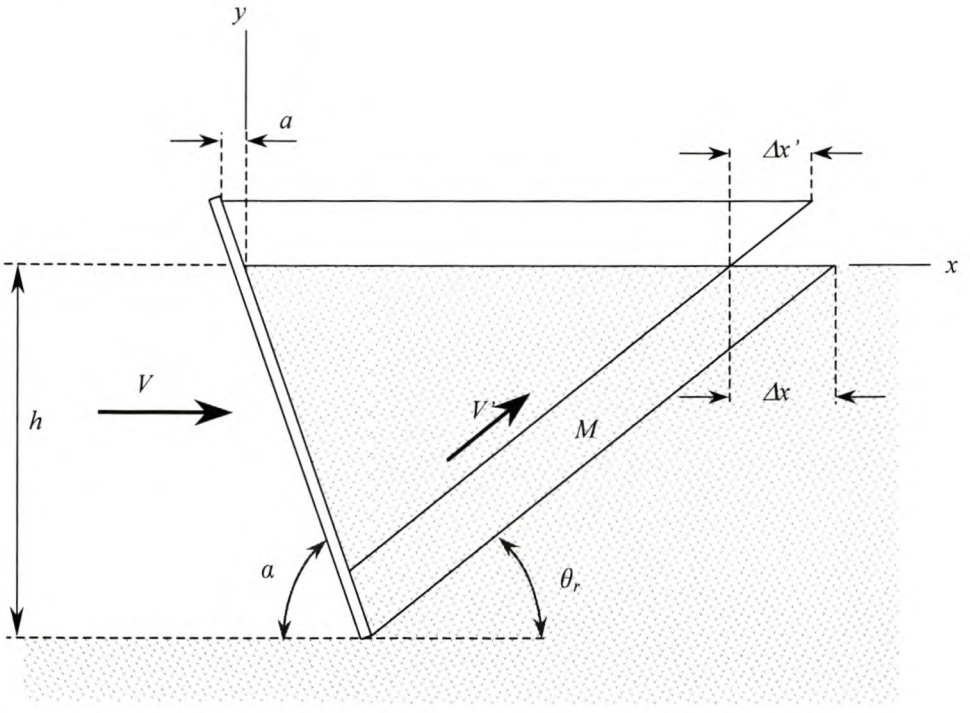

Figure 2.3 – *Inertial force calculation*

When the blade moves forward a distance Δx, the wedge of soil is lifted along the soil rupture surface inclined at angle θ_r, and along the blade at angle a. The forward speed of the soil wedge is not the same as that of the tool speed V because the soil moves backwards relative to the blade by a distance a. The actual soil speed is V' along the instantaneous rupture plane, and the forward movement of the soil $\Delta x'$ is less than that of the blade over a time interval Δt.

$$\Delta x = \Delta x' + a = \Delta x'\left[1 + \tan(\theta_r)\cot(\alpha)\right] \tag{2.17}$$

The soil speed is

$$V' = \frac{\Delta x'}{\Delta t \cos(\theta_r)} = \frac{\Delta x}{\Delta t \cos(\theta_r)[1 + \tan(\theta_r)\cot(\alpha)]}$$

$$= \frac{V}{\cos(\theta_r)[1 + \tan(\theta_r)\cot(\alpha)]} = \frac{V \sin(\alpha)}{\sin(\alpha + \theta_r)} \tag{2.18}$$

Stellenbosch University http://scholar.sun.ac.za

Over each time interval, a mass M is added to the soil being lifted by the blade. The inertial force F_a required to accomplish the acceleration of this mass to the speed V' of the soil wedge is calculated by variation of Newton's law relating resultant force to rate of change of momentum.

$$F_a = M\frac{V'}{\Delta t} = \frac{\gamma\,\Delta x\,h\,B\,V'}{\Delta t} = \gamma\,V\,h\,B\,V' = \frac{\gamma\,h\,B\,V^2\sin(\alpha)}{\sin(\alpha+\theta_r)} \tag{2.19}$$

This acceleration force can be added into the balance of forces of both Coulomb's and Perumpral's method. McKyes (1985) made use of experimental results reported by Luth and Wismer to verify this analysis. Dry sand was used and the blade velocity was varied from 0.25 to 2.5 m/s. The predicted values were found to be reasonable compared to the measured values within the range measured.

Other authors have also developed models based on that of Coulomb. Most of them include either dynamic effects, as described above, or three-dimensional failure zones. Other authors made use of empirical solutions. These can be found in McKyes (1978), Zeng and Yao (1992), Swick and Perumpral (1988), McKeyes and Ali (1977), Siemens et al. (1965), Bagster and Bridgwater (1967), Stafford (1984), Luth and Wismer (1971), Grisso et al. (1996) and Albert et al. (1998). A summary of most of these models and methods are given in McKyes (1985).

2.2 Theories of Plasticity

As Coulomb's theory became more general it became apparent that it does not always give accurate results. Experiments showed that the rupture surfaces were in general curved. Theoretical investigations of ideal plastic weightless materials resulted in failure surfaces that were formed by combinations of logarithmic spirals and straight lines. Theories of plasticity are based on the assumption that a state of failure exists at any point within a certain area (zone ruptures) or on a certain curve (line ruptures). By means of this assumption, in connection with the equations of equilibrium, it is possible to solve soil pressure problems.

Stellenbosch University http://scholar.sun.ac.za

The material is assumed to be macroscopically homogeneous and in a critical state. The definition for critical state is when the material or part of the material is stressed to the limit of the Mohr-Coulomb strength criterion at the point just before slip occurs. The analysis is conducted for static equilibrium and no dynamic effects are taken into account. Deformation effects such as compaction or dilatation are not accounted for.

Only the outline of the theory is given here. A detailed description is given in Appendix C.

2.2.1 Stress Components at a Point

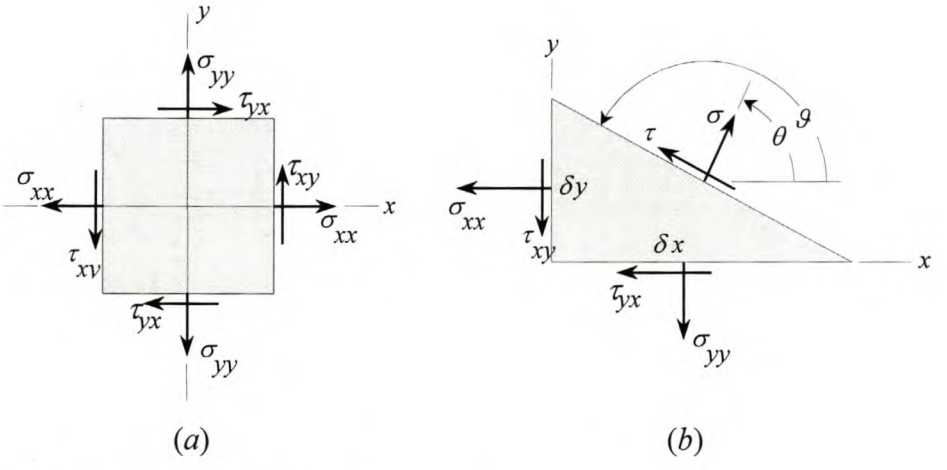

Figure 2.4 – *Biaxial or plane stress*

Figure 2.4(a) illustrates a state of biaxial or plane stress at a point. The outwardly directed normal or tensile stresses σ_{xx} and σ_{yy} on the element are defined as positive. The shear stresses τ_{xy} and τ_{yx} are defined positive on a face of an element if they act in the positive direction of the reference axis. Since the element is in static equilibrium, the negative faces will have shear stresses acting in the opposite direction, which are also defined as positive. Consider the oblique plane in Fig 2.4(b) that cuts the stress element at an angle ϑ to the x-axis. Let θ be the angle from the x-axis to the normal to the plane. The relationship between the angles is

$$\vartheta = \theta + \frac{\pi}{2} \tag{2.20}$$

Stellenbosch University http://scholar.sun.ac.za

The normal and shear stresses on the oblique plane are obtained from equilibrium of forces. The extreme values of the normal stress are known as the principle stresses. The principle stresses are arranged in ascending order $\sigma_1 \leq \sigma_2$ and are given by

$$\begin{aligned}\sigma_1 &= \tfrac{1}{2}(\sigma_{xx}+\sigma_{yy}) - \tfrac{1}{2}\sqrt{(\sigma_{xx}-\sigma_{yy})^2+4\tau_{xy}^2} \\ \sigma_2 &= \tfrac{1}{2}(\sigma_{xx}+\sigma_{yy}) + \tfrac{1}{2}\sqrt{(\sigma_{xx}-\sigma_{yy})^2+4\tau_{xy}^2}\end{aligned} \tag{2.21}$$

The average stress or pressure is defined as

$$p = \tfrac{1}{2}(\sigma_2+\sigma_1) = \tfrac{1}{2}(\sigma_{xx}+\sigma_{yy}) \tag{2.22}$$

The stresses in the x-y plane can also be given in terms of the principal stresses and angles θ_2 and ϑ_2 associated with the major principle stress σ_2.

$$\begin{aligned}\sigma_{xx} &= p+\tfrac{1}{2}(\sigma_2-\sigma_1)\cos(2\theta_2) &&= p-\tfrac{1}{2}(\sigma_2-\sigma_1)\cos(2\vartheta_2) \\ \sigma_{yy} &= p-\tfrac{1}{2}(\sigma_2-\sigma_1)\cos(2\theta_2) &&= p+\tfrac{1}{2}(\sigma_2-\sigma_1)\cos(2\vartheta_2) \\ \tau_{xy} &= \tfrac{1}{2}(\sigma_2-\sigma_1)\sin(2\theta_2) &&= -\tfrac{1}{2}(\sigma_2-\sigma_1)\sin(2\vartheta_2)\end{aligned} \tag{2.23}$$

2.2.2 Conditions of Critical State and Differential Equation of Equilibrium

Referring to Fig. 2.4(b), consider a point in a granular material with a plane passing through it. Of interest for this study is the critical state of maximum shear stress without any slip occurring. Coulomb's law states that

$$|\tau_c| = c_o - \sigma_c \tan(\phi) \tag{2.24}$$

with σ_c and τ_c the critical stress components in that state.

This critical condition is depicted on the Mohr circle in Fig. 2.5(a) with the two critical lines ξ and η for clockwise and counter-clockwise shear stresses respectively. It is clear from the Mohr circle that the angles of the two critical planes with respect to the x-axis are given by $\theta_2 \pm \mu + \pi/2$, which is equal to $\vartheta_2 \pm \mu$. The angle μ is given by

$$2\mu = \frac{\pi}{2} - \phi \tag{2.25}$$

Stellenbosch University http://scholar.sun.ac.za

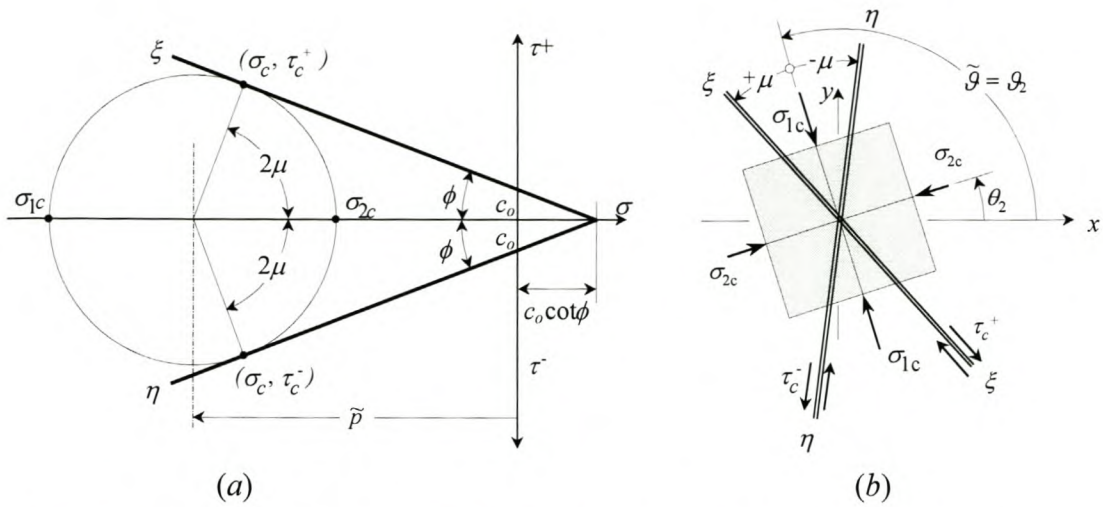

Figure 2.5 – *(a) Critical state according to Mohr-Coulomb strength criterion*
(b) Directions of yield planes for critical state

In the critical state, the principal stresses are constrained because of the strength criterion of Eq. 2.24. By using the Mohr diagram (Fig. 2.5a) together with Eq. 2.23, it can be shown that the stresses in the critical state in the *x*- and *y*-directions is given by

$$\begin{aligned}
\sigma_{xx} &= \tilde{p}\left(1+\sin(\phi)\cos(2\tilde{\vartheta})\right) - c_o\cos(\phi)\cos(2\tilde{\vartheta}) \\
\sigma_{yy} &= \tilde{p}\left(1-\sin(\phi)\cos(2\tilde{\vartheta})\right) + c_o\cos(\phi)\cos(2\tilde{\vartheta}) \\
\tau_{xy} &= \tilde{p}\sin(\phi)\sin(2\tilde{\vartheta}) \qquad - c_o\cos(\phi)\sin(2\tilde{\vartheta})
\end{aligned} \tag{2.26}$$

where $\tilde{p}$ is the average stress for the critical state

$$\tilde{p} = \frac{\sigma_{2c}+\sigma_{1c}}{2} = \frac{\sigma_{1c}+c_o\cos(\phi)}{1+\sin(\phi)} = \frac{\sigma_{2c}-c_o\cos(\phi)}{1-\sin(\phi)} \tag{2.27}$$

and $\tilde{\vartheta} = \vartheta_2$ which is the angle of the plane associated with the major principal stress σ_2.

Next the conditions for equilibrium in a changing stress field are investigated.

Stellenbosch University http://scholar.sun.ac.za

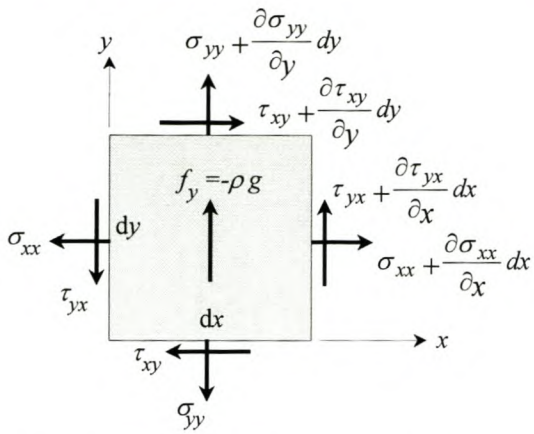

Figure 2.6 – *Equilibrium condition on a differential element*

Consider the differential element in a varying stress field depicted in Fig. 2.6. Assume the only body force is gravitation in the negative y-direction. The equilibrium conditions for forces in the x- and y-directions are then

$$\frac{\partial\sigma_{xx}}{\partial x}+\frac{\partial\tau_{xy}}{\partial y}=0, \qquad \frac{\partial\tau_{xy}}{\partial x}+\frac{\partial\sigma_{yy}}{\partial y}=\rho\, g \tag{2.28}$$

with ρ the bulk density of the material and g the gravitation acceleration. Substitution of Eq. 2.26 into Eq. 2.28 leads to a system of partial differential equations. The equations can be solved using the method of characteristics which, after considerable algebra, leads to the differential equations of the *characteristics curves.*

$$\left.\frac{dy}{dx}\right|_{\xi}=\tan\left(\tilde{\vartheta}+\mu\right)$$

$$d\,\tilde{p}-2\tan(\phi)(c_o\cot(\phi)-\tilde{p})\,d\tilde{\vartheta}-\rho\, g\tan(\phi)\,dx-\rho\, g\,dy=0 \tag{2.29}$$

and

$$\left.\frac{dy}{dx}\right|_{\eta}=\tan\left(\tilde{\vartheta}-\mu\right)$$

$$d\,\tilde{p}+2\tan(\phi)(c_o\cot(\phi)-\tilde{p})\,d\tilde{\vartheta}+\rho\, g\tan(\phi)\,dx-\rho\, g\,dy=0 \tag{2.30}$$

Stellenbosch University http://scholar.sun.ac.za

It can be shown that a characteristic is the path of propagation of a physical disturbance, in this instance a slip line or shear plane in the material. It has the property that the governing partial differential equations can be manipulated into total differential equations along, and only along, these lines. A characteristic is also a curve across which the derivatives of a physical property may be discontinuous, while the property itself remains continuous. Note that the first equation of each family gives the slope of the characteristic lines $\xi(x,y)$ or $\eta(x,y)$, while the second gives the change of the two unknown properties $\tilde{p}(x, y)$ and $\tilde{\vartheta}(x, y)$ along the specific lines.

These equations can only be solved if sufficient material properties and boundary conditions are known. Analytical solutions are only possible for some simple cases, such as a perfect smooth blade and weightless material. This is a valid assumption only if the material strength characteristics are dominated by the cohesion and not the internal friction. Figure 2.7 shows the result from such an analysis for a straight blade. The outer characteristic line, ξ_9 in this case, is defined as the *rupture line*.

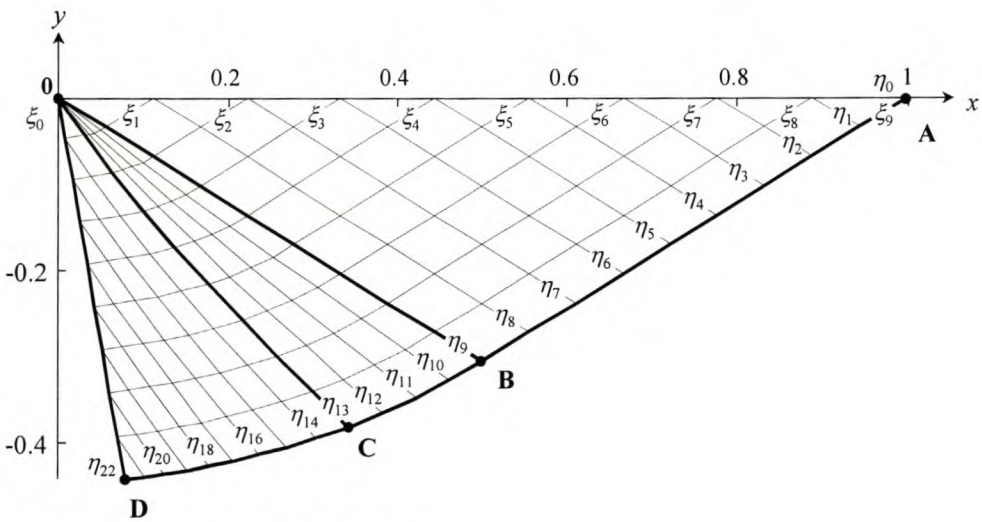

Figure 2.7 – *Sample calculation*

The details of the numeric and analytical integration processes and the handling of boundary conditions are given in Appendix C.

Stellenbosch University http://scholar.sun.ac.za

2.2.3 Approximation for Material Weight

The governing equations can only be solved numerically for $\rho \neq 0$ and $\delta \neq 0$. For pure frictional material ($c_o = 0$) the assumption that $\rho = 0$ is not valid.

Ohde devised a way of including the weight of the soil. The analytical solution of the differential equations showed that, for a weightless assumption, the rupture surface consists of a logarithmic spiral (*AB* in Fig. 2.7) and straight line (*BD* in Fig. 2.7). Ohde also assumed the rupture surface to be partly a logarithmic spiral and partly a straight line, but added the weight of the soil and solved for the blade force using static equilibrium conditions (similar to the method used by Coulomb and Perumpral). This is in effect an extreme method based on the shape of the rupture line as obtained from the plasticity theory.

The logarithmic spiral is defined by the equation,

$$r = r_0 \, e^{\theta \tan \phi} \tag{2.31}$$

This spiral is shown in Fig. 2.8 as curve *bd*.

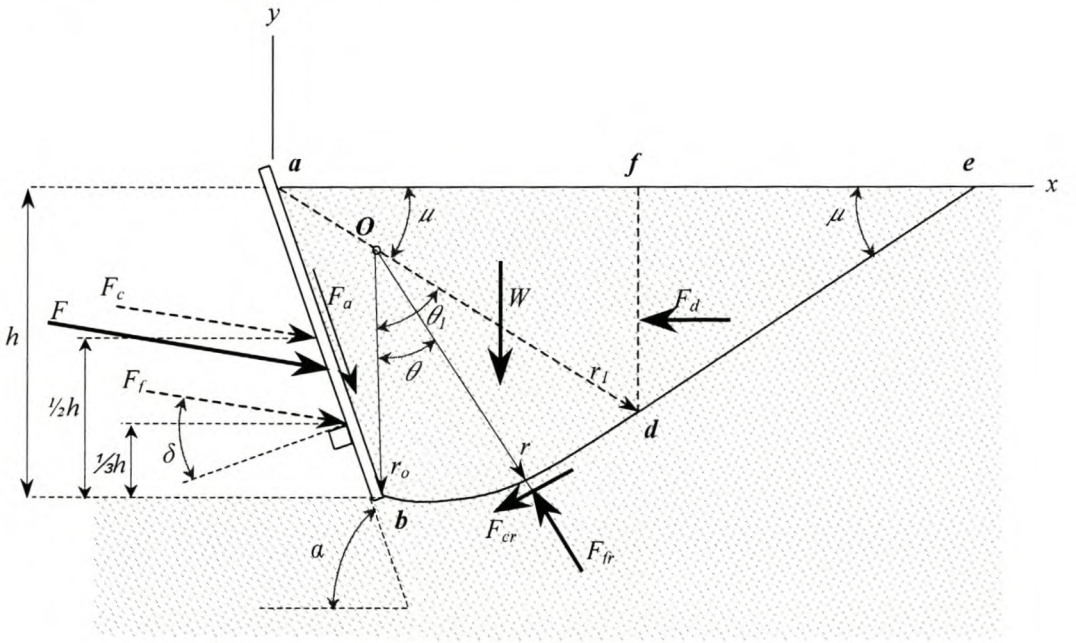

Figure 2.8 – *Ohde's logarithmic spiral method*

Stellenbosch University http://scholar.sun.ac.za

The following symbols are defined in the figure.

F_c = blade force acting due to cohesion of material only
F_f = blade force due to frictional forces of material only
F = total blade force = vector sum of F_c and F_f
h = immersed depth
F_a = adhesion force on blade
F_{cr} = force on rupture surface due to cohesion only
W = total weight of soil within area *abde*
F_{fr} = force on rupture surface due to friction only with components F_{sr} and F_{sr} in the shear and normal directions respectively
F_d = force on *df* due to the soil within *fde*
r = spiral radius
θ = spiral angle

Since the spiral is tangent at *d* to the straight part *de*, the centre of the spiral must be located on the line *ad* which is inclined at μ to the horizontal. The nature of the spiral is that a radius makes an angle ϕ with the normal to the spiral at the point where the radius intersects the curve. Since ϕ is the angle of internal friction, the resultant rupture force ΔF_{fr} on any element of the surface of rupture also makes an angle ϕ with the normal to the element, and its direction coincides with that of the radius that spans the element. Every radius passes through the origin and hence so does the resultant F_{fr} of all the normal and shear stresses that act on curve *bd*. This fact simplifies the calculations.

The total blade force F can be calculated by considering the equilibrium of the soil in region *abdf*. The forces acting on this *free body* of soil are W, F, F_a, F_{cr}, F_{fr} and F_d. The soil within the triangle *ade* is in the passive Rankine state as is shown by the plasticity method. Therefore, the shearing stress on the vertical section *df* is zero and the force F_d is horizontal. By using Rankine theory, the force F_d can be divided into two components: a component due to the material being a pure frictional material F_{df} and a component assuming the material is purely cohesive F_{dc}.

$$F_{df} = \frac{1}{2}\gamma\,(df)^2\,N_\phi \tag{2.32}$$

Stellenbosch University http://scholar.sun.ac.za

This force acts at a distance *df*/3 from *d* along *df* (*df* is the length from *d* to *f*). The cohesion component is given by

$$F_{d\,c} = 2\,c_o\,(df)\sqrt{N_\phi} \tag{2.33}$$

and it acts at a distance *df*/2 from *d* along *df*. The Rankine theory is given in Appendix C.2.

In order to determine the total force F, we must calculate F_f and F_c separately and then add them together. With the material internal friction angle known, the direction of line *ad* and *de* is fixed. Choose the centre of the spiral somewhere along *ad*. With the centre O known, the first radius of the spiral r_o is simply the distance from O to *b*. This radius corresponds to a spiral angle $\theta = 0°$. The angle θ_1 can now be determined and subsequently the position of *d*. The straight-line portion of the rupture surface can be completed by drawing a line from *d* to the surface at an angle μ as indicated. This yields the position of *e* and the rupture- or failure-length.

Now, to calculate F_f, we assume the material to be cohesionless, i.e. the only forces acting on the body *abdf* is W, F_f, F_{fr} and F_{df}. The rupture surface is known and thus the weight of the soil W and F_{df} is known from Eq. 2.32. By taking moments of forces about O, the force F_f can be solved since the moment of F_{fr} about O is zero.

$$F_f = \frac{1}{L_1}(W\,L_2 + F_{df}\,L_3) \tag{2.34}$$

where the moment arms are indicated in Fig. 2.9.

Stellenbosch University http://scholar.sun.ac.za

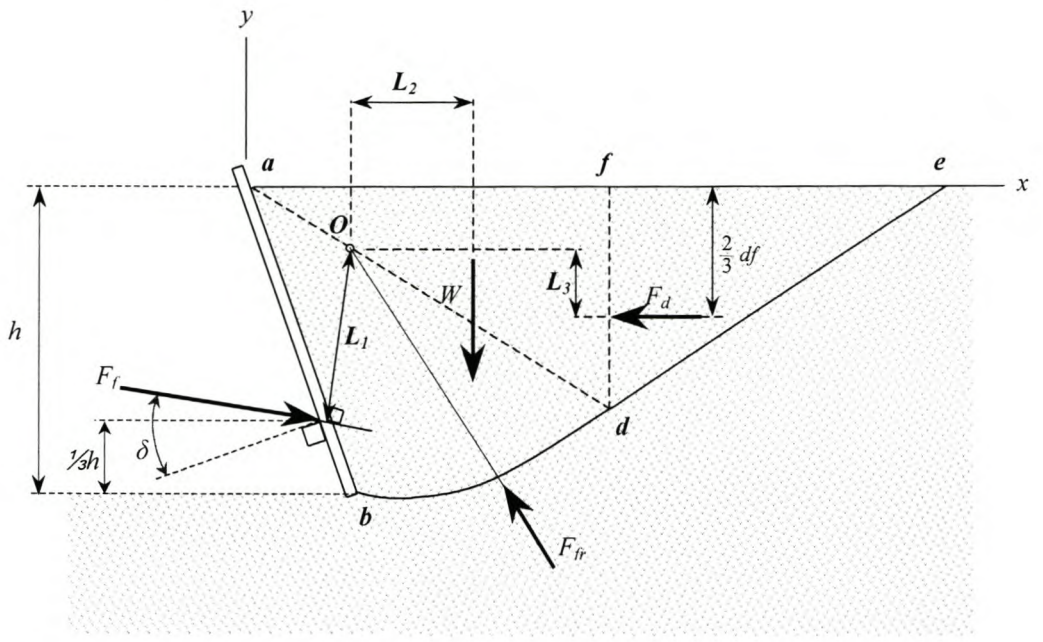

Figure 2.9 – *Logarithmic spiral, calculation of F_f*

Next we calculate the value of F_c. This is the value of F with $\gamma = 0$. First calculate the value of F_{dc} as given by Eq. 2.33. The point of application of this force is at the mid-height of *df*. The influence of the cohesion c_o along *bd* may be evaluated by considering an element having a length *ds*. The cohesion force is equal to $c_o ds$ and the moment of this incremental force about *O* is

$$d M_c = r c_o ds \cos\phi = r c_o \frac{r d\theta}{\cos\phi} \cos\phi = c_o r^2 d\theta$$

and the total moment is

$$M_c = \int_0^{\theta_1} d M_c = \frac{c_o}{2 \tan\phi} (r_1^2 - r_0^2) \tag{2.35}$$

Taking moments of forces F_{dc}, F_{fr}, F_{cr} and F_c about point *O* yields

$$F_c = \frac{1}{L_1} (M_c + F_{dc}\, L_3) \tag{2.36}$$

The total passive force acting on the blade is now simply the sum of F_f and F_c, which are given by Eq. 2.34 and Eq. 2.36 respectively. This blade force, of course, goes along

Stellenbosch University http://scholar.sun.ac.za

with the chosen position of the spiral centre. It is to complex too write the blade force as a function of the spiral centre position. By making use of small steps, the centre of the spiral can be moved along the line *ad* and the total blade force calculated for each centre position. By plotting a graph of blade force versus centre position, the minimum force can be found. If there is any adhesion c_a between the material and the blade, the effect thereof can be added to the force F.

Ohde made use of a graphical method to solve the problem. This is relatively easy and quick if only one problem is to be solved. To perform multiple calculations, e.g. with different material properties and rake angles, it is best to write a computer program to perform the calculations. Note that in order to obtain the minimum force it may be necessary to extend *ad* above the free surface.

Stellenbosch University http://scholar.sun.ac.za

CHAPTER 3

EXPERIMENTAL SETUP AND PROCEDURES

This section gives a detailed description of the experimental apparatus used and the procedures followed during experiments.

3.1 2-D Test Rig

Barnard (1999) has done most of the detail design of the test rig as part of his final year project.

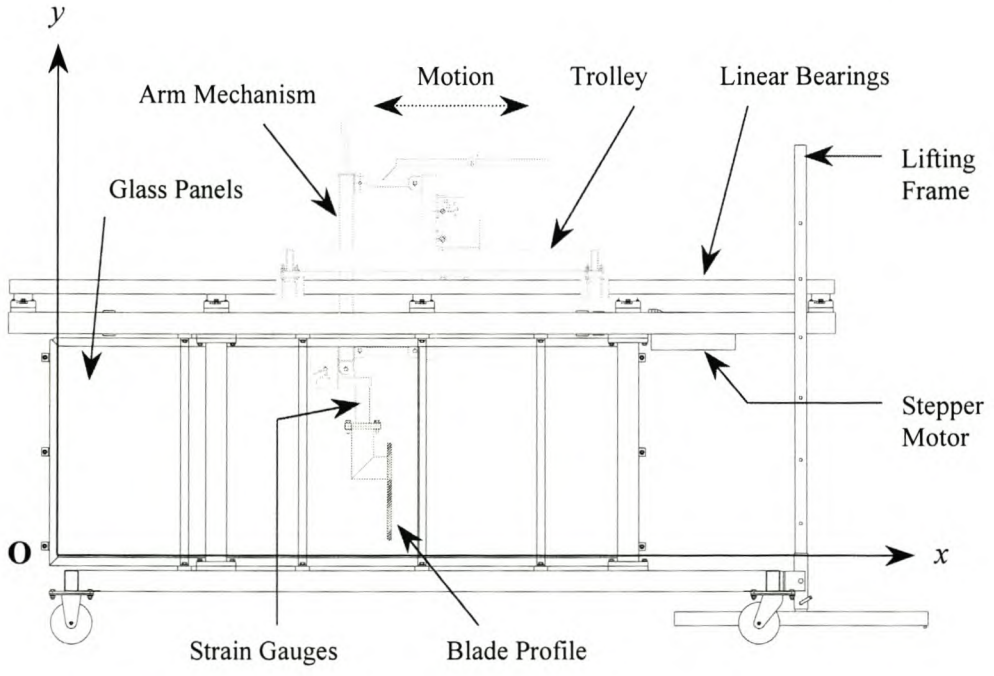

Figure 3.1 - *2-D test rig*

Figure 3.1 shows the main components of the test rig. Two glass panels (2200 × 820 mm) are mounted on the base structure. The distance between these two panels is about 200 mm and is slightly adjustable (±20 mm) to ensure that the profile is lined up between the two panels. The one panel (viewing side) consists of two glass sheets, one 10 mm and one 6 mm thick. The 10 mm glass is to resist the high lateral pressures created by the material being pushed forward by the blade. The 6 mm glass

Stellenbosch University http://scholar.sun.ac.za

sheet can easily be replaced if it gets scratched. The other panel (non-viewing side) consists of a 3 mm steel sheet and a 6 mm glass sheet. The steel mainly resists the lateral pressure while the function of the glass is only to get the friction on both contact sides the same.

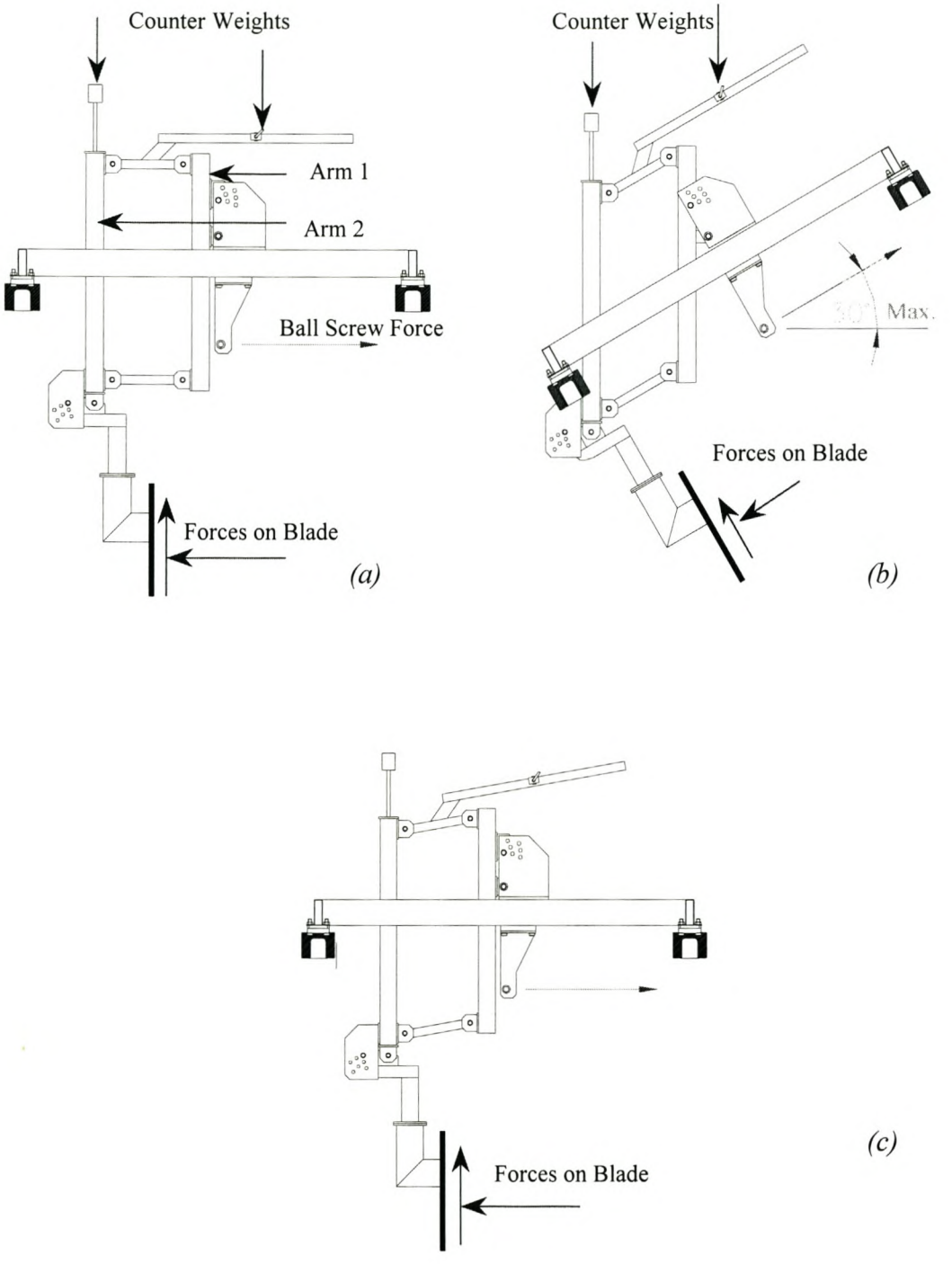

Figure 3.2 - *Arm mechanism*

Stellenbosch University http://scholar.sun.ac.za

The profile is attached to the trolley via a system of arms. The trolley is mounted on two sets of linear ball bearings (*SKF LUCT* ϕ 50 mm). A stepper motor connected to a ball screw moves the trolley forwards and backwards. Figure 3.2 shows the use of the arm-mechanism. When ground-engagement tools such as dragline buckets are used, the bucket must have freedom of motion in both the vertical and horizontal directions for 3-D simulations and at least freedom of motion in the vertical direction for 2-D simulations. The arm-mechanism allows freedom of motion in the vertical direction.

Arm 1 is always fixed to the trolley (Fig. 3.2a), while arm 2 can move freely in the vertical direction (Fig. 3.2c). Counter weights can be added at the positions indicated. This allows the weight of the bucket to be changed and the weight of the arms and linkages to be cancelled. For simulation of other ground-engagement tools such as bulldozer blades and cutting tools, arm 2 can be locked. It is possible, for further experiments, to control the y-velocity of the profile hydraulically or mechanically. This, however, is not used in this project.

The whole test rig can be inclined with the use of the lifting frame. This can be used to simulate the drag angle of draglines or any other tool working on an incline. The test rig can be inclined in steps of 5° up to a maximum of 30°. When the test rig makes an angle β with the horizontal, the two vertical arms are also at an angle β to the vertical. This means that the freedom of motion is no longer in the vertical direction. To overcome this problem arm 1 can be rotated relative to the trolley as in Fig. 3.2(b). This ensures that arm 2 stays in a vertical position. Further, the angle of the profile relative to vertical arm 2, i.e. the attack angle, can be changed since it is a parameter that influences the profile performance.

The profiles are fitted with two wipers, one on each side, to prevent particles from "leaking" past the profile. If particles were allowed to pass between the profile and the glass, the glass could be damaged and the true 2-dimensional flow patterns would not be visible. Figure 3.3 shows the use of the wipers on the blade. Each Teflon wiper fits into a slot in the side of the blade. Six studs (ϕ 3 mm) are threaded into the "bottom" of the slot. A coil spring is inserted over each stud and the Teflon, with drilled holes at the position of each stud, is inserted into the slot. The springs push the

Stellenbosch University http://scholar.sun.ac.za

Teflon outward against the glass to prevent any particles passing between the blade and the glass. The bucket is fitted with similar wipers.

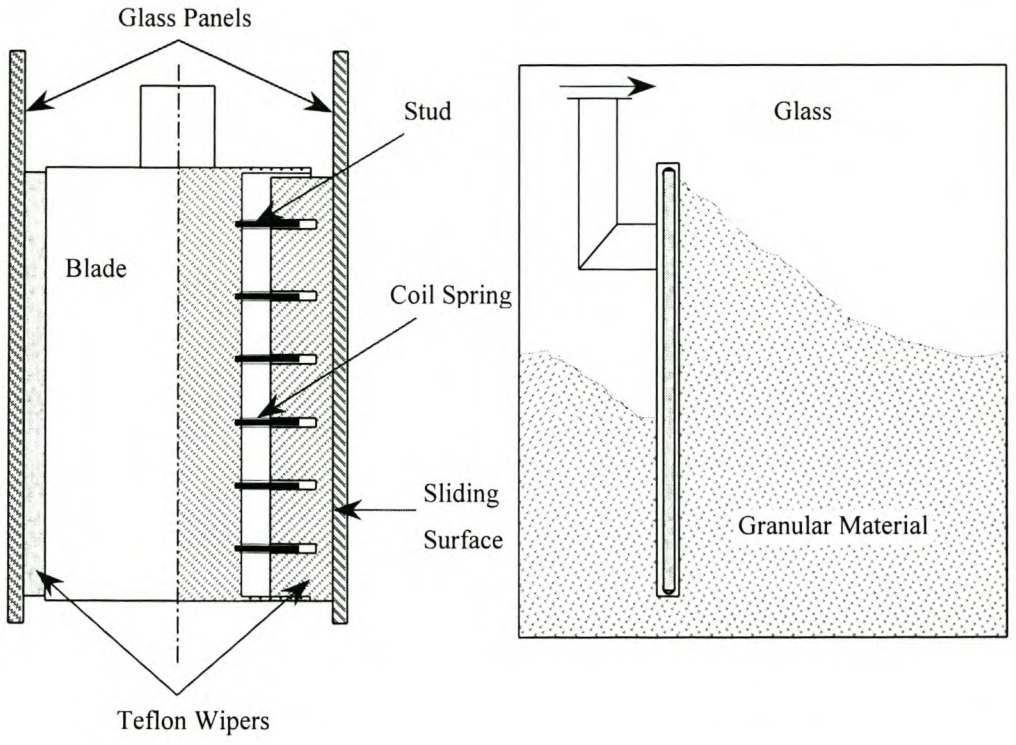

Figure 3.3 - *Blade with wipers*

3.2 Motion Control

A *STEBON 35/SDT1103-120-150 L* stepper motor fitted with a *HOHNER* incremental shaft encoder is used. The motor's maximum holding torque is 13 Nm. Figure 3.4 shows a schematic representation of the motion control setup.

Stellenbosch University http://scholar.sun.ac.za

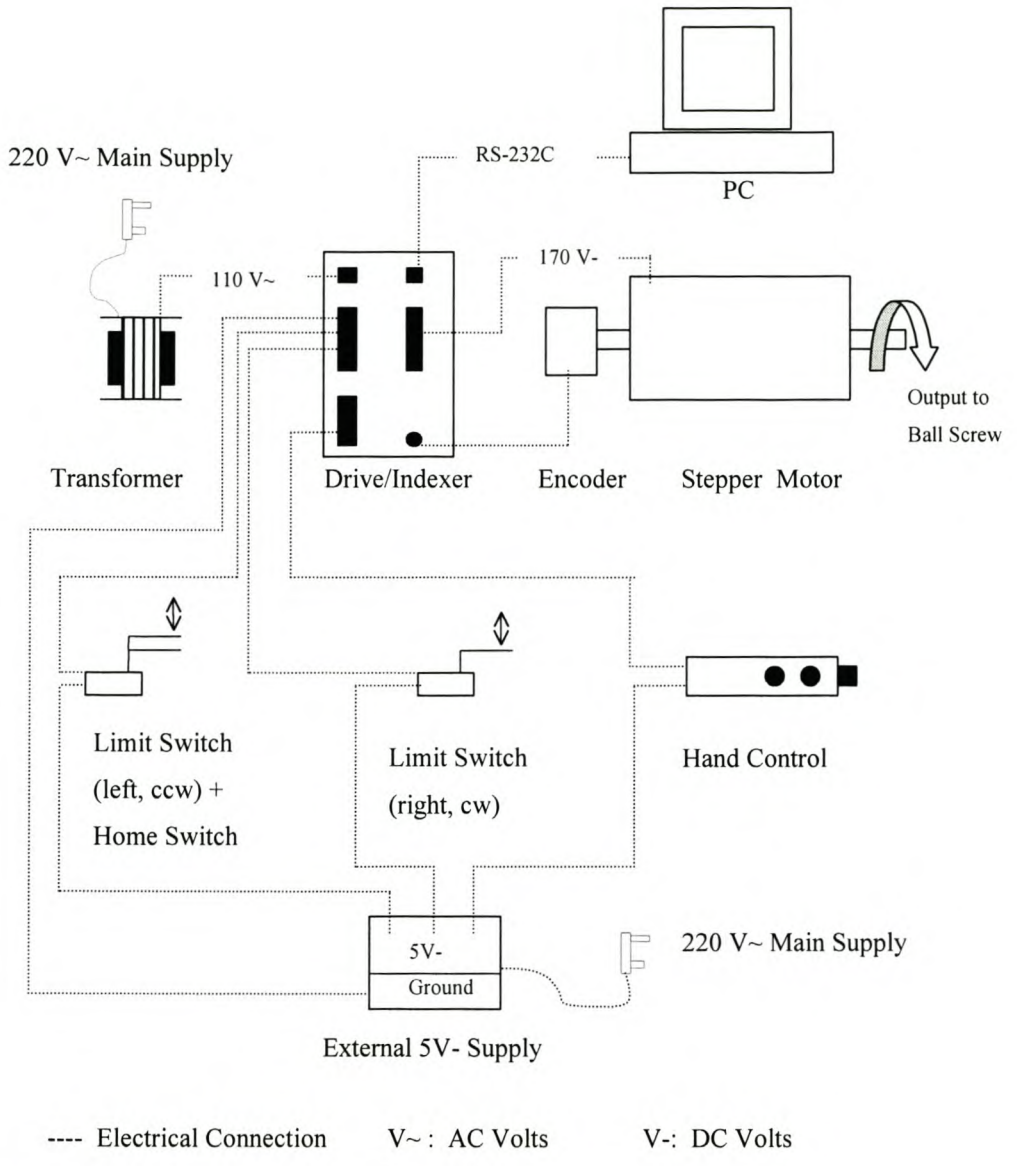

Figure 3.4 - *Motion control schematic*

The motor is driven by a *COMPUMOTOR SX8* microstepping drive/indexer. The drive is connected to a transformer with a rated output of 110 V~ 8 A. The drive is easily programmed over an RS-232C interface. *Compumotor's* X-programming language is used to program the drive to perform specified sequences. This programming is similar to the *G*-code*s* used to program CNC machines.

A sequence of commands can be programmed and stored in the drive's memory. This sequence can then be performed by simply sending the sequence's number to the drive via the RS-232C interface.

Stellenbosch University http://scholar.sun.ac.za

The drive has a 5 Volt DC internal power supply that is primarily designed to power an encoder. An external 5 Volt DC supply is used as power supply for all I/O switches. The rig is set up so that a clockwise rotation of the motor results in a movement of the trolley from left to right. The drive has two dedicated hardware end-of-travel limits, clockwise (CW, right) and counter-clockwise (CCW, left). These normally closed limit switches are attached to the linear bearing shafts and the position thereof can be changed. If the power supply to these switches would fail, the motor will stop immediately. A normally open home switch is also attached to the left side of the rig. This switch is used to start every cycle at the same position. A hand-held control with three normally closed switches is used to control the motion of the motor during simulations.

3.3 Test Rig Nomenclature

The coordinate system used is indicated in Fig. 3.1. The origin is in the lower left corner of the glass box with the x-axis in the direction of trolley displacement. This coordinate system is fixed to the test rig in such a way that if the rig is tilled the coordinate system will also be tilled. In this way the experimental setup is exactly the same as the numeric model. When the rig is in the horizontal position the gravity components will simply be $(g_x, g_y) = (0, -9.81)$ and when the rig is tilled it will be $(g_x, g_y) = (-9.81 \cdot \sin\beta, -9.81 \cdot \cos\beta)$ where β is the angle of the rig with the horizontal.

The blade force components that are of interest are as follows:

- F_x, blade force in the x-direction, often called the *draft* force
- F_y, blade force in the y-direction
- F_n, the force acting normal to the blade's face
- F_s, the force acting in the tangential direction on the face of the blade (shear force)
- F, the total blade force – vector sum of F_n and F_s or F_x and F_y
- M, the moment about point O (Fig. 3.8)

Stellenbosch University http://scholar.sun.ac.za

Note: All force components are defined as the force exerted *by* the blade *on* the material. It will be stated clearly if a force is the force exerted by the granular material on the blade (e.g. in some graphs). Force F_x and F_y are taken to be positive in the direction of the positive axis and the moment is positive in the counter-clockwise direction (right hand rule). F_n and F_s are taken to be positive in the directions they are shown in Fig. 3.5(a). If the blade angle a is equal to 90°, $F_x = F_n$ and $F_s = F_y$. The total force acting on the blade can be resolved into two components: either F_n and F_s or F_x and F_y. Experimentally the moment M is measured at the point O as in Fig. 3.8. In the numeric model the moment of forces is taken about the same point and thus the two results can be easily compared.

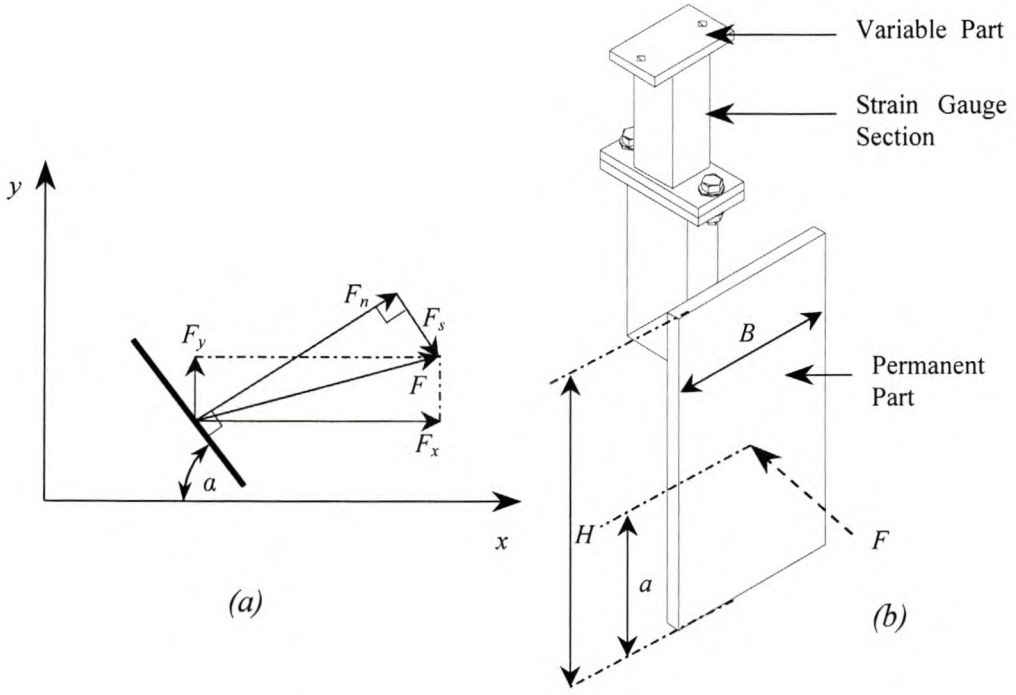

Figure 3.5 - *Blade assembly and forces*

The blade assembly is shown in Fig. 3.5(b). It consists out of two main parts. The permanent part is only changed if another profile is to be tested. The variable part is a 130 mm long square tubing with strain gauges bonded to it. For this force transducer to be sensitive enough, tubing with the correct dimensions must be chosen according to the magnitude of the forces that act on the profile. The profile is attached to the trolley with two bolts through the top flange of the variable part. The total height of the profile is defined as H while the total width is B. The total force F works in on a

Stellenbosch University http://scholar.sun.ac.za

distance a from the bottom edge of the blade. The ratio a/H is defined as b. h is the initial distance that the profile's bottom edge is below the horizontal free surface of the granular material, i.e. the immersed depth and $d = h/H$ (Fig. 3.6). D is the average fill height of the test rig before any motion of the profile. This height is used to determine the average fill density of the assembly. The total length of the test rig is 2.2 m. The velocity of the trolley is V_x and will always be in the direction of the x-axis. If the arm assembly is locked, the profile will have no velocity in the y-direction.

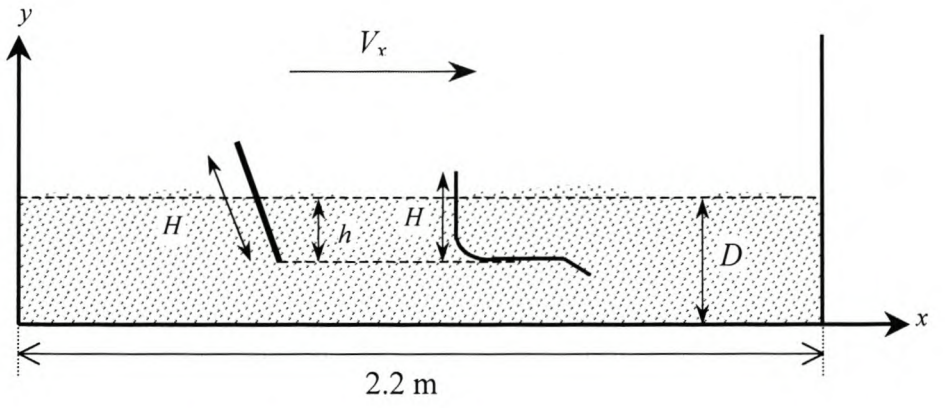

Figure 3.6 – *2-D rig definitions*

Figure 3.7 shows the bucket with the definition of positive forces. It is not possible to break the total force up into shear and normal components, as is the case for the blade. It is only the force in the x-direction, the y-direction and the moment about point O that are of interest.

Stellenbosch University http://scholar.sun.ac.za

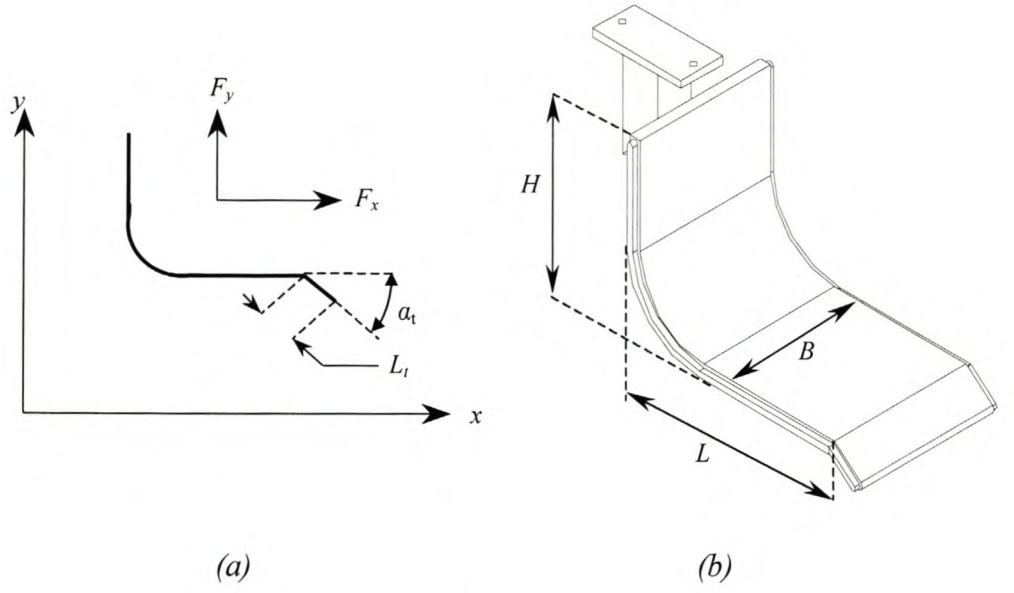

Figure 3.7 - *Bucket assembly and forces*

3.4 Force Measurement

Two different ways to measure the forces on the blade have been tested. Both methods make use of strain gauges, but it is the position where some of the gauges are bonded that differs.

3.4.1 First Method

As stated above, strain gauges are bonded to the square tubing of the force transducer. If F_n, F_s and M are known, all other force components (F_x, F_y) and the distance a can be determined. Figure 3.8(a) shows the positions of the strain gauges and the distances to where the forces act on the profile. Three sets of strain gauges are used: one to measure the total moment about point O, one to measure the axial force F_s in the tube and the other to measure the normal force F_n. Figure 3.8(b) shows the well-known Wheatstone bridge connection. The strain gauges in the bridge are numbered 1 to 4 and these numbers correspond to the numbers assigned to the gauges in Fig. 3.8(a).

Stellenbosch University http://scholar.sun.ac.za

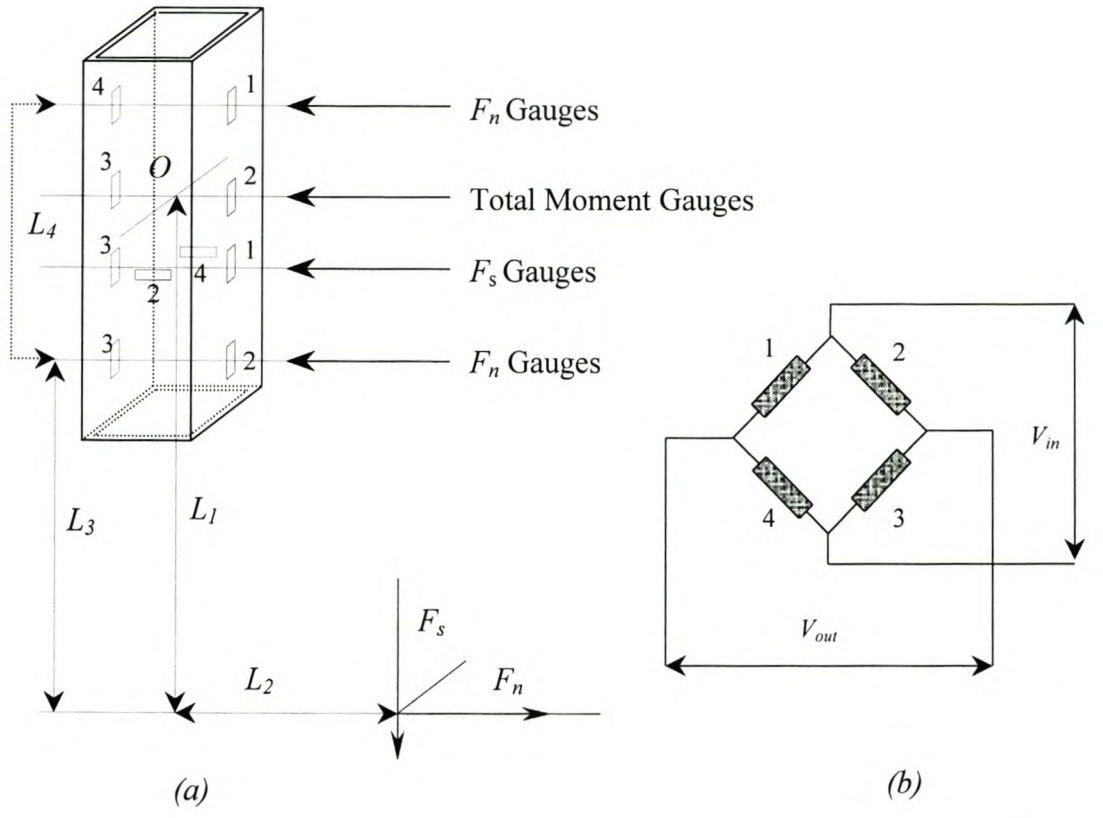

Figure 3.8 - *Strain Gauges*

For the Wheatstone bridge the following relation holds:

$$\frac{V_{out}}{V_{in}} = \frac{K_s}{4}(\varepsilon_1 - \varepsilon_2 + \varepsilon_3 - \varepsilon_4) \tag{3.1}$$

where V_{out} and V_{in} are the output and input voltages of the bridge respectively. K_s is the so-called strain gauge *k-factor* and the ε's are the strain experienced by each gauge respectively.

Two gauges are used to measure the total moment about point *O*. These two gauges are connected to a half-bridge where the two other gauges are substituted by resistors within the bridge amplifier. Gauge 1 and 2 will experience the same strain but opposite in sign and from Eq. 3.1 it can be seen that these two values will add up to give

Stellenbosch University http://scholar.sun.ac.za

$$\frac{V_{out}}{V_{in}} = \frac{K_s}{2}\varepsilon \tag{3.2}$$

where ε is the magnitude of the strain experienced by one of these gauges. Let Z be the beam's cross section modulus [m^3] in the bending direction, then the magnitude of the stress in the beam as experienced by the gauges is given by

$$\sigma = \frac{M}{Z} \tag{3.3}$$

Using *Young's modulus E*, the strain can be written as

$$\varepsilon = \frac{M}{E\,Z} \tag{3.4}$$

Substituting this back into Eq. 3.2 yields the final result.

$$\frac{V_{out}}{V_{in}} = \frac{K_s\,M}{2\,E\,Z} \tag{3.5}$$

The output of the bridge is directly proportional to the moment M. This connection to measure the moment is compensating for any axial force and torque since gauges 1 and 2 will measure the same strain in magnitude and sign during these loading conditions.

A set of four gauges is used to measure the axial force in the beam, i.e. F_s. These gauges are bonded in a *Poisson* fashion as can be seen in Fig. 3.8(a). Gauges 1 and 3 will measure the same strain ε (magnitude and sign) while gauges 2 and 4 will each measures $-\nu\varepsilon$, where ν is *Poisson's ratio*. Substituting these values into Eq 3.1 gives

$$\frac{V_{out}}{V_{in}} = \frac{K_s\,\varepsilon}{2}(1+\nu) \tag{3.6}$$

The strain in the beam due to the axial force F_s is

Stellenbosch University http://scholar.sun.ac.za

$$\varepsilon = \frac{F_s}{E\,A_{cross}} \tag{3.7}$$

where A_{cross} is the sectional cross-area. Substituting into Eq. 3.6 gives

$$\frac{V_{out}}{V_{in}} = \frac{K_s\,F_s}{2\,E\,A_{cross}}(1+\nu) \tag{3.8}$$

This configuration is compensating for any moment.

To measure F_n a set of four gauges is used. Two gauges are bonded near the top edge of the beam and the other two near the bottom edge. The distance L_4 between these two subsets of gauges is fixed and so is the distance L_2. The strain experienced by the gauges is as follows

$$\varepsilon_4 = -\varepsilon_1 = \frac{F_n(L_3 + L_4) - F_s L_2}{EZ}$$

$$\varepsilon_3 = -\varepsilon_2 = \frac{F_n L_3 - F_s L_2}{EZ} \tag{3.9}$$

Substituting this back into Eq. 3.1 gives the final result

$$\frac{V_{out}}{V_{in}} = \frac{-K_s\,F_n\,L_4}{2\,EZ} \tag{3.10}$$

Thus the output is only dependent on the variable F_n. L_3 does not feature in this equation and the output is independent of the line of action of the force F.

To determine the line of action of the force F, the moment (Eq. 3.5) comes into play. The moment in Eq. 3.5 can be written as

$$M = -F_s L_2 + F_n L_1 \tag{3.11}$$

Stellenbosch University http://scholar.sun.ac.za

Since M is known from Eq. 3.5, F_s from Eq. 3.8, F_n from Eq. 3.10 and L_2 is always known, the length L_1 can be solved.

$$L_1 = \frac{M + F_s L_2}{F_n} \tag{3.12}$$

The force application height a can now easily be solved since the dimensions of the whole assembly is known.

To summarise:

- F_s is calculated by Eq. 3.8
- F_n is calculated by Eq. 3.10
- M is calculated by Eq. 3.5
- L_1 (and subsequently a) is determined by Eq. 3.12

Each set of strain gauges was calibrated individually by applying dead weights. The calibration curves for the shear force F_s and the moment M proved to be linear. The measurement of the normal force F_n was, however, insensitive and non-linear.

3.4.2 Second Method

Figure 3.9 shows the position where the strain gauges are bonded to the trolley assembly. A set of four strain gauges is bonded to the two vertical arms connecting the trolley to the ball screw.

The ball screw goes through the ball nut, which is located in the box. The block pivots around the pin that connects the block to the trolley. The ball screw is aligned with the linear bearings and thus the motion of the trolley. This means that the force exerted by the ball screw-nut on the trolley will always be parallel to the direction of the trolley.

Stellenbosch University http://scholar.sun.ac.za

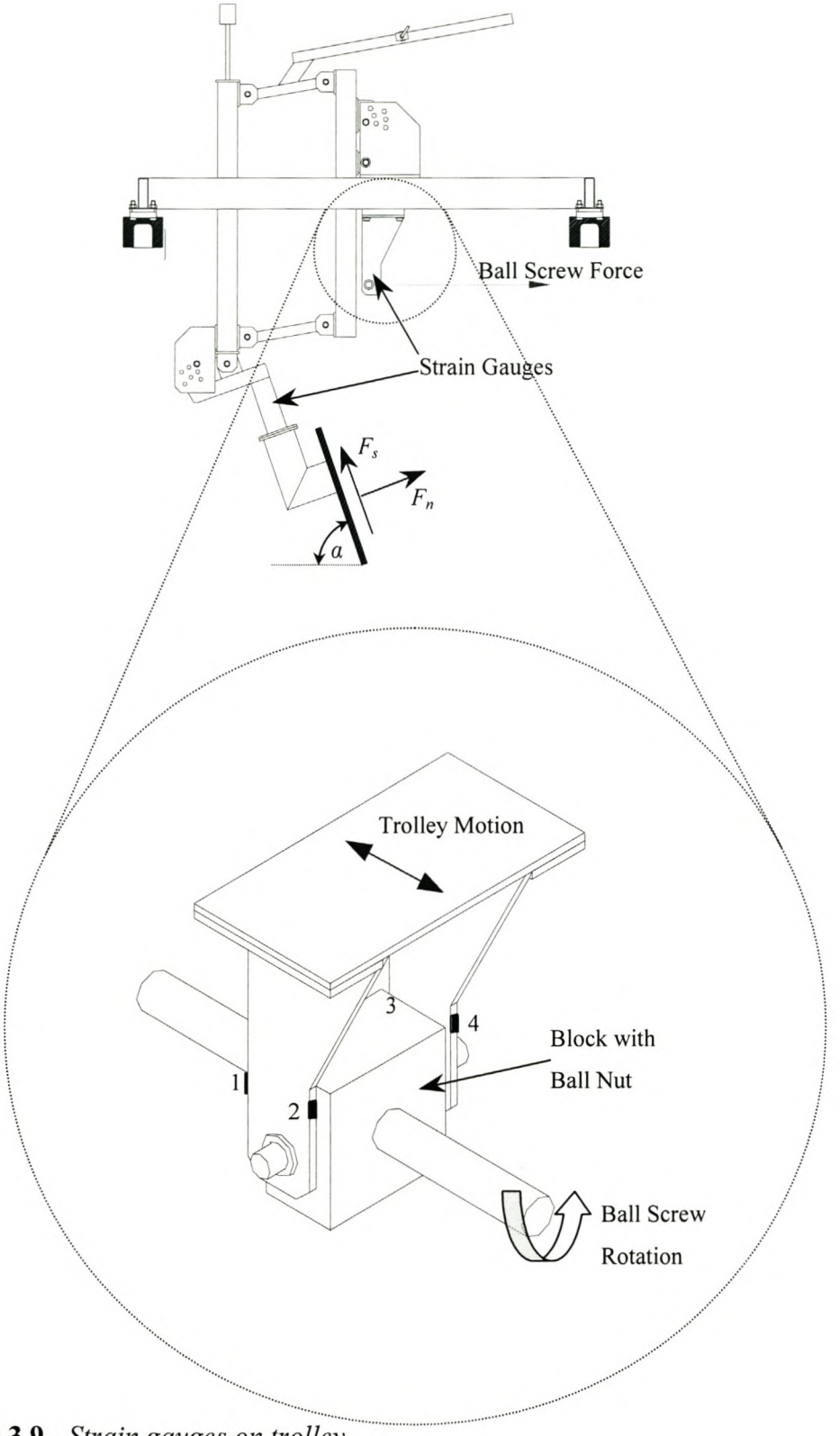

Figure 3.9 - *Strain gauges on trolley*

The strain gauges are numbered 1 to 4. The set of gauges actually measures the bending moment on the two arms, but because the line of action and the application point of the force are fixed, the output is proportional to the force exerted by the ball screw on the trolley. The bridge output will be

Stellenbosch University http://scholar.sun.ac.za

$$\frac{V_{out}}{V_{in}} = K_s \varepsilon \tag{3.13}$$

where ε is the strain experienced by each gauge. The strain can be written as

$$\varepsilon = \frac{M}{E Z} \tag{3.14}$$

which is the same as Eq. 3.4. Substituting into Eq. 3.13

$$\frac{V_{out}}{V_{in}} = \frac{K_s M}{E Z} \tag{3.15}$$

The moment is directly proportional to the force F_x and so is the bridge output.

$$\frac{V_{out}}{V_{in}} \propto \frac{K_s F_x}{E Z} \tag{3.16}$$

The gauges bonded to the square tubing (First Method) are still used to determine the shear force F_s and the moment M. The gauges bonded to the trolley (Second Method) are used to determine F_x.

The friction of the linear bearings is minimal, but by zeroing the bridge while the trolley is running (with no load on the profile) the effect of the friction can be cancelled. By using Eq. 3.8 the shear force F_s can be determined. The force F_x is known from Eq. 3.16 and by equating the sum of the forces in the x-direction

$$\sum F_x : \quad F_x = F_n \sin\alpha + F_s \cos\alpha$$

or

$$F_n = \frac{F_x - F_s \cos\alpha}{\sin\alpha} \tag{3.17}$$

The moment M is calculated by Eq. 3.5 and the distance L_1 and subsequently the distance a by Eq. 3.12. With F_n , F_s and a known, F_y can easily be determined.

Stellenbosch University http://scholar.sun.ac.za

For the bucket only two force components and one moment are of interest. Figure 3.10 shows the two force components F_x and F_y. These components are measured in exactly the same way that it is measured on the blade. With the two components known, the magnitude and direction of the total force can be calculated

$$\tan(\theta) = \frac{F_y}{F_x} \tag{3.18}$$

where θ is the angle the total force makes with the x-direction.

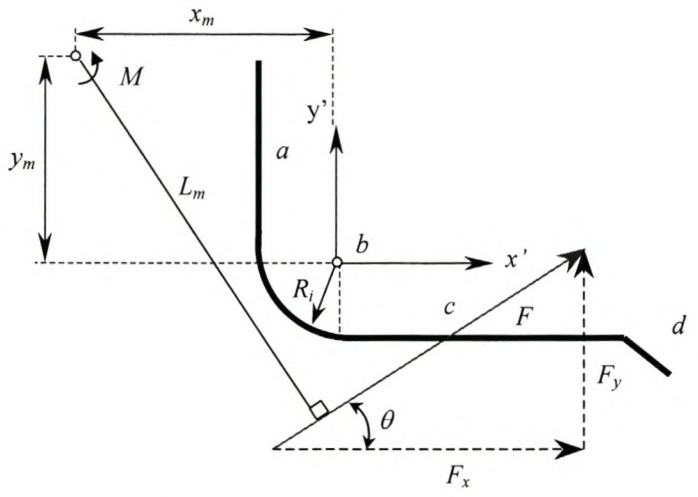

Figure 3.10 - *Bucket forces*

It is possible to calculate the force application point on the bucket. With the total force and moment known, the moment arm L_m can be calculated to be

$$L_m = \frac{M}{F} \tag{3.19}$$

The local coordinate system $x'y'$ has its origin at the centre of the circular arc. The coordinates of the intersection point between the line L_m and the line containing the force vector are

$$\begin{aligned} x_i' &= L_m \sin(\theta) - x_m' \\ y_i' &= y_m' - L_m \cos(\theta) \end{aligned} \tag{3.20}$$

Stellenbosch University http://scholar.sun.ac.za

where x'_m and y'_m are defined in the figure. The equation of the line containing the total force vector can be written as

$$y' = \tan(\theta)x' + (y'_i - \tan(\theta)x'_i) \tag{3.21}$$

The bucket is divided into four parts numbered from *a* to *d*. The equation for each part is as follows.

$$x' = -R_i \qquad 0 \le y' \le (H - R_i) \qquad \text{for part } a \tag{3.22}$$

$$y' = \pm\sqrt{R_i^2 - x'^2} \qquad x < 0; \quad y < 0 \qquad \text{for part } b \tag{3.23}$$

$$y' = -R_i \qquad 0 \le x' \le (L - R_i) \qquad \text{for part } c \tag{3.24}$$

$$y' = -\tan(\alpha_t)x' + [\tan(\alpha_t)(L - R_i) - R_i]$$

$$(L - R_i) \le x' \le (L - R_i + L_t\cos(\alpha_t)) \qquad \text{for part } d \tag{3.25}$$

R_i is the inside radius of the circular arc and L_t and a_t are the tooth length and angle respectively. By solving Eq. 3.21 with each of the Eqs. 3.22 to 3.25 the coordinates of the application point can be determined. After some manipulation the solved results are presented below.

$$y'_{app} = -\tan(\theta)R_i + y'_i - \tan(\theta)x'_i \qquad \text{for part } a \tag{3.26}$$

and if $0 \le y'_{app} \le (H - R_i)$, the x'-coordinate will be $x'_{app} = -R_i$.

$$x'_{app} = \frac{-1}{1 + \tan^2(\theta)}\left(\tan(\theta)y'_i - \tan^2(\theta)x'_i \right.$$
$$\left. \pm\sqrt{R_i^2\left(1 + \tan^2(\theta)\right) - \tan^2(\theta)x_1'^2 - y_i'^2 + 2y'_i x'_i\tan(\theta)}\right) \tag{3.27}$$

Stellenbosch University http://scholar.sun.ac.za

for part b, and if $x' < 0$ and $y' < 0$, x'_{app} can be solved by using either Eq. 3.21 or Eq. 3.23.

$$x'_{app} = \frac{-(R_i + y'_i - \tan(\theta)x'_i)}{\tan(\theta)} \qquad \text{for part } c \tag{3.28}$$

and if $0 \le x'_{app} \le (L - R_i)$, $y'_{app} = -R_i$.

$$x'_{app} = \frac{[\tan(\alpha_t)(L - R_i) - R_i] - [y'_i - \tan(\theta)x'_i]}{\tan(\theta) + \tan(\alpha_t)} \qquad \text{for part } d \tag{3.29}$$

and if $(L - R_i) \le x'_{app} \le (L - R_i + L_t \cos(\alpha_t))$, y'_{app} will be given by Eq. 3.21.

3.5 Calibration

To obtain good experimental results it is necessary to do a thorough calibration of the force transducers. All three transducers, x-force, y-force and moment, were calibrated by using dead weights. All the calibrations were performed using loads within the range that would be experienced during typical simulations. The calibration curves (Fig. 3.11 to Fig. 3.13) have proved to be linear and identical over long periods.

Stellenbosch University http://scholar.sun.ac.za

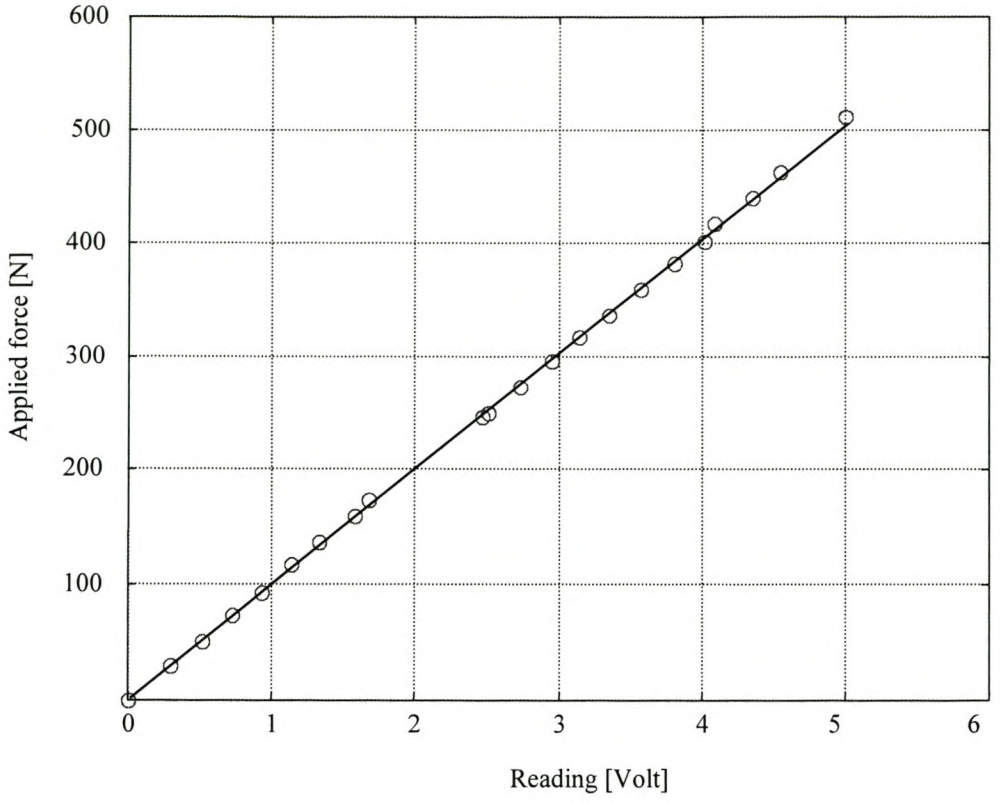

Figure 3.11 – *Draft force calibration curve*

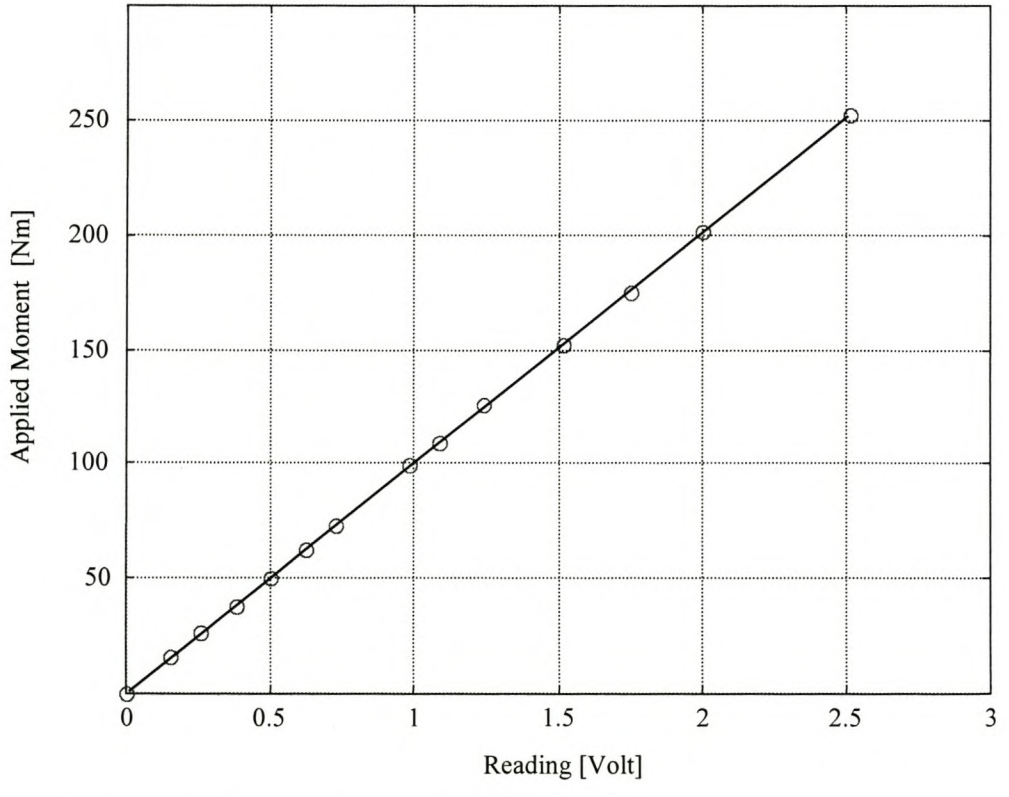

Figure 3.12 – *Moment calibration curve*

Stellenbosch University http://scholar.sun.ac.za

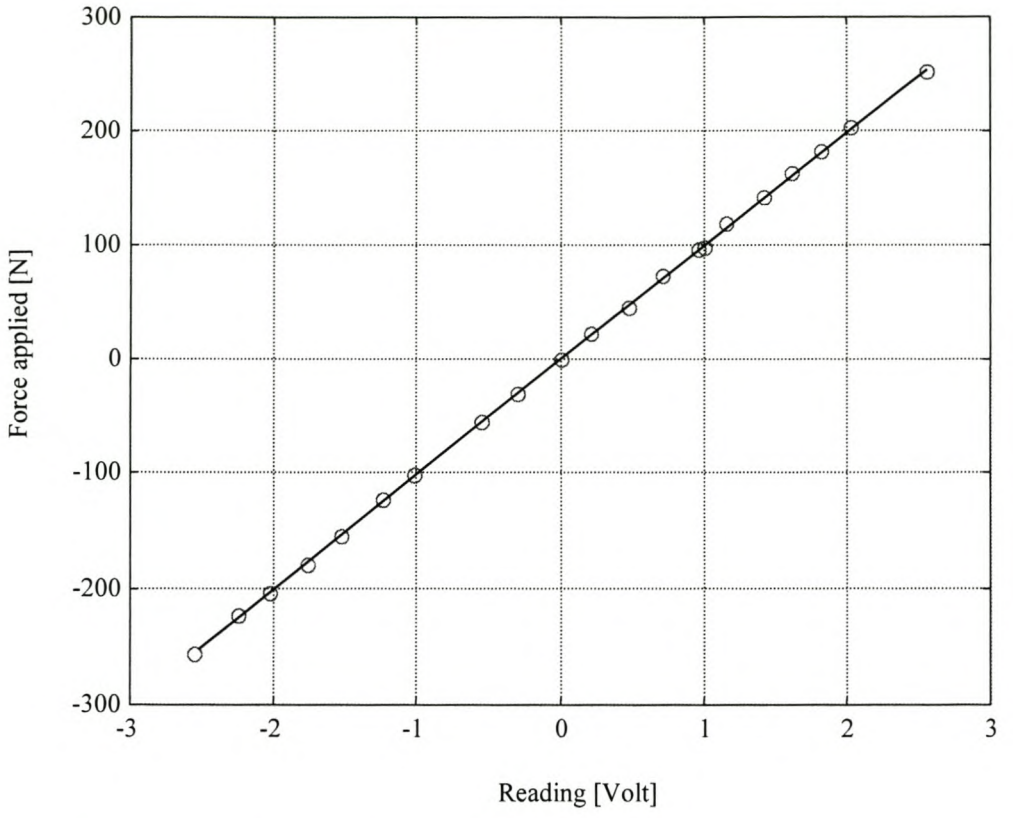

Figure 3.13 – *Shear force calibration curve*

The following calibration relations hold

$$\begin{aligned} F_x(N) &= 100.998 \cdot V_{out} \\ M(Nm) &= 100.456 \cdot V_{out} \\ F_s(N) &= 99.857 \cdot V_{out} \end{aligned} \tag{3.30}$$

where V_{out} is the reading on the bridge amplifier.

3.6 Data Acquisition

A HBM bridge amplifier is used to amplify the signals from the force transducers. The amplified signals are connected to a personal computer via a filter and an analog-digital card. A signal from the encoder is used to determine the exact position of the trolley and a linear displacement sensor is used to determine the profiles' vertical displacement.

Stellenbosch University http://scholar.sun.ac.za

CHAPTER 4

NUMERICAL SIMULATION AND CALIBRATION

Numerical simulation models have been applied successfully in many engineering applications. Commonly known examples are Finite Element Methods (FEM) and Computational Fluid Dynamics (CFD). Less known is the Discrete Element Method or (DEM). This method, in general, simulates the mechanical behaviour of a system of arbitrarily shaped bodies. The distinct particles displace independently from one another and interact only at contacts with other particles and/or walls.

4.1 The Numerical Method

DEM was introduced by Cundall (1971) for the analysis of rock-mechanics problems and then applied to soils by Cundall and Strack (1979). To develop your own DEM code can be time-consuming and expensive. Commercial packages are available and PFC^{2D} from *Itasca Consulting Group, Inc* has been used for all simulations.

PFC^{2D} models the movement and interaction of stressed assemblies of rigid circular particles using DEM. The particles are assumed to be rigid and a soft contact approach is used in which a finite normal and tangential stiffness is taken to represent the measurable stiffness that exists at a contact. Much more complex behaviour can be modelled by introducing cohesion and adhesion through contact and parallel bonds. This is accomplished by allowing the particles to be bonded together at their contact points. These bonds can be broken when the magnitude of the contact force exceeds the bonding strength. Coulomb friction theory is used to dissipate energy at contacts.

The following particle properties exist in a PFC^{2D} model (using the linear contact law):

- k_n, particle stiffness in the contact normal direction, [N/m]
- k_s, particle stiffness in the contact tangential direction, [N/m]
- μ, particle Coulomb friction coefficient

Stellenbosch University http://scholar.sun.ac.za

- ρ, particle material density, [kg/m^3]
- r, the particle radius, [m]

Contact bonds are created at contacts:

- F^n_{con}, normal contact bond strength, [N]
- F^s_{con}, shear contact bond strength, [N]

and parallel contact bonds are defined by:

- $k^n_{(p)}$, bond normal stiffness, [N/m^3]
- $k^n_{(p)}$, bond shear stiffness, [N/m^3]
- $\sigma_{(p)}$, normal strength, [N/m^2]
- $\tau_{(p)}$, shear strength, [N/m^2]
- $R_{(p)}$, bond radius, [m]

As default, *PFC*^{2D} uses non-viscous damping with a damping value of 0.7. A detailed description of DEM is given in Appendix B.

4.2 The Calibration Process

Although it is relatively easy to assign chosen properties to a model, it is often difficult to choose such properties so that the behaviour of the resulting synthetic material resembles that of an intended physical material. A calibration process in which the response of the synthetic material is compared directly with the measured response of the physical material is needed to determine the appropriate micro-properties. This comparison can be made at both laboratory and field scale. The following quotation from Itasca (1999) shows that the calibration process is not straightforward: "It should be noted that our current understanding of this calibration process is still incomplete – i.e., we still do not now how to construct a *PFC* material that produces a given strength

Stellenbosch University http://scholar.sun.ac.za

envelope or one that reproduces a given ratio of unconfined compressive strength to Brazilian tensile strength."

Due to practical difficulties, only frictional materials were thoroughly investigated and no friction-cohesion materials. This left only the particle size, shape and density, the particle stiffness and friction to be determined. Calibration for this thesis was performed in four steps.

- First the particle size, shape and density were determined experimentally and directly used in the numeric model.
- Secondly, a *confined compression* test was performed to determine the material stiffness. Other names for this test are *one-dimensional compression test, consolidation test* and the *oedometer* test.
- The second test was a shear test in which a shearbox was used to determine the strength envelope.
- As a final check, the angle of repose of the material was determined experimentally and numerically.

The material-steel friction coefficient δ_m was determined by replacing the lower half of the shearbox with a steel sheet. A series of iterative numeric experiments or simulations equivalent to those described above were performed until the results closely resembled those of the experiments.

The rest of this chapter describes each calibration process in more detail and gives some general aspects regarding the soil tool simulations.

4.3 Particle Size, Shape and Average Density

Simulating relatively small systems and large particles make it possible to use the real physical size of the particles in the numeric model. With large systems, such as a full-scale bulldozer pushing a heap of sand, it is impossible to make the particles in the model the same size as in the physical system. This will simply take too much running time. Fortunately it is not necessary to make use of the physical size of the particles; the

Stellenbosch University http://scholar.sun.ac.za

size and shape of the particles are just parameters that influence the macro-behaviour of the whole system. On the other hand, DEM can also be used to simulate the behaviour of solid materials. Itasca (1999) has shown that the strength and cracking behaviour of hard rock, like granite, can be predicted using discrete particles. These simulations were conducted using a sample of 550 and 4900 bonded particles. The results were only slightly affected by particle size.

The average material density was measured by filling a cylindrical container with material. The container with material was weighed and the internal dimensions of the container measured to calculate the volume. The bulk density was simply defined as the mass of material divided by the volume occupied. The material was poured into the container from a low height to obtain a loose or low-density state similar to the filling of the 2-D test rig.

Seed grains are suitable for experimental testing and closely resemble natural granular flow (Rowlands, 1991). The grains have a relatively low friction coefficient with glass, which makes it a perfect experimental material for testing in the 2-D rig. No problems were encountered with high lateral forces and subsequent damage of the glass panels as was the case with granite gravel. Seed grains were also suitable for numeric simulations because the stiffness of the grains was less than the stiffness of gravel. The smaller stiffness resulted in a larger time step. For a close-packed assembly the stable time step is roughly inversely proportional to the particle stiffness.

4.3.1 Corn

Figure 4.1 shows a picture of the corn used. All of the grains have a "tear drop" shape but differ in size. The size range is given in Fig. 4.2(a); this is the maximum and minimum measured dimension. The first approach was to make use of single circular particles. It was, however, impossible to calibrate these particles to behave similarly to the physical material in all tests. The second approach was to make use of "clumps".

Clump logic provides a means to create and modify groups of slaved particles. A clump behaves as a rigid body; i.e. the particles comprising the clump remain at a fixed

Stellenbosch University http://scholar.sun.ac.za

distance from each other. Particles within a clump may overlap to any extent and contact forces are not generated between these particles. Clumps will not break up during simulations regardless of the forces acting upon them. Figure 4.2(b) shows the chosen clump dimensions.

Figure 4.1 - *Corn*

Each circular particle radius and the centre distance were picked from a uniform distribution within the given range. Using dimensions that represent the physical size of the grains eliminated one of the calibration variables, namely the particle size and shape.

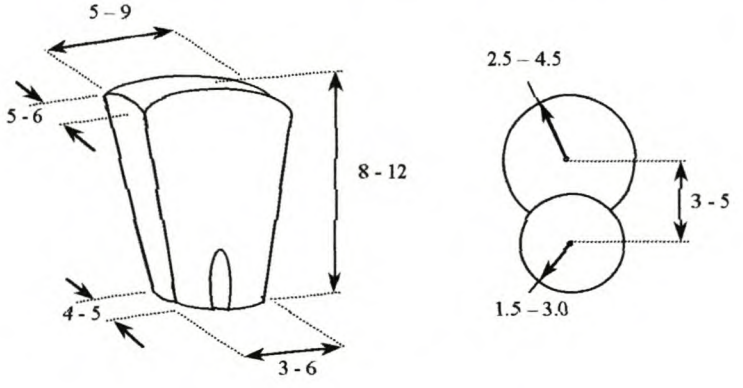

Figure 4.2 – *Corn grain dimensions (mm) and numeric representation*

Stellenbosch University http://scholar.sun.ac.za

The average density of the material was measured and used as input for the numerical model. The density obtained was 778 kg/m^3. Particles could be modelled as either spheres or cylinders (disks).

The particle type only influences the total mass of the particle and the moment of inertia. The principal moment of inertia of a cylindrical particle is 25% higher than the inertia of a spherical-shaped particle with the same total mass and radius. Using spherical-shaped particles makes it difficult to interpret the results.

Cylindrical particles with a width of 200 mm (width of 2-D test rig) were used in all the simulations. All particles were initially given a material density of 800 kg/m^3. The assembly of particles was then allowed to reach an equilibrium state and the average density calculated using the total mass of all the particles and the total volume occupied. Using an iterative procedure, the density of all the particles was changed until the average density was close to 778 kg/m^3. After each change in particle density the system had to be allowed to reach equilibrium again. This procedure converged within three to four iterations with the final average density within 0.1 kg/m^3 of the experimental value. The final particle density was 855 kg/m^3.

PFC^{2D} makes use of two ratios to determine whether the system is in an equilibrium state or not. These ratios are defined as

$$average\ ratio = \frac{average\ resultant\ force\ of\ all\ particles}{average\ contact\ force\ of\ all\ contacts} \tag{4.1}$$

$$maximum\ ratio = \frac{maximum\ resultant\ force\ of\ all\ particles}{maximum\ contact\ force\ of\ all\ contacts} \tag{4.2}$$

These ratios are checked after each cycle and when one of them falls below a prescribed value, cycling stops and the system is considered to be in equilibrium. Ratios of 0.0001 or 0.01% were used. An alternative method of establishing static equilibrium is to cycle the model until the total kinetic energy is negligible or the weight is equilibrated by the boundary forces (Bohatier and Nouguier, 1999).

Stellenbosch University http://scholar.sun.ac.za

4.3.2 Wheat

Figure 4.3 shows the wheat grains used in the experimental work. The grains have an elongated shape and Fig. 4.4 shows the maximum and minimum measured dimensions as well as the numeric equivalent grains used for numeric modelling.

Figure 4.3 - *Wheat*

The size of the numeric particle is influenced by only one parameter R that is chosen from a normal distribution. The two constitutive circular particles have the same radius due to the fact that the grains have a near symmetric shape. The average wheat density was measured as 703 kg/m^3. This average density required a particle density of 874 kg/m^3.

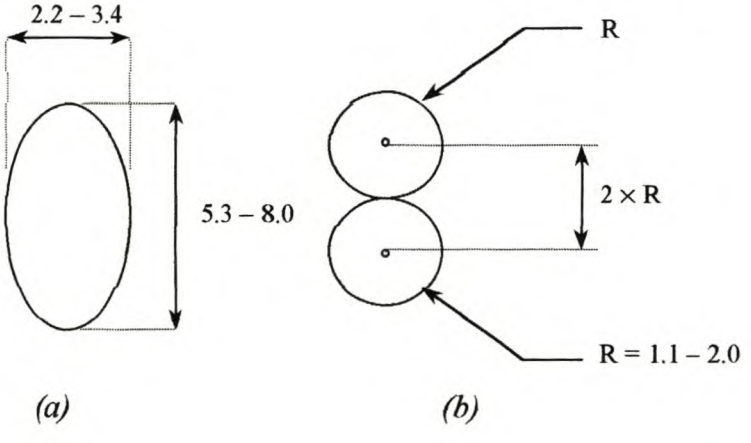

Figure 4.4 – *Wheat grain dimensions (mm) and numeric representation*

Stellenbosch University http://scholar.sun.ac.za

4.4 Confined Compression Test

Stresses set up in a granular material cause deformations (strains) of the material, which can occur in three ways.

- Elastic deformation of the particles.
- Change in volume resulting from the expulsion of fluid from the voids between the particles, known as consolidation.
- Slippage of particles, one on another, which may lead to sliding of one body of material relative to the surrounding mass, known as shear failure.

In the confined compression test, stress is applied to the soil specimen along the vertical axis, while strain in the horizontal directions is prevented. Shear stresses and shear strains as well as compressive stresses and volume changes occur in this test, but since the soil is prevented from failing in shear, compression is the dominant source of strain.

4.4.1 Background

The test is popular because it is relatively simple to perform and because the strain condition is approximately similar to one frequently encountered in actual problems. In the common form of the compression test the lateral stress developed is not measured.

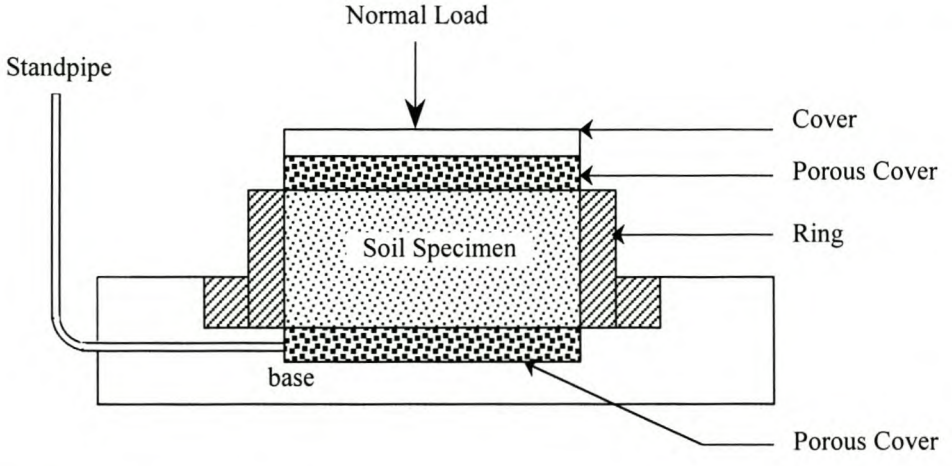

Figure 4.5 – *Fixed-ring oedometer*

Stellenbosch University http://scholar.sun.ac.za

Figure 4.5 shows a cross-sectional view through a typical oedometer. The major experimental difficulty with the test is side friction. Shear forces develop along the cylindrical surface of the specimen as vertical strains occur. To minimise the effect of these side friction forces the thickness-diameter ratio of the specimen is kept as small as practicable, usually 1:3 to 1:4. Use of a floating ring container also helps to minimise the effects of side friction.

Usually this test is used to determine the soil consolidation ratios. Here it has been used to determine the elasticity of the material, similar to a uniaxial tensile test on an elastic material. There are, however, differences between the confined compression test performed here and a uniaxial tensile test. During a uniaxial tensile test stress is applied in the axial z-direction. There is no stress in the *x*- and *y*-directions, but strain in all three directions, ε_z, ε_y and ε_x (Fig. 4.6). *Young's modulus of elasticity* is defined as

$$E = \frac{\sigma_z}{\varepsilon_z} \tag{4.3}$$

During confined compression the direct strain in the *x*- and *y*-directions is constrained to be zero. This has the result that normal stresses develop in the *x*- and *y*-directions. The well known stress-strain relation

$$\sigma_z = \frac{\nu E}{(1+\nu)(1-2\nu)}\left(\varepsilon_x + \varepsilon_y + \varepsilon_z\right) + \frac{E}{(1+\nu)}\varepsilon_z \tag{4.4}$$

together with the fact that $\varepsilon_x = \varepsilon_y = 0$ can be used to calculate the *confined Young's modulus E'*

$$\sigma_z = E\varepsilon_z\left(\frac{1-\nu}{(1+\nu)(1-2\nu)}\right)$$

$$\therefore E' = E\left(\frac{1-\nu}{(1+\nu)(1-2\nu)}\right) \tag{4.5}$$

Stellenbosch University http://scholar.sun.ac.za

where v is *Poisson's ratio*. It is the value of E' that was used to determine the particle stiffness.

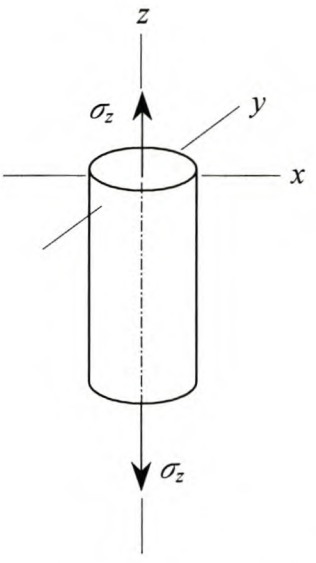

Figure 4.6 – *Uniaxial tensile test*

4.4.2 Experiments and Simulations

The experiments were performed with a ϕ250 mm cylinder and a specimen height of 80 mm. According to Head (1988) as a general rule, the particle size should not exceed one-tenth of the specimen height. Side friction will always play a role in this test and therefore it had to be included in the numeric model. The wall friction was set to the specific material-steel friction coefficient. Figure 4.7 shows typical experimental results obtained from unloading and reloading. Only a portion of the strain that occurs during initial loading is recovered during subsequent unloading. The strains that resulted from sliding between particle or from fracturing of particles are largely irreversible. The rebound upon unloading is caused by the elastic energy stored within the particles, as the assembly was loaded. However, there can be some reverse sliding between particles during unloading. Only a small amount of permanent strain results from the next two cycles. All experiments were performed with a low compression rate to avoid any dynamic effects, i.e. quasi-static conditions were assumed. Experiments were stopped after three cycles.

Stellenbosch University http://scholar.sun.ac.za

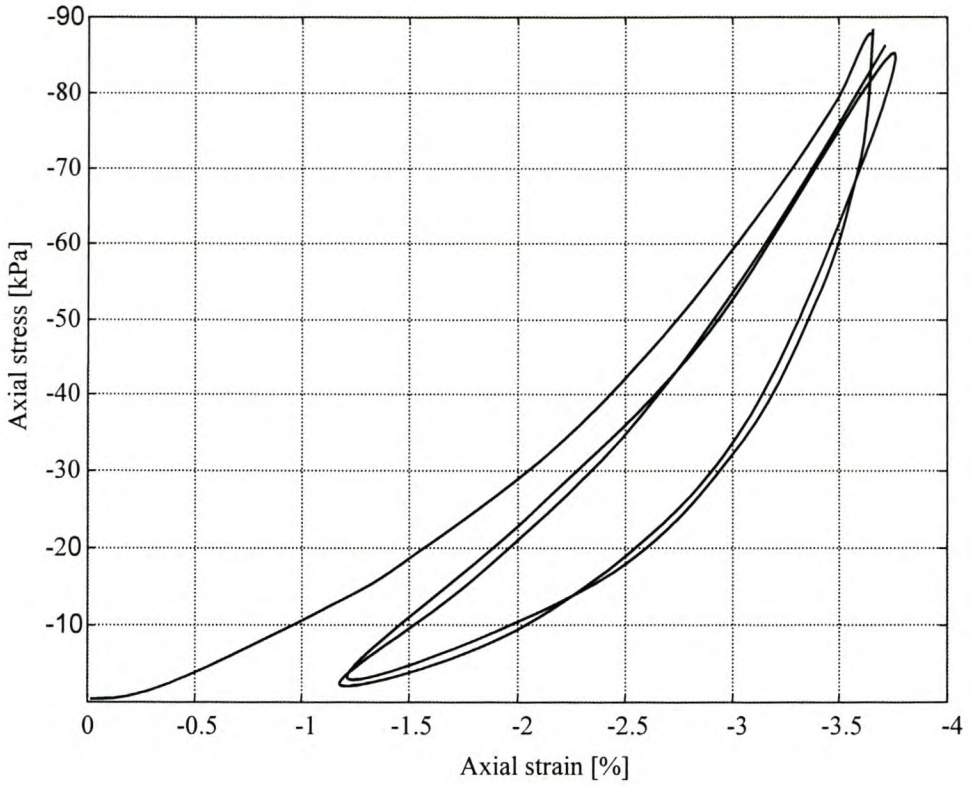

Figure 4.7- *Confined compression test, wheat experiment.*

Note - the negative axes

The second and third cycles follow a stable hysteresis loop. These stable cycles were used to determine the stiffness of the system of particles. The *confined Young's modulus* for each set of results is defined as

$$E' = \frac{\sigma_{80} - \sigma_{10}}{\varepsilon_{80} - \varepsilon_{10}} \tag{4.6}$$

where σ_{80} is a normal stress of 80 kPa and ε_{80} the equivalent strain. When higher axial stresses were applied (up to 400 MPa) the hysteresis loop never became stable. The reason for this is that some of the grains either collapsed under the load or underwent plastic deformation that resulted in global plastic deformation and an unstable hysteresis loop. Figure 4.8 shows the result obtained from a numeric simulation.

Stellenbosch University http://scholar.sun.ac.za

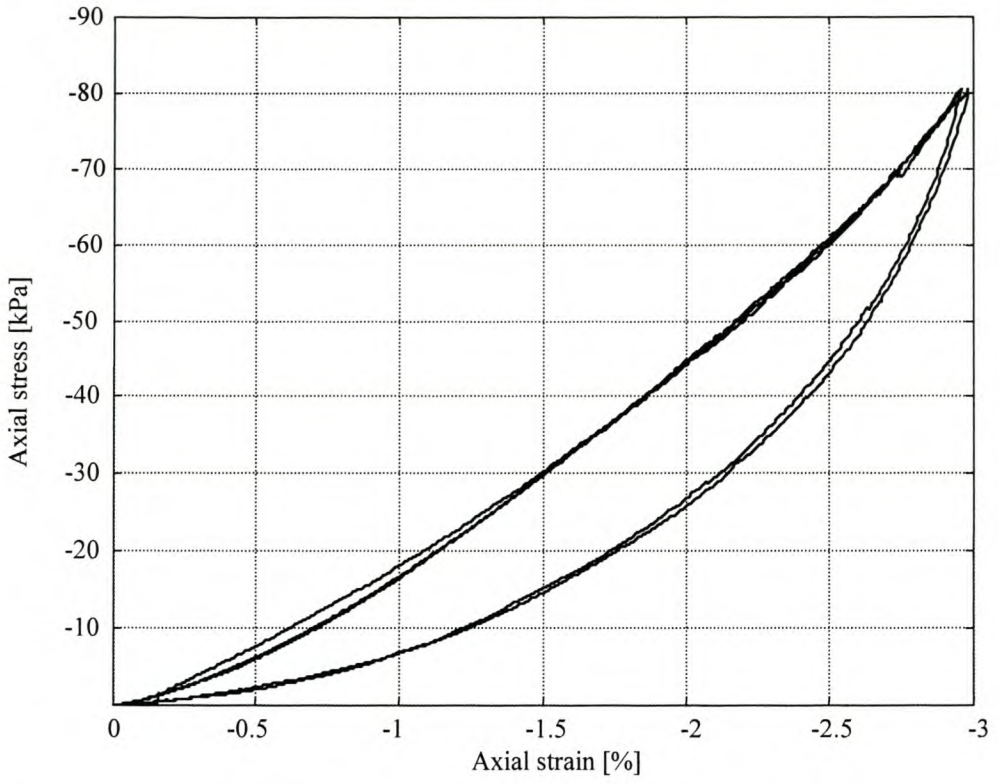

Figure 4.8 – *Confined compression test, wheat numeric simulation*

The stress-strain curve obtained from simulations is closer to a straight line than those obtained from experiments. The contact constitutive model is expected to have an effect on the assembly stiffness. With a Hertz contact model, which is non-linear rather than linear as the model used in the simulations, one would expect a different stress-strain curve. The same procedure as used for experimental data was followed to obtain the *confined Young's modulus* for simulations. A series of simulations, each with different particle stiffness and/or friction values, were performed. It was found that the friction had little to no effect on the system stiffness and a linear relation existed between particle stiffness and the *confined Young's modulus* (Fig. 4.9). From the figure it can be seen that a particle stiffness value of 450 kN/m resulted in a modulus (1.52 MPa) close to the experimental value of 1.60 MPa.

Stellenbosch University http://scholar.sun.ac.za

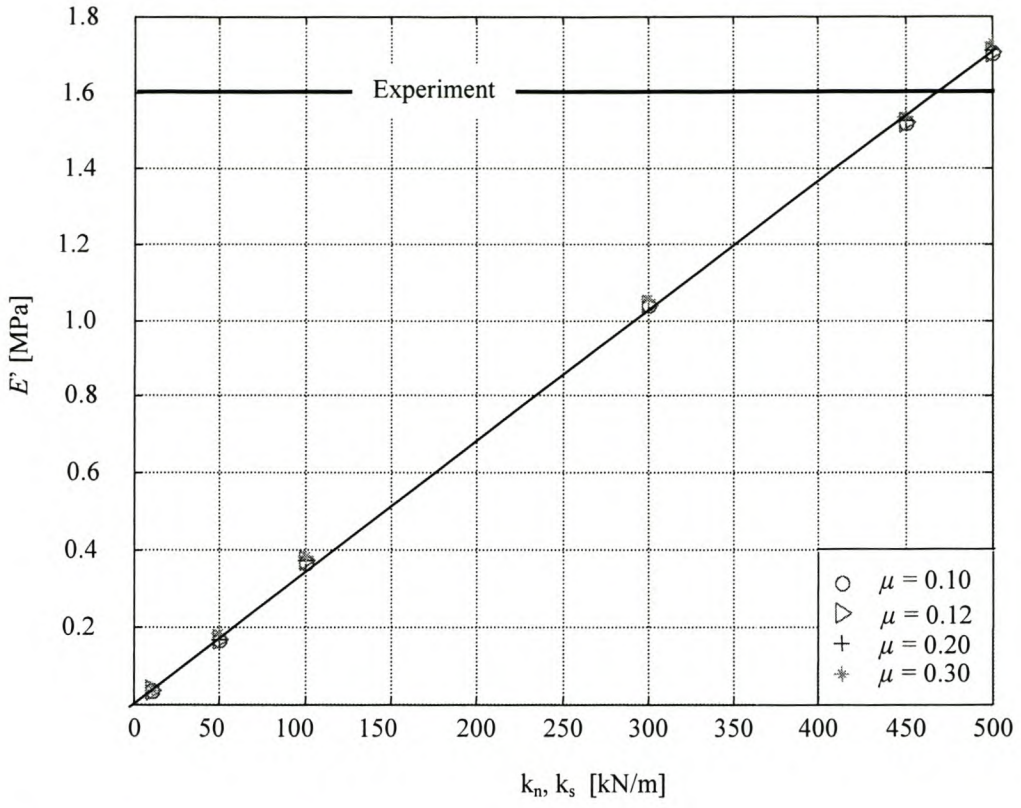

Figure 4.9 – *Confined compression series*

The stiffness of the system of particles can also be described in terms of a global stiffness value measured in N/m, equivalent to the particle stiffness. This is accomplished by multiplying the *confined Young's modulus* by a factor A/L where A is the area over which the axial stress is applied and L the initial specimen height. When a straight line is fitted to this data the global stiffness is found to be 0.83 times the particle stiffness value.

Stellenbosch University http://scholar.sun.ac.za

4.5 Direct Shear Tests

Shear failure occurs when shear stresses set up in the material exceed the maximum shear resistance that the material can offer, i.e. its shear strength.

4.5.1 Background

Shear strength of soil can vary with time and the value measured in the laboratory is likewise dependent upon the conditions imposed during the test and in some instances upon the duration of the test. The shearbox test is the simplest, the oldest and the most straightforward procedure for measuring the "immediate" or short-term shear strength of soils in terms of total stresses.

In principle the shearbox test is an "angle of friction" test, in which one portion of soil is made to slide along another by the action of a steady increasing horizontal shearing force, while a constant load is applied normal to the plane of relative movement. The angle of internal friction is more correctly called the "angle of shear resistance" of the soil.

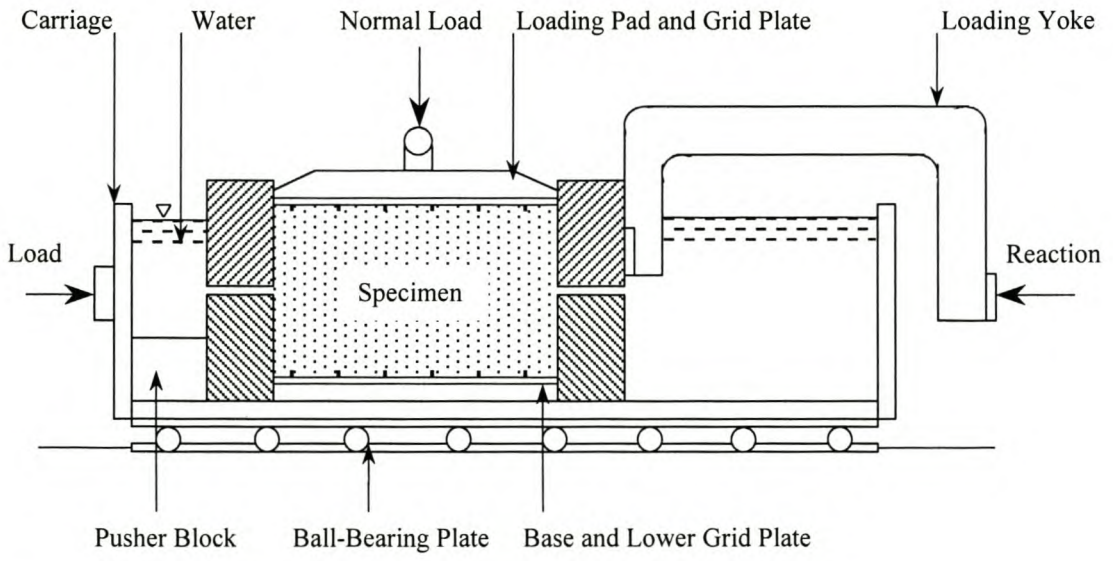

Figure 4.10 – *Conventional shearbox apparatus*

Stellenbosch University http://scholar.sun.ac.za

Figure 4.10 shows a conventional shearbox and its components. The most common standard box sizes are 60×60, 100×100 and 300×300 mm. The normal load applied to the specimen produces a vertical stress and a steady increase in displacement is applied to one half of the sample in a horizontal direction, while the other half is restrained by the load-measuring device. The shear stress is induced on the pre-determined plane of slip. The shape of the shear stress/displacement graph depends on the type of soil being tested. Figure 4.11 shows the shear characteristics of intermediate materials (friction and cohesion). For dense materials a definite peak strength can be observed and plotted against the normal stress to obtain the Coulomb envelope, the angle of internal friction and apparent cohesion. Looser material does not show such a peak strength but rather reaches a residual value.

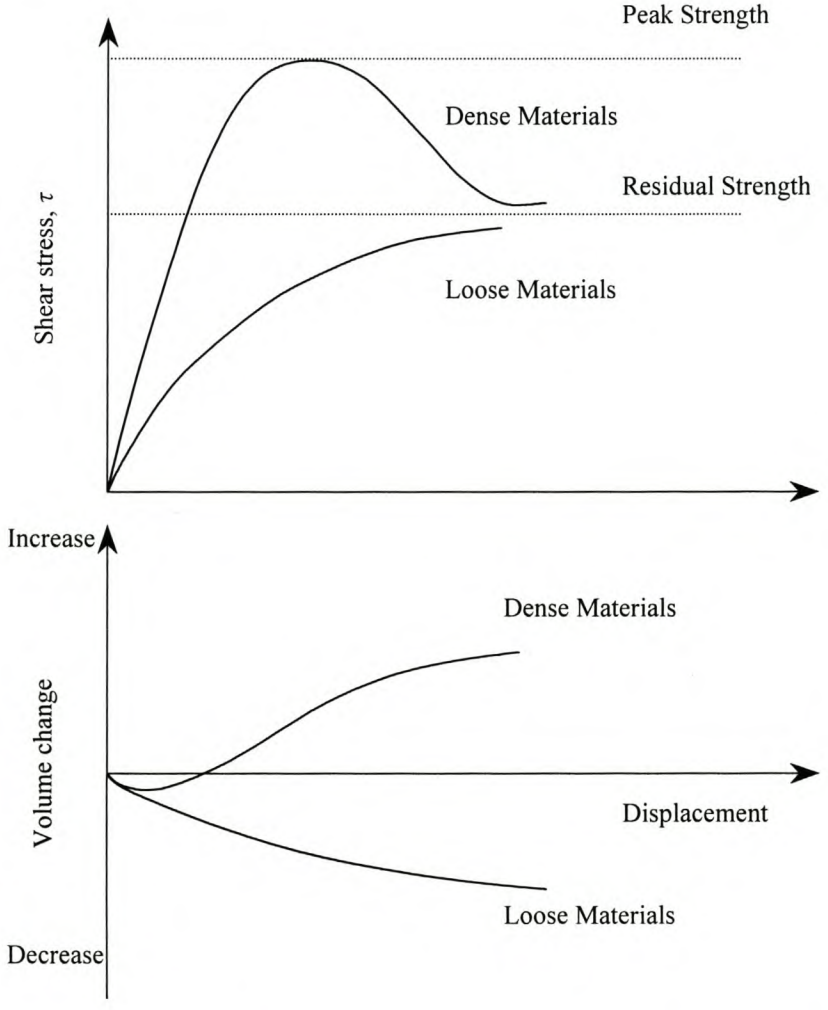

Figure 4.11 – *Shear characteristics of intermediate materials*

Stellenbosch University http://scholar.sun.ac.za

4.5.2 Experiments and Simulations

An experimental shearbox was used to determine internal friction angles and the friction angle with steel and glass. The box had dimensions of 375 × 375 mm with a total height of approximately 175 mm and seemed to be large enough for testing particles up to 12 mm. A standard box size of 305 mm (12 in) square is suitable for materials containing particles up to 37.5 mm (Head, 1988). The normal stresses imposed during the tests were chosen to be within the range experienced during 2-D rig experiments. A numerically equivalent model with the same dimensions as the physical apparatus was constructed and tests were performed under the same conditions. All tests were performed according to British standards BS 1377:1975, which is similar to the US standards under ASTM 3080. Typical shear stresses are shown in Fig. 4.12. The material was poured into the shearbox from a small height to obtain a low density. The shape of the graph also reveals that the tested material was in a loose or low-density state.

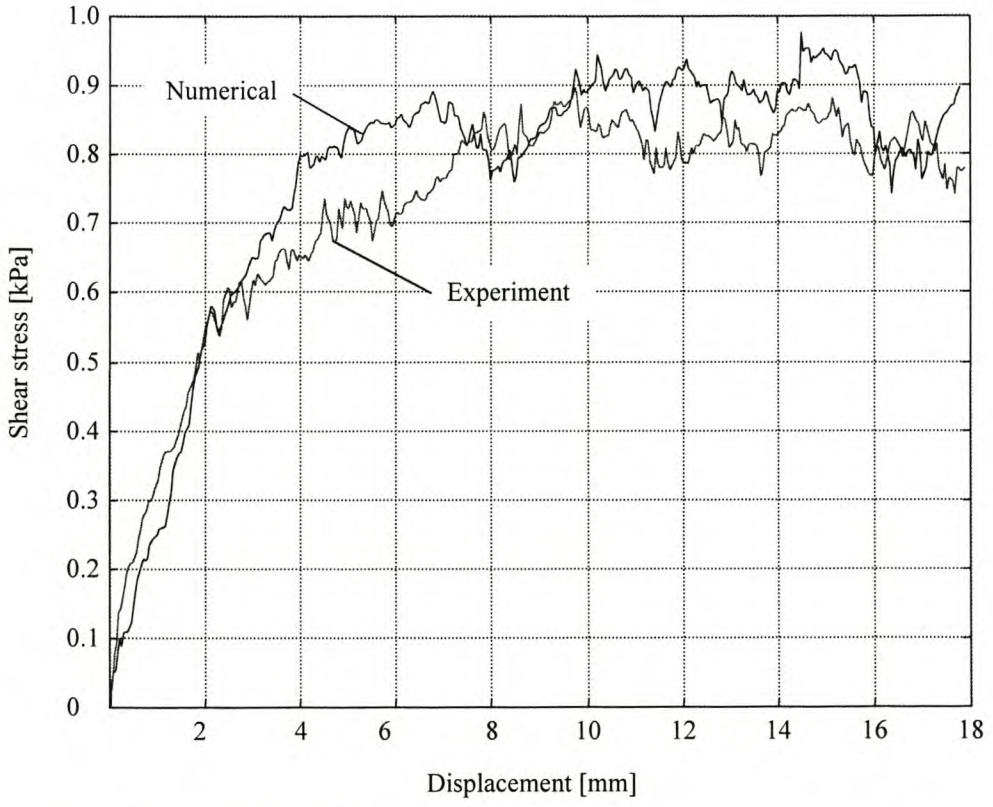

Figure 4.12 – *Wheat shear stress with σ_n =-2 kPa*

Stellenbosch University http://scholar.sun.ac.za

Figure 4.13 shows the numerical model before and after a typical simulation. The grid was generated by changing the particle colour after the normal stress had been applied. A servocontrol mechanism was used to keep the normal stress within 1% of the desired value. It can be seen that distortion is not limited to a single plane as assumed in theory but rather a region surrounding the theoretical slip plane. Fig. 4.14 shows the force chains during shear testing. There was a near uniform distribution of forces after the normal stress had been applied, which is desired, and the force chains tended to line up along the diagonal during displacement of the upper part of the box. The maximum shear stress up to a displacement of 18 mm (4.8% strain) was used to calculate the friction angle.

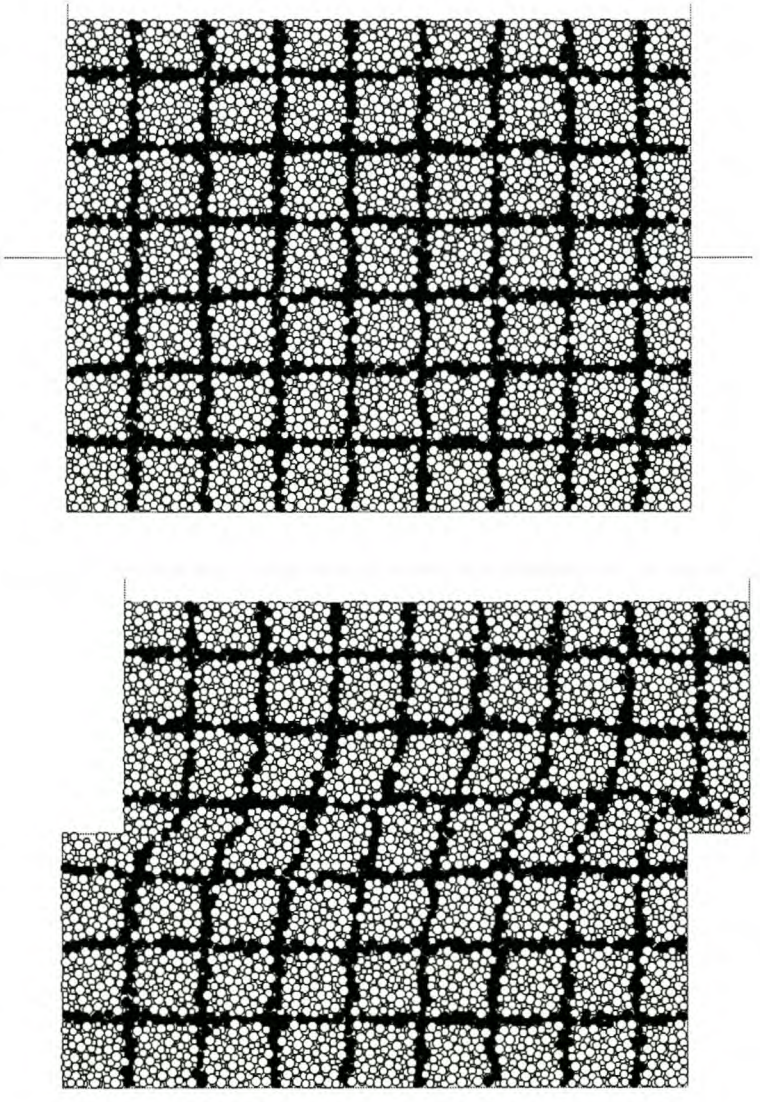

Figure 4.13 - *Shear test using a corn sample*

Stellenbosch University http://scholar.sun.ac.za

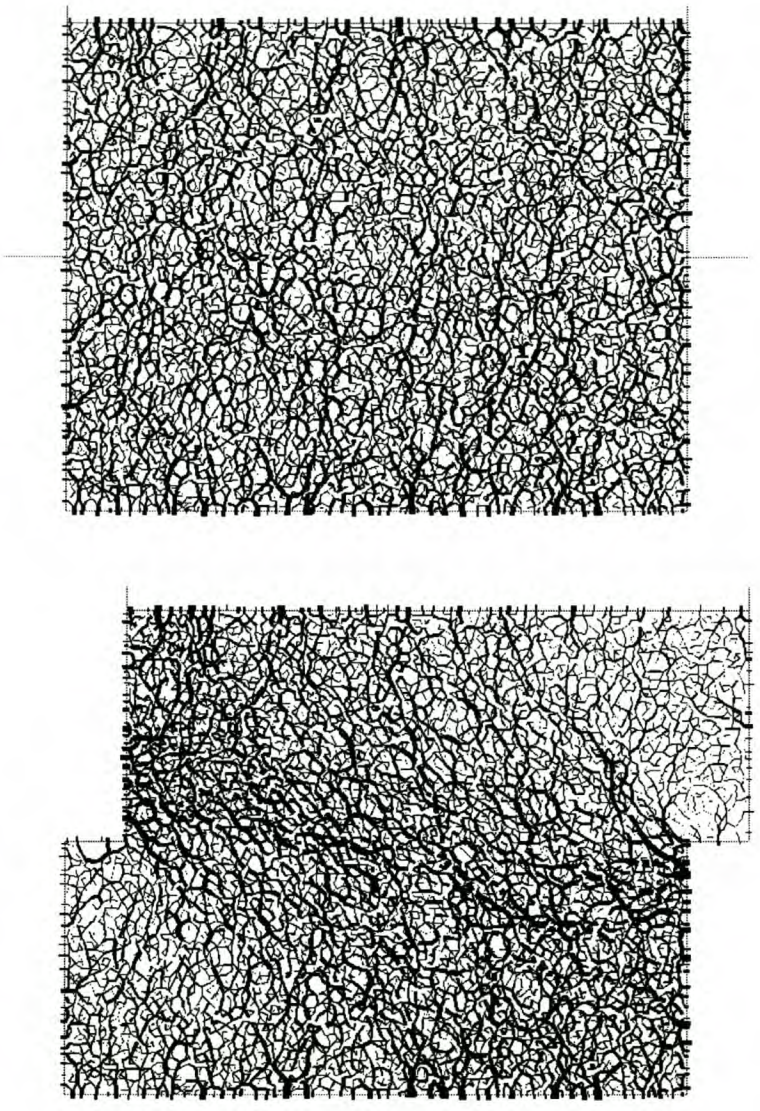

Figure 4.14 - *Force chains during shear testing*

The strength of an unbonded material, according to Itasca (1999), is controlled by the particle size distribution, average density and particle friction coefficient and no general relation exists between particle friction angle and material internal friction angle. With the seed grains being a cohesionless material and with the particle size and shape as well as the density and stiffness fixed, all that remains is the particle friction coefficient. A series of shear tests were performed using a range of particle stiffness and friction values. It was in fact not necessary to use different stiffnesses since the value thereof had been fixed by the compression test.

Stellenbosch University http://scholar.sun.ac.za

Shear tests were, however, performed prior to compression tests and it was thought that this would be sufficient to determine the material micro-properties. The shear simulations showed that the internal friction angle depended on both the particle stiffness and friction coefficient, especially in the low stiffness range. Only thereafter were compression tests performed to determine the particle stiffness.

The shear results, as presented here, do give some more information about the process as opposed to a single stiffness approach. Note that the ratio of k_n/k_s has an influence on the material *Young's modulus* and *Poisson's ratio* (Itasca, 1999). The *Poisson's ratio* given by a 2-D biaxial simulation can strictly not be compared with laboratory-measured values since conditions in a 2-D biaxial test are neither plane strain nor plane stress. Consequently, *Poisson's ratio* was not used in the calibration process. The results for wheat are shown in Fig. 4.15. It is clear that the material internal friction angle does depend on the stiffness values and not only on the particle friction coefficient μ. This dependence seems to decrease with an increase in particle stiffness.

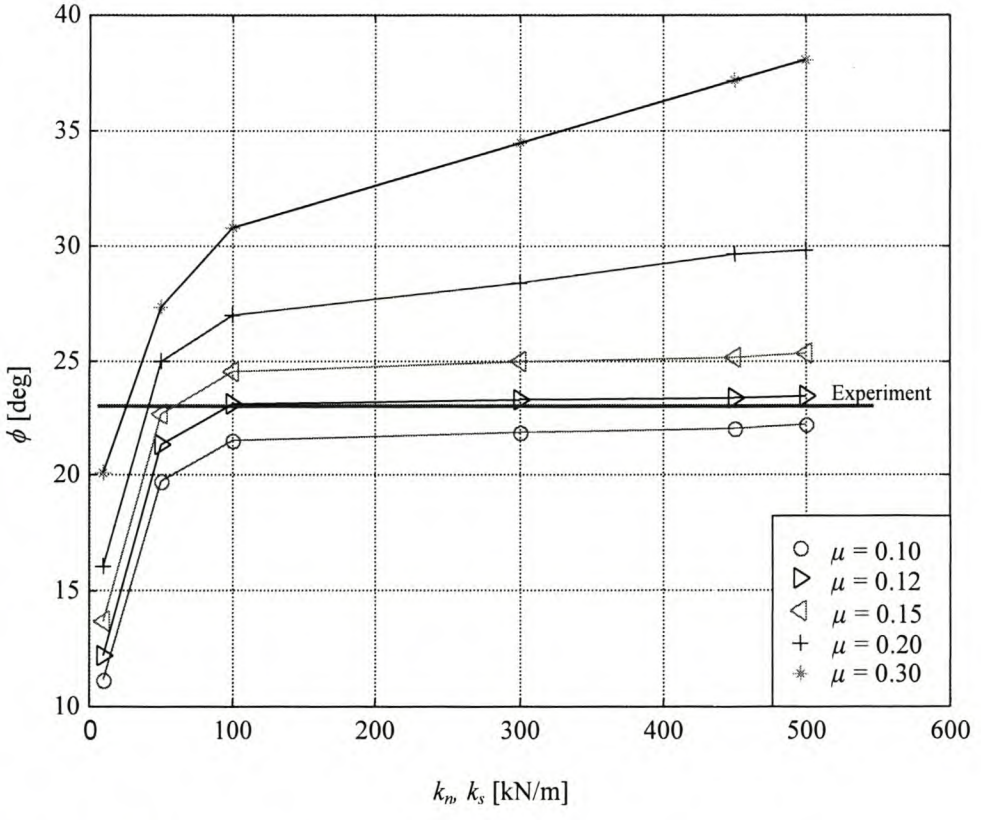

Figure 4.15 - *Wheat internal friction angle*

Stellenbosch University http://scholar.sun.ac.za

Corriveau et al. (1996) studied the effect of particle friction on the internal friction angle numerically by using a linear-spring-dashpot and the Walton & Braun contact model. They performed biaxial tests which are the two dimensional equivalent of triaxial tests with an assembly of 1250 and 300 circular disks. Their results show that the internal friction angle depends strongly on the particle friction coefficient in the lower range of μ. In the upper range there is only a slight increase in ϕ with an increase in μ. They also show that as the particle size distribution is made wider, the magnitude of ϕ increases.

It is clear from the figure that more than one combination of the particle friction coefficient and stiffness values can give you the experimentally measured value of the internal friction angle. Using the compression test results one can see that the particle stiffness value should be approximately 450 kN/m. Now, using the shear test results and a stiffness of 450 kN/m, we see that the friction coefficient should be close to 0.12.

The friction angle with steel and glass is measured by replacing the lower part of the shearbox with a steel and glass sheet respectively. Some of the results are shown in Fig. 4.16. The corn-steel friction angle was determined to be 14.3° and the corn-glass friction angle 11.7°. The internal friction angle is also shown in the figure.

The PFC^{2D} constitutive model makes use of Coulomb type friction in the contact shear direction. When two bodies in contact have different friction coefficients the lower one of the two coefficients is used. This creates problems when particles with a low friction coefficient come into contact with a wall. Particles with a friction coefficient of $\mu = 0.12$ were found to have similar behaviour to that of the physical material (wheat in this case), but with these particles in contact with a wall the material-wall friction coefficient obtained from a shear test was also 0.12 (friction angle of 6.8°). This is far below the experimental value of 15.8°. The problem was solved by checking all the contacts that form during a time step and changing the friction coefficient of the particles in contact with the wall to $\tan^{-1}(15.8°) = 0.283$. The friction coefficient of particles that lost contact with the wall was restored. This procedure gave better results but increased simulation time.

Stellenbosch University http://scholar.sun.ac.za

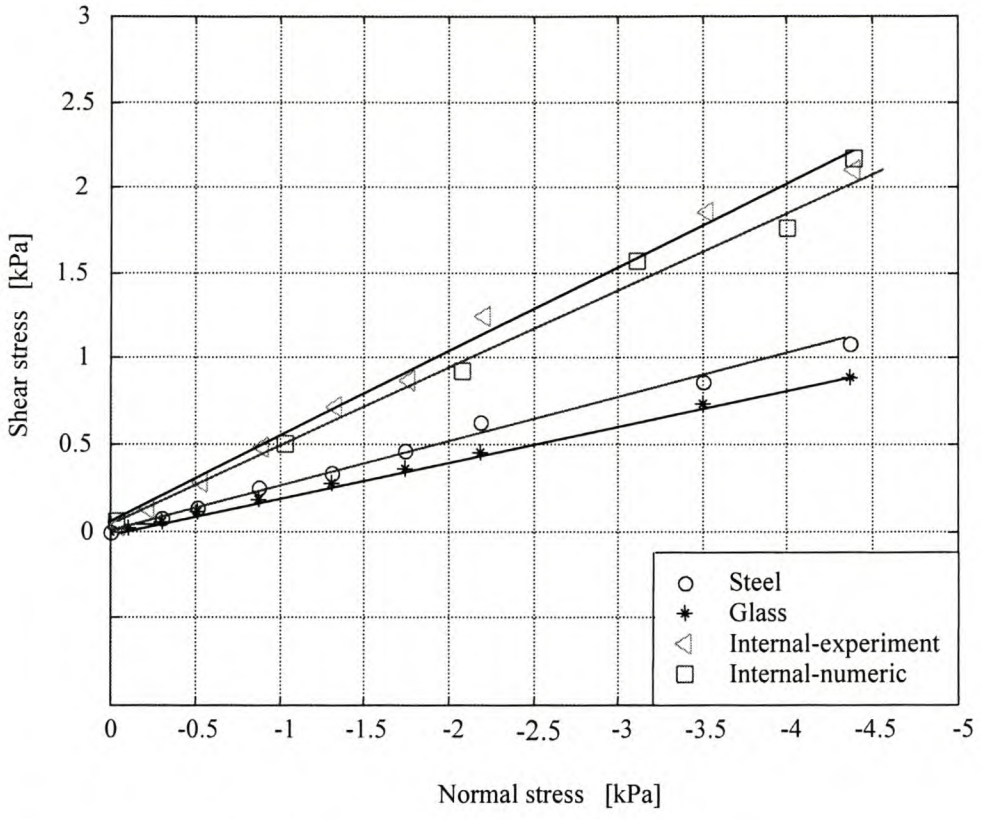

Figure 4.16 – *Corn friction angle calculations*

4.6 Angle of Repose

With the particles calibrated, the angle of repose ϕ_r was determined experimentally and numerically as a final test. Albert et al. (1997) describes the formation of a slope as follows. Unlike liquids a granular material is stable when its container is tilted slightly as long as the top surface is at a slope less than the angle of maximal stability ϕ_m. When the slope is increased above ϕ_m, the grains begin to flow and an avalanche of particles occurs; the angle of the slope (pile) decreases to the angle of repose. All of the motion occurs in thin layers at the surface. When building up a heap experimentally one finds that the slope does not depend on the number of particles.

Grains were added to a pile against a vertical wall and between two horizontal glass panels. The formation of the heap could be observed through the glass and the angle of repose measured to the nearest 1°. This value was compared to values obtained from numerical simulations. Remember that the first approach was to make use of single

Stellenbosch University http://scholar.sun.ac.za

circular-shaped particles. The angle of repose using these particles was found to be dependent on the number of particles, using samples of 300 and 800 particles.

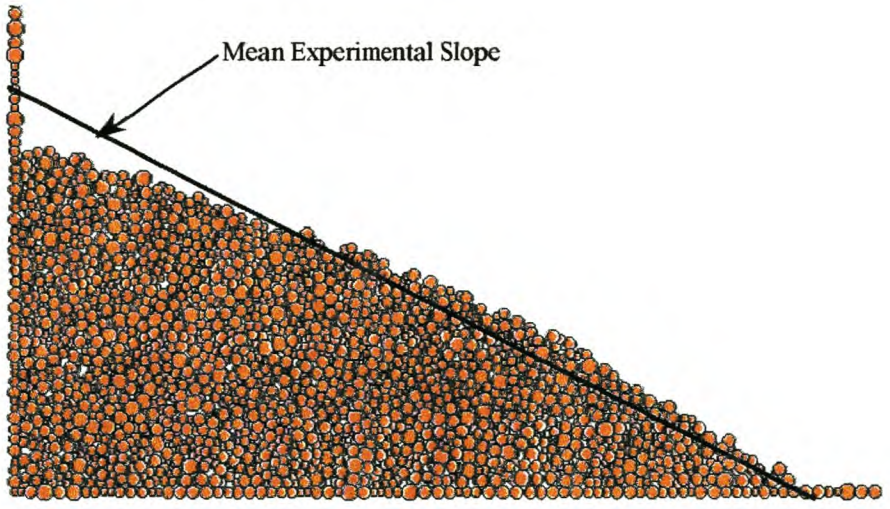

Figure 4.17 – *Angle of repose, corn*

However, the angle of repose was found to be independent of the number of *clumped* particles. This is in agreement with results obtained by Buchholtz and Poschel (1993) and Frick et al. (1999) who made use of DEM and particle numbers ranging from 300 to 1200. Narayan and Nage (1999) states that a real granular material does not have a well-defined angle of repose and Barabasi et al. (1999) showed experimentally that ϕ_r depends on the liquid content of the granular material but not on the system (pile) size. Figure 4.17 shows the numeric result with 1000 *clumped* corn particles as well as the mean experimental angle of repose.

It is well known that the angle of repose is a measure of the internal friction angle for frictional material (Bagster and Bridgwater, 1967). Lambe and Whitman (1969) describe limit equilibrium of slopes as follows. By considering the equations of equilibrium of a free body element near the surface of the slope, it can be shown that the angle of repose of a cohesionless granular medium is equal to the internal friction angle. The free body element is shown in Fig. 4.18 and it is assumed that the slope is infinite and very wide in the direction normal to the cross-section. Only the stresses that

Stellenbosch University http://scholar.sun.ac.za

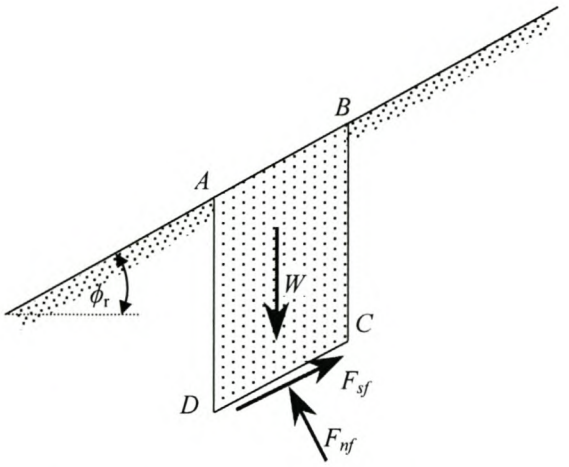

Figure 4.18 - *Analysis of an infinite slope*

act in the plane of the cross-section are considered. By assuming an infinite slope it is reasonable to assume that the stresses on the two vertical faces are equal and balance each other exactly. The equilibrium is analysed in terms of the forces F_{sf} and F_{nf} acting on the face *CD*. The slope is taken to be at an arbitrary angle ϕ_r. The equilibrium equations in the vertical and horizontal directions for this situation are as follows.

$$W - F_{sf}\sin(\phi_r) - F_{nf}\cos(\phi_r) = 0 \tag{4.7}$$

$$F_{sf}\cos(\phi_r) - F_{nf}\sin(\phi_r) = 0 \tag{4.8}$$

$$\therefore\ F_{sf} = F_{nf}\tan(\phi_r) \tag{4.9}$$

If the full shear resistance is mobilised so that $F_{sf} = F_{nf}\,tan(\phi)$, then $\phi_r = \phi$. The measured angle of repose of corn, 27°± 2°, corresponds well to the internal friction angle of 26.4°. Thus, for frictional granular material the angle of repose can be used as an estimate of the internal friction angle.

Stellenbosch University http://scholar.sun.ac.za

4.7 Material Properties

Table 4.1 summarises the macro- and final micro-properties.

Properties	Corn		Wheat	
Macro	Experiment	Simulation	Experiment	Simulation
Internal friction angle, ϕ [deg]	26.4	23.6	23.0	23.4
Angle of repose, ϕ_r [deg]	27±2	28±1	25±1	24±1
Average density, ρ [kg/m^3]	778	778	703	703
Bulk modulus, E' [MPa]	3.07	2.05	1.60	1.52
Material-steel friction, δ_m [deg]	14.3	14.3	15.8	15.8
Material-glass friction, δ_g [deg]	11.7	-	12.9	-
Micro		Simulation		Simulation
Particle stiffness, $k_n = k_s$ [kN/m]	-	420	-	450
Particle density, ρ_p [kg/m^3]	-	855	-	874
Particle friction coefficient, μ	-	0.10	-	0.12

Table 4.1 - *Material properties*

The macro-properties measured by Reimbert and Reimbert (1976) are given in Tab. 4.2. There is a good correspondence between the measured angle of repose of both materials and those measured by Reimbert and Reimbert (1976). The measured corn density is close to the minimum value while the wheat density is well below the values given. Low-grade wheat was used which may explain why it had such a low density. It is difficult to compare the measured material-steel friction angles to that of Reimbert and Reimbert (1976) because the finishing of the steel will have an influence on the friction.

Macro-properties	Corn	Wheat
	Experiment	Experiment
Angle of repose, ϕ_r [deg]	26-29	24-26
Average density, ρ [kg/m^3]	780-820	750-840
Material-steel friction, δ_m [deg]	17-23	20-25

Table 4.2 – *Material properties, Reimbert and Reimbert (1976)*

Stellenbosch University http://scholar.sun.ac.za

The *coordination number* of the *clumped* particles varied from 5.7 to 6.2. The *coordination number* is defined as the average number of contacts per particle. Porosity for a 2-D system of particles is defined as

$$n = \frac{A_{void}}{A_{measure}} = \frac{A_{measure} - A_{particle}}{A_{measure}} = 1 - \frac{A_{particle}}{A_{measure}} \qquad (4.8)$$
$$= 1 - \frac{\rho}{\rho_p}$$

where A_{void} and $A_{particle}$ are the total areas occupied by voids and particles respectively, and $A_{measure}$ is the area for which the porosity is being calculated. In the numeric models the porosity values ranged from 0.160 to 0.195.

Mixed results, i.e. some results from wheat experiments and simulations and others from corn experiments and simulations, were presented in this chapter. In general, the two materials showed the same trends.

4.8 Soil Tool Simulations

Soil tool simulations were performed using particle properties obtained from measured material properties. The initial equilibrium was found numerically by filling the rig with particles falling from randomly selected initial positions and orientations. This closely resembled the experimental procedure. The blade and bucket were divided into several parts so that the role that each individual part played could be analysed. A straight blade was used rather than the typical curved blade of bulldozers. The blade can resemble a "idealised" bulldozer blade, cutting and tillage tools or even the cutting edge of a bucket. The blade was divided in four parts: the front, the back and the top and bottom edges. The bucket is shown in Fig. 4.19. It is emphasised that the bucket profile used does not resemble that of a specific earthmoving machine. The goal was rather to look at bucket filling in general and to investigate the reliability with which the process can be described and predicted by DEM. The way in which the bucket was moved through the material, i.e. being dragged in the x-direction with freedom of

Stellenbosch University http://scholar.sun.ac.za

motion in the vertical direction and no rotational degree of freedom, is the same used by Rowlands (1991) to investigate dragline bucket filling. The angle of attack of the bucket remains zero, i.e. the bottom of the bucket stays parallel to the free surface of the material.

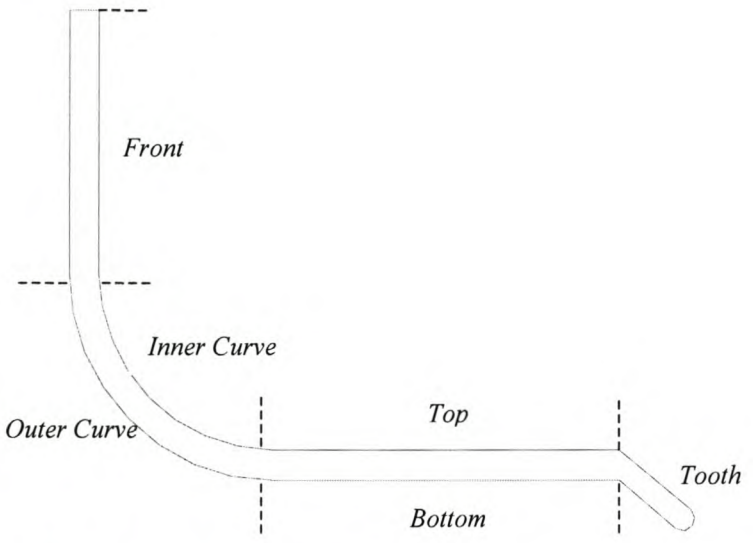

Figure 4.19 – *Bucket divisions*

This model of bucket motion was adopted and seemed to be reliable in the study of bucket filling in general. Comparisons could also be made with the results of Rowlands (1991). The motion can also be envisioned as the filling of a loader bucket (Fig. 4.20) and a scraper (Fig. 4.21). Figure 4.22 shows a typical loader bucket. The position of the teeth and lip is indicated. In both the experiments and simulations the bucket was equipped with only one single tooth and no lip. It is based on a 2-D, longitudinal, vertical slice through the centre of the bucket.

The sides of the bucket may converge or diverge in the flow direction. These effects are fully three-dimensional but are of secondary importance. The purpose of the teeth is to break the material apart and to begin lifting it into the bucket. The lip lift the remaining material, between the teeth, into the bucket.

Stellenbosch University http://scholar.sun.ac.za

Figure 4.20 - *Loader*

Figure 4.21 - *Scraper*

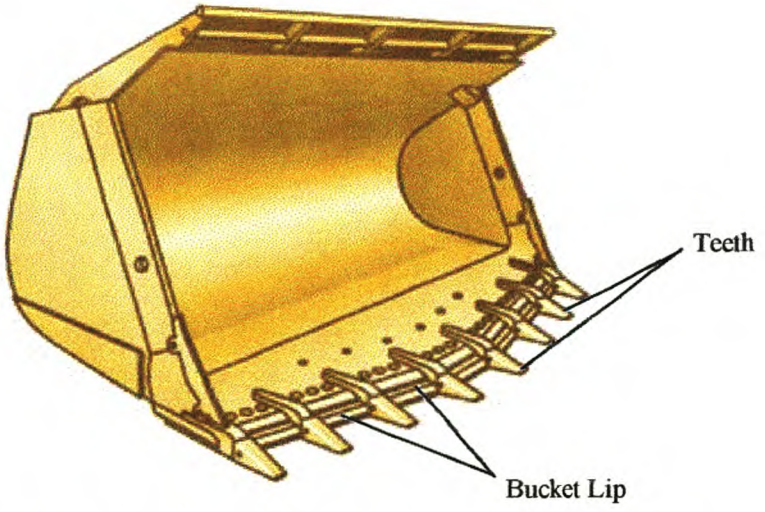

Figure 4.22 – *Typical loader bucket for loading rocks*

Stellenbosch University http://scholar.sun.ac.za

PFC^{2D} is not able to do motion calculations of buckets or of any "walls", for that matter; i.e. it excludes the dynamics of walls. The motion of a wall is defined by the user in the form of two velocity components and the rotational velocity. These velocity components can be any user-defined function of time or position. With additional programming, dynamics of walls can be included. This was thought not worth while the effort. It will be necessary if the filling of dragline buckets is under investigation since the bucket is not rigidly mounted as in the case of a loader where the bucket position and rotation are controlled by the operator. A scraper bucket has only a relatively small amount of rotational freedom, also controlled by the operator.

Experimentally, a constant vertical load was applied to the bucket by means of counter weights at the top of the 2-D test rig. The results show that under these loading conditions, the bucket experienced an almost constant vertical velocity while being dragged in the x-direction, also at constant velocity. The numeric bucket was given the same x-and vertical-velocity components. Experimentally the blade was only given a constant x-velocity that was relatively easy to simulate.

Stellenbosch University http://scholar.sun.ac.za

CHAPTER 5

BLADE RESULTS

This chapter presents the results obtained from both experimental tests and numerical simulations. The results can be divided in two categories. The first category looks at the forces and moments that act on the tool (blade and bucket). This includes energy requirements and energy distribution. The second category of results includes details of rupture planes (lines) and the flow of material. The shape of these planes is studied, and experimental and numerical results are compared to analytical results.

5.1 The Effect of Tool Velocity

There seems to be different opinions on the effect of velocity on the draft force of soil tools. Some researchers maintain that the draft force on tillage tools depends on the velocity with which the tool is moved through the soil while others present proof on the contrary.

Two velocity regimes can be identified: a *low velocity regime* and a *high velocity regime*. External forces acting on a granular medium are concentrated into a network of static force chains. It is these force chains that act against the motion of the object and the object cannot move relative to the medium until the grains opposing the motion are reorganised. As an object moves through the medium it repeatedly encounters a static set of force chains.

If this is true, the draft force, in the *low velocity regime*, is independent of the velocity since the distance between the consecutive static grain configurations depends only on the medium characteristics, such as intergrain friction. This reasoning can not be applied to the *high velocity regime*. In this regime the tool has a high velocity that caurses the grains in the vicinity of the tool to be fluidised. Fluidisation apparently causes the draft force to first decrease and then increase with increasing velocity. The

Stellenbosch University http://scholar.sun.ac.za

boundary between low and high velocity regimes is not well defined and depends on factors such as soil friction, cohesion and tool shape.

Calculations performed by Albert et al. (1998) show that the draft force on an object that extends from above into a granular medium is independent of the velocity of the moving object. This is in contrast to the viscous drag force in a liquid medium, which depends strongly on the velocity. They used a cylinder with a vertical axis that extended into equal-sized spherical granules. The cylinder was moved through the grains at a constant velocity ranging from 0.1 mm/s to 1.5 mm/s. The experimental results confirmed that in this velocity range the draft force is independent of the tool velocity.

According to a simple model proposed by Bohatier and Nouguier (2000), the draft force depends on the velocity squared. In their formulation, based on the linear momentum equation for a deformable control volume, the total force on the blade can be divided into a static and dynamic component. The dynamic force differs from the static force by a factor

$$\varepsilon = \frac{V_x^{\,2} \tan(\theta_r)}{g\,h \tan(\theta_r + \phi)} \tag{5.1}$$

where V_x is the draft velocity, h the immersed depth, θ_r the slip plane angle, ϕ the internal friction angle and g gravitational acceleration. Bohatier and Nouguier (2000) divided the flow into three categories

$\varepsilon < 0.1$	- quasi-static flow
$0.1 \leq \varepsilon \leq 10$	- intermediate flow
$\varepsilon > 10$	- dynamic flow

See Appendix E for a complete description of this model.

Grisso et al. (1996) investigated the effect of velocity and tillage depth on the draft force of a tandem disk, chisel plough and field cultivator. Travel speeds were 4.8, 6.4 and

Stellenbosch University http://scholar.sun.ac.za

9.7 km/h. The experimental results showed that the tandem disk and chisel plough draft are not influenced by the velocity while the field cultivator draft force is linearly dependent on speed. A clay loam soil was used and wide ranges of soil moisture contents and bulk density did not significantly affect the tool draft forces.

Siemens et al. (1965) experimentally investigated the influence of a moving blade on the mechanics of the soil through which it moves. Velocity ranged from 0.8 to 3.2 km/h. Their experimental results show that the draft force is a square function of the velocity. The general perception is that the increase in draft force is only due to the acceleration of the soil and this increase should be proportional to the square of the velocity. They made use of Eq. 2.19 to account for the acceleration forces.

$$F_a = \frac{\gamma h B V^2 \sin(\alpha)}{\sin(\alpha + \theta_r)} \tag{5.2}$$

According to Siemens the difference in calculated acceleration forces between two speeds was not nearly enough to explain the increase in the tool forces they measured.

Bagster and Bridgwater (1967) measured the force needed to move blades through a bed of cohesionless granules. They showed that the draft force does depend on the travel velocity (0 to 250 mm/s). When ballotini is used, the draft force is independent of the velocity for velocities below 50 mm/s. For velocities above 50 mm/s the draft force is directly proportional to the velocity. This linear relationship between velocity and draft force is in contrast with the results of other researchers, Luth and Wismer (1971), who showed it to be a quadratic relation.

From the literature study it seems that the tool forces are only significantly influenced at relatively high velocities (> 1 km/h). The shape of the tool and the soil properties also showed to have an influence. It is well known that the shear strength of soil is dependent on the shear rate, especially in soil with a high cohesion factor, e.g. clay.

We will now turn to experiments performed for this thesis. Experimental velocities could be varied continuously between 0.1 and 100 mm/s (0.36 km/h). Tests with the

Stellenbosch University http://scholar.sun.ac.za

blade at rake angles of 60°, 70°, 80°, and 90° and depths of 100, 150, 200, 250, 300 and 350 mm show that the velocity does not influence the draft and vertical forces.

When using Eq. 5.1 and typical experimental conditions, the factor ε is in the order of 10^{-3}, indicating that the flow is quasi-static. The acceleration force given by Eq. 5.2 is in the order of 0.25 N, which is less then 1% of the total draft force on the blade. Experimental results are shown in Fig. 5.1 for two blade angles, $\alpha = 90°$ and $\alpha = 80°$.

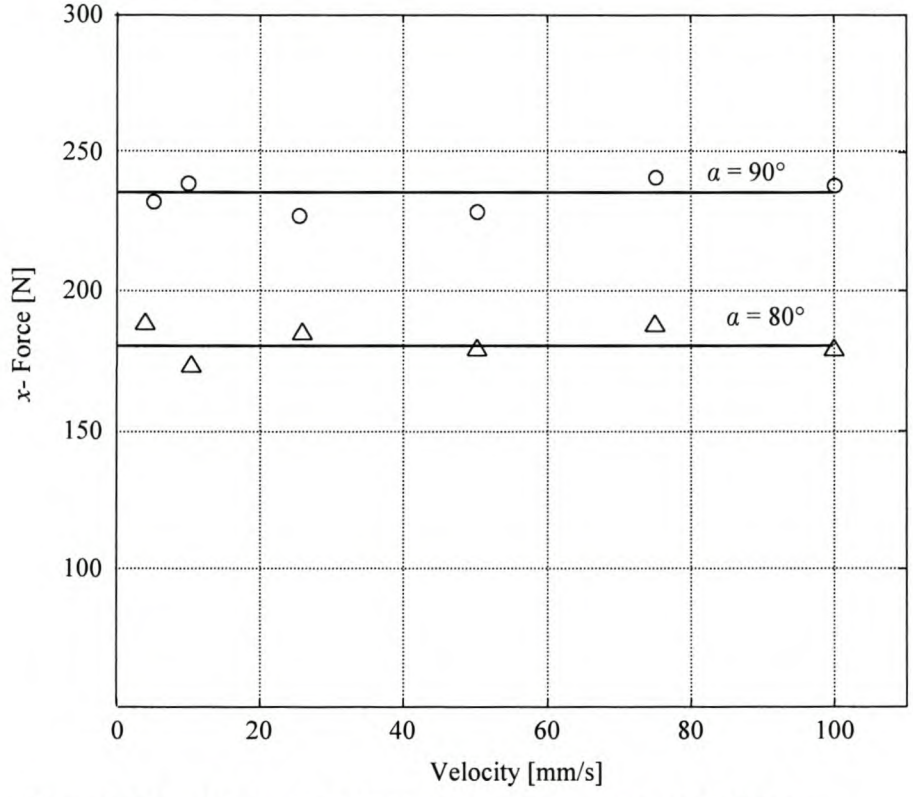

Figure 5.1 – *Blade draft force after a displacement of 100 mm using corn, h = 200 mm*

Bucket forces are also not influenced by the drag velocity. Experiments were performed with drag angles of 0°, 10° and 20°, allowing the bucket to move freely in the y-direction. The y-velocity is found to be constant over the whole drag and directly proportional to the drag velocity. This has the effect that the y-displacement is only a function of the drag distance, the weight of the bucket and the drag angle β. The influence of these variables will be discussed later in the chapter. Figure 5.2 shows the relation between y- and drag-velocity.

All other bucket results are presented in Chapter 6. The numerical simulations showed the draft force increases linearly with velocity and is influenced by the damping

Stellenbosch University http://scholar.sun.ac.za

constant. The reason for this dependence is the damping model used in the simulations. Only one damping value $\alpha = 0.70$ was used for all the simulations.

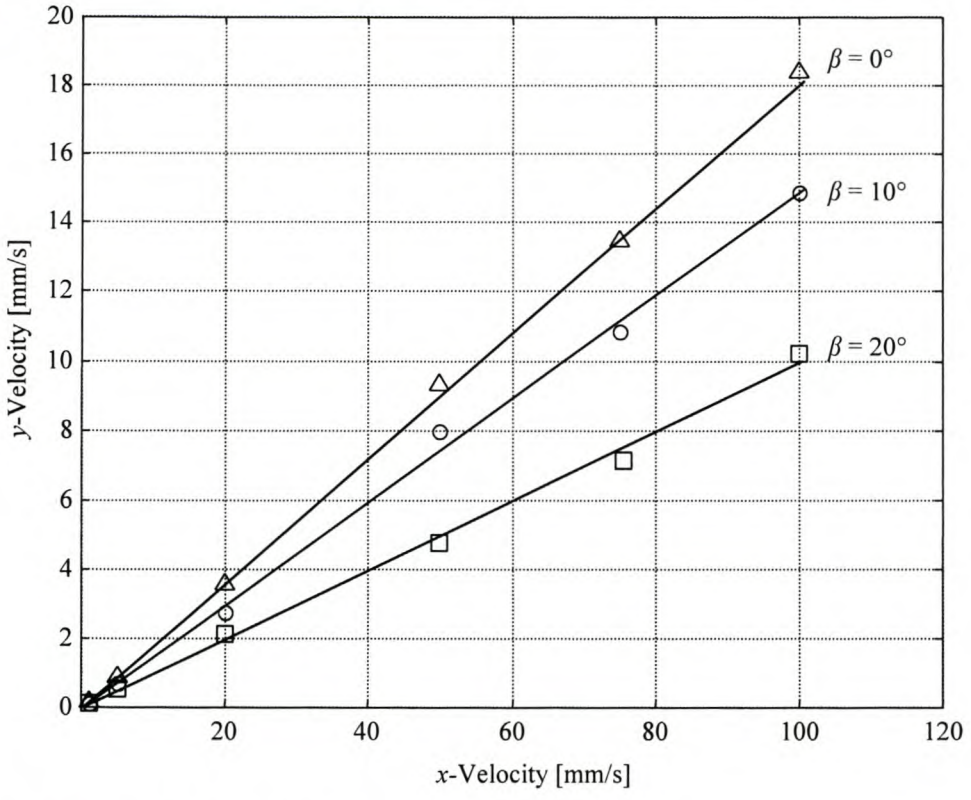

Figure 5.2 – *Bucket y-velocity, corn, $W_b = 138.3$ N*

5.2 Compressibility of Granular Medium

The free surface of the bed was always kept flat and parallel to the base of the test rig with the bottom edge of the blade at least 150 mm above the bottom of the bed. The bed was always remixed before each test to ensure a uniform consistency.

All of the following experiments and simulations were performed with a blade velocity of 10 mm/s and the rig angle $\beta = 0°$. Figure 5.3 shows the blade at an initial depth of $h = 200$ mm and $a = 90°$. Snapshots were taken every 100 mm starting at 100 mm. If we look at the shape of the heap in front of the blade, the simulation corresponds well to the experiment. The heap is, however, somewhat smaller in the case of the simulation. This is clear if we compare the maximum height at the blade. Possible reasons for this difference in heap size are given later.

Stellenbosch University http://scholar.sun.ac.za

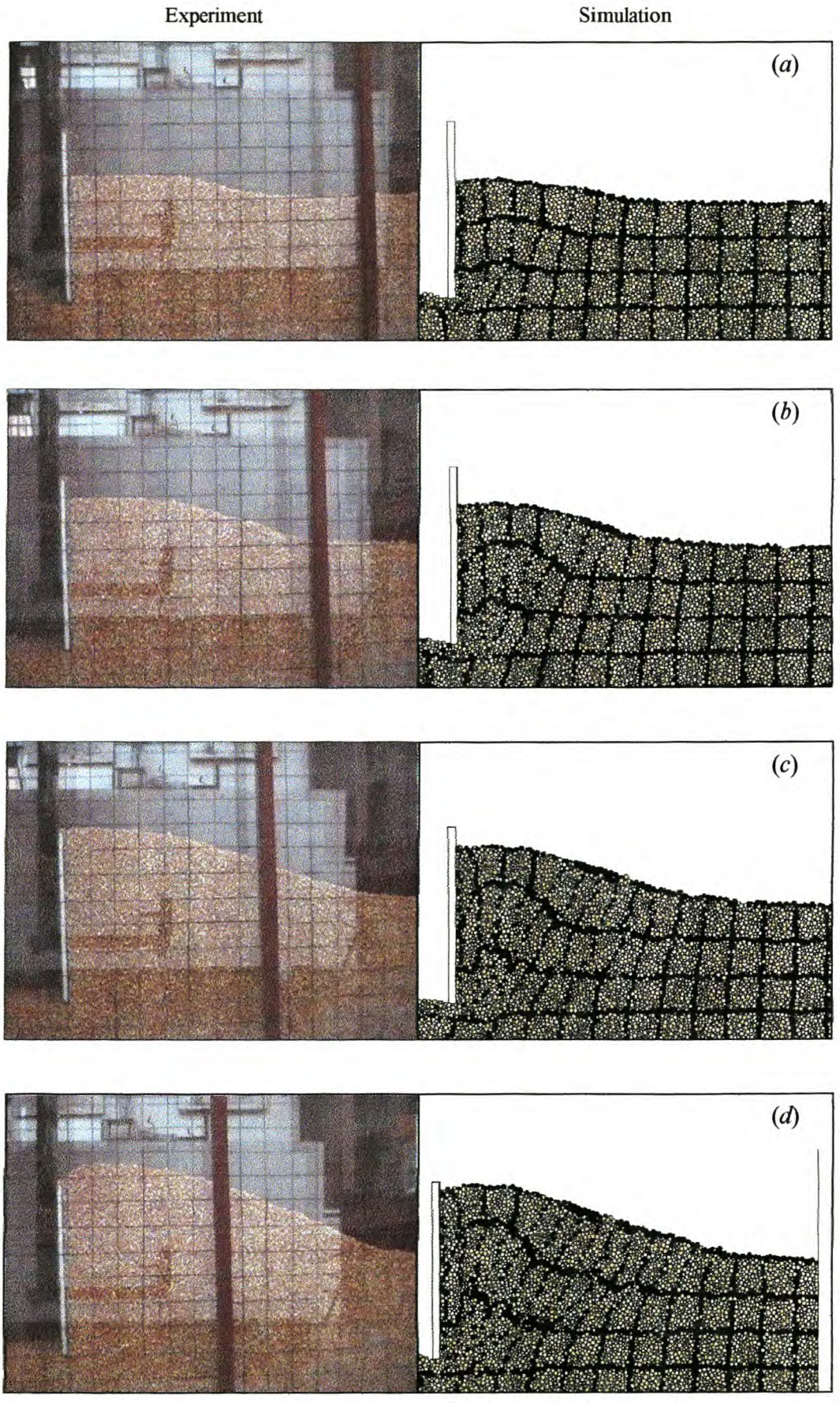

Figure 5.3 – *Blade moving through corn*

Stellenbosch University http://scholar.sun.ac.za

What became evident during experimental testing is that the volume of material heaved above the initial height is less than the volume the blade has displaced. This means that the material is compressed in front of the blade. To investigate this phenomenon snapshots were taken at 50 mm increments. The outlines were manually digitised to determine their areas. Figure 5.4 shows such a digitised image. The compressibility factor ψ is defined as

$$\psi = \left(1 - \frac{A_l}{A_d}\right) = \left(1 - \frac{A_l}{x\,h}\right) \tag{5.3}$$

where x is the displacement of the blade and A_l the area of the material above h.

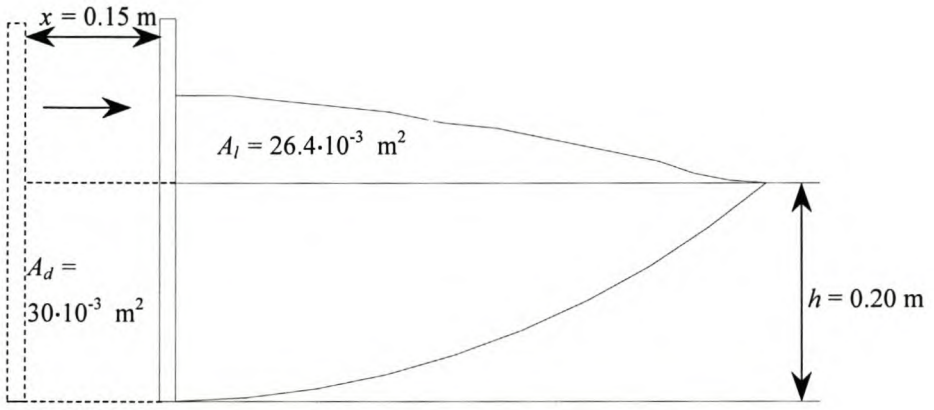

Figure 5.4 – *Compressibility calculation*

The compressibility factor is calculated for rake angles $\alpha = 60°$ and $\alpha = 90°$ and depths of h = 100, 150 and 200 mm. The result shows that ψ depends on the depth h and that the angle α has a fairly insignificant effect. The experimental results are shown in Fig. 5.5 and the simulation results in Fig. 5.6. The compressibility values are plotted against the dimensionless group (displacement/H) where H is the total blade height. The dependence on the depth can be explained as follows. With a low depth the average density of the material is lower than with a high depth, due to the weight of the material above. With a relative low density the material can be more compressed than the same material with a higher average density. For this reason, the cases with a high depth show less compressibility values.

Stellenbosch University http://scholar.sun.ac.za

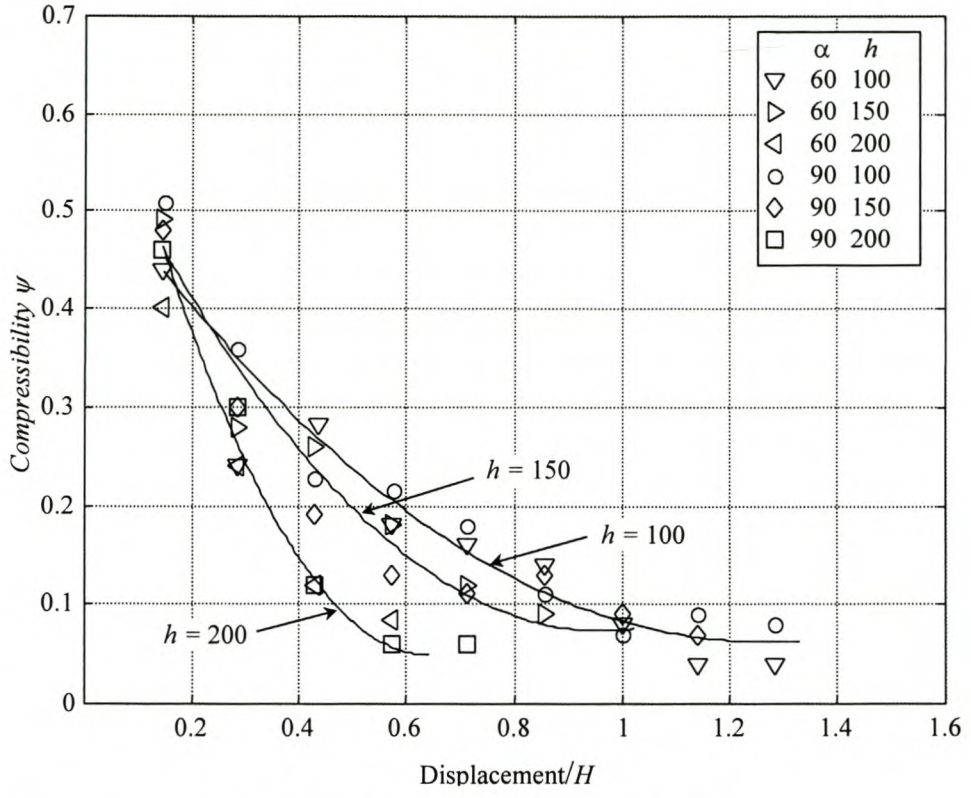

Figure 5.5 – *Corn experimental compressibility values*

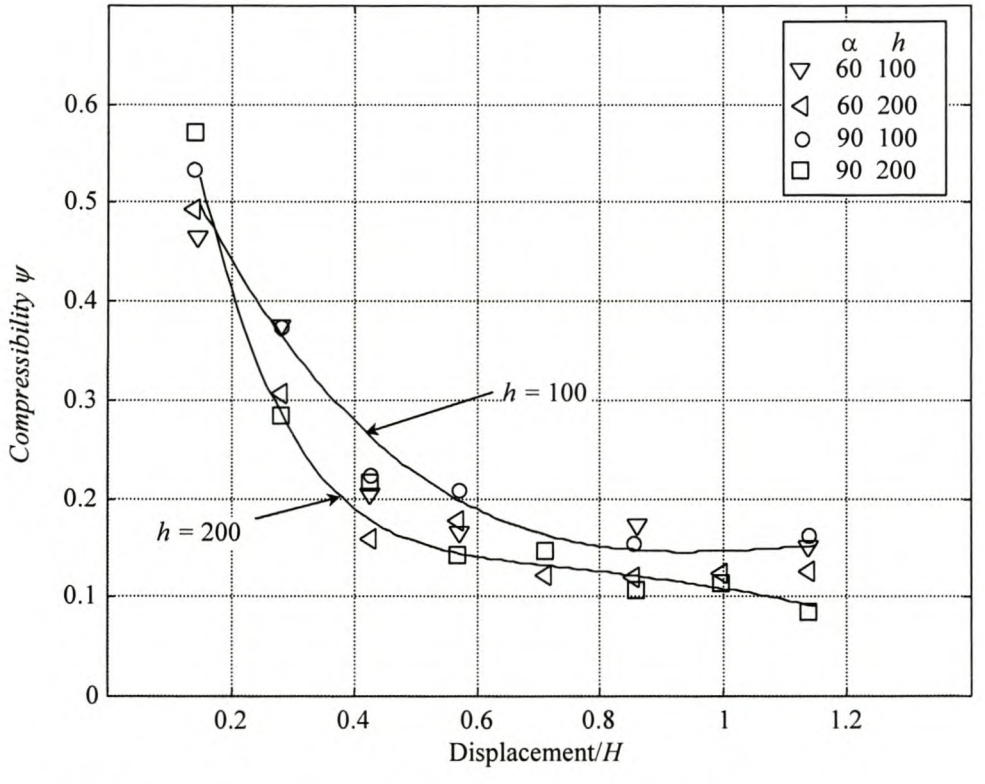

Figure 5.6 – *Corn simulation compressibility values*

Stellenbosch University http://scholar.sun.ac.za

The numeric equivalent results are shown in Fig. 5.6 for the two cases, h = 100 and 200 mm. Again the rake angle seems to have a very small influence on the compressibility. If we compare the two sets of results, we see that, for the same test, the simulation compressibility is slightly higher than the experimental compressibility. It is this difference in compressibility that causes the simulation heaps to be smaller than the experimental ones. The compressibility is influenced by the initial porosity, the particle shape and the particle stiffness values. With a smaller initial porosity and higher stiffness values it will, however, be possible to "fine tune" the calibration process to obtain still better compressibility results. The fact that the simulations are in 2-D will also have an effect on the results.

5.3 Forces and Energy

Fig. 5.7 to Fig. 5.9 show the forces and moments acting on the blade during a typical experiment and simulation. The negative y-force indicates that the blade is being pushed upwards (positive y-direction) by the material. Remember that the experimental and numerical simulations were not performed under exactly the same conditions. It is very difficult to incorporate the glass friction into the numeric model or to remove it experimentally. For this reason, the experimental forces are expected to be higher than the simulation forces. The vertical force shows high fluctuations during both experiments and simulations.

Stellenbosch University http://scholar.sun.ac.za

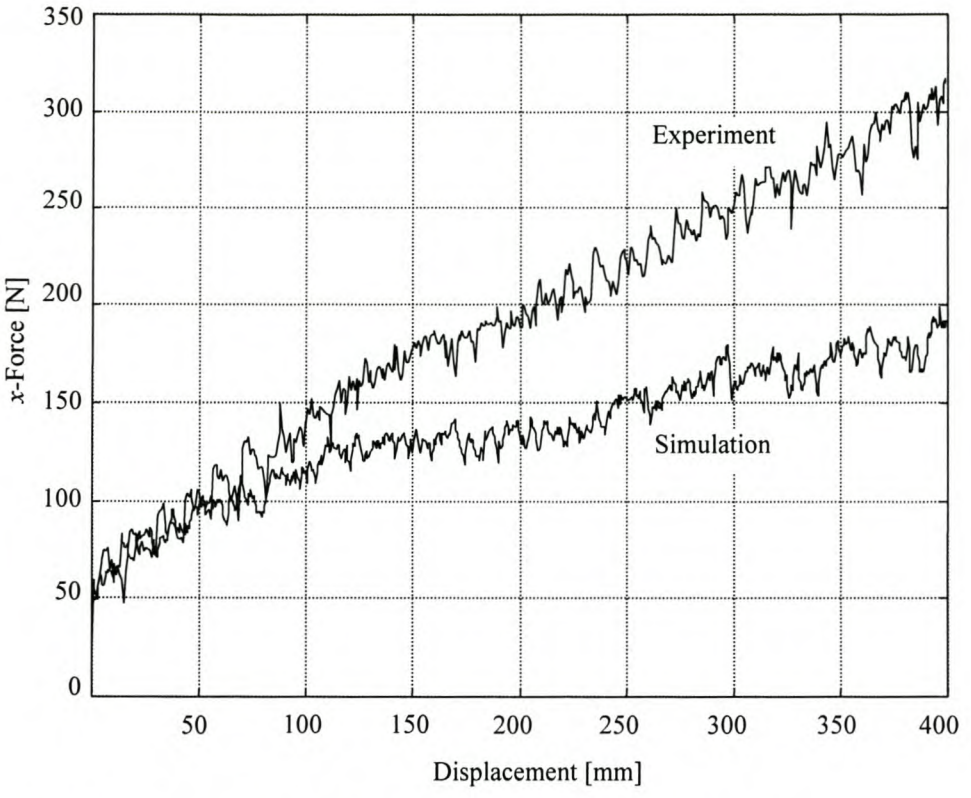

Figure 5.7 – *Blade draft forces, $\alpha = 90°$ $h = 200$ mm - corn*

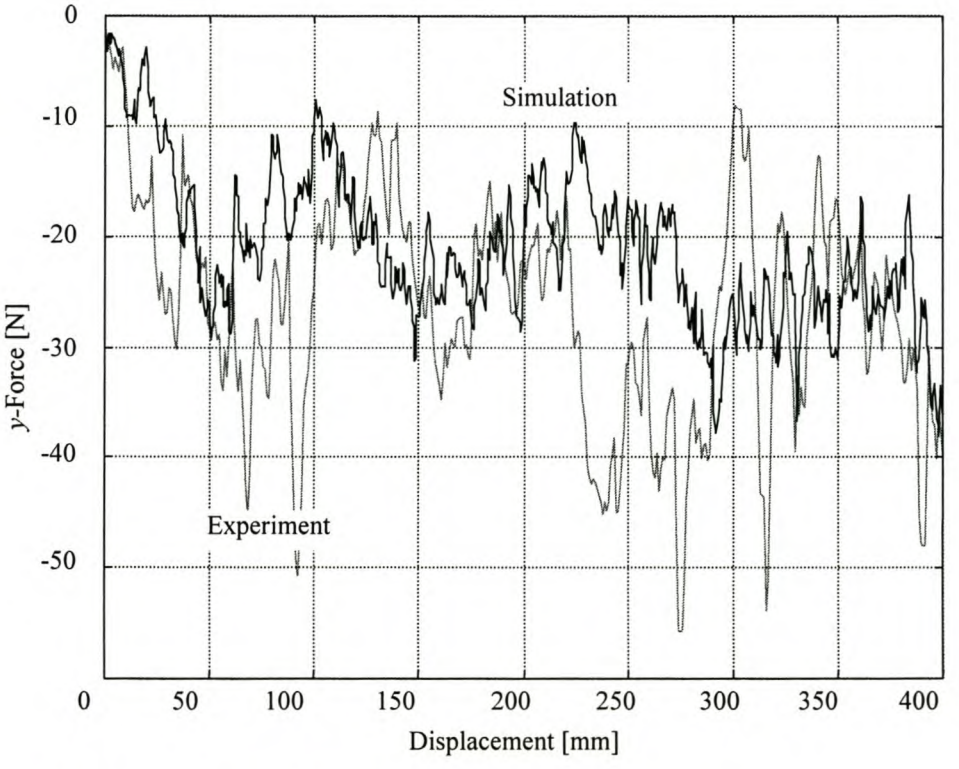

Figure 5.8 – *Blade y-forces, $\alpha = 90°$ $h = 200$ mm - corn*

Stellenbosch University http://scholar.sun.ac.za

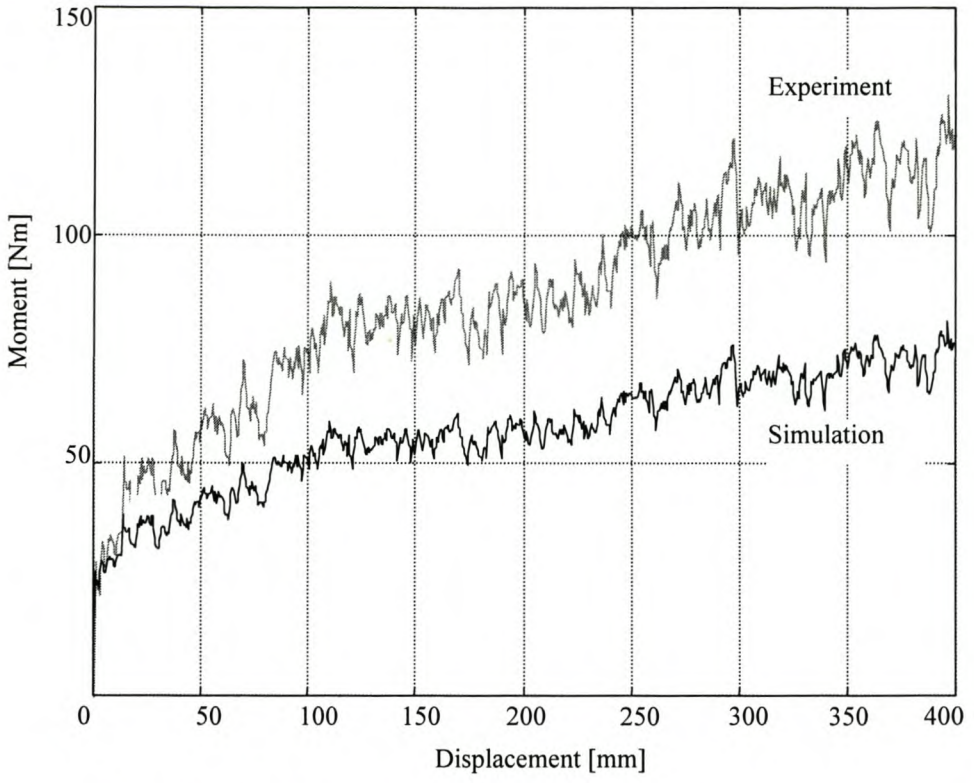

Figure 5.9 – *Blade moments, $\alpha = 90°$ $h = 200$ mm - corn*

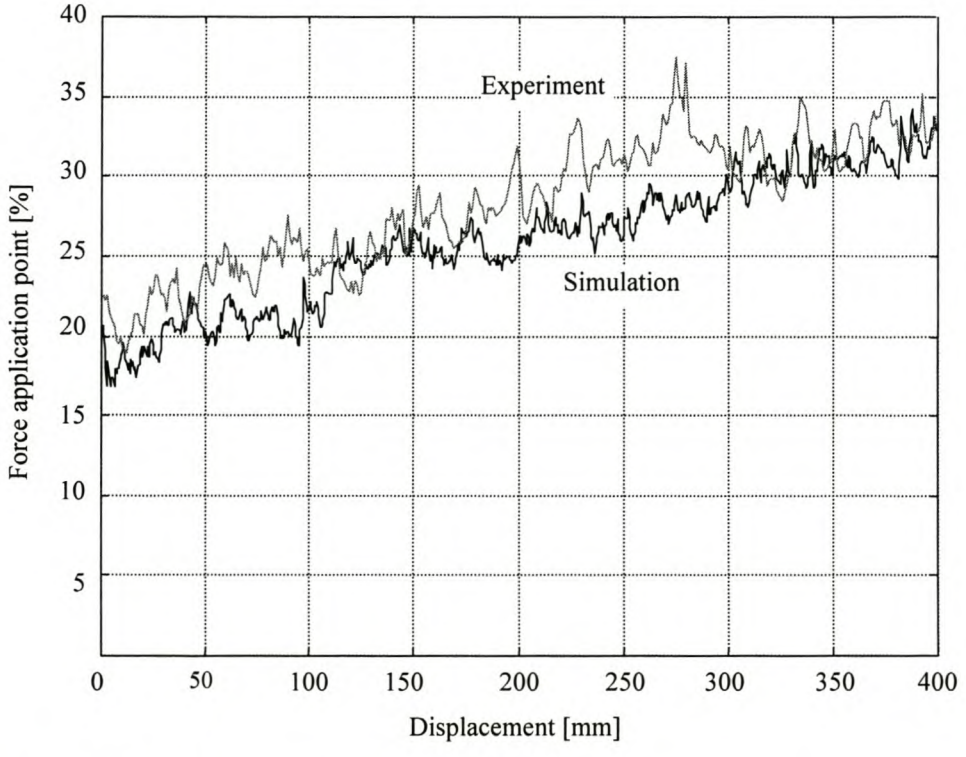

Figure 5.10 – *Blade force application point*

Stellenbosch University http://scholar.sun.ac.za

Figure 5.10 shows the force application point measured from the bottom of the blade as a percentage of the total blade height H. The application point shifts upward during the experiment/simulation as material builds up in front of the blade. The application point was found to be always between 30% to 50% of the immersed or covered blade height h from the bottom edge. According to the plasticity theory the pressure against the blade is a near linear function of the depth which means that the total force application point is equal to $h/3$.

Next we look at a breakdown of the total energy involved in moving the blade through the material. The aim is to show the trends in energy distribution and the importance of some components. This analysis is based only on the numeric simulations and the results shown here are from a simulation with corn as material and $a = 60°$ and 90° and the initial immersed depth equal to 200 mm. Energy is supplied to the system in the form of boundary work, E_w. The only moving boundary is the blade that moves in the x-direction. Thus, the total boundary work is the area under the x-force-displacement curve. The energy is consumed in five major processes,

- body work, E_b
- strain energy, E_s
- kinetic energy, E_k
- frictional work, E_f
- damping work, E_d

Body work is the work done by all body forces (gravity) on the assembly. E_s is the strain energy of the entire assembly stored at all contacts (normal and tangential direction). The kinetic energy accounts for both translational and rotational motion of all the particle. Frictional work is the total energy dissipated by frictional sliding at all contacts, while damping work is the total energy dissipated by the damping force acting on each particles. Note that the blade has no mass and hence no kinetic or gravitational potential energy. To start with, the system has no kinetic energy (particles in equilibrium with zero velocity) and the total strain energy is set to zero. Figure 5.11 shows the distribution of energy up to a total displacement of 400 mm. This displacement corresponds to the point where the particles start to fall over the top of the blade.

Stellenbosch University http://scholar.sun.ac.za

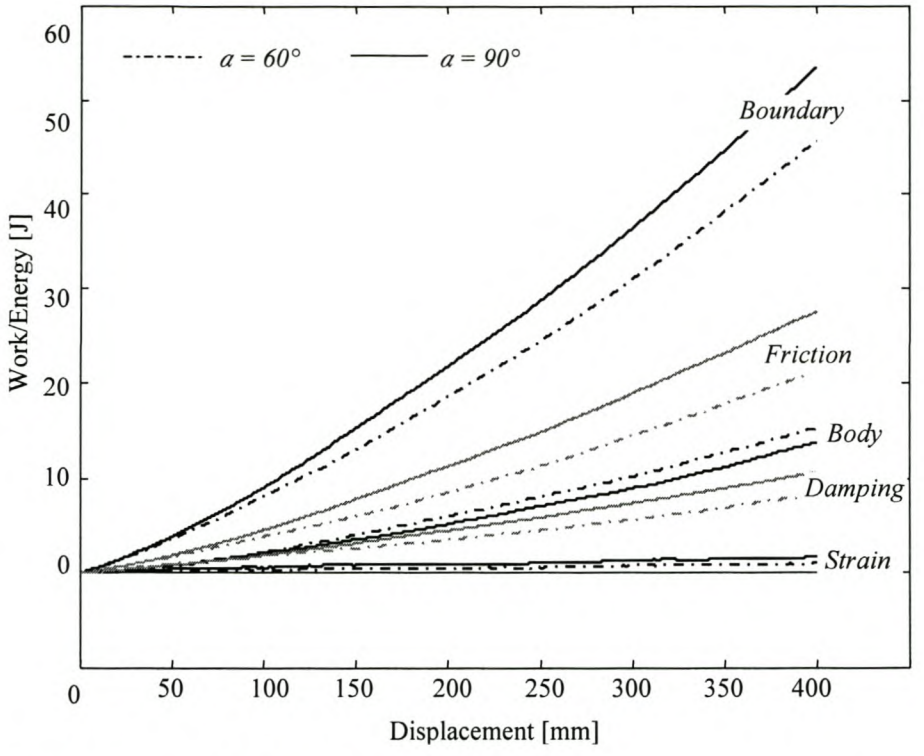

Figure 5.11 – *Blade energy distribution*

All the components, except for body work, are less for $\alpha = 60°$. Figure 5.12 shows the ratio of the different forms of energy/work relative to the boundary work.

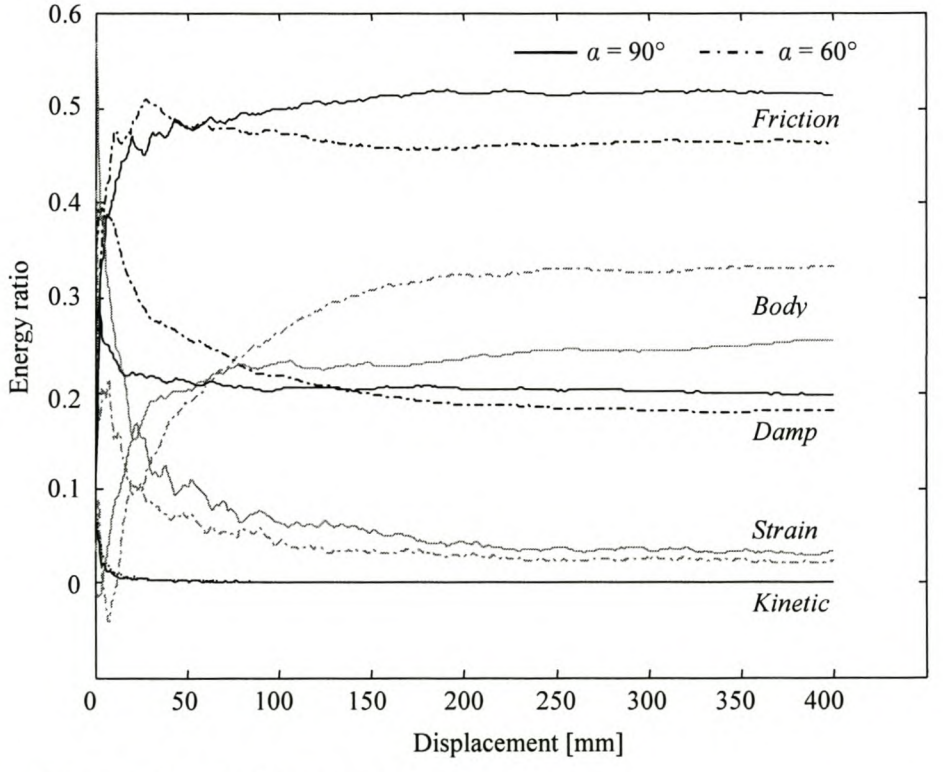

Figure 5.12 – *Blade energy ratios*

Stellenbosch University http://scholar.sun.ac.za

It will be shown later that a decrease in rake angle at constant depth h produces a draft force that decreases up to a point, and then starts to increase again. For this reason, the boundary work necessary to move the blade with $\alpha = 60°$ a certain distance, is less than the energy necessary to move the blade the same distance but with $\alpha = 90°$. It is clear that for both angles the total kinetic energy can be neglected since it is less than 0.005 % of the boundary work. We see that the strain energy increases slightly, which shows that the material is compressed as the blade is moving forward. Initially about 40% of the boundary work go into strain energy, but this ratio decreases to less than 5% after a displacement of 150 mm.

Body work increases as the particles rise above their original height. We see that 25% and 35% of the boundary work goes into body work for $\alpha = 90°$ and 60° respectively. This is to be expected since there is more movement of particles in the vertical direction with a decrease in rake angle. Friction work accounts for most of the energy, between 46% and 52%. Frictional sliding can only occur at contacts; these are particle-particle contacts and particle-blade contacts. Investigating the material-blade friction loss further, Fig. 5.13 shows that between 12% and 15% of the total friction loss occurs between the blade and the material for $\alpha = 60°$ and between 2% and 4% for $\alpha = 90°$.

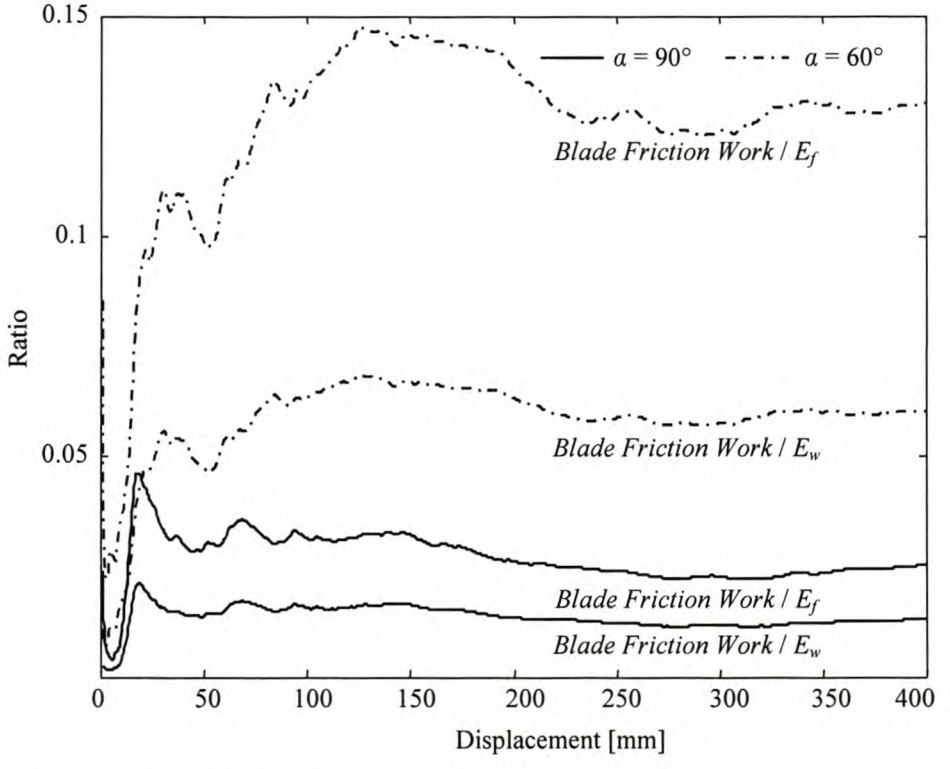

Figure 5.13 – *Blade friction ratios*

Stellenbosch University http://scholar.sun.ac.za

If we compare this loss in energy to the boundary work, between 5.5% and 7% of the boundary energy is lost due to friction at the blade with $\alpha = 60°$ and about 1.2% for $\alpha = 90°$. None of these observations is really surprising, but it is clear that the rake angle does influence the forces acting on the blade and the percentage of the boundary (input) work lost due to blade-material friction.

It is the draft force that is of great significance to the agricultural industry, since it determines the required power. The vertical force is supported by the ground and has no significant influence on the total power requirement. It does, however, influence the maximum traction available to the implement that pulls/pushes the tool. It has also been shown that the friction loss increases with a decrease in rake angle. This leads to an increase in implement wear which of course can decrease the lifetime of the implement dramatically. The rake angle also has an influence on the tillage process, which has the effect of improving the soil condition. Thus, when decreasing the rake angle in order to minimise the required draft force, the other influences need to be considered too.

It is impossible to collect enough data to give a broad picture of the way in which the various factors affect the problem because there are too many factors involved. The number of variables can be reduced by the use of dimensional analysis. By applying the Pi theorem the following relation can be written.

$$\frac{F}{\rho g B^2 H} = f\left(\frac{h}{H}, \alpha, \phi, \delta\right) \tag{5.4}$$

The force F can be the draft force F_x or the vertical force F_y A series of graphs can be produced to show the influence of each dimensionless parameter. The parameter on the left-hand side of Eq. 5.4 is called the *dimensionless force* while the parameters on the right-hand side are called the *dimensionless height*, *rake angle*, *internal friction angle* and *material-blade friction angle* respectively.

Soil mechanics and realistic material properties were used to develop a series of graphs (Fig. 5.14). In Fig 5.14(a) the *dimensionless x-* and *y-force* are plotted against the rake angle α with h kept constant. The magnitude of the x-force increases with an increase in

Stellenbosch University http://scholar.sun.ac.za

a. With $\alpha < (\pi/2 - \delta)$ the *dimensionless y-force* is positive, i.e. the blade is being forced downwards by the material. At $\alpha = (\pi/2 - \delta)$ there is no force acting on the blade in the *y*-direction and with $\alpha > (\pi/2 - \delta)$ the blade is being forced upwards which results in a negative *y*-force. Not shown in this figure is that the draft force decreases to a minimum value and then starts to increase again with decreasing *a*. This minimum can, in extreme cases, occur at rake angles as high as 75° and as low as 25° (McKyes and Ali 1977) and depends on the material properties. The handling of low rake angles (defined in Appendix C) with the plasticity theory has not been implemented yet. When Coulomb's theory is used, the angle for which the draft force is a minimum for corn and wheat is 29° and 32° respectively. The value for natural soil is typically in the order of 30° (Osman, 1964).

In the rest of Fig. 5.14 a = 90°. In Fig. 5.14(b) the *dimensionless forces* are plotted against the *dimensionless height* squared. The result is straight lines, which indicate that the force is a function of the height squared. The forces are only slightly influenced by the internal friction angle ϕ at low values of ϕ (Fig. 5.14c). The dependence on ϕ, however, increases dramatically with an increase in ϕ. Figure 5.14(d) shows that the *dimensionless x-force* increases with an increase in δ and the *dimensionless y-force* becomes more negative. Note that with $\alpha < (\pi/2 - \delta)$ the *dimensionless y-force* would start off as a positive value and with an increase in δ it will go through zero and become negative.

The plasticity theory, Coulomb's method and the logarithmic spiral method give the same general trends and are surprisingly close to each other. The logarithmic spiral method corresponds better to the plasticity theory than Coulomb's method. This is to be expected since Coulomb's method assumes a straight rupture line while the logarithmic spiral method makes use of the more correct curved rupture surface. Coulomb's method always overestimates the magnitude of the *x*- and *y*-force. For rake angles less than 77°, the logarithmic spiral method underestimates the force magnitude and for angles above 77° it overestimates the force magnitudes. The difference in the predictions is simply due to the assumptions on which each model is based.

Stellenbosch University http://scholar.sun.ac.za

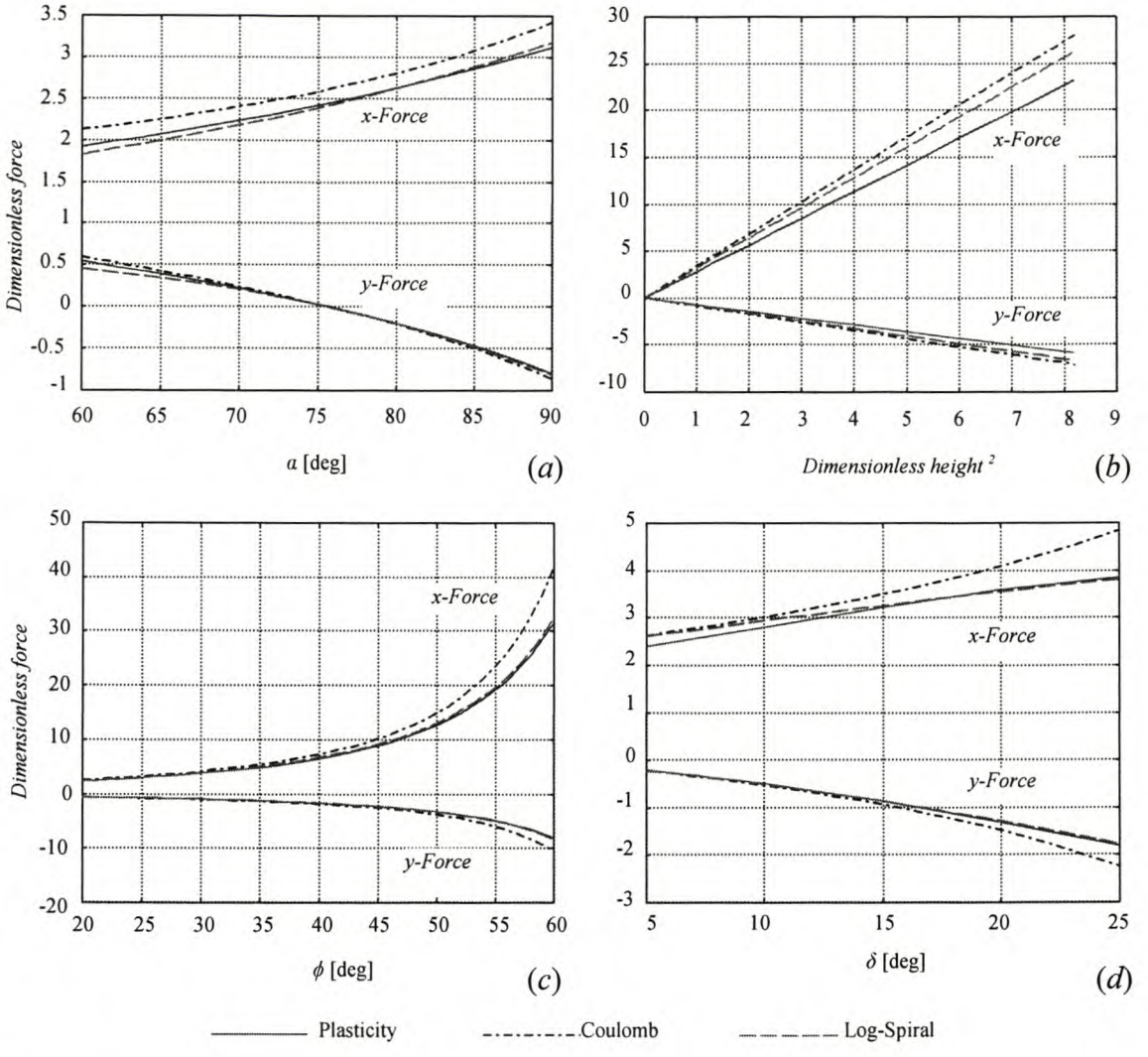

Figure 5.14 – *Dimensional analysis*

The formation of a heap can only be incorporated into the analytical analysis (plasticity theory, Coulomb's method, etc.) in a semi-empirical way. These theories can not predict the formation of the heap and it can only be included if the shape of the heap is known from experiments. It can also not predict the forces on the blade during the initial compression stage but only after a slip plane has formed. To make comparisons, special experiments were conducted. In these experiments, the blade was given a velocity of 0.5 mm/s and the immersed depth h was kept constant by carefully removing the excess material, i.e. the material rising above h. This procedure is similar to that performed by Osman (1964). The same procedure was followed during simulations. The shear forces F_s showed high fluctuations but the draft force is practically more important. For this reason, only the draft forces were used for comparison purposes.

Stellenbosch University http://scholar.sun.ac.za

Figure 5.15 shows the results with α = 80° and h = 300 mm. It can be seen that the initial 150 mm causes compression of the material as the draft force increases to a maximum value. Note that this corresponds well to the results from the energy analysis where it was shown that the strain energy steadily increases over the first 150 mm (Fig. 5.12). All simulations and experiments showed this behaviour and three values of the draft force between 150 and 250 mm were used for comparison purposes. The maximum, minimum and average values were computed for four different rake angles (60°, 70°, 80° and 90°) and depths of 100, 150, 200, 250, 300 and 350 mm.

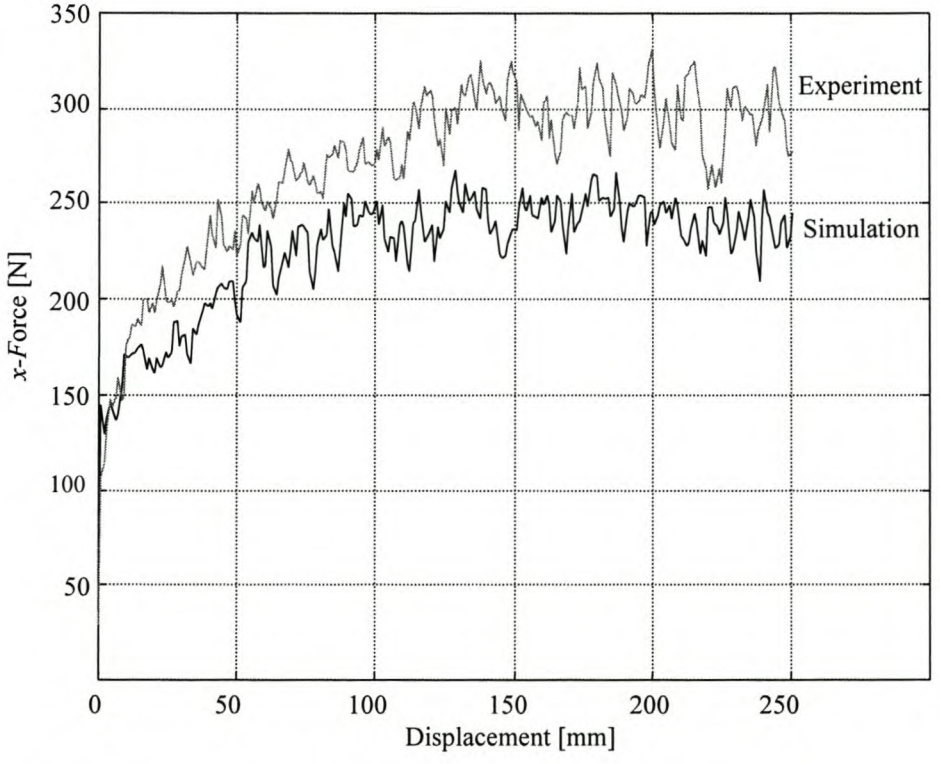

Figure 5.15 – *Blade draft force with no heap formation, corn with α = 80° and h = 300 mm*

The maximum, minimum and average values obtained are plotted against the corresponding predicted values, using the plasticity theory, in Fig. 5.16. These values are also plotted versus h and according to α in Appendix D.

Stellenbosch University http://scholar.sun.ac.za

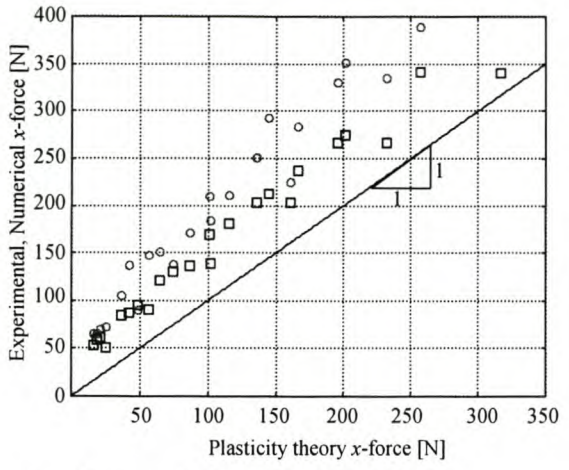

(a) Corn maximum forces

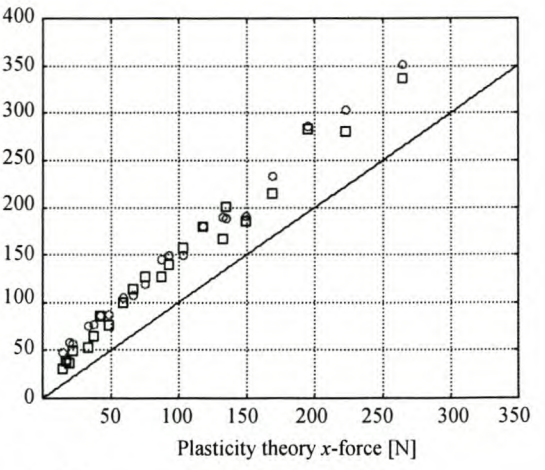

(b) Wheat maximum forces

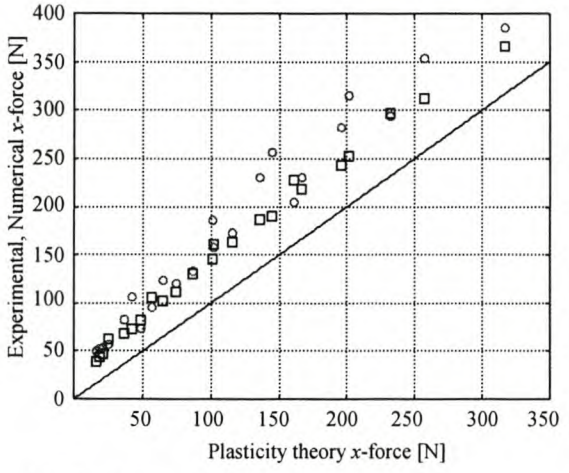

(c) Corn average forces

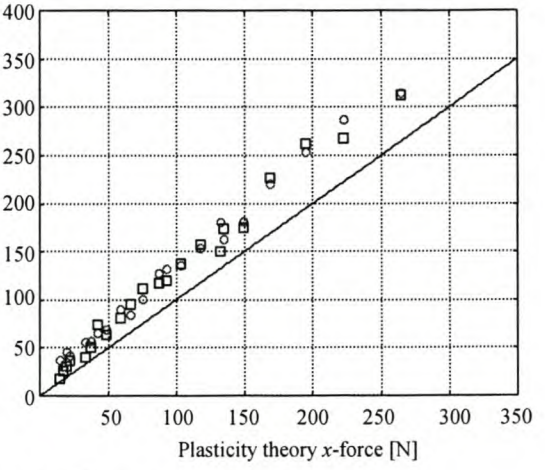

(d) Wheat average forces

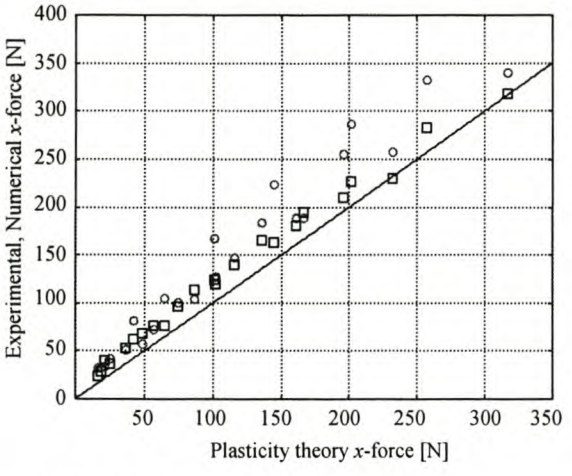

(e) Corn minimum forces

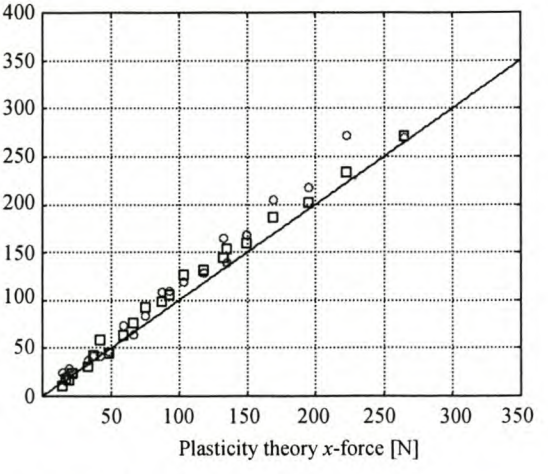

(f) Wheat minimum forces

Figure 5.16 – *Draft force comparison:* ○ *Experimental* □ *Numerical*

Stellenbosch University http://scholar.sun.ac.za

If the theoretical model is perfect all points shown in the figure should fall on the straight line with a slope of one. The maximum, average and minimum forces, both experimental and numerical, are higher than the predicted values. The minimum values show the best correlation. Perumpral et al.(1983) (Perumpral's method), Swick and Perumpral (1988) (Perumpral's method) and Osman (1964) (logarithmic spiral method) all reported the theoretical predictions to be lower than the measured values of draft force. The side panel friction definitely increases the measured forces. The above-mentioned authors, however, did not make use of a 2-D rig and still found that the models underestimated the draft force. Studying of the results as given in Appendix D reveals that the values predicted by theoretical methods are more accurate for high values of a. The accuracy decreases with a decrease in a. This is also reported by Osman (1964). The wheat results are in general closer to the theoretical ones.

For the above comparison, the plasticity theory was used, but the logarithmic spiral and Coulomb's theory can also be used. There is, however, no big difference in the results. In the range of parameters used, the biggest difference between the plasticity theory and the logarithmic spiral method is 8.1% with an average difference of 5.6%. The maximum difference between Coulomb's theory and the plasticity theory is 9.9% with an average difference of 6.4%.

An extremely good correlation between the experimental and numerical results is obtained as depicted in Fig. 5.17. Here it is also evident that there is a better agreement between the wheat results compared to that of the corn. The most likely reason for this can be found when comparing the macro-properties of the natural material to that of the synthetic material (Tab. 4.1). It can be seen that the wheat properties compare better than that of the corn. The corn data is more scattered than the wheat data. The reason for this may be that the size of the wheat grains is about one-third to a half of the corn grain size while the size of the total system is the same.

Stellenbosch University http://scholar.sun.ac.za

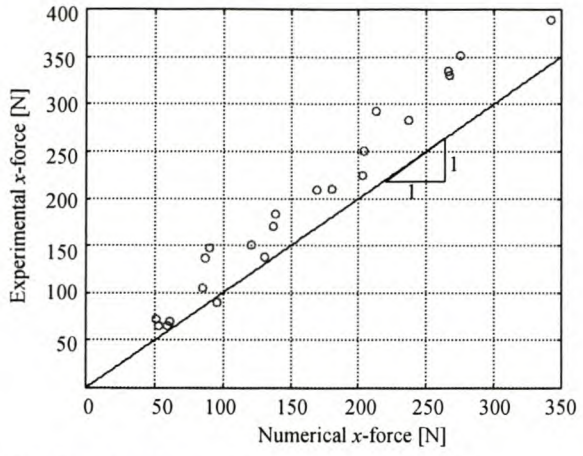

(a) *Corn maximum forces*

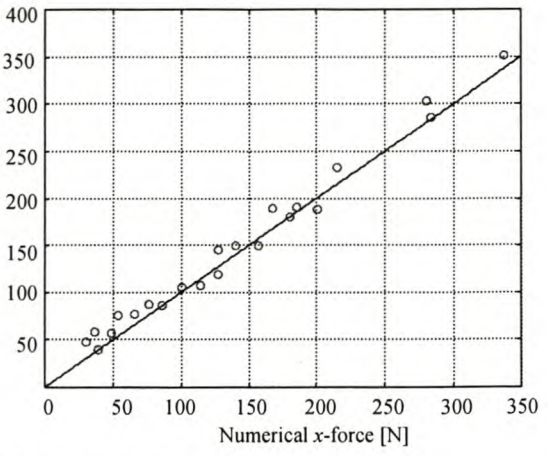

(b) *Wheat maximum forces*

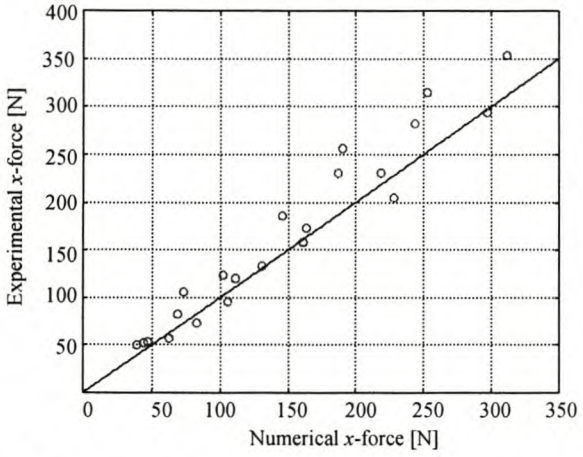

(c) *Corn average forces*

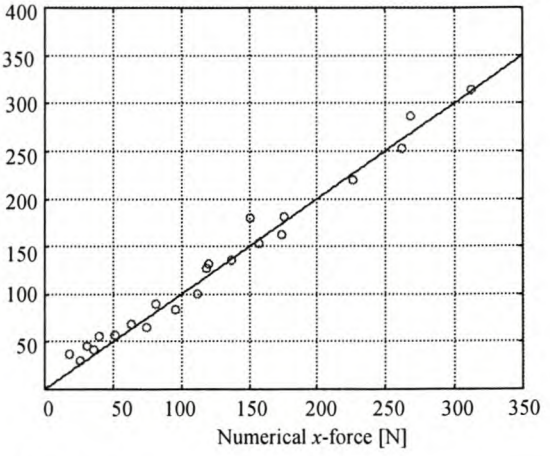

(d) *Wheat average forces*

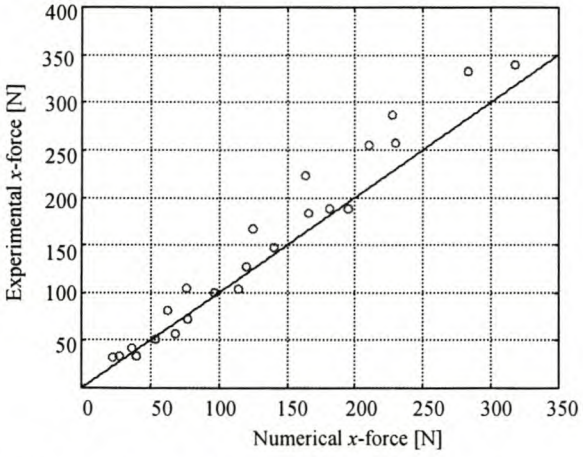

(e) *Corn minimum forces*

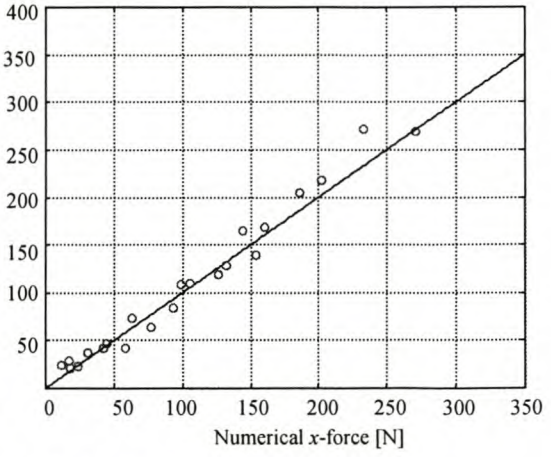

(f) *Wheat minimum forces*

Figure 5.17 – *Draft force comparison*

Stellenbosch University http://scholar.sun.ac.za

5.4 Rupture Lines

The plasticity theory discussed in Appendix C can be used to predict the slip (shear) lines, the outer-most of which is called the rupture line. The logarithmic spiral method can also be used to predict the rupture line but not the other slip lines. In this section the predictions using these theories are compared to experimental results. The ability of DEM to predict the formation of rupture lines is also investigated.

The first approach to predict the rupture lines with DEM is to look at the magnitude of the absolute particle displacements. The following procedure is followed.

The blade is given a displacement of 150 mm to ensure the formation of a rupture line. The displacement vector of each particle is then set to zero. The blade is given a further displacement of 10 mm and the magnitude of the absolute displacement vectors is determined. The particle displacement ratio, *PDR*, is defined as the ratio of the magnitude of the particle absolute displacement vector to the magnitude of the blade displacement vector. The particles are then coloured according to their individual *PDR* values. The result of such a simulation is shown in Fig. 5.18.

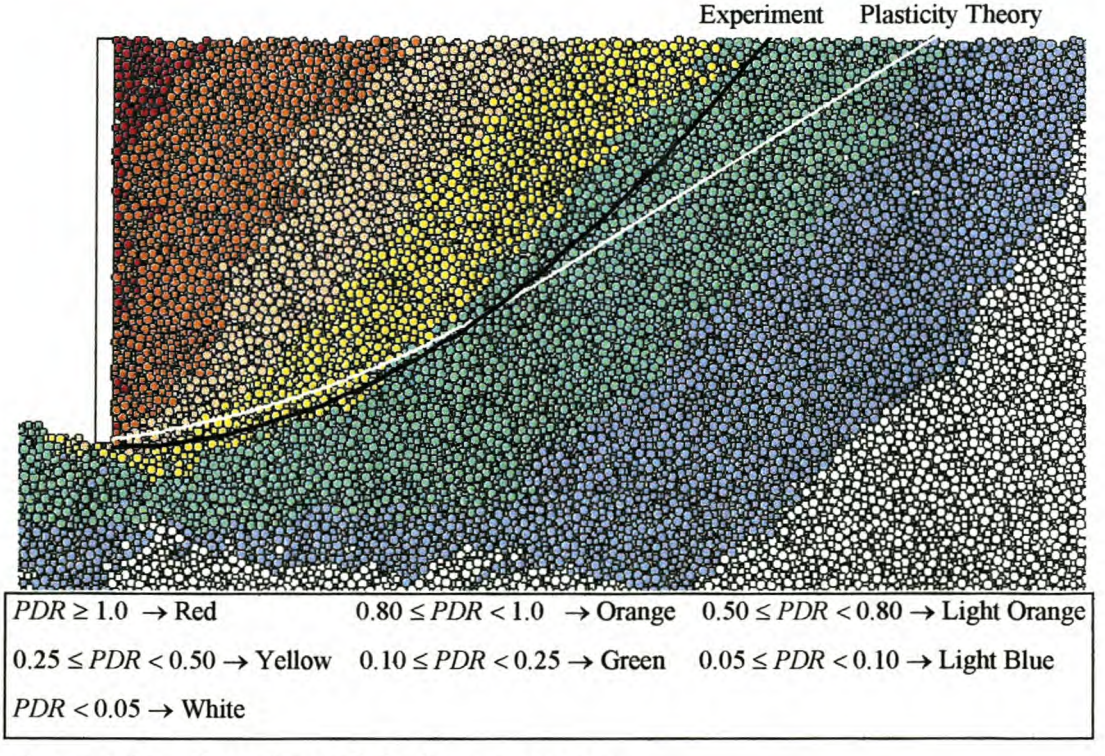

Figure 5.18 – *Particle total displacement ratios*

Stellenbosch University http://scholar.sun.ac.za

The measured rupture line as well as the line predicted by the plasticity theory is indicated in black and white respectively. The experimental line is more curved than the theoretical one, and both are within the green region, with *PDR* values ranging form 10 to 25%. A large range of particles outside these rupture lines, however, has *PDR* values between 5 and 10%. Figure 5.19 shows the *PDR* values of the same system but based only on the particle *y*-displacements.

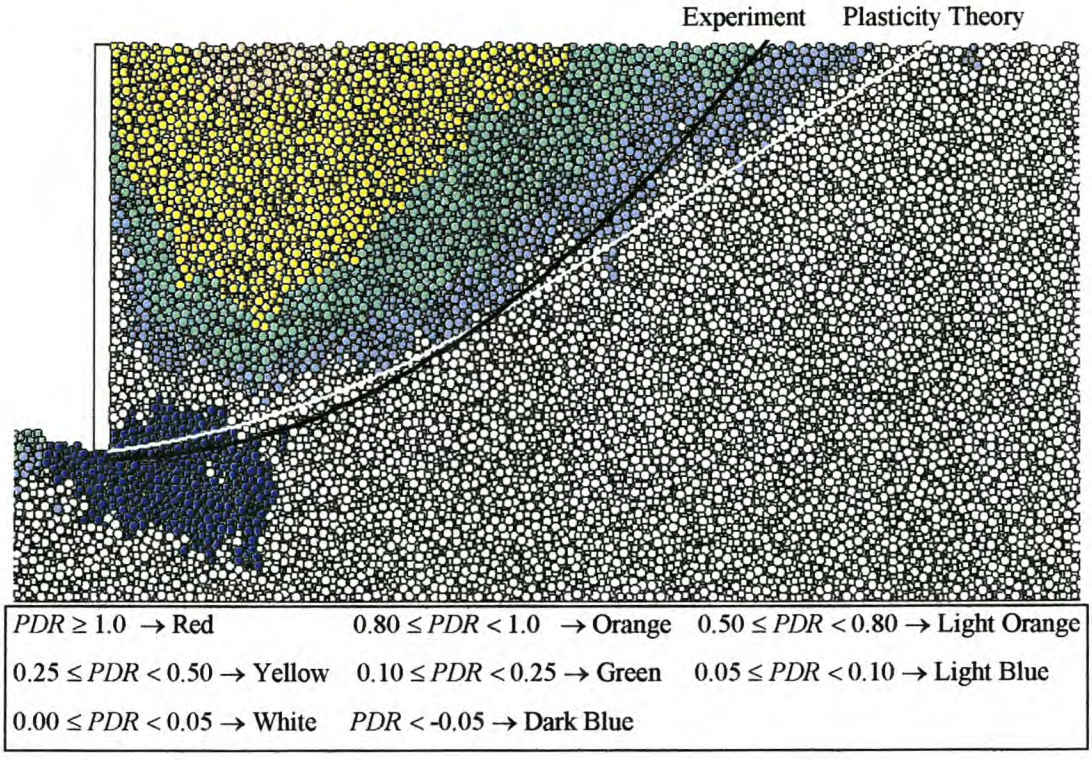

Figure 5.19 – *Particle y-displacement ratios*

Note that it is possible for this ratio to be negative as indicated by the dark blue particles. There will always be negative *y*-displacements due to the finite size of the particles and the effect of the blade's bottom edge. What is clear from this figure is that all the particles with *PDR* values ≥ 5% are within the rupture zone as defined by the plasticity theory. The material outside this zone, but included in Fig. 5.18, experiences only displacement in the *x*-direction. This forms part of a compression region in front of the rupture line. The size of this compression zone increases up to a point and then remains constant. This is in agreement with the compressibility results obtained in section 5.2.

Stellenbosch University http://scholar.sun.ac.za

Reasoning that for particles at the free surface to be within the rupture zone they must have at least a y- and x-displacement component, Fig. 5.20 can be created. In this figure a single *PDR* value (based on total particle displacement) is adjusted until the contour joins the contour based on only the y-displacement (Fig. 5.19) at the free surface. Although this rupture zone is slightly larger than the experimental one, the shape of the rupture lines is very similar.

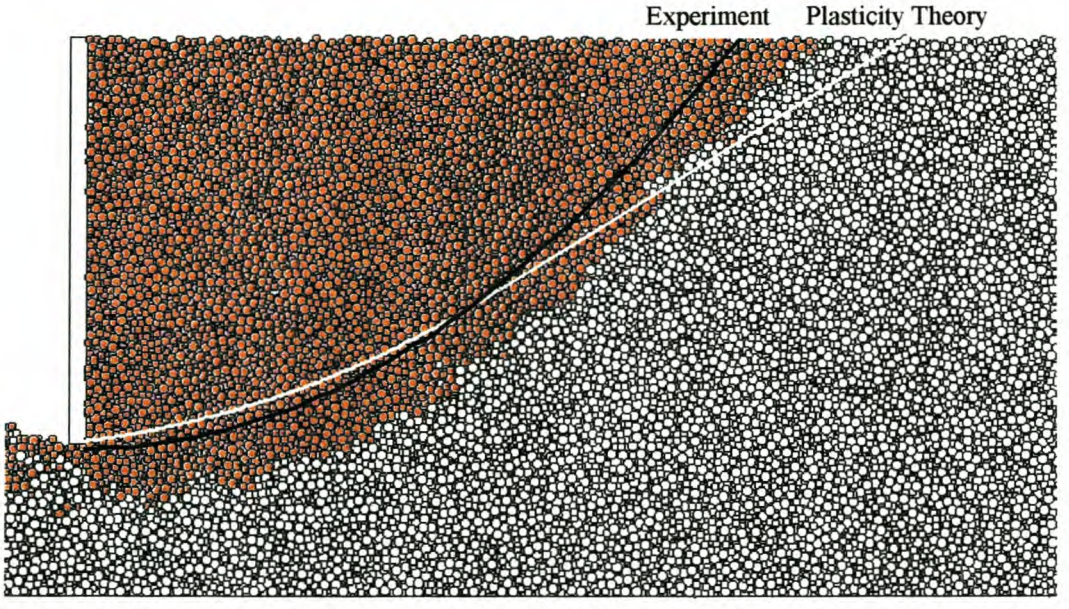

Figure 5.20 – *Particle total displacement ratio of 0.15*

This at least indicates that the displacement contours assume the shape of the rupture surface.

In the search for the rupture line, it was observed that a shock wave forms immediately after the blade starts its motion. The wave is clearly visible after a blade displacement of only 0.01 mm and moves through the material with an average velocity of ±6750 times the velocity of the blade. The wave dies out after a blade displacement of 0.2 mm, as shown in Appendix D.

A totally different approach is one that is based on particle relative displacements. The blade is again given a displacement of 150 mm to make sure that a rupture line has formed. Using a "parent-child" structure the position of all the particles and their contacting neighbours are then stored in an array. The blade is give a further displacement of 10 mm and the new position of each particle is then determined. The

Stellenbosch University http://scholar.sun.ac.za

new distance between the centres of two original parent- and child-particles is then determined and compared to the original centre distance. If the centre distance has increased by 2% or more, the colour of both particles is changed. The particles below the lower edge of the blade are ignored.

The results are shown in Fig. 5.21 and Fig. 5.22 for α = 90° and 60° respectively. Excellent agreement with experimental results is obtained for β = 90° although the predicted line is not totally smooth as with the previous method.

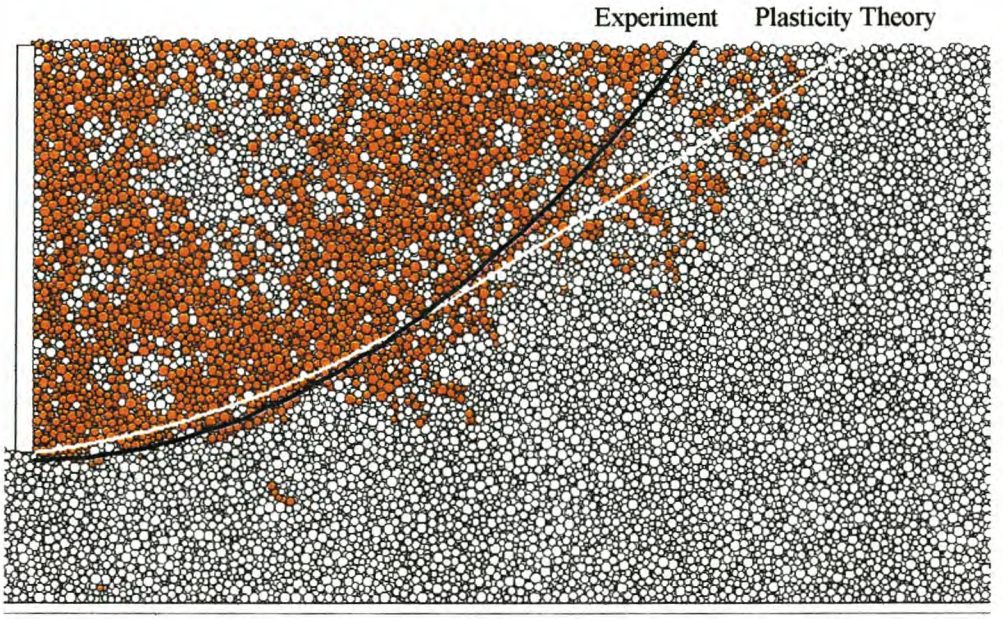

Figure 5.21 – *Rupture line based on relative particle displacements, β = 90°*

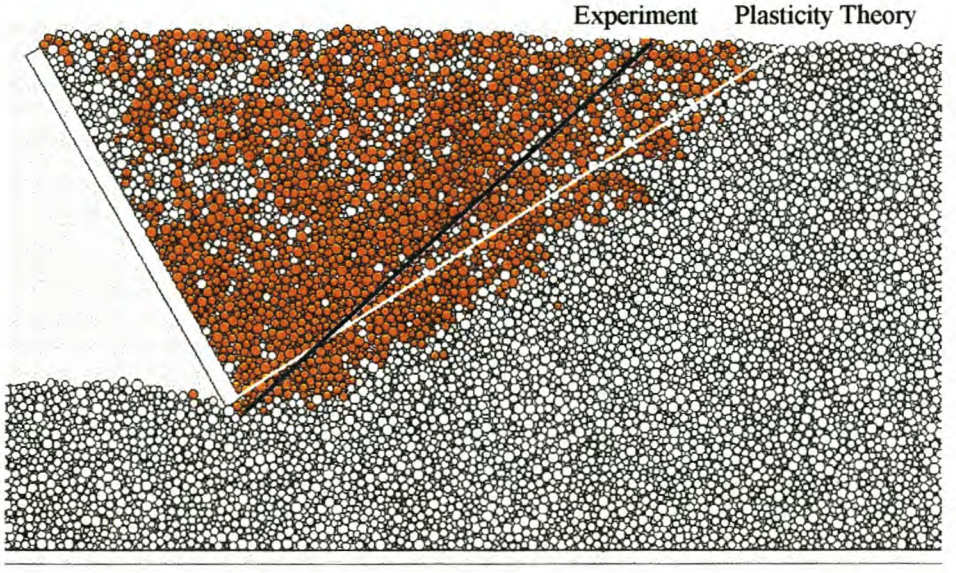

Figure 5.22 - *Rupture line based on relative particle displacements, β = 60°*

Stellenbosch University http://scholar.sun.ac.za

The rupture line becomes a straight line with a decrease in α and with $\alpha = 60°$ it is for all practical purposes a perfect straight line. The theoretical slope of this line is equal to $(45°-\phi/2)$, which yields 32° in the case of corn, compared to the measured value of 41°. There will always be a difference between the theoretical and measured rupture line due to the finite size of the particles. Reasoning along these lines, one feels intuitively that the wheat should give better results, but for reasons unknown, it does not.

In general, the theoretical rupture zones are larger than the measured ones and the rupture lengths longer. The rupture lines predicted by the logarithmic spiral method are for all practical purposes exactly the same as those predicted by the plasticity theory and when plotted on the same graph the difference is barely visible.

All the results presented here were obtained with corn; results for wheat are given in Appendix D.

It is interesting to note the differences with small rake angles, which is defined as $\alpha \le \frac{\pi}{2} - \frac{1}{2}\left[\delta + \sin^{-1}\left(\frac{\sin(\delta)}{\sin(\phi)}\right)\right]$ for cohesionless material. The shape of the rupture lines changes if the influence of the blade overlaps with the Rankine zone. This is left for further study.

Stellenbosch University http://scholar.sun.ac.za

CHAPTER 6

BUCKET RESULTS

This chapter presents all the results obtained from experiments and simulations with the bucket profile.

6.1 Displacement and Velocity

During all the experiments, the bucket was given a velocity of 10 mm/s in the x-direction. Weights were added to the arm-mechanism to vary the vertical load on the bucket. If the results are associated with dragline filling, the weights added can be seen as the weight of the bucket W_b itself (Rowlands, 1991). Bucket weights of 49.1, 93.2, 138.3 and 202.1 N were used. The vertical velocity can be broken down in two components: one in the x- and one in the y-direction. Figure 6.1 shows the experimental y-displacement for corn with $\beta = 10°$ and all four bucket weights.

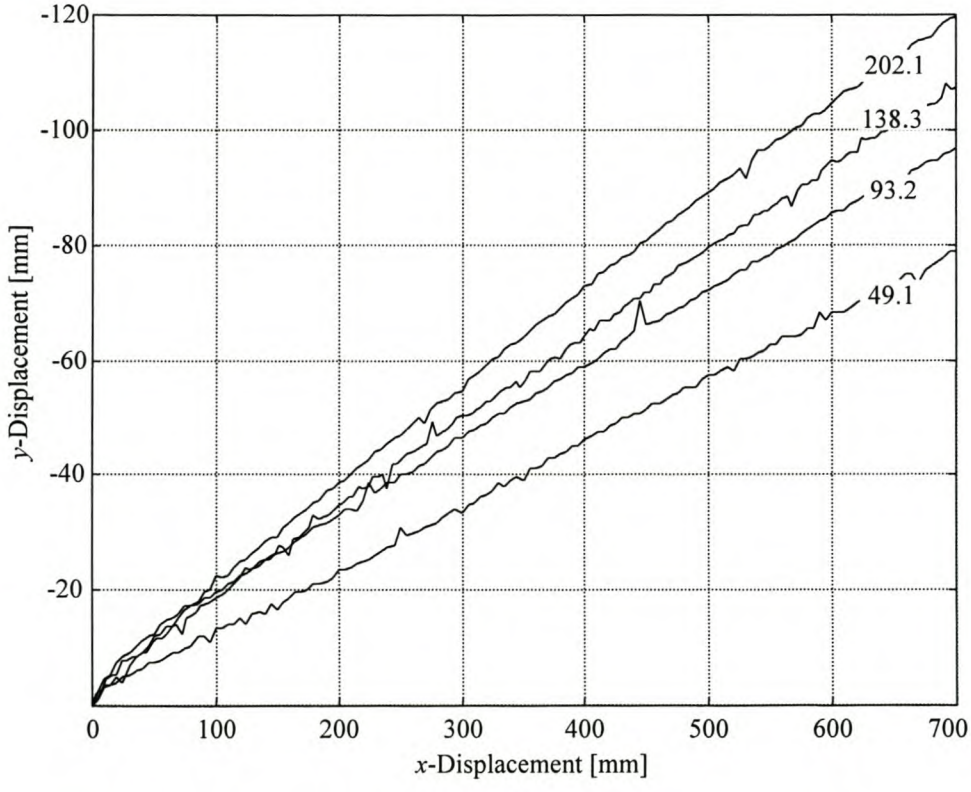

Figure 6.1 – *Bucket displacements with $\beta = 10°$, W_b indicated in N*

Stellenbosch University http://scholar.sun.ac.za

It can be seen that these displacement curves are practically straight lines. The gradient of these lines, i.e. the displacement or velocity ratio, was determined by fitting a straight line between 100 and 700 mm in x-displacement. The Bucket Velocity Ratio (BVR) is defined as

$$BVR = \frac{-\,y\ velocity}{x\ velocity} = \frac{-\,y\ displacement}{x\ displacement} \tag{6.1}$$

As expected, an increase in W_b causes an increase in y-displacement. Figure 6.2 shows the BVR as a function of both W_b and the drag angle β.

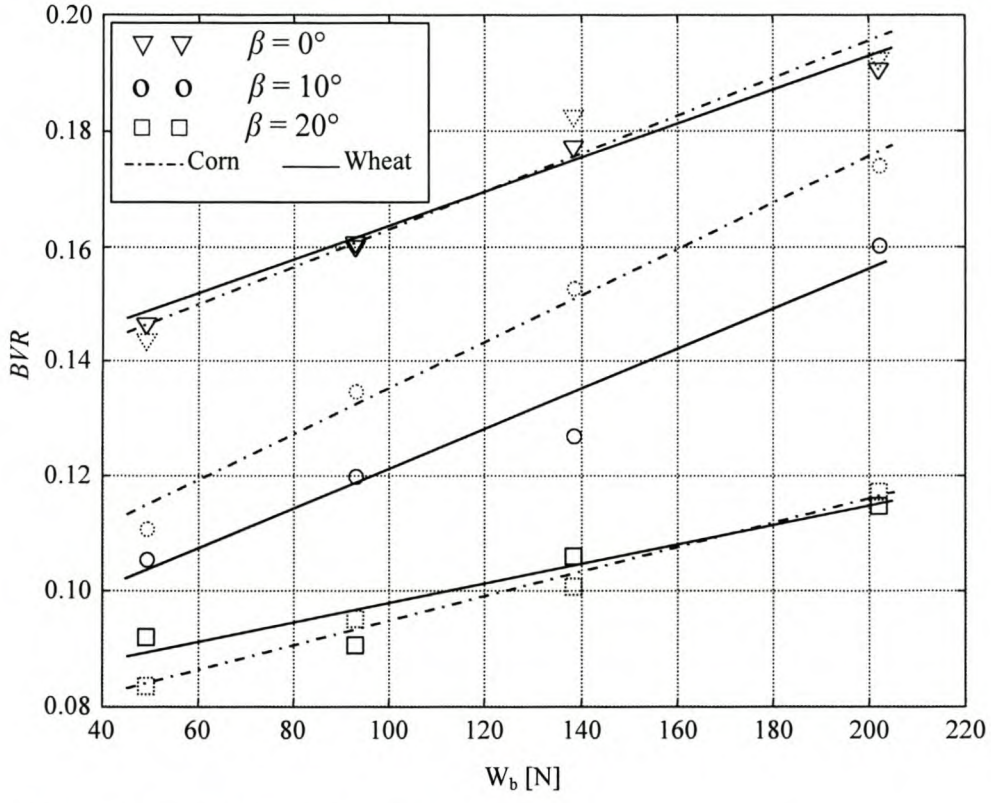

Figure 6.2 – *Blade velocity ratios*

It is clear that with an increase in β there is a decrease in y-displacement. The forces applied to the bucket are the draft force F_x and the bucket weight W_b. The payload W_p increases as the bucket moves through the material and adds to the bucket weight. The bucket interacts with the material and by breaking down the total interaction force into a normal F_n and tangential F_t component (Fig. 6.3), it can be shown that

Stellenbosch University http://scholar.sun.ac.za

$$F_n = (W_b + W_p)\cos(\beta) \tag{6.2}$$

$$F_x = (W_b + W_p)\sin(\beta) + F_t \tag{6.3}$$

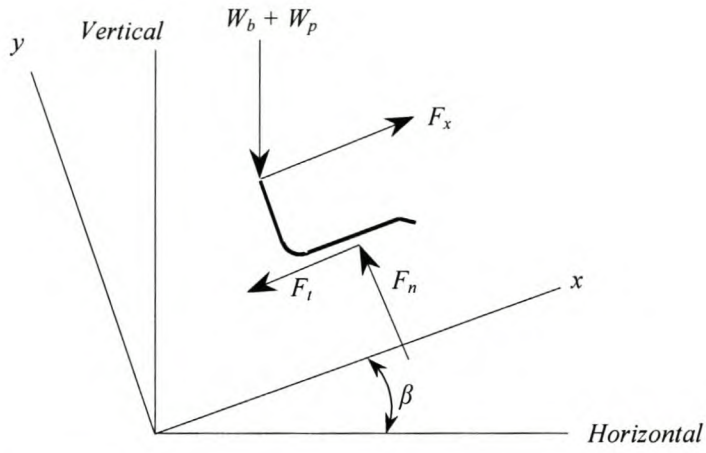

Figure 6.3 – *Bucket forces*

F_n acts in the y-direction and is the force with which the bucket is being "forced" into the material. Further, from Eq. 6.2, with an increase in bucket weight and payload there is an increase in F_n and subsequently an increase in y-displacement. Also, with an increase in β there is a decrease in F_n and y-displacement. This simple model accurately verifies the trends observed. The above reasoning, however, assumes that the payload is not influenced by β. As will be shown later, this is not true. Although a decrease in β tends to decrease F_n through the $\cos(\beta)$ term, it also causes an increase in payload which tends to increase F_n. The resultant behaviour is a combination of these two factors. Assuming this model to be correct and using the results in Fig. 6.2, one can say that the $\cos(\beta)$ term in Eq. 6.2 has a greater influence on the y-displacement as does the increase in payload.

The *BVR* is shown to be a linear function of W_b for all β's. For $\beta = 0°$ and $20°$ the results for wheat and corn are practically the same, but there is a rather big difference in *BVR* for $\beta = 10°$. There is no resultant force acting on the bucket in the y-direction since there is practically no acceleration although the payload increases during filling. This means that the interaction force F_n also increases with an increase in payload.

Stellenbosch University http://scholar.sun.ac.za

6.2 Forces and Energy

The force measured in the y-direction is only that of the weights and not F_n. For this reason, we are only interested in the draft force. Figure 6.4 shows typical *engaging forces* F_e obtained from experiments and simulations. The draft force transducer was zeroed with the rig tilled so that the measured force does not include the effect of the bucket weight, i.e. the $W_b \sin(\beta)$ term in Eq. 6.3. The *draft force* is simply

$$F_x = F_e + W_b \sin(\beta) = \left[W_p \sin(\beta) + F_t\right] + W_b \sin(\beta) \tag{6.4}$$

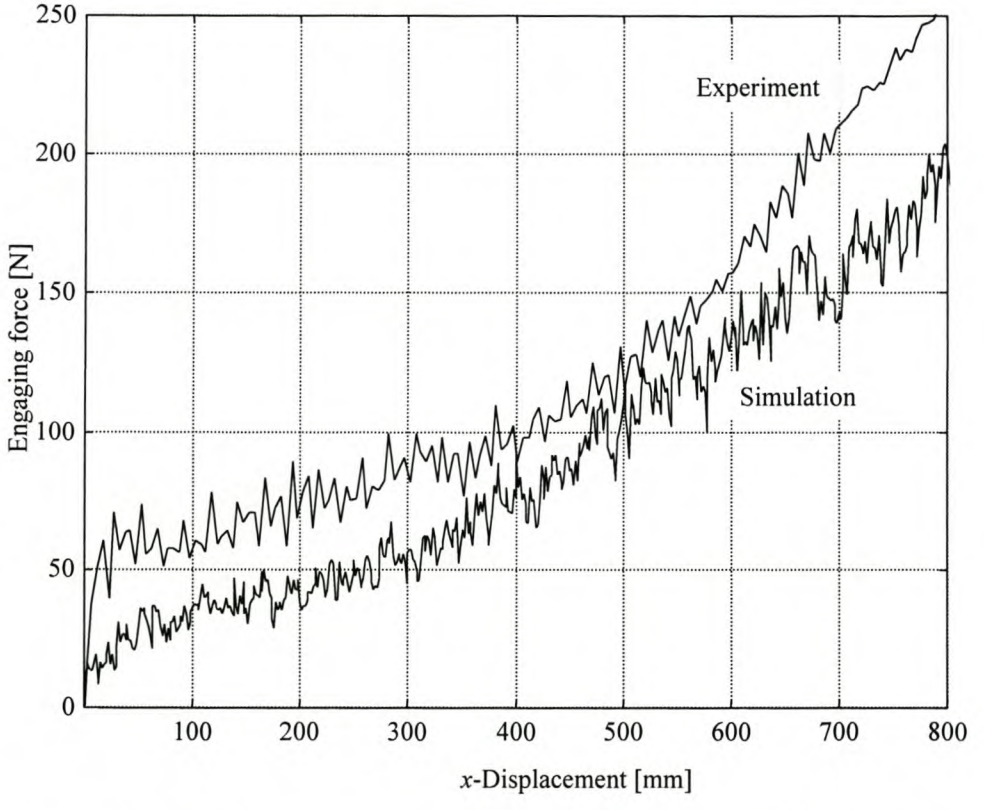

Figure 6.4 – *Bucket engaging force: Corn, β = 10°, W_b = 138.3 N*

In the numeric model the bucket is assumed to be weightless and the force on the bucket in the x-direction is per definition the *engaging force*. As was the case with the blade, all the experimental engaging forces are higher than those predicted by simulations. The main reason for this is expected to be the side friction against the glass panels. Again, it is very difficult to quantify the influence of the side friction. The shape of the

Stellenbosch University http://scholar.sun.ac.za

graphs is, however, very similar. The "noise" arises principally from the discrete nature of the particles.

To compare the results we make use of the energy required to fill the bucket. This "smoothes out" the noise and comparisons can be made more easily. The engaging energy E_e is defined as the area under the F_e-displacement graph and the draft energy E_x as the area under the F_x-displacement graph. First, we have a look at the influence of W_b on the energy requirements. Figure 6.5 shows the engaging energy of both corn and wheat with W_b = 138.3 N and $\beta = 0°$, 10° and 20°.

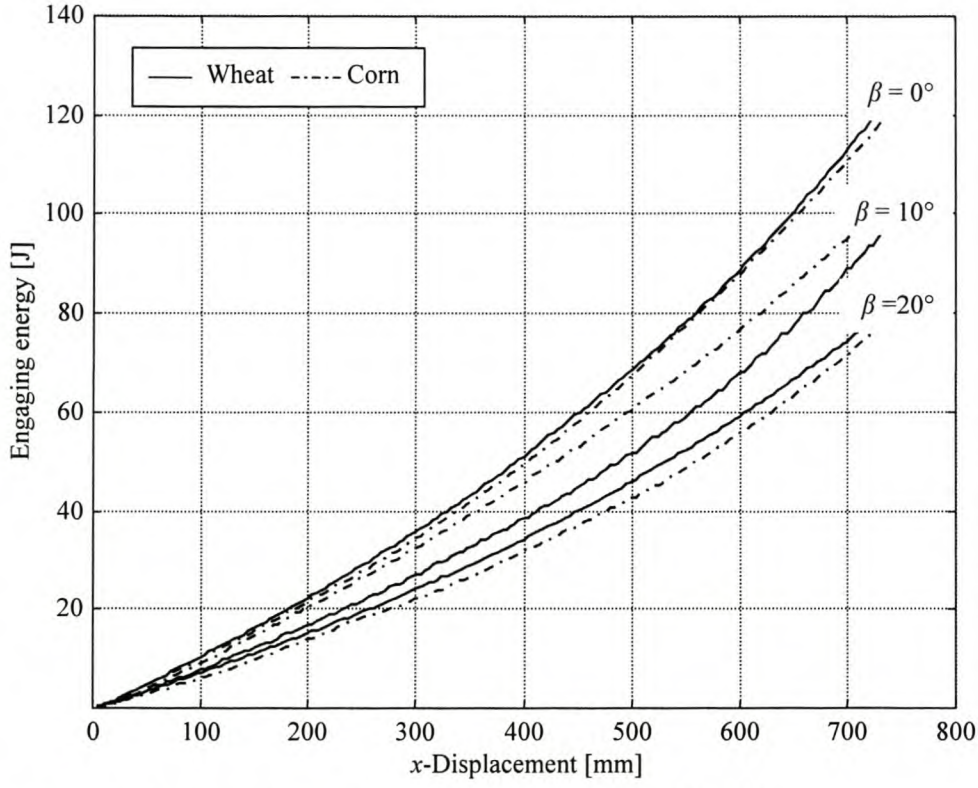

Figure 6.5 – *Experimental engaging energy, W_b = 138.3 N*

The first thing to observe is that the engaging energy required decreases with an increase in β. This is a direct result from the fact that the y-displacement decreases with an increase in β, i.e. the engaging force decreases with an increase in β. Again, there is not a big difference between the two materials. If we now calculate the draft energy (Fig. 6.6), we see that the graph of β = 10° and 20° shifts closer to that of β = 0°. Therefore, looking at this graph it seems as if there is no benefit, with respect to energy requirements, to increase the drag angle. We return to this point when fill rates are discussed.

Stellenbosch University http://scholar.sun.ac.za

Figure 6.7 shows both the experimental and numerical engaging energy requirements to move the bucket a distance of 700 mm. As expected, the energy requirement increases linearly as a function of W_b.

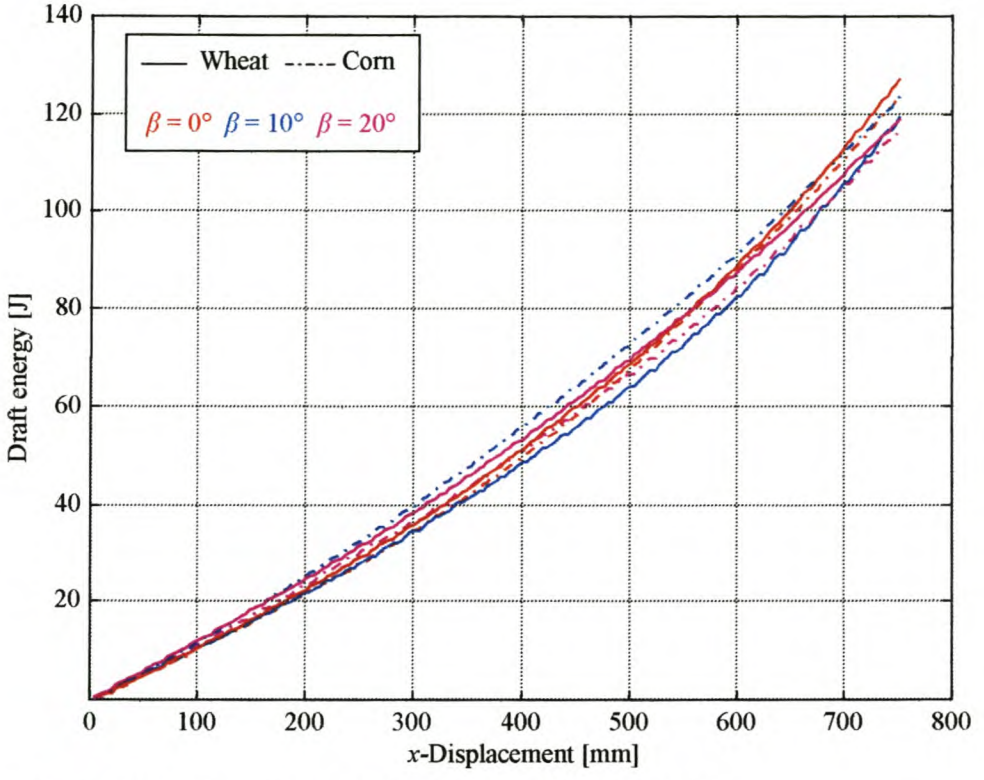

Figure 6.6 – *Experimental draft energy, W_b = 138.3 N*

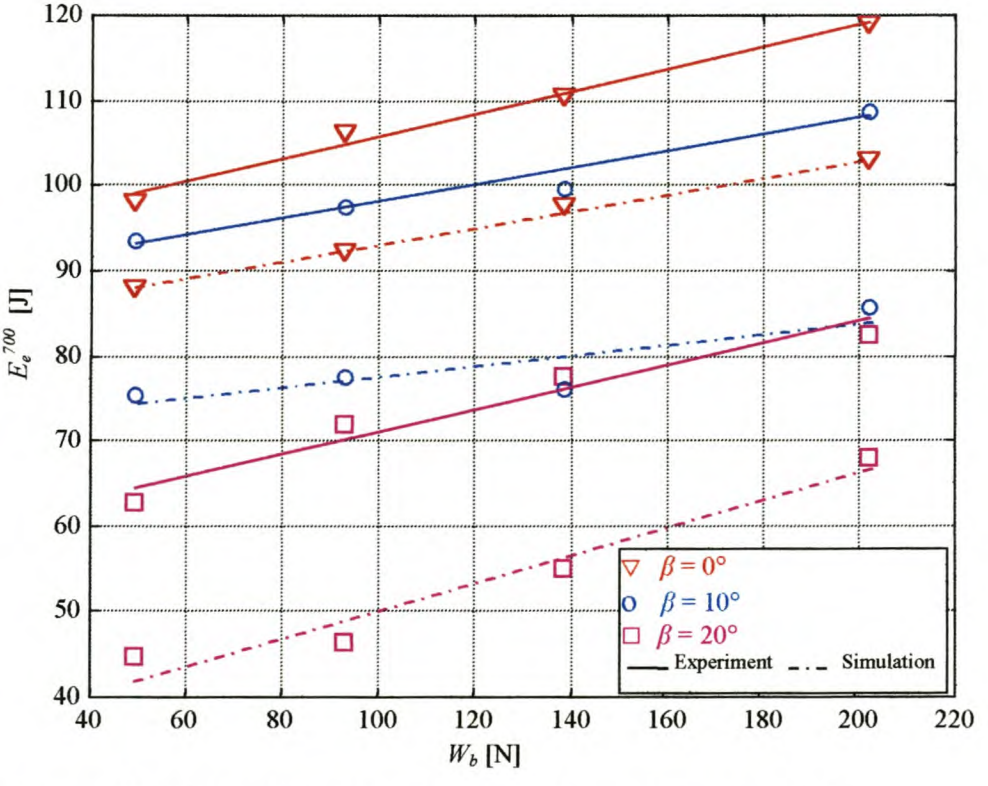

Figure 6.7 – *Experimental and numerical engaging energy: Corn*

Stellenbosch University http://scholar.sun.ac.za

Quantitatively, a good comparison between the experimental and numerical results is obtained. The numerical results are less than the experimental ones and the ability to predict the energy required decreases with increasing drag angle. The wheat showed the same general trends, experimentally and numerically.

Assume for the moment that the bucket is that of a loader. Assume furthermore that the bucket is weightless, and that it is forced into the material with a constant y-velocity so that it follows the same path as those during the experiments. The direction and position of the resultant force exerted by the bucket can be calculated with F_x, F_y and M known. The result obtained from a simulation with $\beta = 10°$ and corn as material is shown in Fig. 6.8. Each vector corresponds to a further x-displacement of 50 mm and the length thereof is an indication of the force magnitude.

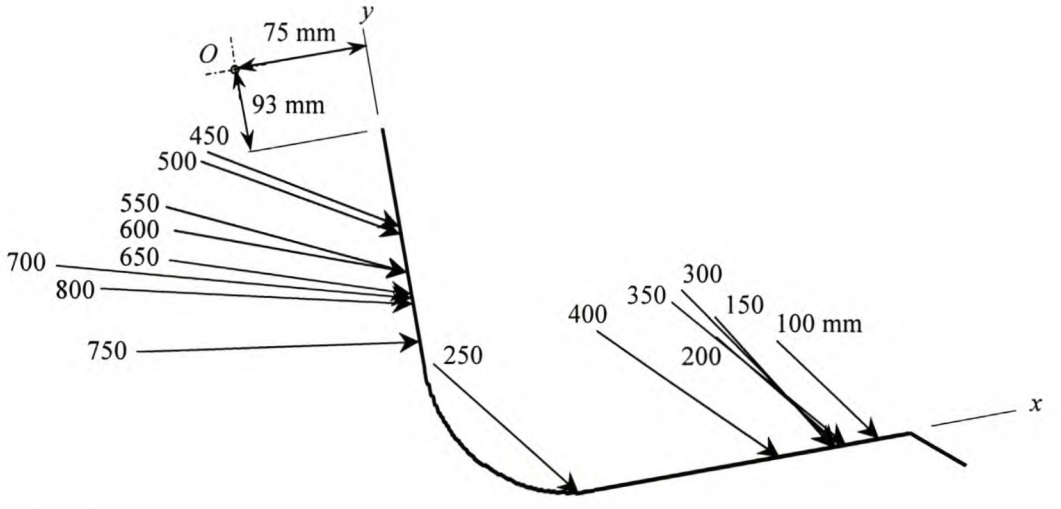

Figure 6.8 – *Resultant force application point and direction, W_b = 138.3 N*
The x-displacement is indicated in mm at the start of each vector

The resultant force starts near the tooth with a y-component greater than the x-component. As more and more material enters the bucket, the application point shifts backwards. As the payload increases, the required y-force component decreases. The reason for this is that the payload contributes to the total y-force. The increasing payload, of course, also requires an increasing x-force in cases with $\beta > 0°$, though most of the x-force component is necessary to overcome material friction. From 450 mm onwards the resultant force acts on the back of the bucket.

Stellenbosch University http://scholar.sun.ac.za

Figures 6.9, 6.11 and 6.13 show the raw data obtained from the same simulation. Note that the forces and moments shown in these figures are those exerted by the bucket on the material. The x-force component of each part of the bucket as well as the total x-force is shown in Fig. 6.9. There is a force on the *tooth* from the start as it cuts through the material. The force on the *bottom* is due to friction. The *inner curve* only starts to contribute to the total force after a displacement of 300 mm and the *front* after 500 mm. This, of course, corresponds to the distances when the material inside the bucket reaches the specific part of the bucket. The contribution of the *top* is less than the *bottom*, which indicates that the material inside the bucket tends to move along with the bucket and results in less friction than on the *bottom*. The *outer curve* has no significant influence since it is not really in contact with the material.

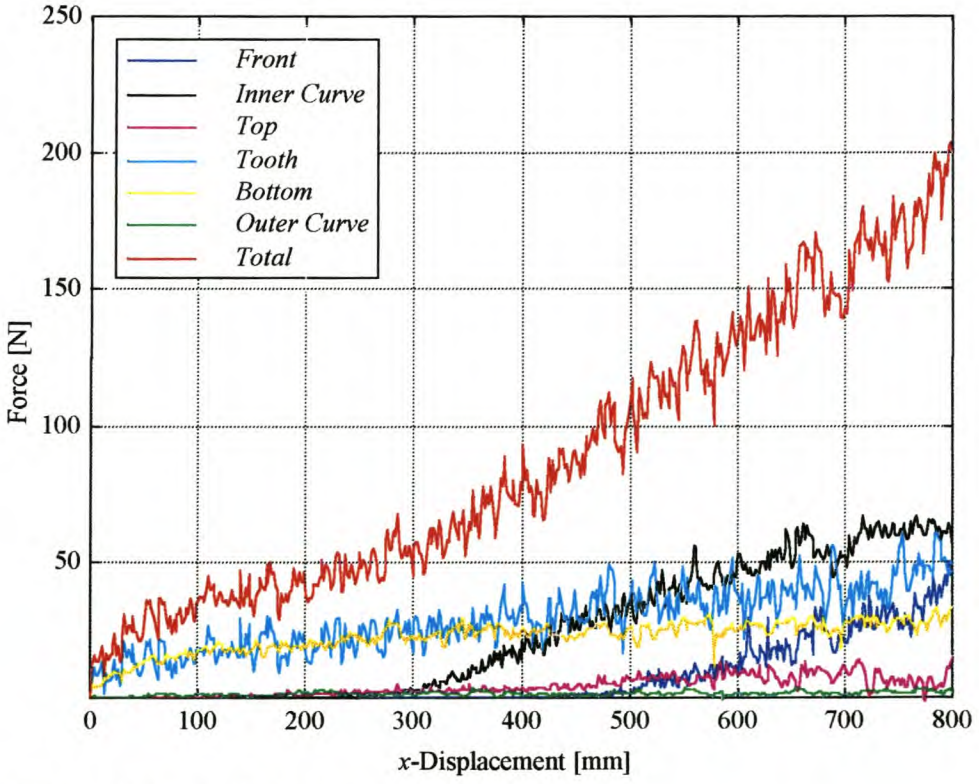

Figure 6.9 – *Bucket x-forces*

Figure 6.10 shows the ratio of the contribution of each part to the total x-force. Polynomials have been fitted to get rid of the noise. Geometrically the tooth is small in comparison with the rest of the bucket, but it still carries 20 to 30% of the load. Rowlands (1991) investigated the effect of tooth attack angle and length on both the fill rate and tooth force. The results show that, with an increase in tooth length and angle of attack there is an increase in fill rate but also an increase in tooth force. The increase in

Stellenbosch University http://scholar.sun.ac.za

fill rate is desired but the increase in force requires improved bucket design. The force on the teeth can be predicted by assuming it to be a flat blade and all the general trends shown in Chapter 5 are applicable. The other major contributions to the total x-force come from the *bottom*, *inner curve* and the *front* during the latter part of filling.

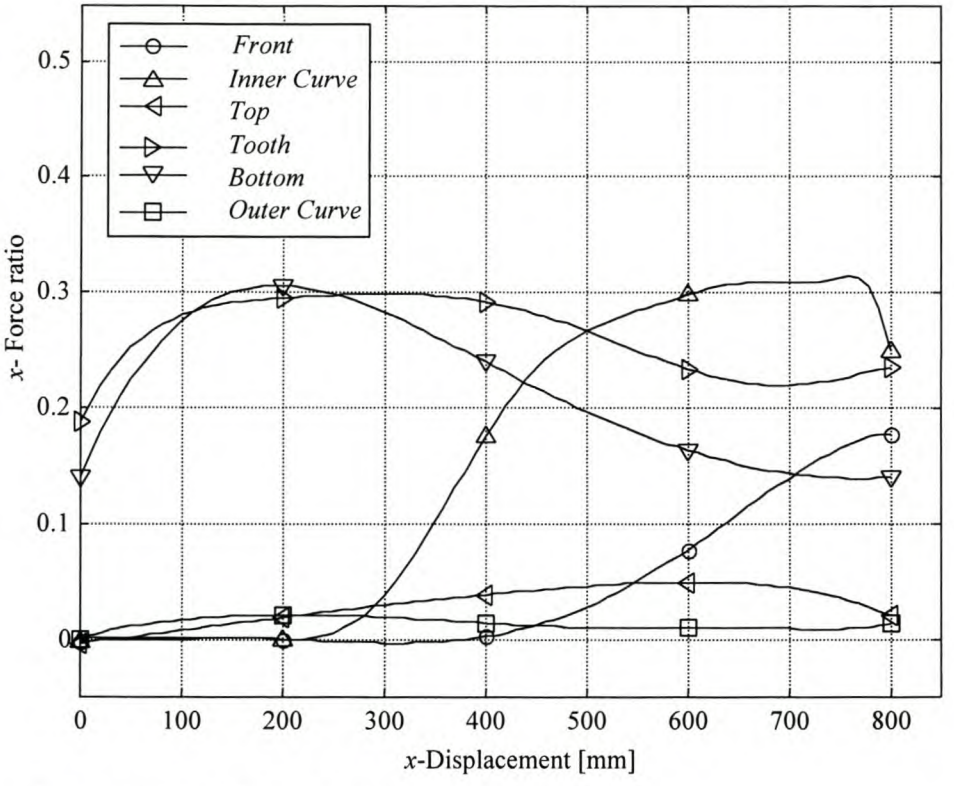

Figure 6.10 – *x-Force ratios*

Figure 6.11 shows the y-forces. Up to about 400 mm, 70 to 85% of the total force acts on the *bottom*. Thereafter the influence of the payload is visible through the forces on the *top* and *inner curve*. The tooth does not have such a great influence on the total y-force (2–15%) as it has on the total x-force (20–30%) (Fig. 6.12).

Moments of forces were taken about point O, of which the position is indicated in Fig. 6.8. Figure 6.13 shows the moment of each part and the total. The total moment indicates that initially the bucket exerts a negative (clockwise) moment, i.e. the material tends to rotate the bucket counter-clockwise. This is to be expected since the only force acting on the bucket is at the bottom. After ±400 mm the exerted moment changes to positive as the forces on the *top*, *inner curve* and *tooth* increases. Figure 6.14 shows the moment ratios and it is clear that the *bottom* contributes the most to the total moment. The *tooth's* ratio remains between 20 to 30% while that of the *top* and *inner curve* increases with displacement.

Stellenbosch University http://scholar.sun.ac.za

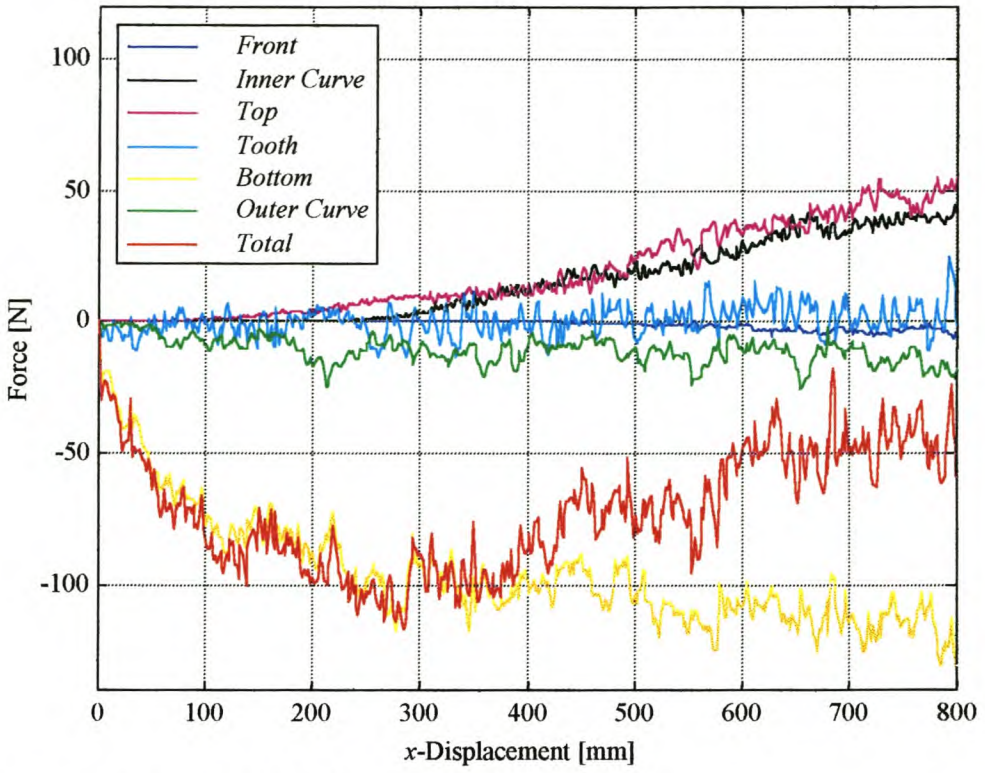

Figure 6.11 – *Bucket y-forces*

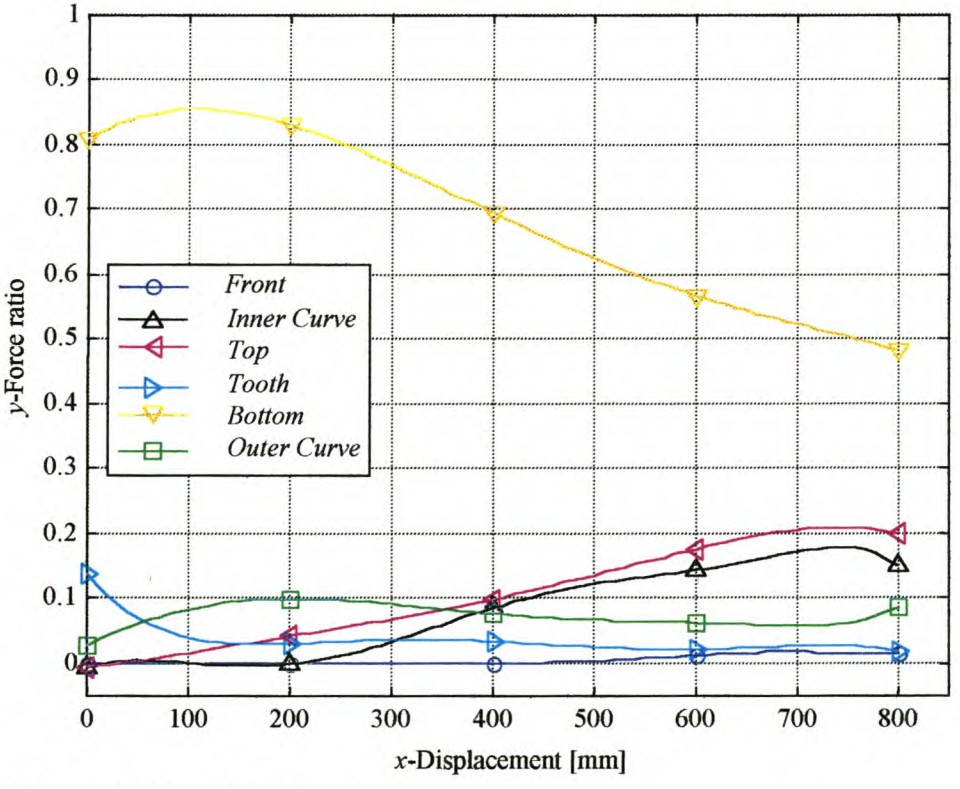

Figure 6.12 – *y-Force ratios*

Stellenbosch University http://scholar.sun.ac.za

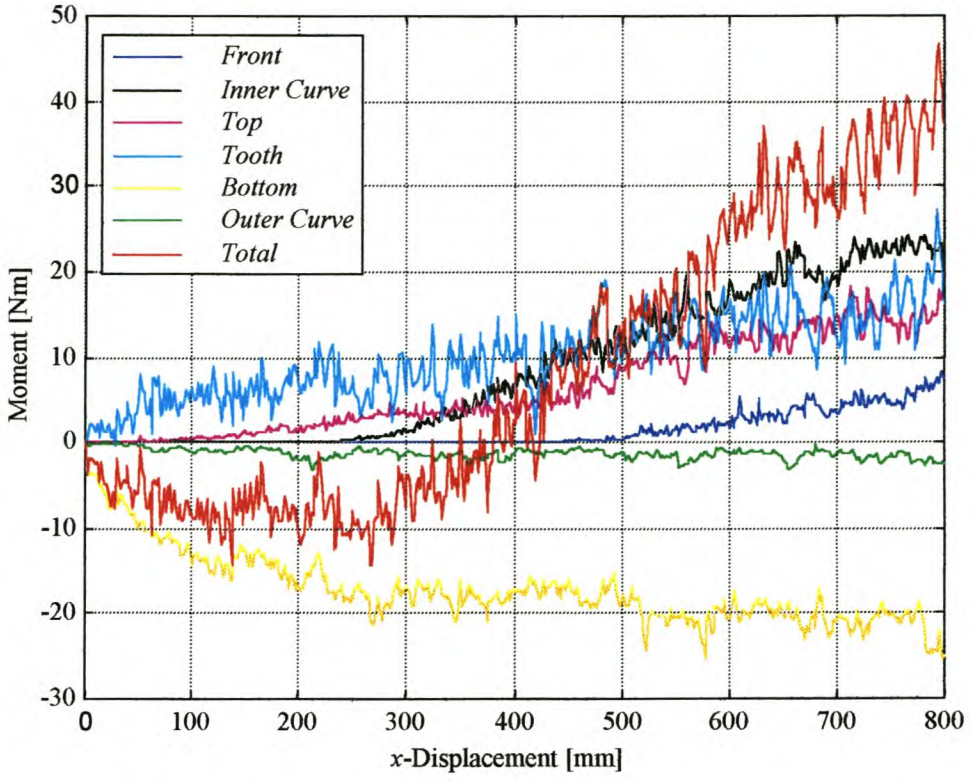

Figure 6.13 – *Bucket moments*

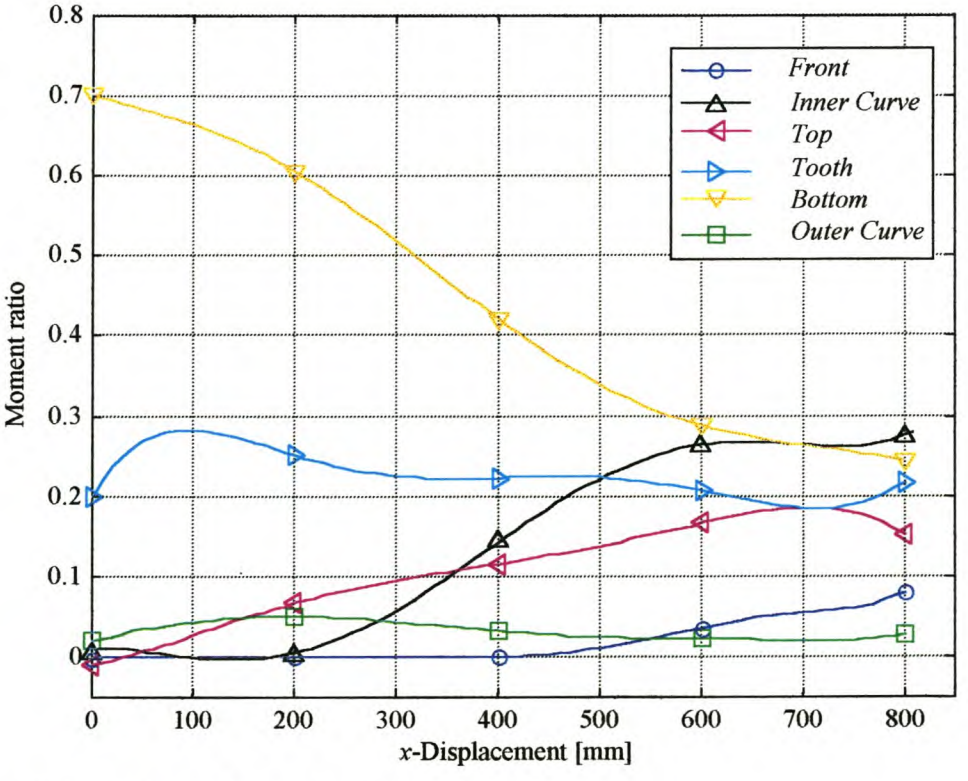

Figure 6.14 – *Moment ratios*

Stellenbosch University http://scholar.sun.ac.za

Having already made use of the draft energy to compare the experimental and numerical results, we now consider the distribution of energy within the whole system. Figure 6.15 shows the breakdown in energy for the entire particle assembly. The boundary work is divided in two parts, a x- and y-component, which contribute roughly 85 and 15% respectively to the total boundary energy.

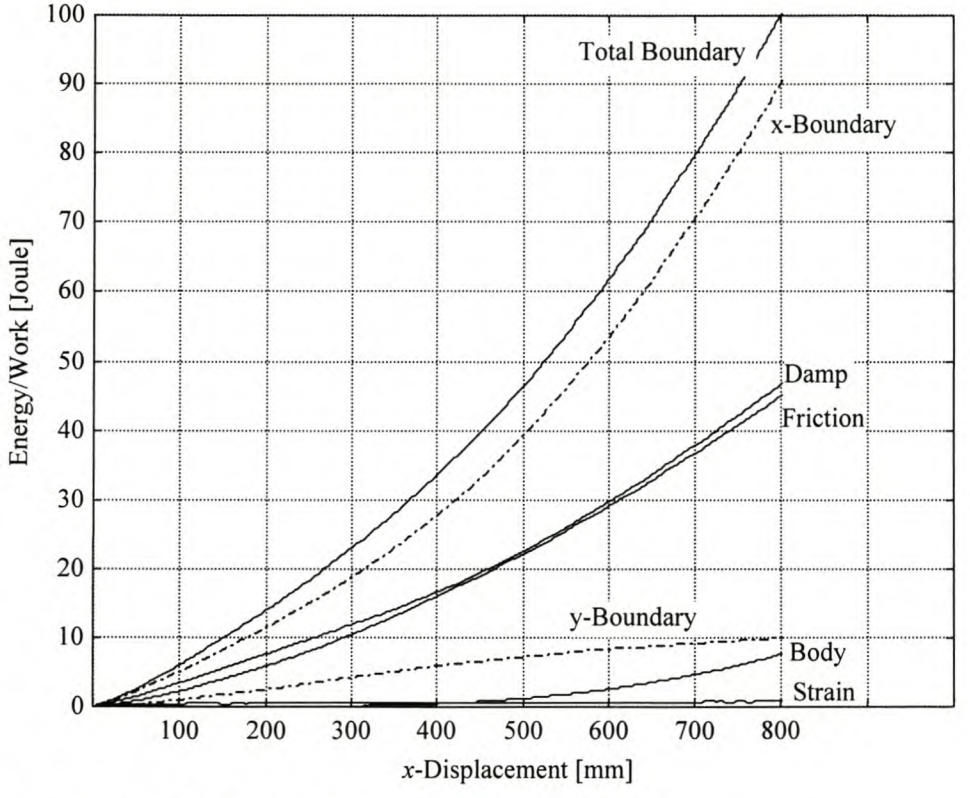

Figure 6.15 – *System energy distribution*

The accumulative boundary work increases approximately as a function of the displacement squared. Energy is dissipated through damping and friction, which are determined by the damping ratio and the friction coefficient respectively. With the chosen properties (μ = 0.1 and α = 0.7), the loss due to damping and friction is practically the same. The material gains potential energy as it rises above its original position due to the action of the bucket. A small increase in strain energy can also be observed. This is much clearer in Fig. 6.16 where the ratio of each component relative to the total boundary energy is plotted. It can also be seen that ±90% of the energy is dissipated through damping and friction.

Friction loss occurs at particle-particle and particle-bucket contacts. Of the total friction loss, 21-40% is lost at particle-bucket contacts. Expressed as a percentage of the total

Stellenbosch University http://scholar.sun.ac.za

boundary energy, 12-18% is lost at particle-bucket contacts. This can be seen as an indication of tool wear. Less than 0.1% of the energy goes into increasing the kinetic energy of the particles and can be ignored.

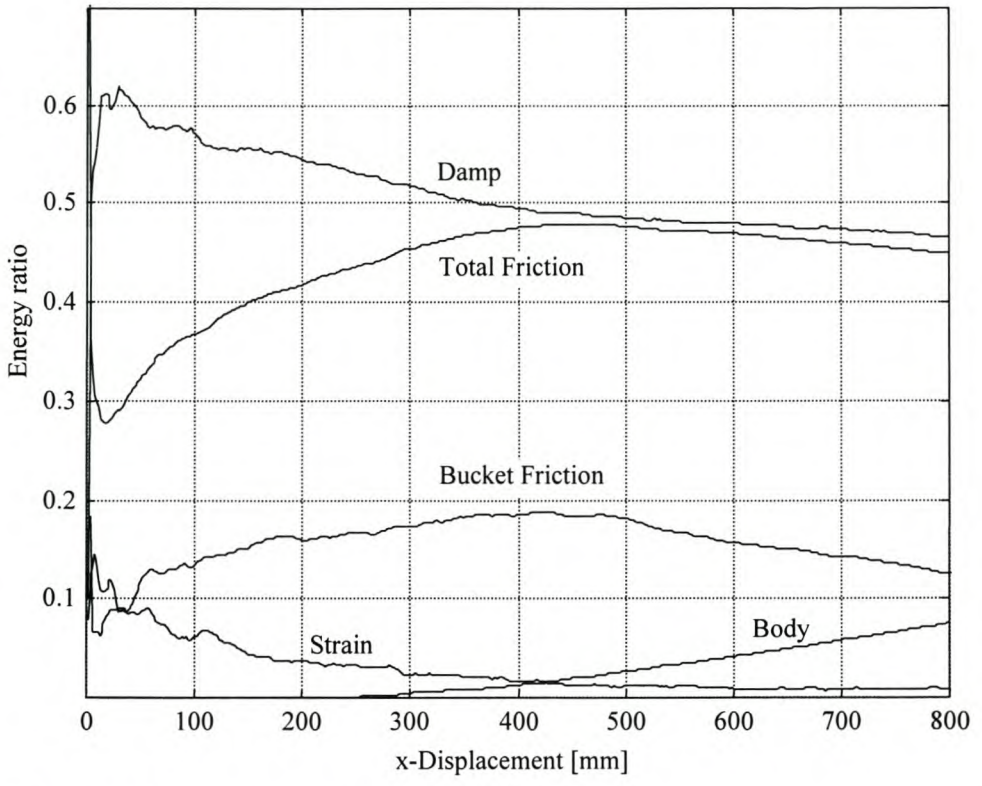

Figure 6.16 – *Energy ratios*

These results are difficult to verify experimentally due to practical difficulties. A theoretical analysis based on approximations can, however, be used to show trends in energy distribution. The theory is given in Appendix G and only the results are given here. For the purpose of this analysis, the energy is consumed in four major processes: increase in potential energy as the material is being raised by the bucket, increase in kinetic energy, bucket-material friction loss and material-material friction loss.

To make a comparison between these results and those obtained from simulations, the total material energy is defined as the material-material friction energy loss added to the energy dissipated through damping and the increase in strain energy. Table 6.1 sets out the energy breakdown expressed as a percentage of the total boundary energy for the same conditions as in the above simulation and after a drag distance of 800 mm.

Stellenbosch University http://scholar.sun.ac.za

Energy Component	Analytical	Simulation
Potential	6.9	7.6
Acceleration	0.0	0.0
Friction: Bucket-Material	40.1	31.9
Material energy	53.0	60.5
Total	100.0	100.0

Table 6.1 – *Energy breakdown as a percentage of the total boundary energy*

Both analyses show that most of the energy goes into the material where it is either lost due to friction and damping or used to increase the strain. Less than 10% of the energy goes into increasing the potential energy and the rest is lost through bucket-material friction. The drag angle has no significant effect on this ratios except that the potential energy increases up to 11.5% of the total boundary energy with $\beta = 20°$. The material properties of wheat and corn are to close too cause any significant difference in the ratios.

6.3 Material Flow and Rupture Lines

In this section we focus on the flow of material into the bucket and the formation of rupture lines. Figures 6.17(a,b) and 6.18(a,b) show the filling of the bucket with corn during both experiments and numeric simulations. $\beta = 0°$ and 20° respectively. All the pictures are 100 mm in x-displacement apart. Only one bucket weight, 138.3 N, was used to investigate the fill behaviour. A good comparison between the experimental and simulation filling procedure is obtained up to a displacement of 400-500 mm. Thereafter the simulations fail to predict the outline of the payload entering the bucket. The free surface stays parallel to the y-axis. The reason for this is unknown but it may lie in the fact that the synthetic material is more compressible than the natural material. The friction on the side panels may also influence the experimental results somewhat.

Stellenbosch University http://scholar.sun.ac.za

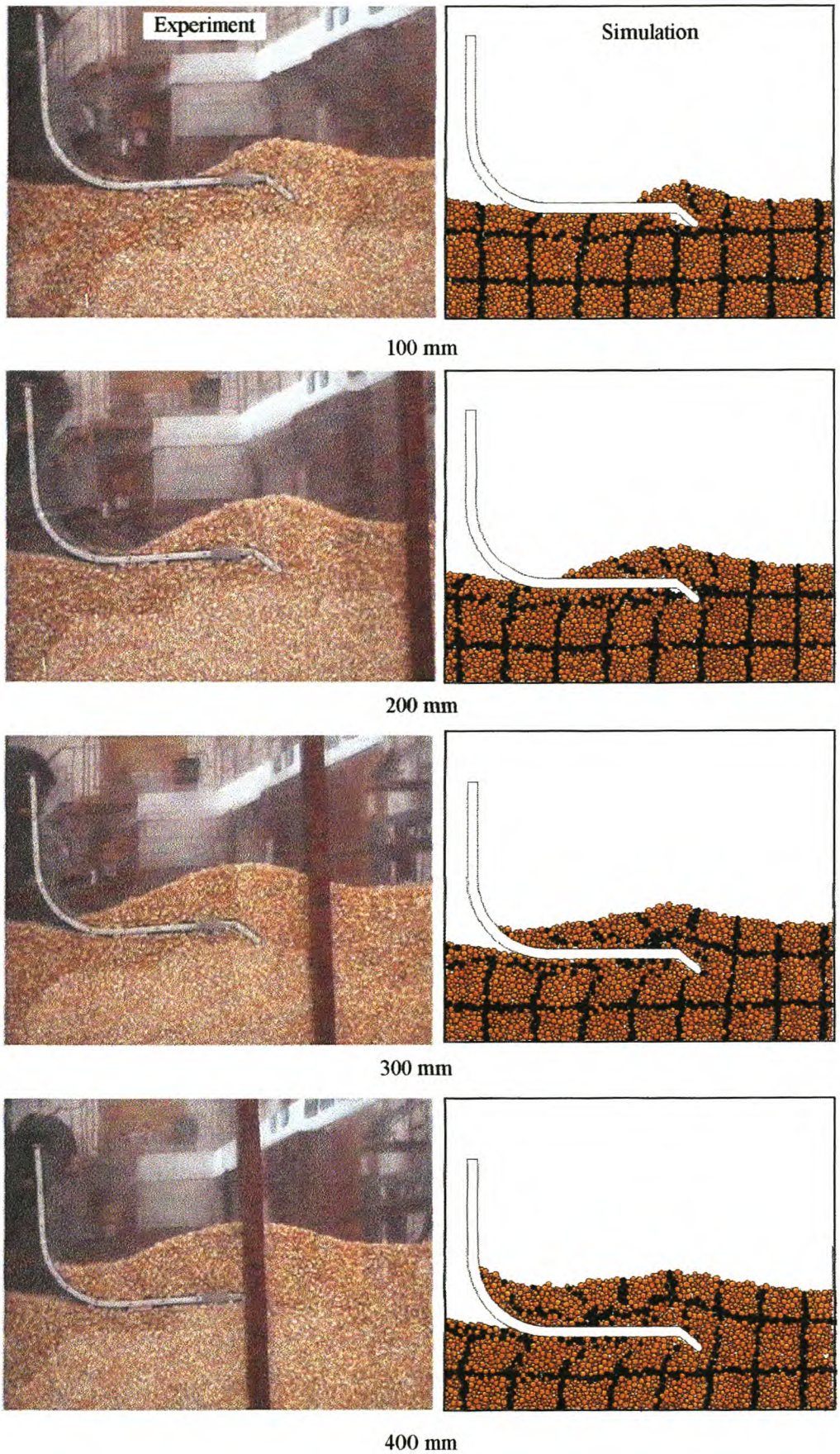

Figure 6.17a – *Bucket filling with corn and $\beta = 0°$*

Stellenbosch University http://scholar.sun.ac.za

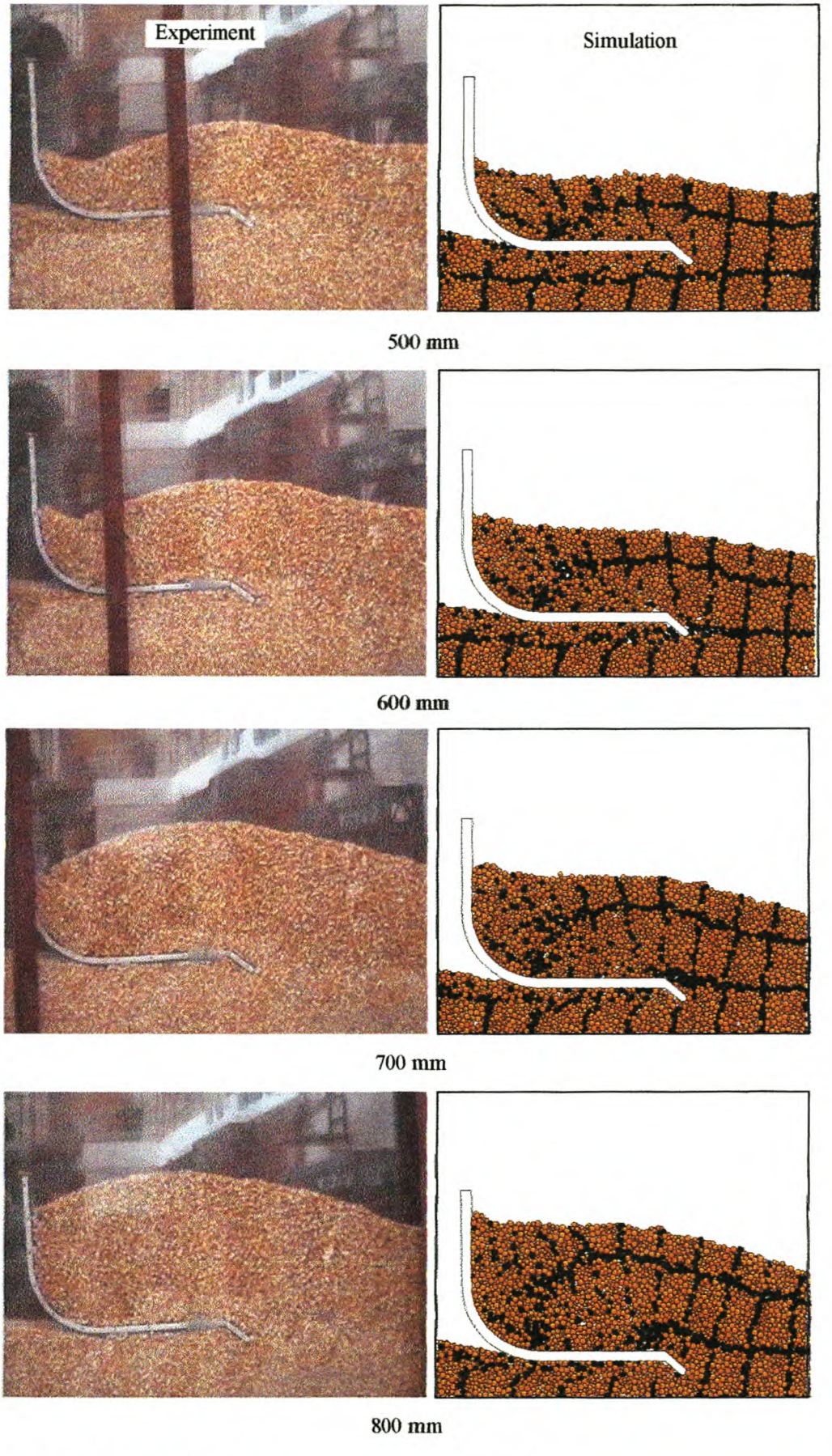

Figure 6.17b – *Bucket filling with corn and* $\beta = 0°$

Stellenbosch University http://scholar.sun.ac.za

Figure 6.18a – *Bucket filling with corn and $\beta = 20°$*

Stellenbosch University http://scholar.sun.ac.za

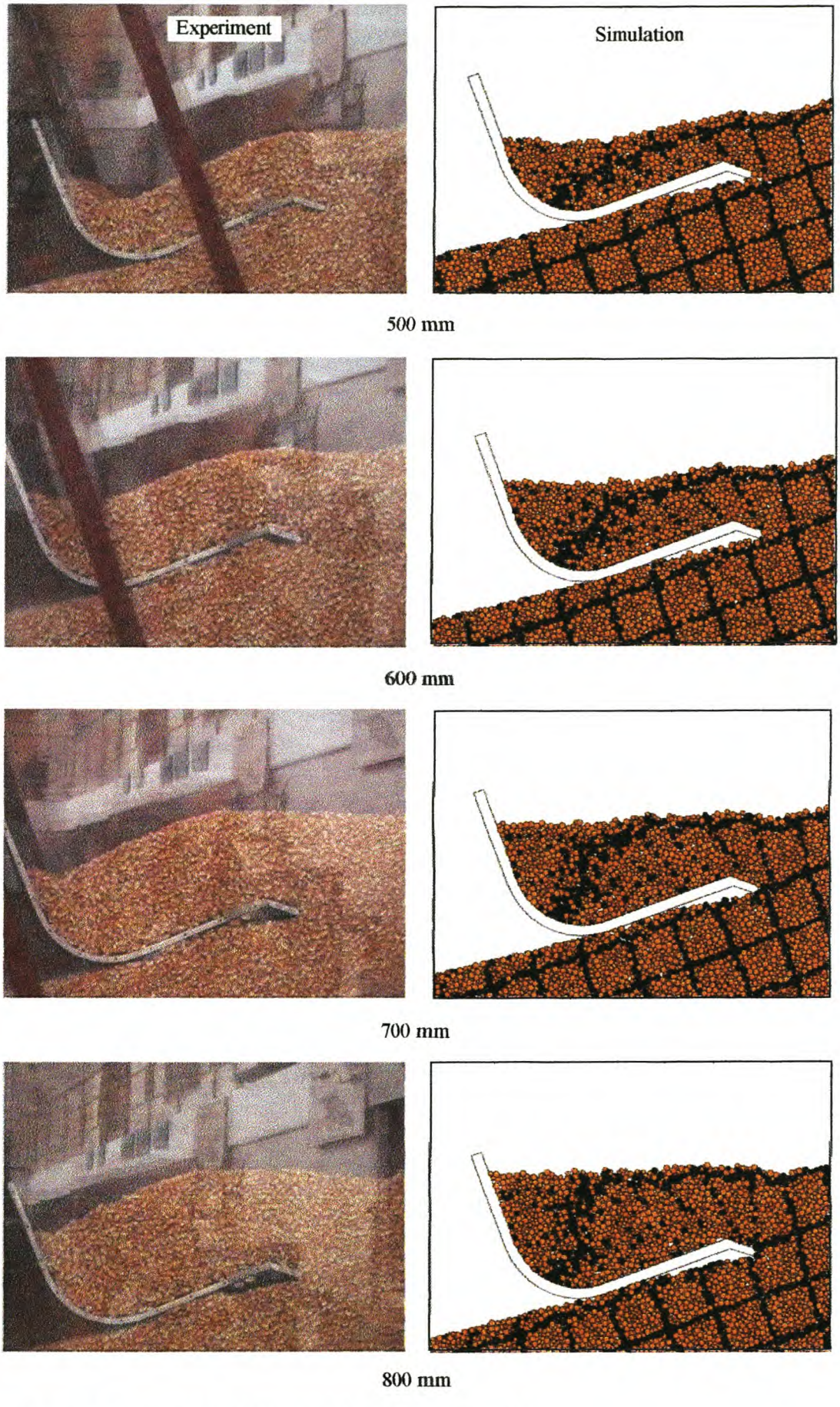

Figure 6.18b – *Bucket filling with corn and* $\beta = 20°$

Stellenbosch University http://scholar.sun.ac.za

Rowlands (1991) made use of mixtures of millet, peas and corn in his 2-D test rig. The observation of the filling behaviour led to the development of a theory that describes the flow characteristics and patterns of material entering the bucket. Rowlands (1991) named this concept the *Shear Zone Theory*. He observed that definite planes of shear (rupture) formed between distinct moving material regimes. These shear planes changed orientation and location depending on initial setup and during the filling process itself.

The experiments with corn and wheat confirmed the existence of this theory. The generalised theory is shown in Fig. 6.19. The movements of the material relative to the bucket are indicated by the arrows.

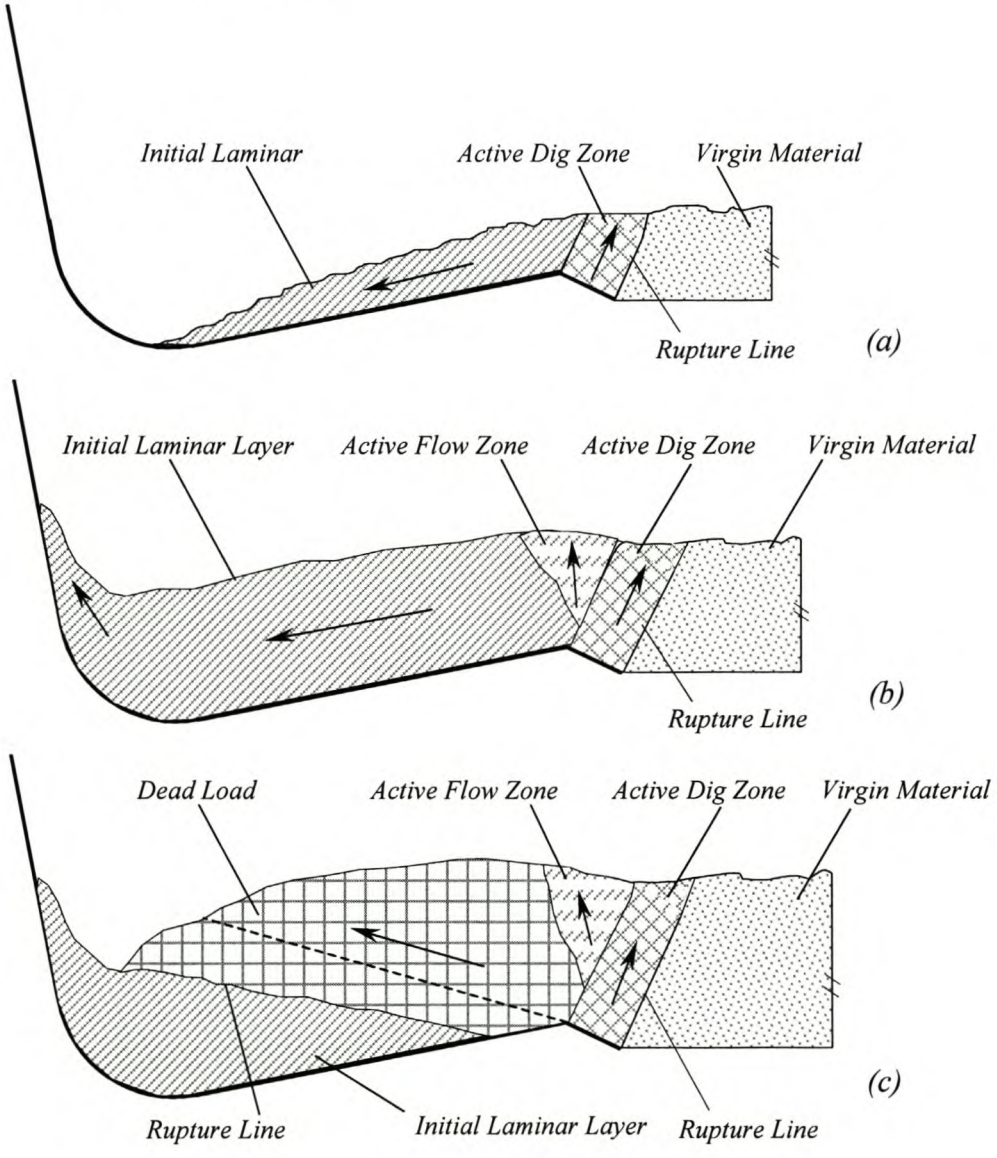

Figure 6.19 - *Shear Zone Theory – flow regimes*

Stellenbosch University http://scholar.sun.ac.za

The *Virgin Material* remains largely undisturbed until the final third of the drag during which "bulldozing" occurs. The *Initial Laminar Layer* flows into the bucket during the first third of the drag (Fig. 6.19a). After entering to a certain distance, this layer fails at the bucket lip and subsequently becomes stationary with respect to the bucket for the remainder of the drag (Fig. 6.19b,c). At steeper drag angles, the material flows more rapidly towards the rear because of the added gravity assistance. This effect can be seen by comparing Fig. 6.17 with Fig. 6.18 at x-displacements up to 300 mm.

With the laminar layer becoming stationary, a new zone, the *Active Flow Zone*, develops (Fig. 6.19b). In this zone, the material displacement is predominantly in the y-direction. The *Active Dig Zone* is located above the teeth and bucket lip. This area develops as material starts to enter the bucket and increases in size after failure of the *Initial Laminar Layer*. In this zone, the *Virgin Material* fails and either flows into the bucket as part of the laminar layer during the first part of filling or moves into the *Active Flow Zone* during the latter part of filling.

The *Dead Load* that has resulted from "live" material in the *Active Flow Zone* ramps up and over the *Initial Laminar Layer*. Some of the material in the *Initial Laminar Layer* fails and starts to form part of the *Dead Load* (Fig.6.19c). During experiments, a definite rupture line could be observed here. With an increase in drag angle, the *Active Dig Zone* and *Active Flow Zone* tended to join into one continuous band.

During experiments two definite rupture lines could be observed. The one extended from the tip of the tooth up to the free surface. This is known as the C*utting Rupture Line*. The second line is the one between the *Initial Laminar Layer* and the *Dead Load*, called the *Dead Load Rupture Line*. With $\beta = 0°$ the *Dead Load Rupture Line* stretches from the tooth up to the free surface with an angle close to the material internal friction angle (measured relative to the bottom part of the bucket). This is indicated by the dotted line in Fig. 6.19(c). With an increase in β, the *Dead Load Rupture Line* shifts (30 to 65 mm) into the bucket with its origin somewhere along the bottom of the bucket, also with an angle close to the internal friction angle (within $\pm$ 4°). This line is indicated as a rupture line in Fig. 6.19(c).

Stellenbosch University http://scholar.sun.ac.za

Wooden dowels were used to investigate the flow of material into the bucket. The dowels, with a length of 200 mm, were put in strategic positions with their axis in the z-direction. The dowels were marked and their positions traced during filling. The dowels were found not to disturb the flow of material. Besides the flow directions, the effect of the *Dead Load Rupture Line* on the results can also be seen. Figure 6.20 shows the flow field for the two cases: $\beta = 0°$ and $\beta = 10°$.

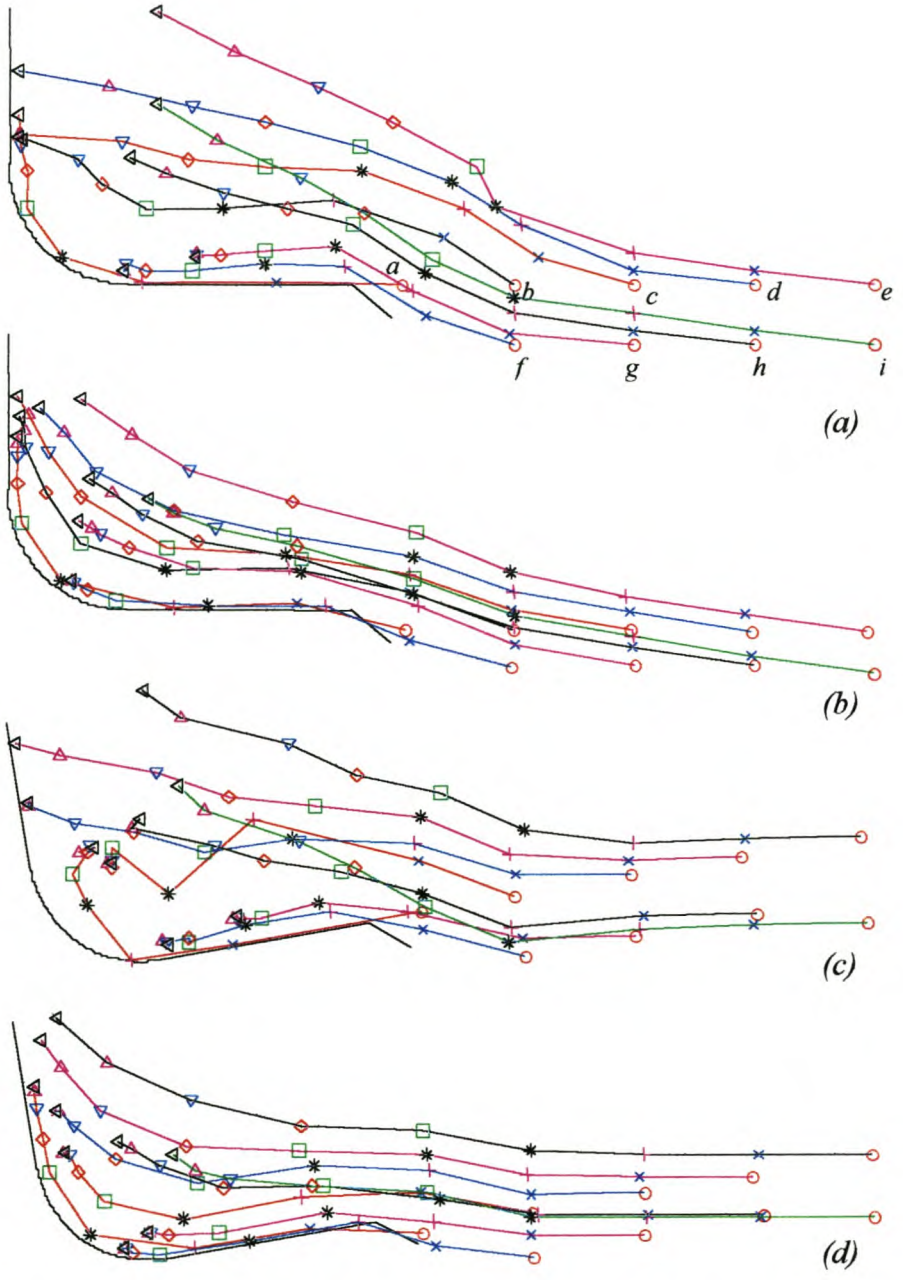

Figure 6.20 – *Corn flow field (a) $\beta = 0°$ - experiment (b) $\beta = 0°$ - simulation (c) $\beta = 10°$ - experiment (d) $\beta = 10°$ - simulation*

Stellenbosch University http://scholar.sun.ac.za

Both experimental and numerical results are included with the position of the particles recorded at intervals corresponding to 100 mm drag displacement increments.

Following the movement of the particles in Fig. 6.20(a), it can be seen that up to a displacement of about 300 mm particles *a, f* and *g* form part of the laminar layer. This material flows into the bucket with little or no displacement in the *y*-direction. Thereafter, the material that enters the bucket is given a *y*-displacement as it passes through the active digging and flow zones. Comparing the positions of particles *a, b, f* and *g* at 700 mm with those at 600 mm, it is clear that these particles become stationary while all the other particles still have large displacements. These particles now form part of the stationary laminar layer behind the *Dead Load Rupture Line*.

In general, the numeric results show the same general flow patterns and the presence of a rupture line is visible. The only major difference is that the material shows less displacement in the *y*-direction near the tooth. A possible explanation for this is a smaller *Active Flow Zone*.

The displacement field can be used to determine the approximate velocity field relative to the bucket. The velocity is assumed to be constant between consecutive points. Figure 6.21 and 6.22 show the results for $\beta = 0°$ and 10°. The velocity vectors are drawn in at midpoints and the markers correspond to that of the second position as indicated in Fig. 6.20. The outline of the material is indicated as well as the *Cutting Rupture Lines* and *Dead Load Rupture Lines* (the dotted lines) observed during experiments. The absolute velocity vector of the bucket is indicated by the arrow just below the bucket. The effect of β on the *Initial Laminar Layer* can be seen by looking at particles *a* and *b*. With $\beta = 10°$ (Fig. 6.21) these two particles have relative velocities greater (in magnitude) than the absolute bucket velocity over the first 250 mm. These particles are "disturbed" by the bucket tooth and flow (avalanche) into the bucket under the influence of gravity. This does not happen with $\beta = 0°$. With $\beta = 0°$, particles *a, f, g* and *h* start to decelerate as early as at 450 mm. Between 450 and 550 mm, a definite rupture line forms and the above-mentioned particles become totally stationary. With $\beta = 10°$, it is particles *a, b, f* and *g* that show the same behaviour.

Stellenbosch University http://scholar.sun.ac.za

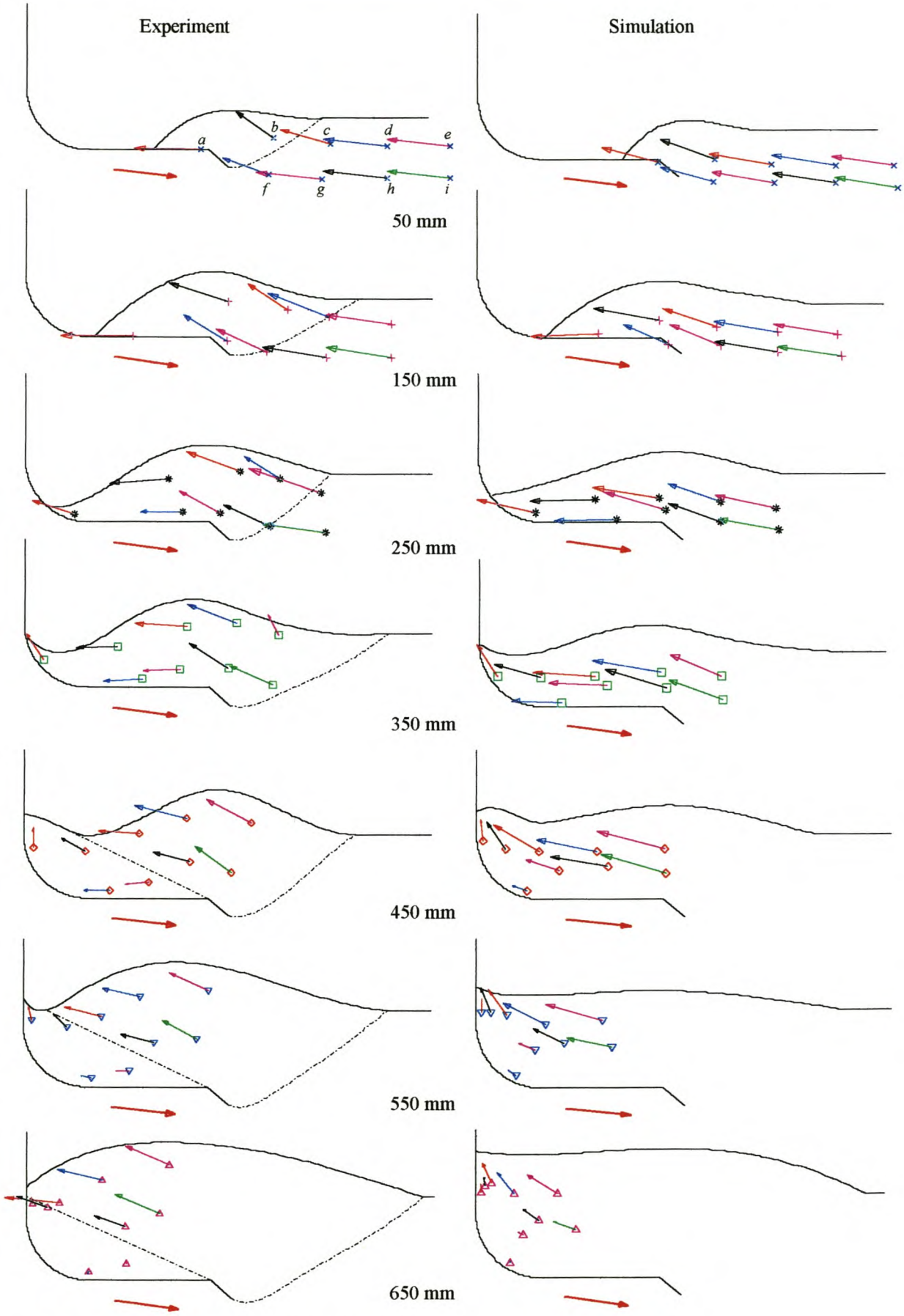

Figure 6.21 – *Corn velocity field, $\beta = 0°$*

Stellenbosch University http://scholar.sun.ac.za

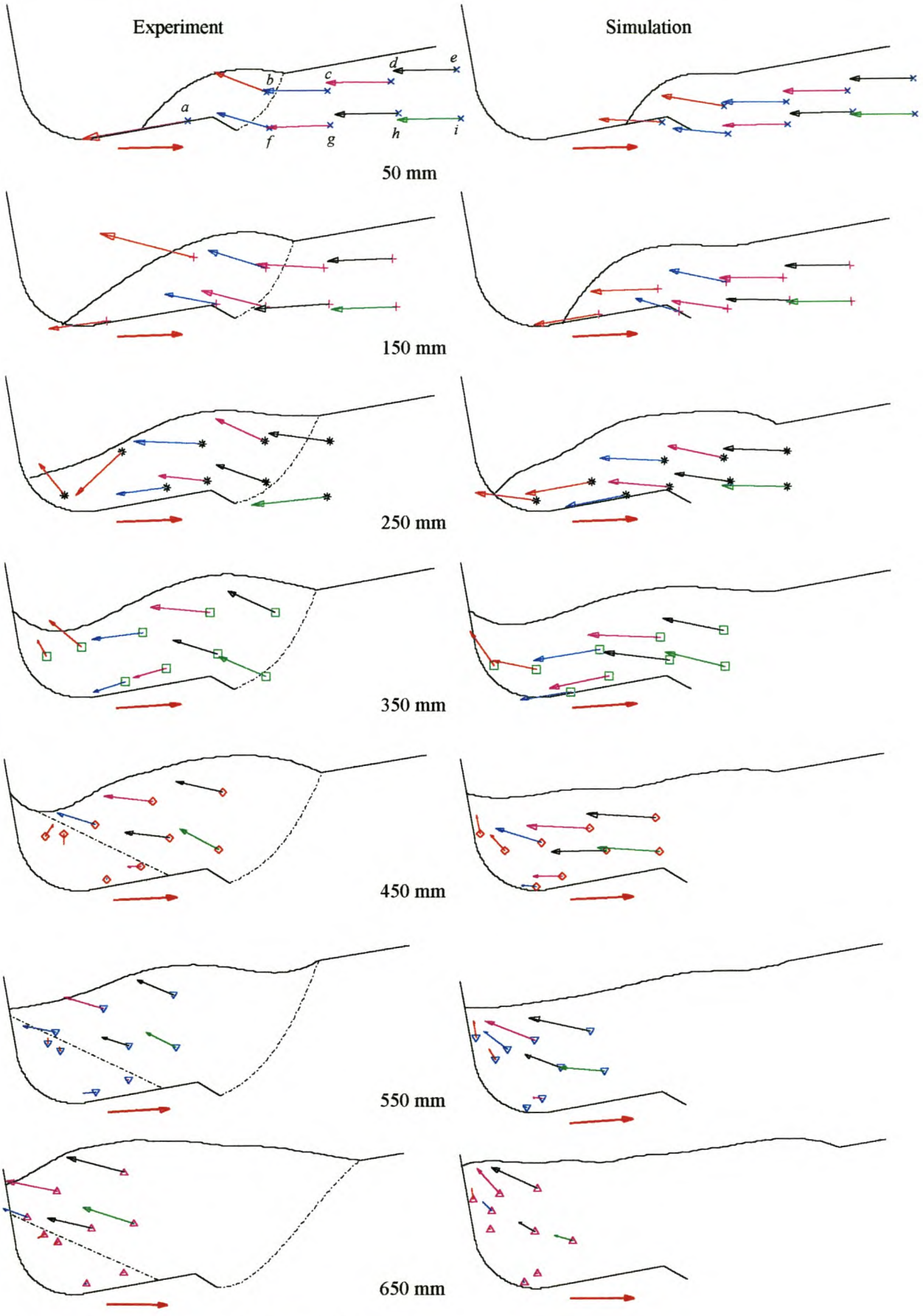

Figure 6.22 – *Corn velocity field, β = 10°*

Stellenbosch University http://scholar.sun.ac.za

The ability of DEM to predict the material displacement and velocity fields has been shown. There is enough evidence to believe that DEM can predict the formation of the *Dead Load Rupture Line*.

To investigate this phenomenon further the following procedure is followed. The bucket is moved through the material and "paused" after each 100 mm. The displacement vector of each particle is then set to be zero after which the bucket is given a further displacement of 10-15 mm (1-3 particle lengths). The particle displacement ratio *PDR* is defined as the ratio of the magnitude of the particle absolute displacement vector to the magnitude of the bucket absolute displacement vector. The particles are then coloured according to their individual *PDR* values. The result is shown in Fig. 6.23. This is in effect the average velocity ratio over a short period.

The flow regimes as predicted by the *Shear Zone Theory* are indicated in the figure. The three pictures correspond to the three pictures given in Fig. 6.19. During the initial part of motion, the *Active Dig Zone* is clearly visible with $0.40 \leq PDR < 0.65$. The *Initial Laminar Layer* moves into the bucket with $0.10 \leq PDR < 0.25$. After 500 mm, the *Active Flow Zone* can be seen with $0.10 \leq PDR < 0.25$. Although the *PDR* is relatively low, the displacement is predominantly in the y-direction. In the back of the bucket, the *Initial Laminar Layer* starts to become stationary relative to the bucket as the *PDR* increases. After 800 mm, the *Active Flow* and *Active Dig Zone* can not be distinguished from the *Dead Load*. The existence of the *Dead Load Rupture Line* is however clearly visible. This line is drawn in with an angle of 30° relative to the bottom of the bucket. This value is slightly higher than the experimentally measured value of 23±4°.

It is believed that the orientation of the *Dead Load Rupture Line* can be predicted using plasticity theory based on a flat blade with a small rake angle. This still needs further investigation. More of these wheat and corn results are given in Appendix F.

Stellenbosch University http://scholar.sun.ac.za

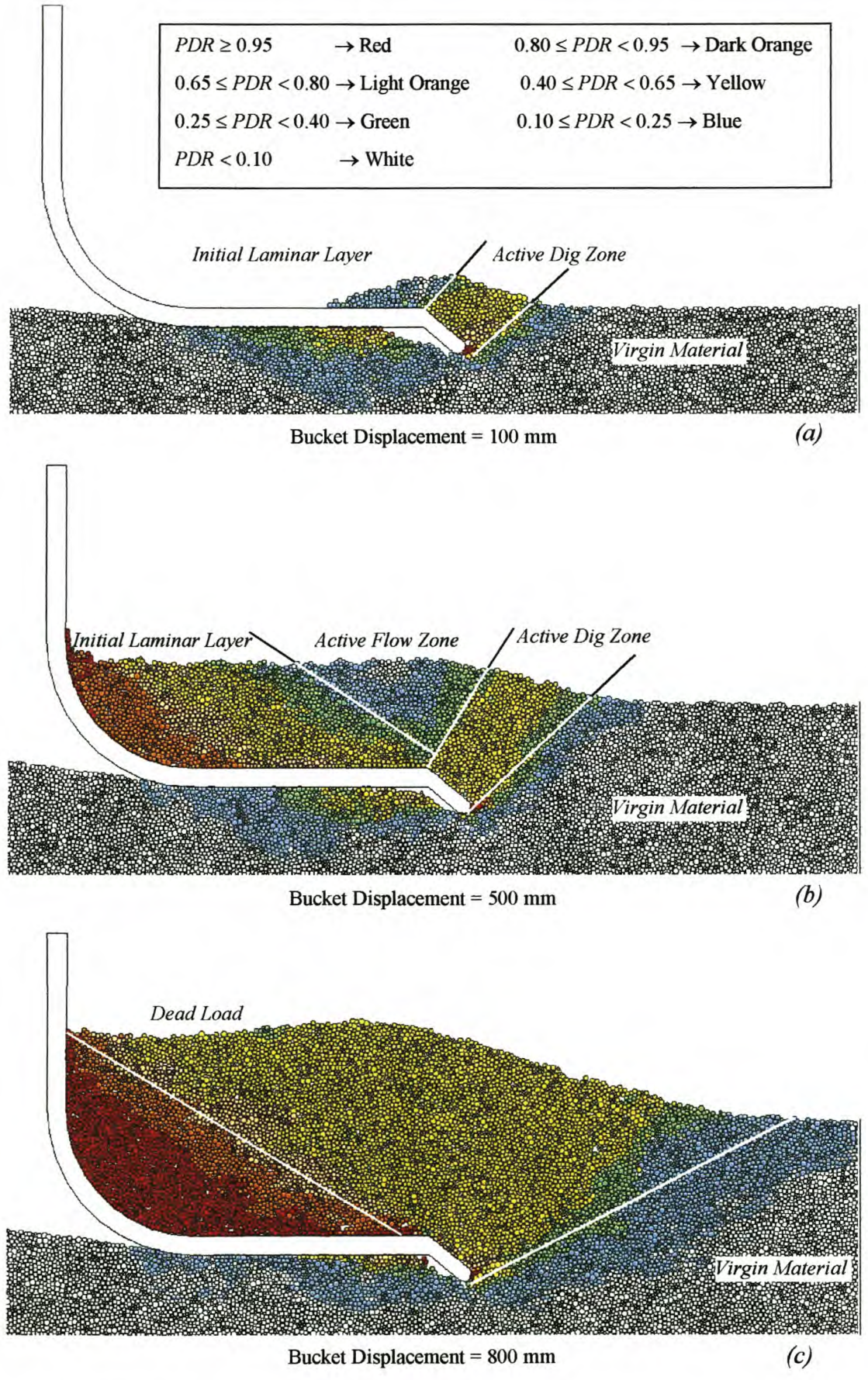

Figure 6.23 – *Particle displacement ratio, PDR*

Stellenbosch University http://scholar.sun.ac.za

6.4 Fill Percentages

The outline of the material entering the bucket was manually digitised and the areas determined. These areas are used to calculate the fill percentage and fill rates. Figure 6.24(a) shows the definition of the bucket areas. A_t is the total area of the bucket while the reduced area A_r takes the repose angle of the material into account. The amount of material that stays in the bucket depends on the way the bucket is disengaged.

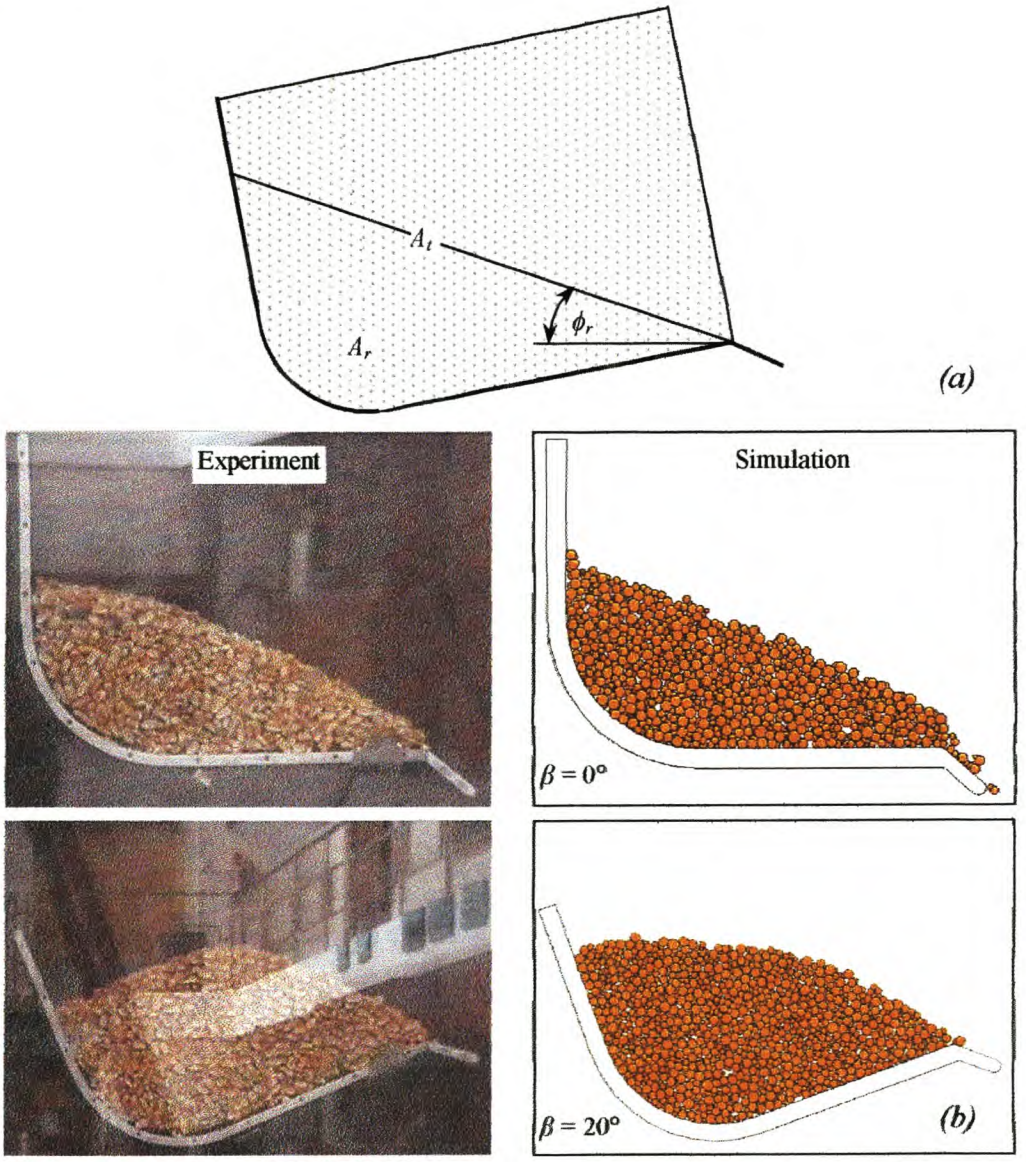

Figure 6.24 – *(a) Definition of fill areas*
(b) Effect of β on the fill percentage of corn

Stellenbosch University http://scholar.sun.ac.za

Only the material within A_r will stay in the bucket when it is disengaged unless the bucket is closed by a gate as in the case of a scraper. The area A_r depends on the orientation of the bucket as can be clearly seen in Fig. 6.24(b). If the bucket is rotated before or during disengagement, A_r increases. This is the case with loaders. For this analysis the bucket is assumed to disengage without any rotation, i.e. it assumes the drag angle β after disengagement.

First, we use the total area within A_t covered by material to calculate the *total fill percentage*. Figures 6.25 and 6.26 show the fill percentage of corn and wheat respectively. For both materials, the fill percentage increases with an increase in drag angle form 0° to 10°. The reason for this is the added gravitational assistance, although the y-displacement decreases as shown in Fig. 6.2. With a further increase in β from 10° to 20° the fill percentage decreases. The reason for this decrease is that the decrease in y-displacement due to the $\cos(\beta)$ term in Eq. 6.2 has a greater influence than the increase in payload. For $\beta = 0°$ there is little difference between the fill percentage of corn and wheat. For $\beta = 10°$ and 20° there is, however, a slight difference. The angle of repose of wheat is less than that of corn, so it is expected that the fill percentage of wheat will be higher with an increase in β.

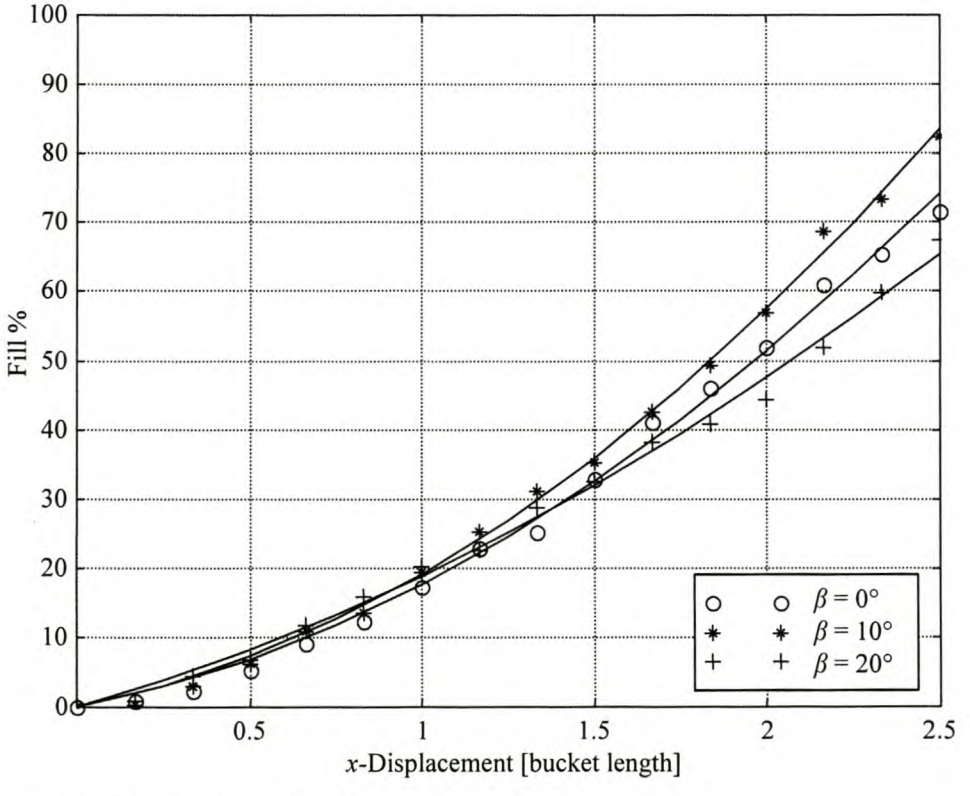

Figure 6.25 – *Corn total fill percentage*

Stellenbosch University http://scholar.sun.ac.za

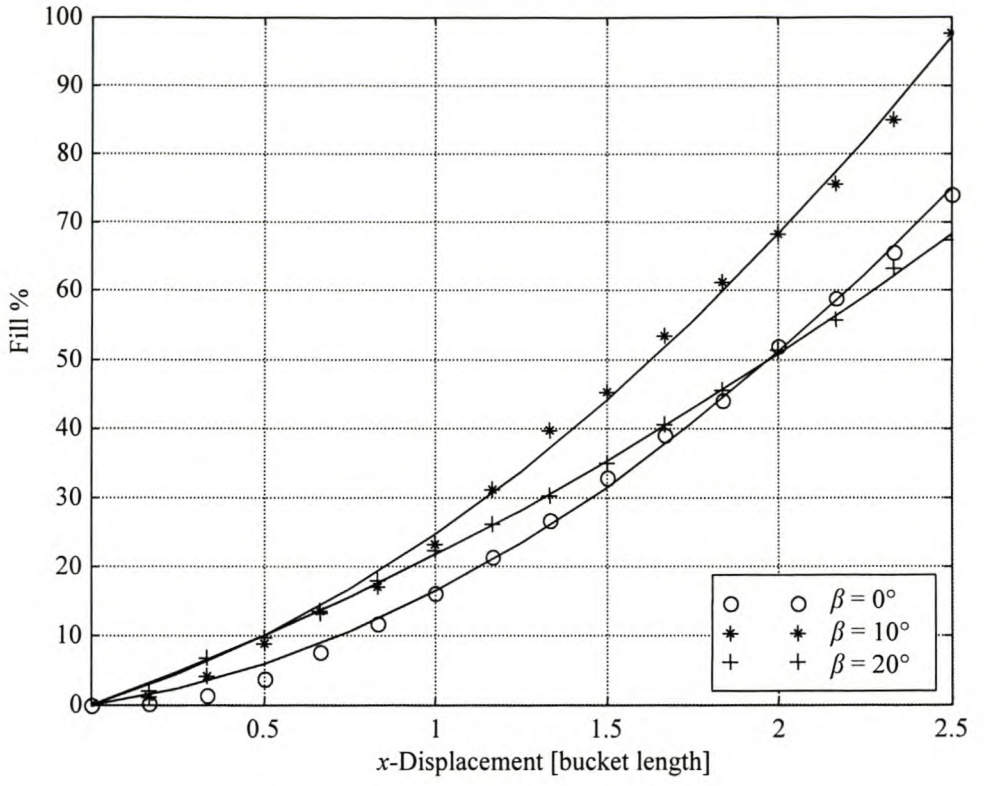

Figure 6.26 – *Wheat total fill percentage*

Another way of determining the fill percentage is to make use of only the material that will stay in the bucket after disengagement, i.e. only the area within A_r that is covered by material is used. The percentage is, however, still calculated using the total area A_t and is defined as the *reduced fill percentage*.

The results are shown in Fig. 6.27 and Fig. 6.28. There is, as expected, a decrease in fill percentage compared to the previous method of calculation. The ratio A_r/A_t for each case is also indicated. The first thing to note is that the *reduced fill percentage* increases with an increase in β. It can also be seen that for $\beta = 0°$ the bucket is filled to its maximum capacity after a displacement of 2.25 and 2.0 bucket lengths for corn and wheat respectively. Further drag will increase the *total fill percentage*, but all of the additional material will be lost when the bucket is disengaged. The same is expected to happen with other drag angles, but with the allowable drag distance too short it can not be confirmed.

Stellenbosch University http://scholar.sun.ac.za

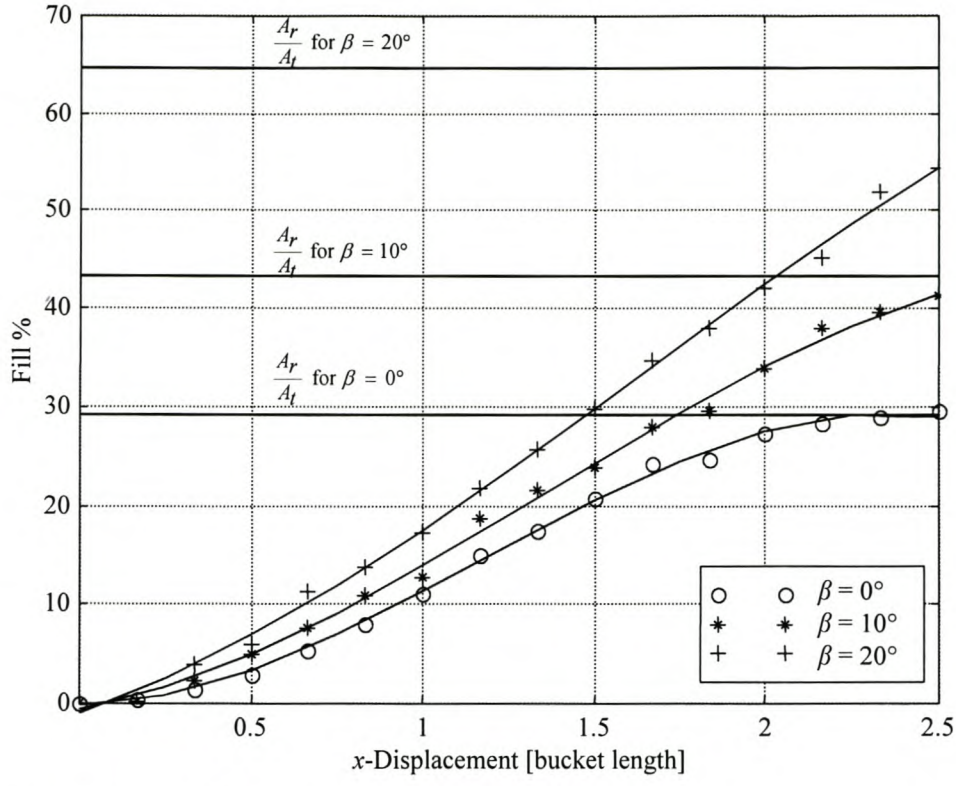

Figure 6.27 – *Corn reduced fill percentage*

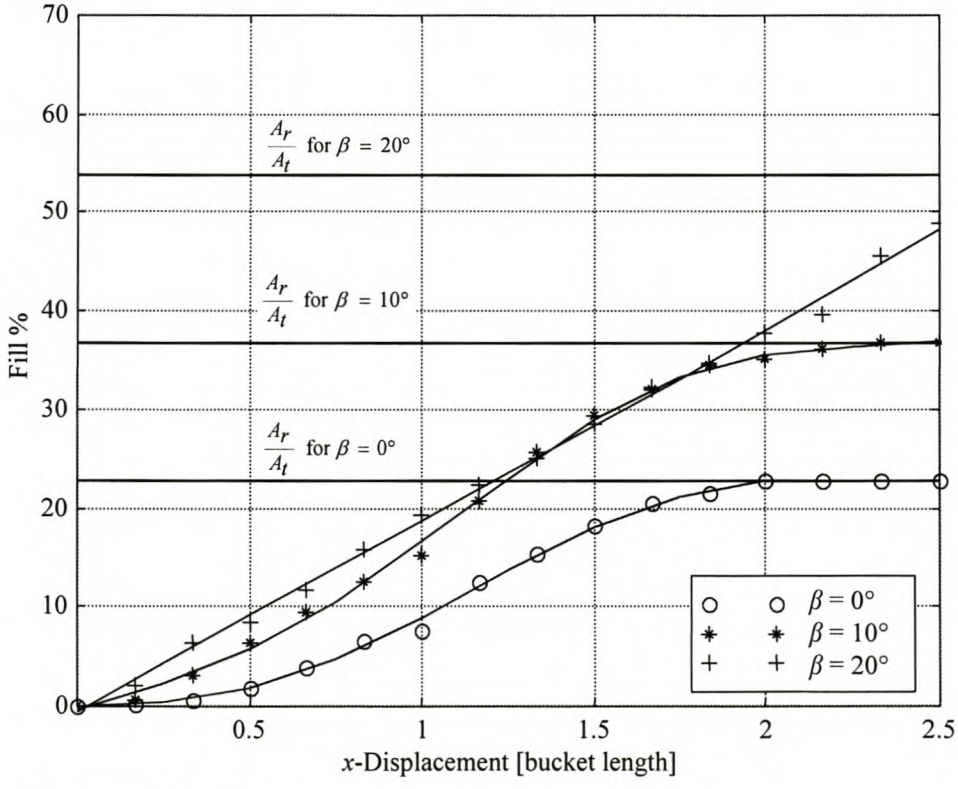

Figure 6.28 – *Wheat reduced fill percentage*

Stellenbosch University http://scholar.sun.ac.za

In Fig. 6.6 it was shown that there is no big difference in draft energy requirements for different drag angles. Taking for example Fig. 6.27, it can be seen that after a displacement of two bucket lengths the bucket with $\beta = 20°$ is 43% filled while the bucket with $\beta = 0°$ is only 27% filled and the same amount of draft energy is required.

The *reduced fill percentage* is used to compare the simulation results with the experimental ones. Figure 6.29 shows the numerical values plotted against the experimental values calculated at x-displacements of 100, 200, 300, 400, 500, 600 and 700 mm.

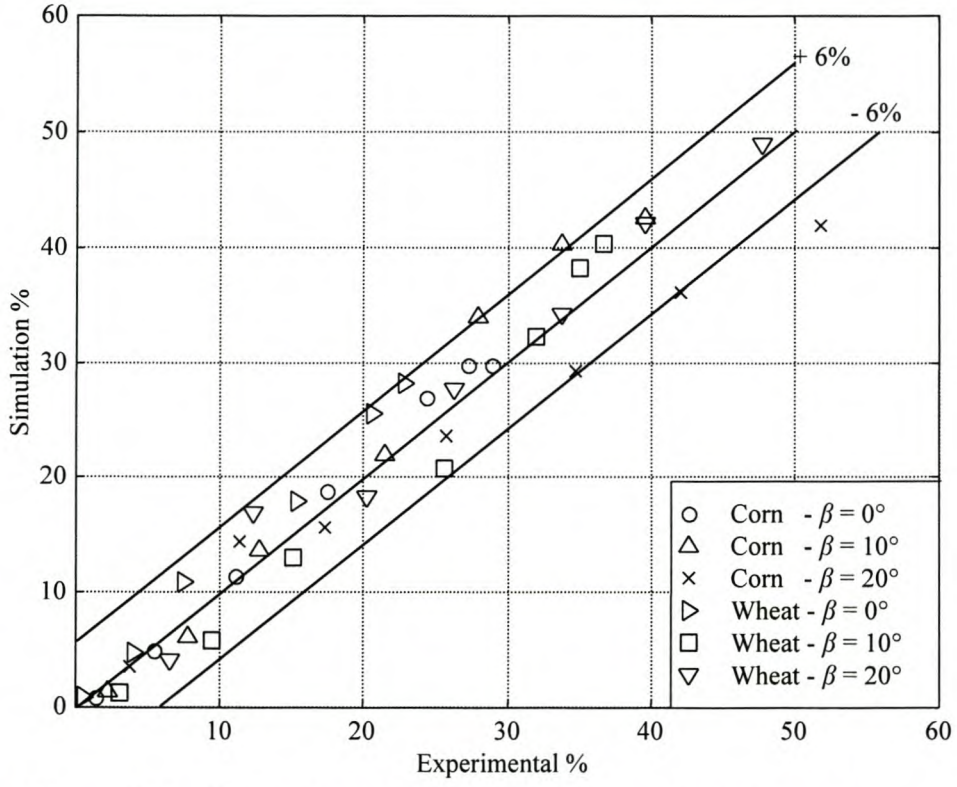

Figure 6.29 – *Comparison between simulation and experimental reduced fill percentages*

Except for two, all the simulation values are within ±6% of the experimental values.

Stellenbosch University http://scholar.sun.ac.za

CHAPTER 7

CONCLUSION AND RECOMMENDATIONS

The effect of tool velocity on draft force was investigated. The velocity varied from 0.1 to 100 mm/s. In this velocity range, the draft force was found to be independent of the tool velocity. This is in agreement with the results obtained by Albert et al. (1998). Other authors have shown that the draft force is a function of the velocity squared. Siemens et al. (1965) used sandy soil and velocities of 0.8 to 3.2 km/h. In general it can be stated that the velocity significantly influences the draft force only at high velocities (>1km/h). The shear strength of granular material is well known to be dependent on the shear rate. Grisso et al. (1996) showed that the shape of the tool influences the effect that the tool velocity has on the draft forces. The main reason for this is that the tool shape influences the shear rate.

Soil mechanics methods for modelling soil-tool interaction were investigated. The ability of these models to predict flat blade draft forces and rupture lines in two-dimensions was validated using experimental results. Corn and wheat grains were used as material. There is little difference between the predictions of the logarithmic spiral method and the plasticity theory. The logarithmic spiral method is simple and easy to use. Its accuracy is good enough for practical purposes and rough estimates. It does, however, not reveal much about the material behaviour and stresses.

For all rake angles and immersion depths, the theory predicts draft force values lower than the measured values. The glass panels add additional friction forces, which would increase the draft force. Perumpral et al. (1983), Swick and Perumpral (1988) and Osman (1964) all reported the theoretical predictions to be lower than the measured values of draft force. The above-mentioned authors, however, did not make use of a 2-D rig and still found the models to underestimate the draft force.

The models give more accurate predictions at high rake angles (90°). With a decrease in rake angle (60°) the accuracy of the models decreases.

Stellenbosch University http://scholar.sun.ac.za

The effect of blade rake angle and immersed depth was investigated. The draft force was found to be a function of the depth squared and decreases with a decrease in rake angle.

Good agreement between experimental and theoretical rupture lines was obtained. In general the predicted rupture zones were found to be larger then the measured zones. For high rake angles the rupture lines are curved (logarithmic spiral) and with a decrease in rake angle the rupture lines become perfectly straight.

Only blades with large rake angles were investigated. With small rake angles the blade's effective zone overlaps the Rankine zone which alters the shape of the slip lines. This still needs further investigation.

Two earthmoving tools were modelled with DEM, namely the flat blade and a bucket. In each case the study was motivated by a desire to understand the application better, to understand the importance of different parameters, and to make progress on validating the predictions of DEM simulations.

Synthetic (numeric equivalent) materials were created and the micro-properties determined through a calibration process. This process included uniaxial compression tests, shear tests and angle of repose tests. The ability of DEM to predict the tool forces, material compressibility, material flow, bucket fill rates and rupture lines was investigated.

The predicted blade and bucket draft forces were found to be lower than the measured forces. The main reason for this is the additional side friction experienced during experiments. Quantitatively very good comparisons were obtained. An analysis of bucket energy showed that ±40% of the total boundary energy goes into material friction, damping and strain. ±50% is dissipated at bucket-material contacts and is an indication of bucket wear. This is in close agreement with a simple calculation proposed by Rowlands (1991).

The predicted displacement and velocity field for material flowing into the bucket was found to be very accurate up to a displacement of 400 mm. Thereafter the simulations

Stellenbosch University http://scholar.sun.ac.za

failed in predicting the outline of the payload. The filling was further analysed and the fill percentage calculated. Despite the failure to predicting the flow of material accurately, DEM accurately predicts the amount of payload in the bucket.

The ability of DEM to predict the *Dead Load Rupture Line* was also investigated. Although the slope of the line is not predicted accurately, good quantitative results were obtained.

All the predictions were found accurate enough and can be used to optimise tool designs. Ways to reduce fill times, decrease wear on tooth and liners (to extend lifespan of tools and reduce maintenance costs) and decrease in energy consumption can be explored using numeric simulations such as this.

Wear on tools is produced by the impact or sliding of particles on the tools' surface. The main mechanism is however the scratching of the ductile metal by the particles as they slide along the boundary. Cleary (1988) obtained realistic wear results (peak wear rate of 340 mm of steel per 1000 operating hours for full-scale dragline buckets) using a model suggested by Finnie. The model essentially uses the kinetic energy of the incoming particle and knowledge about the impact angle to predict erosion rates. In DEM calculations, precise information is known for every collision and the Finnie model can easily be employed.

FEM analysis of tool structures is presently part of the tool design process. This is limited by the lack of information available on the dynamic loads experienced by the tool during operation. The collisional forces along the surface of the tool can be accumulated during a DEM simulation process. By collecting data over small time intervals and spatially smoothing it, the time-varying dynamic load on the tool can be predicted. This could then be used as input to the FEM analysis.

In future DEM developments the following issues may be addressed:

- Inclusion of particle cohesion.
- Improvement of calibration process (biaxial or triaxial compression tests)
- Inclusion of wear rates.

Stellenbosch University http://scholar.sun.ac.za

- Inclusion of tool dynamics.
- Extension to three-dimensions with more realistic particle shapes.
- Investigation of curved blades (two- and three-dimensional).
- Understanding the effect of bucket geometry on the forces and flow behaviour of material.

Cleary (1999) has already shown that 3-D DEM can be used with great success to model industrial processes such as ball mills and hoppers.

The ability of continuous (FEM) models to predict earthmoving processes also needs further investigation.

Stellenbosch University http://scholar.sun.ac.za

APPENDIX A

NOTATION AND VECTOR OPERATIONS

For analysis, a mathematical notation that can distinguish between different bodies in a multibody system is needed. A combination of the matrix tensor notation proposed by Hassenpflug (1993) and index notation is used. Kinematic and dynamic relations are described in matrix tensor notation and the index notation is used to distinguish between the various bodies in the system. All vectors are in 3-dimensional Euclidean space (R^3).

Vector

A column vector is indicated by an overbar.

$$\bar{\mathbf{v}} = \begin{bmatrix} v_1 \\ v_2 \\ v_3 \end{bmatrix} \tag{A.1}$$

A row vector is indicated by an underbar.

$$\underline{\mathbf{v}} \equiv \begin{bmatrix} v_1 & v_2 & v_3 \end{bmatrix} \tag{A.2}$$

The transpose changes the row column character of a vector and therefore the transpose vector has a transposed vector bar symbol.

$$\left[\bar{\mathbf{v}}\right]^T = \underline{\mathbf{v}^T} \tag{A.3}$$

$$\left[\bar{\mathbf{v}}\right]^{\mathrm{T}} = \underline{\mathbf{v}^{\mathrm{T}}} \tag{A.4}$$

Matrix

Matrices are indicated by an underbar as well as an overbar.

Stellenbosch University http://scholar.sun.ac.za

$$\underline{\overline{\mathbf{M}}} \equiv \begin{bmatrix} m_{11} & m_{12} & m_{13} \\ m_{21} & m_{22} & m_{23} \\ m_{31} & m_{32} & m_{33} \end{bmatrix} \tag{A.5}$$

Multiplication Rules

Vector bars cancel diagonally across the multiplication sign and the remaining vector bar symbols on both sides of the equation must be equal after calculation.

$$\underline{\overline{\mathbf{A}}} \cdot \overline{\mathbf{v}} = \overline{\mathbf{r}} \tag{A.6}$$

Scalar Product

The scalar or dot product of two vectors is a scalar.

$$\begin{aligned} \overline{\mathbf{a}} \bullet \overline{\mathbf{c}} \equiv \underline{\mathbf{a}}\, \overline{\mathbf{c}} &\equiv |\overline{\mathbf{a}}||\overline{\mathbf{c}}| \cos(\theta) \\ &\equiv a_1 c_1 + a_2 c_2 + a_3 c_3 \end{aligned} \tag{A.7}$$

It can be seen that the scalar product of two column vectors may be obtained by multiplying the one vector with the transpose of the other vector.

Norm

The norm of a vector is the magnitude or length of the vector.

$$|\overline{\mathbf{v}}| \equiv v \equiv \sqrt{\overline{\mathbf{v}} \bullet \overline{\mathbf{v}}} = \sqrt{\underline{\mathbf{v}}\, \overline{\mathbf{v}}} = \sqrt{{v_1}^2 + {v_2}^2 + {v_3}^2} \tag{A.8}$$

Physical Vectors

Physical vectors are indicated by an arrow above the vector name, $\vec{\mathbf{v}}$.

Stellenbosch University http://scholar.sun.ac.za

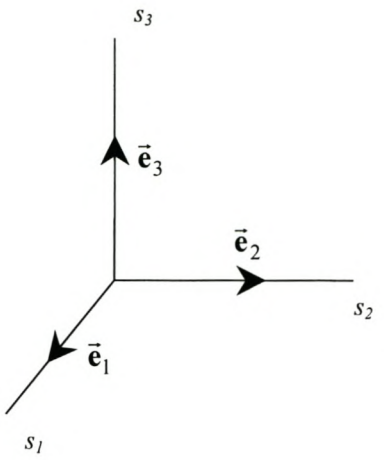

Figure A.1 – *Coordinate axis and base vectors*

Figure A.1 shows three orthogonal coordinates axes s_1, s_2, s_3 and three unit vectors $\vec{\mathbf{e}}_1$, $\vec{\mathbf{e}}_2$ and $\vec{\mathbf{e}}_3$. Any physical vector in 3D Euclidean space can be described as

$$\vec{\mathbf{v}} \equiv \vec{\mathbf{e}}_1 v_1 + \vec{\mathbf{e}}_2 v_2 + \vec{\mathbf{e}}_3 v_3 \tag{A.9}$$

The unit vectors have the physical dimensions of direction only and a numerical size of 1. These vectors form a base of R^3.

Base

The base vectors have a very important physical meaning and are defined as a single quantity. The row vector of the orthogonal base vectors is defined as

$$\underline{\vec{\mathbf{E}}} \equiv \left[\vec{\mathbf{e}}_1 \;\; \vec{\mathbf{e}}_2 \;\; \vec{\mathbf{e}}_3\right] \tag{A.10}$$

With this relation one can write Eq. A.9 as

$$\vec{\mathbf{v}} = \underline{\vec{\mathbf{E}}} \cdot \bar{\mathbf{v}} \tag{A.11}$$

Stellenbosch University http://scholar.sun.ac.za

We distinguish a base of a coordinate system by adding the name to the underbar of the base. We define the base of coordinate system s as $\underline{\vec{\mathbf{E}}}_s = [\vec{\mathbf{e}}_{s1} \ \vec{\mathbf{e}}_{s2} \ \vec{\mathbf{e}}_{s3}]$. The components of a vector measured in a base are subscripted similarly to the direction vectors. The base name is added to the vector bar.

$$\bar{\mathbf{v}}^s = \begin{bmatrix} v_{s1} \\ v_{s2} \\ v_{s3} \end{bmatrix} \tag{A.12}$$

Using this relation, one can describe a physical vector in base $\underline{\vec{\mathbf{E}}}_s$ with the equation:

$$\begin{aligned} \vec{\mathbf{v}} &= \vec{\mathbf{e}}_{s1} v_{s1} + \vec{\mathbf{e}}_{s2} v_{s2} + \vec{\mathbf{e}}_{s3} v_{s3} \\ &= [\vec{\mathbf{e}}_{s1} \ \ \vec{\mathbf{e}}_{s2} \ \ \vec{\mathbf{e}}_{s3}] \cdot \begin{bmatrix} v_{s1} \\ v_{s2} \\ v_{s3} \end{bmatrix} \\ &= \underline{\vec{\mathbf{E}}}_s \cdot \bar{\mathbf{v}}^s \end{aligned} \tag{A.13}$$

The base is an orthogonal matrix because its columns $\vec{\mathbf{e}}_1$, $\vec{\mathbf{e}}_2$ and $\vec{\mathbf{e}}_3$ form an orthogonal set. The inverse of the base is equal to its transpose.

$$[\underline{\vec{\mathbf{E}}}]^{-1} = [\underline{\vec{\mathbf{E}}}]^T = \underline{\overline{\mathbf{E}}} \tag{A.14}$$

With this relation the following outer product can be written

$$[\underline{\vec{\mathbf{E}}}]^{-1} \cdot \underline{\vec{\mathbf{E}}} = \underline{\overline{\mathbf{E}}} \cdot \underline{\vec{\mathbf{E}}} = \underline{\overline{\mathbf{E}}} = \underline{\bar{\mathbf{I}}} \tag{A.15}$$

with $\underline{\bar{\mathbf{I}}}$ the (3×3) identity matrix.

Stellenbosch University http://scholar.sun.ac.za

Transformations

From the discussion of bases, it is obvious that a physical vector $\vec{\mathbf{v}}$ can be expressed in respect to any arbitrary set of Cartesian coordinate systems. Consider two Cartesian coordinate systems *s* and *r* as shown in Fig. A.2.

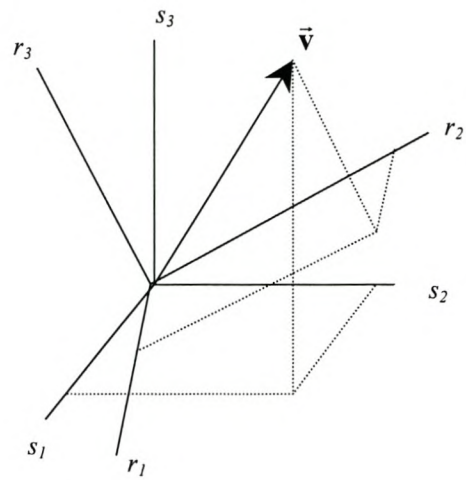

Figure A.2 – *Representation of a vector in two sets of right-handed Cartesian axes with different orientation*

The base of coordinate systems is defined by

$$\underline{\vec{\mathbf{E}}}_s = \left[\vec{\mathbf{e}}_{s1} \;\; \vec{\mathbf{e}}_{s2} \;\; \vec{\mathbf{e}}_{s3}\right] \tag{A.16}$$

$$\underline{\vec{\mathbf{E}}}_r = \left[\vec{\mathbf{e}}_{r1} \;\; \vec{\mathbf{e}}_{r2} \;\; \vec{\mathbf{e}}_{r3}\right] \tag{A.17}$$

The direction vectors of base *r* can be described in base *s* by applying Eq. A.13 to each of the physical base vectors of base *r*.

$$\begin{aligned}\left[\bar{e}_{r1}^{\,s} \;\; \bar{e}_{r2}^{\,s} \;\; \bar{e}_{r3}^{\,s}\right] &= \left[\underline{\vec{\mathbf{E}}}^{\,s} \cdot \vec{\mathbf{e}}_{r1} \;\; \underline{\vec{\mathbf{E}}}^{\,s} \cdot \vec{\mathbf{e}}_{r2} \;\; \underline{\vec{\mathbf{E}}}^{\,s} \cdot \vec{\mathbf{e}}_{r3}\right] \\ &= \underline{\vec{\mathbf{E}}}^{\,s} \cdot \left[\vec{\mathbf{e}}_{r1} \;\; \vec{\mathbf{e}}_{r2} \;\; \vec{\mathbf{e}}_{r3}\right] \\ &= \underline{\vec{\mathbf{E}}}^{\,s} \cdot \underline{\vec{\mathbf{E}}}_r \\ &= \underline{\bar{\mathbf{E}}}_r^{\,s}\end{aligned} \tag{A.18}$$

Stellenbosch University http://scholar.sun.ac.za

The quantity $\underline{\bar{\mathbf{E}}}_r^s$ is called the transformation matrix between the two sets of coordinate axis *s* and *r* and it is defined as:

$$\underline{\bar{\mathbf{E}}}_r^s \equiv \left[\bar{\mathbf{e}}_{r1}^s \quad \bar{\mathbf{e}}_{r2}^s \quad \bar{\mathbf{e}}_{r3}^s\right] \tag{A.19}$$

This is also an orthogonal matrix and the following relations can be stated:

$$\begin{aligned} \underline{\bar{\mathbf{E}}}_r^s &= \left[\underline{\bar{\mathbf{E}}}_s^r\right]^T \\ &= \left[\underline{\bar{\mathbf{E}}}_s^r\right]^{-1} \end{aligned} \tag{A.20}$$

The physical vector $\vec{\mathbf{v}}$ can be described with respect to both bases as:

$$\begin{aligned} &\vec{\mathbf{v}} = \underline{\vec{\mathbf{E}}}_s \bar{\mathbf{v}}^s = \underline{\vec{\mathbf{E}}}_r \bar{\mathbf{v}}^r \\ &\bar{\mathbf{v}}^s = \left[\underline{\vec{\mathbf{E}}}_s\right]^T \underline{\vec{\mathbf{E}}}_r \bar{\mathbf{v}}^r = \underline{\bar{\mathbf{E}}}_r^s \bar{\mathbf{v}}^r \quad \text{or} \quad \bar{\mathbf{v}}^r = \left[\underline{\vec{\mathbf{E}}}_r\right]^T \underline{\vec{\mathbf{E}}}_s \bar{\mathbf{v}}^s = \underline{\bar{\mathbf{E}}}_s^r \bar{\mathbf{v}}^s \end{aligned} \tag{A.21}$$

The transformation matrix is also called the direction cosine matrix.

Vector or Cross Product

The cross product of two vectors is a vector perpendicular to both these two vectors. The computational rule for the cross product is usually given in the form:

$$\begin{aligned} \vec{\mathbf{a}} \times \vec{\mathbf{c}} &= \begin{vmatrix} \vec{\mathbf{e}}_1 & \vec{\mathbf{e}}_2 & \vec{\mathbf{e}}_3 \\ a_1 & a_2 & a_3 \\ c_1 & c_2 & c_3 \end{vmatrix} \\ &= (a_2 c_3 - a_3 c_2)\vec{\mathbf{e}}_1 + (a_3 c_1 - a_1 c_3)\vec{\mathbf{e}}_2 + (a_1 c_2 - a_2 c_1)\vec{\mathbf{e}}_3 \end{aligned} \tag{A.22}$$

or in orthogonal base notation

Stellenbosch University http://scholar.sun.ac.za

$$\bar{\mathbf{a}} \times \bar{\mathbf{c}} = \begin{vmatrix} \bar{\mathbf{e}}_1 & \bar{\mathbf{e}}_2 & \bar{\mathbf{e}}_3 \\ a_1 & a_2 & a_3 \\ c_1 & c_2 & c_3 \end{vmatrix} = \begin{bmatrix} \bar{\mathbf{e}}_1 & \bar{\mathbf{e}}_2 & \bar{\mathbf{e}}_3 \end{bmatrix} \cdot \begin{bmatrix} a_2 c_3 - a_3 c_2 \\ a_3 c_1 - a_1 c_3 \\ a_1 c_2 - a_2 c_1 \end{bmatrix} \tag{A.23}$$

One can write this equation in matrix form as

$$\bar{\mathbf{a}} \times \bar{\mathbf{c}} = \underline{\tilde{\bar{\mathbf{a}}}} \cdot \bar{\mathbf{c}} \tag{A.24}$$

where $\underline{\tilde{\bar{\mathbf{a}}}}$ is the skew symmetric tensor of the components of the column vector $\bar{\mathbf{a}}$. It is also called the cross product tensor and is defined as:

$$\underline{\tilde{\bar{\mathbf{a}}}} \equiv \begin{bmatrix} 0 & -a_3 & a_2 \\ a_3 & 0 & -a_1 \\ -a_2 & a_1 & 0 \end{bmatrix} \tag{A.25}$$

This tensor has the property that its transpose is equal to the negative of the tensor.

$$\underline{\tilde{\bar{\mathbf{a}}}}^T = -\underline{\tilde{\bar{\mathbf{a}}}} \tag{A.26}$$

Rotating Base

Let $\underline{\vec{\mathbf{E}}}_r$ be a rotating base. The time derivative of a rotating base is given by

$$\begin{aligned} \frac{d}{dt}\underline{\vec{\mathbf{E}}}_r \equiv \dot{\underline{\vec{\mathbf{E}}}}_r &= \vec{\omega} \times \underline{\vec{\mathbf{E}}}_r \\ &= \underline{\tilde{\vec{\omega}}} \cdot \underline{\vec{\mathbf{E}}}_r \end{aligned} \tag{A.27}$$

where $\underline{\tilde{\vec{\omega}}}$ is defined as the cross product tensor of the angular velocity vector $\vec{\omega}$. One can also write

$$\dot{\underline{\bar{E}}}_r^s = \underline{\tilde{\bar{\omega}}}_s^s \underline{\bar{\mathbf{E}}}_r^s \tag{A.28}$$

in the fixed base $\underline{\vec{\mathbf{E}}}_s$.

Stellenbosch University http://scholar.sun.ac.za

Combined Notation

The kinematics and properties of a body are stated in matrix tensor notation. The index notation is used to distinguish between the properties of different bodies in the system. A vector for a particular body is indicated by the normal symbol for a vector in matrix tensor notation to which an index is added. This index is written in brackets and corresponds to the body number.

Stellenbosch University http://scholar.sun.ac.za

APPENDIX B

MULTIBODY DYNAMICS

In this appendix the general dynamics of a system of rigid particles are described. It also discusses the particular application of DEM to a system of bodies by referring to the model used in PFC^{2D} (Itasca 1999).

B.1 The Motion of a Body

In this section the equations of motion of a body. If the body is rigid, the distance between any pair of points in the body is constant. This statement enables the description of the motion of a rigid body by using six coordinates, namely three translational and three rotational. Before the equations of motion of a body can be derived, we must define some kinematic relations.

B.1.1 Kinematic Relations

In order to describe the motion of a rigid body in a multibody system, we assign a coordinate system to each body. Figure B.1 shows two orthogonal reference systems, the inertial system *s* and the body system *b*. $\vec{\mathbf{r}}_{(j)}$ is the position vector of the origin of the body system *b* of body *j*. The body has an angular velocity vector $\vec{\boldsymbol{\omega}}_{(j)}$ as shown. The vector $\vec{\boldsymbol{\rho}}_{(cj)}$ is fixed in the body reference frame and experiences the same motion as the body. Referring to Fig. B.1 the position of any point *c* in the body *j* can be described in terms of the following vectors:

$$\vec{\mathbf{r}}_{(c)} = \vec{\mathbf{r}}_{(j)} + \vec{\boldsymbol{\rho}}_{(cj)} \tag{B.1}$$

This equation can be stated in orthogonal base notation with respect to base $\underline{\vec{\mathbf{E}}}_s$ as

$$\bar{\mathbf{r}}^s_{(c)} = \bar{\mathbf{r}}^s_{(j)} + \bar{\boldsymbol{\rho}}^s_{(cj)} \tag{B.2}$$

Stellenbosch University http://scholar.sun.ac.za

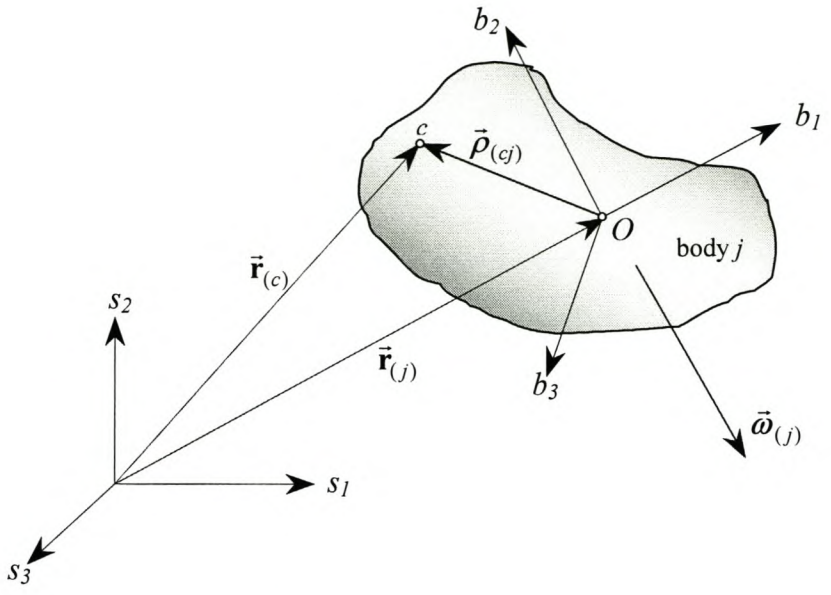

Figure B.1 – *Body Motion*

Taking the first and second time derivative of this equation yields the velocity and acceleration relations:

$$\dot{\vec{\mathbf{r}}}^{s}_{(c)} = \dot{\vec{\mathbf{r}}}^{s}_{(j)} + \dot{\vec{\rho}}^{s}_{(cj)} \tag{B.3}$$

$$\ddot{\vec{\mathbf{r}}}^{s}_{(c)} = \ddot{\vec{\mathbf{r}}}^{s}_{(j)} + \ddot{\vec{\rho}}^{s}_{(cj)} \tag{B.4}$$

If the body is assumed to be rigid, the vector $\vec{\rho}_{(cj)}$ is fixed in the body and will remain constant with respect to the body reference frame during any motion of the body. This implies that with respect to the body reference frame, *b*

$$\dot{\vec{\rho}}^{b}_{(cj)} = \ddot{\vec{\rho}}^{b}_{(cj)} = \overline{\mathbf{0}} \tag{B.5}$$

Lets, for the moment however, assumes the body to be non-rigid. The following relation holds for the vector $\vec{\rho}_{(cj)}$ in the two reference systems, *s* and *b*.

$$\overline{\rho}^{s}_{(cj)} = \underline{\overline{\mathbf{E}}}^{s}_{b}\,\overline{\rho}^{b}_{(cj)} \tag{B.6}$$

Stellenbosch University http://scholar.sun.ac.za

with $\underline{\overline{\mathbf{E}}}_b^s$ the transformation matrix between the two reference frames. By taking the time derivative of Eq. B.6, one obtains:

$$\begin{aligned}\dot{\overline{\rho}}_{(cj)}^s &= \underline{\overline{\mathbf{E}}}_b^s \dot{\overline{\rho}}_{(cj)}^b + \dot{\underline{\overline{\mathbf{E}}}}_b^s \overline{\rho}_{(cj)}^b \\ &= \underline{\overline{\mathbf{E}}}_b^s \left[\dot{\overline{\rho}}_{(cj)}^b + \underline{\overline{\tilde{\omega}}_{(j)}}_s^s \overline{\rho}_{(cj)}^b \right]\end{aligned} \tag{B.7}$$

where $\underline{\overline{\tilde{\omega}}_{(j)}}_s^s = \underline{\dot{\overline{\mathbf{E}}}}_b^s \underline{\overline{\mathbf{E}}}_s^b$ is the cross product tensor of the angular velocity vector off particle j with respect to reference frame s. The acceleration relation can be obtained by taking the time derivative of Eq. B.7.

$$\ddot{\overline{\rho}}_{(cj)}^s = \underline{\overline{\mathbf{E}}}_b^s \left[\ddot{\overline{\rho}}_{(cj)}^b + 2 \underline{\overline{\tilde{\omega}}_{(j)}}_s^s \dot{\overline{\rho}}_{(cj)}^b + \underline{\overline{\dot{\tilde{\omega}}_{(j)}}}_s^s \overline{\rho}_{(cj)}^b + \underline{\overline{\tilde{\omega}}_{(j)}}_s^s \underline{\overline{\tilde{\omega}}_{(j)}}_s^s \overline{\rho}_{(cj)}^b \right] \tag{B.8}$$

The second term on the right-hand side of Eq. B.8 is called the *Coriolis acceleration*. The following relations can also be written:

$$\overline{\omega}_{(j)}^s = \underline{\overline{\mathbf{E}}}_b^s \overline{\omega}_{(j)}^b \tag{B.9}$$

$$\underline{\overline{\tilde{\omega}}_{(j)}}_s^s = \underline{\overline{\mathbf{E}}}_b^s \underline{\overline{\tilde{\omega}}_{(j)}}_b^b \underline{\overline{\mathbf{E}}}_s^b \tag{B.10}$$

Using the relations for the vector $\vec{\rho}_{(cj)}$ (Eq. B.7 and Eq. B.8), we can rewrite the velocity and acceleration relations of Eq. B.3 and Eq. B.4 as:

$$\begin{aligned}\dot{\overline{\mathbf{r}}}_{(c)}^s &= \dot{\overline{\mathbf{r}}}_{(j)}^s + \underline{\overline{\mathbf{E}}}_b^s \left[\dot{\overline{\rho}}_{(cj)}^b + \underline{\overline{\tilde{\omega}}_{(j)}}_s^s \overline{\rho}_{(cj)}^b \right] \\ &= \dot{\overline{\mathbf{r}}}_{(j)}^s + \dot{\overline{\rho}}_{(cj)}^s + \overline{\omega}_{(j)}^s \times \overline{\rho}_{(cj)}^s\end{aligned} \tag{B.11}$$

$$\ddot{\overline{\mathbf{r}}}_{(c)}^s = \ddot{\overline{\mathbf{r}}}_{(j)}^s + \underline{\overline{\mathbf{E}}}_b^s \left[\ddot{\overline{\rho}}_{(cj)}^b + 2 \underline{\overline{\tilde{\omega}}_{(j)}}_s^s \dot{\overline{\rho}}_{(cj)}^b + \underline{\overline{\dot{\tilde{\omega}}_{(j)}}}_s^s \overline{\rho}_{(cj)}^b + \underline{\overline{\tilde{\omega}}_{(j)}}_s^s \underline{\overline{\tilde{\omega}}_{(j)}}_s^s \overline{\rho}_{(cj)}^b \right] \tag{B.12}$$

Stellenbosch University http://scholar.sun.ac.za

In terms of physical vectors it can be written as:

$$\dot{\vec{\mathbf{r}}}_{(c)} = \dot{\vec{\mathbf{r}}}_{(j)} + \dot{\vec{\rho}}_{(cj)} + \vec{\omega}_{(j)} \times \vec{\rho}_{(cj)} \tag{B.13}$$

$$\ddot{\vec{\mathbf{r}}}_{(c)} = \ddot{\vec{\mathbf{r}}}_{(j)} + \ddot{\vec{\rho}}_{(cj)} + 2\vec{\omega}_{(j)} \times \dot{\vec{\rho}}_{(cj)} + \dot{\vec{\omega}}_{(j)} \times \vec{\rho}_{(cj)} + \vec{\omega}_{(j)} \times (\vec{\omega}_{(j)} \times \vec{\rho}_{(cj)}) \tag{B.14}$$

The velocity and acceleration of any point in the rigid body can be described in terms of the translation of the origin of a body reference system and the rotation of the reference system about the origin.

B.1.2 Linear and Angular Momentum of a Rigid Body

Consider again Fig. B.1. Assume that the body reference system origin O corresponds to the centre of mass of the body. Note that the subscript *(j)* refers to body *j*. Using the results from the previous section it can be shown that the linear momentum $\vec{\mathbf{p}}_{(j)}$ of body *j* is given by:

$$\vec{\mathbf{p}}_{(j)} = m_{(j)} \dot{\vec{\mathbf{r}}}_{(j)} \tag{B.15}$$

where $m_{(j)}$ is the total mass of the body. The angular momentum of the body can be shown to be:

$$\vec{\mathbf{h}}_{(j)} = \overrightarrow{\underrightarrow{\mathbf{J}}_{(j)}} \vec{\omega}_{(j)} \tag{B.16}$$

or in orthogonal base notation as

$$\overline{\mathbf{h}}^{s}_{(j)} = \overline{\underline{\mathbf{J}}^{s}_{(j)\,s}} \, \overline{\omega}^{s}_{(j)} \tag{B.17}$$

where the symmetric tensor $\underline{\overline{\mathbf{J}}}^{s}_{s}$ is called the *inertia tensor* with the diagonal elements called *moments of inertia* and the non-diagonal elements called *products of inertia*:

$$\underline{\overline{\mathbf{J}}}^{s}_{s} = \begin{bmatrix} J_{11} & J_{12} & J_{13} \\ J_{21} & J_{22} & J_{23} \\ J_{31} & J_{32} & J_{33} \end{bmatrix} \tag{B.18}$$

Stellenbosch University http://scholar.sun.ac.za

B.1.3 The Equations of Motion

Newton's second law states that for a body with constant mass

$$\begin{aligned}\vec{\mathbf{F}}_{(j)} &= \dot{\vec{\mathbf{p}}}_{(j)} \\ &= \frac{d}{dt}\left(m_{(j)}\dot{\vec{\mathbf{r}}}_{(j)}\right) \\ &= m_{(j)}\ddot{\vec{\mathbf{r}}}_{(j)}\end{aligned} \tag{B.19}$$

where $\vec{\mathbf{F}}_{(j)}$ is the resultant force acting on body j and $\vec{\mathbf{r}}_{(j)}$ is the position vector of the body's centre of mass. Expressed in orthogonal base notation with respect to the inertial system s:

$$\overline{\mathbf{F}}^{s}_{(j)} = m_{(j)}\ddot{\overline{\mathbf{r}}}^{s}_{(j)} \tag{B.20}$$

The equation for the rotational motion of the body can be obtained from the relation between the applied torque and the angular momentum,

$$\vec{\mathbf{M}}_{(j)} = \dot{\vec{\mathbf{h}}}_{(j)} \tag{B.21}$$

where $\vec{\mathbf{M}}_{(j)}$ is the resultant moment acting on the body and $\dot{\vec{\mathbf{h}}}_{(j)}$ is the rate of change of the angular momentum. The expression for the angular momentum has already been given in Eq. B.16. The rate of change of angular momentum can be calculated by simply taking the time derivative. Using the relation given in Eq. B.7 it can be shown that:

$$\vec{\mathbf{M}}_{(j)} = \dot{\vec{\mathbf{h}}}_{(j)} = \underrightarrow{\mathbf{J}_{(j)}}\dot{\vec{\boldsymbol{\omega}}}_{(j)} + \vec{\boldsymbol{\omega}}_{(j)} \times \underrightarrow{\mathbf{J}_{(j)}}\vec{\boldsymbol{\omega}}_{(j)} \tag{B.22}$$

or in orthogonal base notation with respect to the inertial system, note that $\underline{\dot{\mathbf{J}}_{(j)}}^{b}_{b} = \underline{\mathbf{0}}$.

Stellenbosch University http://scholar.sun.ac.za

$$\begin{aligned}\overline{\mathbf{M}}^{s}_{(j)} = \dot{\overline{\mathbf{h}}}^{s}_{(j)} &= \underline{\overline{\mathbf{J}_{(j)}}}^{s}_{s}\,\dot{\overline{\boldsymbol{\omega}}}^{s}_{(j)} + \underline{\overline{\tilde{\boldsymbol{\omega}}_{(j)}}}^{s}_{s}\,\underline{\overline{\mathbf{J}_{(j)}}}^{s}_{s}\,\overline{\boldsymbol{\omega}}^{s}_{(j)} \\ &= \left[\underline{\overline{\mathbf{E}}}^{s}_{b}\,\underline{\overline{\mathbf{J}_{(j)}}}^{b}_{b}\,\underline{\overline{\mathbf{E}}}^{b}_{s}\right]\dot{\overline{\boldsymbol{\omega}}}^{s}_{(j)} + \underline{\overline{\tilde{\boldsymbol{\omega}}_{(j)}}}^{s}_{s}\left[\underline{\overline{\mathbf{E}}}^{s}_{b}\,\underline{\overline{\mathbf{J}_{(j)}}}^{b}_{b}\,\underline{\overline{\mathbf{E}}}^{b}_{s}\right]\overline{\boldsymbol{\omega}}^{s}_{(j)}\end{aligned} \tag{B.23}$$

Equation B.23 is known as *Euler's equation of motion.* The combination of Eq. B.19 and Eq. B.22 is known as the *Newton-Euler equations of motion* and describes the motion of a rigid body.

B.2 The Discrete Element Method

Over the years many methods for the modelling of cohesive frictional materials have been proposed. Main research areas can be found in the enhancement of the discontinuous (micro) and continuum-oriented (macro) modelling techniques with an emphasis on the transition of the results between these two scales.

According to Mühlhaus (2000), the main obstruction in modelling geomechanics and solving geotechnical problems has been the lack of appropriate numerical tools to handle the difficulties arising from material inhomogeneity, brittle fracture, and associated complex damage patterns. The application of grid based discretization procedures such as the Finite Element Method can be problematic even if the material is macroscopically homogenous if, for instance, large deformations are involved. Remeshing is problematic if fracturing occurs on more than one scale, or where history dependence is involved. For these reasons, particle based methods for solid mechanics seem to be increasing in popularity. According to Kun (2000), fracture and fragmentation of solids are difficult problems to handle numerically due to the creation and continuous motion of new surfaces. Commonly used numerical methods solve partial differential equations of continuum mechanics. With classical numerical methods such as Finite Element Methods, a small number of discontinuities may be considered but these methods cannot encompass the entire fracturing process.

The alternative approach is DEM in which the medium is considered to be fully discontinuous; i.e. the elastic solid is assembled of discrete elements.

Stellenbosch University http://scholar.sun.ac.za

DEM was introduced by Cundall (1971) for the analysis of rock-mechanics problems and then applied to soils by Cundall and Strack (1979).

This method, in general, simulates the mechanical behaviour of a system of arbitrarily shaped particles. The distinct particles displace independently from one another and interact only at contacts with either other particles and/or walls. (**Note**: in DEM it is customary to refer to the bodies as particles. It should not be confused with the mechanics definition of a particle where it is taken as a body whose dimensions are negligible and therefore occupies only a single point in space).

One of the main fields of research is to develop and verify different contact constitutive models. It is mainly these different constitutive or contact models that distinguish between different DEM models. The contact forces and displacements of an assembly of particles are found by tracing the movements of the individual particles. The movements result from the propagation through the system of disturbances caused by specified wall and particle motion and/or body forces such as a gravity field.

The system is represented by a timestepping algorithm in which the velocities and accelerations are assumed to be constant within each time step. Calculations performed during a DEM simulation alternate between the application of Newton's second law to the particles and a force-displacement law at the contacts. The motion of each particle is calculated by applying Newton's second law to each particle, while the force-displacement law is used to update the contact forces arising from the relative motion at each contact.

B.2.1 The *PFC*^{2D} Model

PFC^{2D} models the movement and interaction of stressed assemblies of rigid circular particles using DEM. The particles are assumed to be rigid and a soft contact approach is used in which a finite normal and tangential stiffness is taken to represent the measurable stiffness that exists at a contact. Much more complex behaviour can be modelled by introducing cohesion and adhesion. This is accomplished by allowing the

Stellenbosch University http://scholar.sun.ac.za

particles to be bonded together at their contact points. These bonds can be broken when the magnitude of the contact force exceeds the bonding strength.

The model used by PFC^{2D} (Itasca 1999) contains the following assumptions:

1. The particles are treated as rigid bodies, either spheres or disks.
2. The contacts are point contacts (occur over a small area).
3. The behaviour at the contacts uses a soft-contact approach wherein the rigid particles are allowed to overlap one another at a contact point.
4. The magnitude of the overlap is related to the contact force via the force-displacement law, and all overlaps are small in relation to particle sizes.
5. Bonds can exist at contacts between particles.
6. All particles are circular; however, the clump logic supports the creation of arbitrary shaped particles. This is done by intentionally grouping particles together and allowing it to overlap with no forces generated at contacts. The "clump" of particles is treated as a rigid body with a boundary allowing overlaps with other particles and/or the environment.

The assumption of treating particles as rigid bodies is a good one when simulating the deformation of a packed-particle assembly or a granular assembly such as sand. The deformation of the assembly results primarily from the sliding, rotation and interlocking of the particles as rigid bodies and not from the individual particle deformation.

The PFC^{2D} model consists of a two-dimensional assembly of circular particles and thus only two force components and one moment component exist, opposed to the three force components and three moment components that exist in a three-dimensional particle assembly. The model deals with this two-dimensional "world" by totally ignoring the one out-of-plane force component and the two in-plane moment components in the equations of motion and in the force-displacement laws.

The model also includes "walls". The two velocity components of a wall are specified by the user. These velocity components can be changed at any time during a simulation, which means that the velocity can be a function of time. The particles and walls interact with one another via the forces that arise at the contacts. The forces acting on a wall do

Stellenbosch University http://scholar.sun.ac.za

not influence the motion of the wall; i.e. the user-defined velocity components do not change as a result of forces acting on the wall. Contacts can not form between walls; i.e. contacts are either particle-particle or particle-wall.

The remainder of this section describes the DEM by referring to the model used in *PFC*^{2D} (Itasca 1999). The formulation is based on multibody dynamics and is presented for the general three-dimensional case with some emphasis on the limited two-dimensional case.

B.2.2 The Calculation Cycle

The timestepping algorithm repeatedly requires the application of the law of motion (Newton's second law) to each particle, a force-displacement law to each contact and a constant updating of wall positions. Contacts are formed and broken automatically during the simulation. Figure B.2 illustrates the calculation cycle.

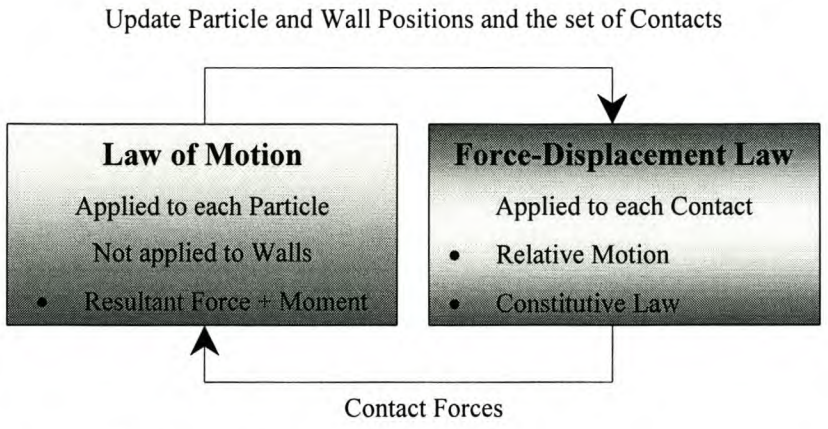

Figure B.2 - *The Calculation Cycle*

At the start of each time step the list of all contacts is updated from the known particle and wall positions. With the contacts known, the force-displacement law is used to update all the contact forces according to the constitutive model. Next, the law of motion is applied to each particle to update its velocity and position based on the resultant force and moment arising from the contact forces and possible body forces acting on the particles. The position of each wall is also updated by simply using the user-defined velocity of each individual wall.

Stellenbosch University http://scholar.sun.ac.za

B.2.3 The Force-Displacement Law

The force-displacement law is used to calculate the contact force between two entities. The force is related to the relative displacement between the two entities at the contact point. The notation used for particle-particle contact is shown in Fig. B.3 and particle-wall contact in Fig. B.4.

In the case of particle-particle contact, $\vec{\mathbf{r}}_{(c)}$ is the position vector of the contact point between the two circular particles and $\vec{\mathbf{r}}_{(i)}$ and $\vec{\mathbf{r}}_{(j)}$ are the two position vectors of the centres of particles i and j respectively, see Fig. B.3. In the case of a particle-wall contact, entity j refers to the wall. The contact point is within the interpenetrating volume of the two entities and is lying on a plane that is defined by a unit normal vector $\vec{\mathbf{n}}$. In the two-dimensional case, this normal vector lies in the plane of the model. In the case of particle-particle contact, the normal vector is directed along the line between the two particle centres; for particle-wall contact the normal vector is directed along the line defining the shortest distance between the particle centre and the wall.

For a particle-particle contact, $R_{(i)}$ and $R_{(j)}$ denote the radii of the two particles respectively and d the distance between the two centres. In the case of particle-wall contact, $R_{(i)}$ refers to the radius of the particle and d is the shortest distance between the particle's centre and the wall. In both the particle-particle and particle-wall case, U^n denotes the magnitude of the overlap.

The contact force is decomposed into a normal component acting in the direction of the normal vector and a shear component acting in the contact plane. The force-displacement law relates the two components of force to the corresponding components of the relative displacement via the normal and shear stiffness at the contact.

Stellenbosch University http://scholar.sun.ac.za

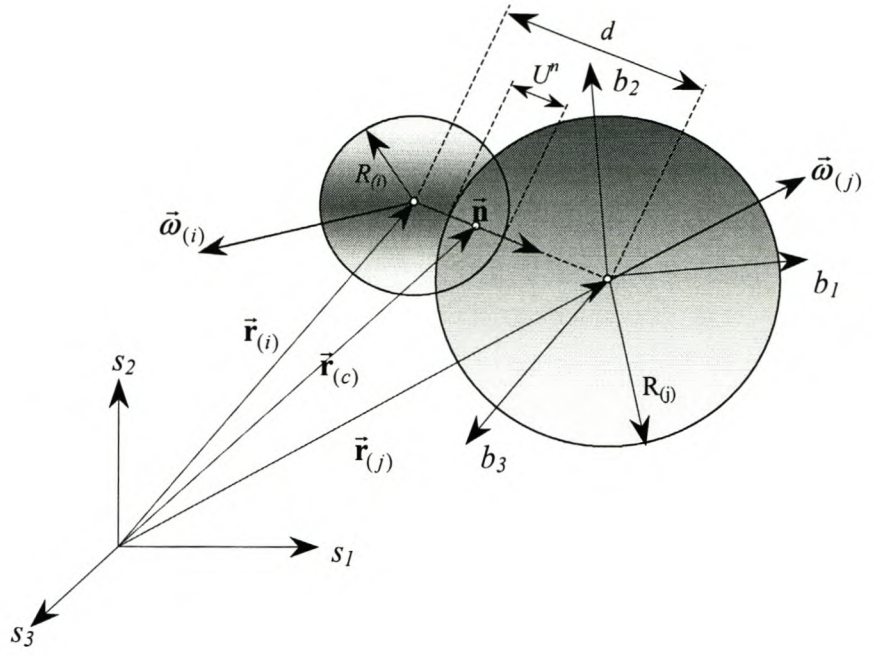

Figure B.3 – *Particle-Particle Contact*

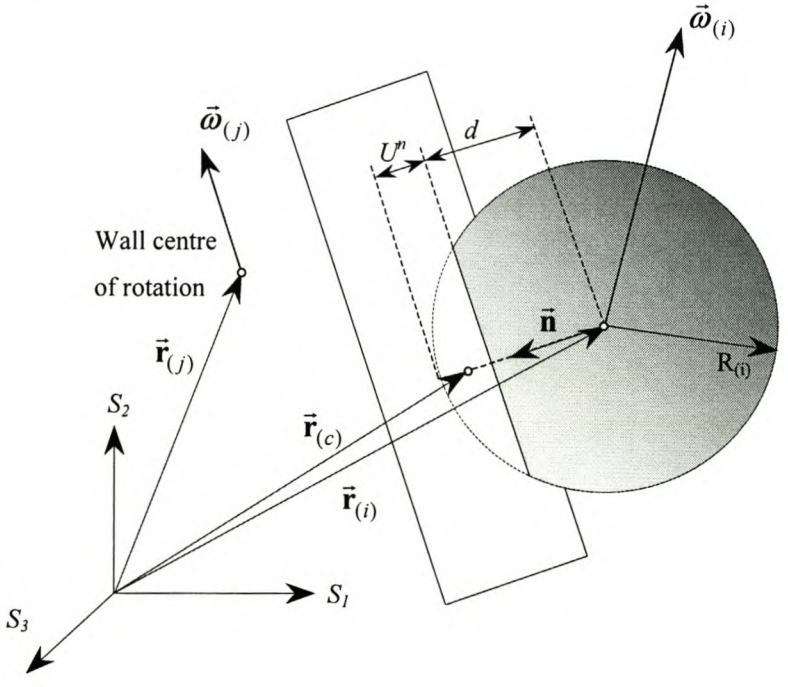

Figure B.4 – *Particle-Wall Contact*

For particle-particle contact the unit normal vector $\vec{\mathbf{n}}$ is given by

$$\vec{\mathbf{n}} = \frac{\vec{\mathbf{r}}_{(j)} - \vec{\mathbf{r}}_{(i)}}{d} \qquad \text{(particle-particle)} \qquad \text{(B.24)}$$

Stellenbosch University http://scholar.sun.ac.za

The distance d between the two centres is given by

$$d = \left| \vec{\mathbf{r}}_{(j)} - \vec{\mathbf{r}}_{(i)} \right| = \sqrt{\left(\vec{\mathbf{r}}_{(j)} - \vec{\mathbf{r}}_{(i)} \right) \cdot \left(\vec{\mathbf{r}}_{(j)} - \vec{\mathbf{r}}_{(i)} \right)} \qquad \text{(particle-particle)} \qquad \text{(B.25)}$$

It is not so simple to define the normal contact vector for particle-wall contacts. The idea is illustrated in Fig. B.5 for the two-dimensional case. Walls are defined with only one side as the active side; i.e. only the active side of the wall can interact with particles. The centre of rotation of a wall is defined by the user and all kinematics are based on this point. In Fig. B.5 regions 1 to 5 are defined as active sides and region 6 as a non-active side. In PFC^{2D}, the active side of a wall is indicated by a right-handed normal vector for an observer standing at C and looking towards B where the wall segment is defined in the same sequence; i.e. from node C to node B. If a particle's centre lies in regions 2 or 4, it will contact the wall along its length, and $\vec{\mathbf{n}}$ will be normal to the wall segment. However, if the particle centre lies in region 1, 3 or 5 it will contact the wall at one of its endpoints and $\vec{\mathbf{n}}$ will lie along the line joining the endpoint and the particle centre.

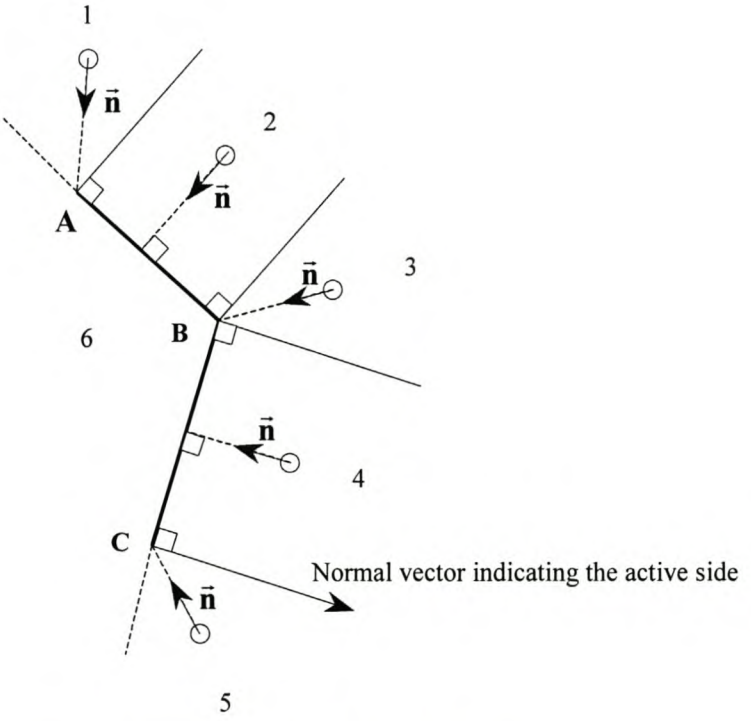

Figure B.5 - *Normal Vectors for Particle-Wall Contact*

Stellenbosch University http://scholar.sun.ac.za

The relative displacement between two entities at the contact point determines the magnitude and direction of the contact force vector. The overlap U^n is defined as this relative displacement in the normal direction and is given by

$$U^n = R_{(i)} + R_{(j)} - d, \qquad \text{(particle-particle)} \tag{B.26}$$

$$U^n = R_{(i)} - d, \qquad \text{(particle-wall)} \tag{B.27}$$

The contact point is defined to be in the middle of the interpenetrating volume of the two entities in contact.

$$\vec{\mathbf{r}}_{(c)} = \vec{\mathbf{r}}_{(i)} + \left(R_{(i)} - \tfrac{1}{2}U^n\right)\vec{\mathbf{n}} \tag{B.28}$$

Two entities are in contact when the overlap U^n between the two is equal to or less than zero. With the position of the two entities known, the position of the contact point and the contact force can be determined. The total contact force vector $\vec{\mathbf{F}}_{(c)}$ can be resolved into a normal and shear component.

$$\vec{\mathbf{F}}_{(c)} = \vec{\mathbf{F}}^n_{(c)} + \vec{\mathbf{F}}^s_{(c)} \tag{B.29}$$

where $\vec{\mathbf{F}}^n_{(c)}$ and $\vec{\mathbf{F}}^s_{(c)}$ denote the normal and shear components respectively. The normal component acts normal to the contact plane and the shear component acts in the contact plane. The normal component can easily be calculated by

$$\vec{\mathbf{F}}^n_{(c)} = K_n U^n \vec{\mathbf{n}} \tag{B.30}$$

where K_n is the normal stiffness (linear or non-linear) at the contact. An in-depth discussion of the contact constitutive models is given in section B.3. Note that $\vec{\mathbf{F}}^n_{(c)}$ acts in the direction of the unit normal vector. The normal stiffness K_n is a secant modulus in that it relates the total displacement or overlap and the total normal force. The shear stiffness K_s is a tangent modulus in that it relates an increment in displacement or

Stellenbosch University http://scholar.sun.ac.za

overlap and an increment in shear force. K_n and K_s usually have magnitudes of the same order (Johnson 1987). When a contact forms, the total shear contact force is initialised to zero. Each subsequent relative tangential displacement increment results in an increment of the shear force that is added to the current value. In order to calculate this increment in shear force, the relative motion at the contact must be known.

$\vec{\mathbf{V}}_{(c)}$ is defined as the relative contact velocity. The comparison between Fig. B.3 and Fig. B.1 can easily be seen. Equation B.7, B.8, B.11 and B.12 have been derived assuming that $\dot{\vec{\rho}}^{\,b}_{(cj)} \neq \bar{\mathbf{0}}^{b}$, $\ddot{\vec{\rho}}^{\,b}_{(cj)} \neq \bar{\mathbf{0}}^{b}$, which is typical if the body is assumed non-rigid. In DEM, maximum overlaps of 0.1%-1.0% (of the particle diameter) is desirable, requiring stiffness constants of the order of 10^5 to 10^7 Nm^{-1} (Cleary 1999) and the particles are usually assumed rigid. It is therefore assumed that $\dot{\vec{\rho}}^{\,b}_{(cj)} = \ddot{\vec{\rho}}^{\,b}_{(cj)} = \bar{\mathbf{0}}$ since its contribution in Eq. B.11 and Eq. B.12 is negligible compared to the other terms. Taking this into account and noting that $\vec{\rho}_{(cj)} = \vec{\mathbf{r}}_{(c)} - \vec{\mathbf{r}}_{(j)}$, $\vec{\rho}_{(ci)} = \vec{\mathbf{r}}_{(c)} - \vec{\mathbf{r}}_{(i)}$, Eq. B.13 can be used to write the relative contact velocity as

$$\begin{aligned}\vec{\mathbf{V}}_{(c)} &= (\dot{\vec{\mathbf{r}}}_{(c)})_{(j)} - (\dot{\vec{\mathbf{r}}}_{(c)})_{(i)} \\ &= (\dot{\vec{\mathbf{r}}}_{(j)} + \vec{\omega}_{(j)} \times (\vec{\mathbf{r}}_{(c)} - \vec{\mathbf{r}}_{(j)})) - (\dot{\vec{\mathbf{r}}}_{(i)} + \vec{\omega}_{(i)} \times (\vec{\mathbf{r}}_{(c)} - \vec{\mathbf{r}}_{(i)}))\end{aligned} \tag{B.31}$$

where $(\dot{\vec{\mathbf{r}}}_{(c)})_{(j)}$ is the absolute (relative to the fixed reference frame *s*) velocity of the contact point with reference particle *j*, $\dot{\vec{\mathbf{r}}}_{(j)}$ is the absolute translational velocity of the centre of mass of particle *j* and $\vec{\omega}_{(j)}$ is the absolute rotational velocity of particle *j*. In the case of a particle-wall contact, $\dot{\vec{\mathbf{r}}}_{(j)}$ and $\vec{\omega}_{(j)}$ refer to the absolute translational velocity of the centre of rotation of the wall and the absolute rotational velocity respectively.

The contact velocity can be resolved into a normal and tangential component with respect to the contact plane

Stellenbosch University http://scholar.sun.ac.za

$$\begin{aligned}\vec{\mathbf{V}}_{(c)}^{s} &= \vec{\mathbf{V}}_{(c)} - \vec{\mathbf{V}}_{(c)}^{n} \\ &= \vec{\mathbf{V}}_{(c)} - \left(\vec{\mathbf{V}}_{(c)} \cdot \vec{\mathbf{n}}\right)\vec{\mathbf{n}}\end{aligned} \tag{B.32}$$

where $\vec{\mathbf{V}}_{(c)}^{s}$ and $\vec{\mathbf{V}}_{(c)}^{n}$ are the shear and normal velocity components respectively. The increment in relative tangential displacement causes an increment in shear force proportional to the shear stiffness. The shear contact displacement-increment vector occurring over a time step of Δt is calculated by

$$\Delta\vec{\mathbf{U}}^{s} = \vec{\mathbf{V}}_{(c)}^{s}\Delta t \tag{B.33}$$

The shear force-increment vector is given by

$$\Delta\vec{\mathbf{F}}_{(c)}^{s} = -K_{s}\Delta\vec{\mathbf{U}}^{s} \tag{B.34}$$

The new shear force is found by summing the old shear force vector existing at the start of the time step with the shear force-increment vector

$$\vec{\mathbf{F}}_{(c)}^{s} \leftarrow \vec{\mathbf{F}}_{(c)}^{s} + \Delta\vec{\mathbf{F}}_{(c)}^{s} \tag{B.35}$$

The contact forces that act on each of the two entities are now given by

$$\vec{\mathbf{F}}_{(i)}^{n} = -\vec{\mathbf{F}}_{(c)}^{n} = -K_{n}U^{n}\vec{\mathbf{n}} \tag{B.36}$$

$$\vec{\mathbf{F}}_{(j)}^{n} = \vec{\mathbf{F}}_{(c)}^{n} = K_{n}U^{n}\vec{\mathbf{n}} \tag{B.37}$$

$$\vec{\mathbf{F}}_{(i)}^{s} = -\vec{\mathbf{F}}_{(c)}^{s} \tag{B.38}$$

$$\vec{\mathbf{F}}_{(j)}^{s} = \vec{\mathbf{F}}_{(c)}^{s} \tag{B.39}$$

where $\vec{\mathbf{F}}_{(i)}^{n}$ and $\vec{\mathbf{F}}_{(i)}^{s}$ are the contact normal and tangential forces acting on particle i and $\vec{\mathbf{F}}_{(c)}^{s}$ is given by Eq. B.35.

Stellenbosch University http://scholar.sun.ac.za

By combining Eq. B.36 to Eq. B.39, the total force acting on each entity due to the contact is given by

$$\vec{\mathbf{F}}_{(i)} = -\left(\vec{\mathbf{F}}^{n}_{(c)} + \vec{\mathbf{F}}^{s}_{(c)}\right) \tag{B.40}$$

$$\vec{\mathbf{F}}_{(j)} = \vec{\mathbf{F}}^{n}_{(c)} + \vec{\mathbf{F}}^{s}_{(c)} \tag{B.41}$$

The moments acting on the entities due to contact forces are given by

$$\vec{\mathbf{M}}_{(i)} = -\left(\vec{\mathbf{r}}_{(c)} - \vec{\mathbf{r}}_{(i)}\right) \times \vec{\mathbf{F}}^{s}_{(c)} \tag{B.42}$$

$$\vec{\mathbf{M}}_{(j)} = \left(\vec{\mathbf{r}}_{(c)} - \vec{\mathbf{r}}_{(j)}\right) \times \vec{\mathbf{F}}^{s}_{(c)} \tag{B.43}$$

Equations (B.40) to (B.43) give the contact force and moment acting on particles *i* and *j*. For particle-wall contact all equations are valid for particle *i* while the motion of the wall is not influenced by the contact forces.

B.2.4 The Law of Motion

The motion of a particle can be determined if the resultant force and moment vectors acting on the particle are known. Since the particles are assumed to be rigid, the motion can be described in terms of the translational motion of a point (particle centre of mass) and the rotational motion of the particle. The equations of motion can be expressed as two vector equations, one relating the resultant force to the translational motion and the other relating the resultant moment to the rotational motion. The translational equation of motion (Eq. B.19) for particle *i*, in physical vector form, is

$$\vec{\mathbf{F}}_{(i)} = m_{(i)}\left(\ddot{\vec{\mathbf{r}}}_{(i)} - \vec{\mathbf{g}}\right) \tag{B.44}$$

or in terms of reference system *s*

$$\overline{\mathbf{F}}^{s}_{(i)} = m_{(i)}\left(\ddot{\overline{\mathbf{r}}}^{s}_{(i)} - \overline{\mathbf{g}}^{s}\right) \tag{B.45}$$

Stellenbosch University http://scholar.sun.ac.za

It is possible for a particle to have contact with more then one particle and/or wall. If this is true, Eq. B.40 to B.43 must be applied to each contact and the contact forces and moments must be summed to obtain the resultant contact force and moment acting on the particle. Since the gravitational field is incorporated into Eq. B.44, the only other force that can act on an entity is the total contact force (vector sum of all the contact forces acting on the entity). This means that the resultant force term in Eq. B.44, $\vec{\mathbf{F}}_{(i)}$, is equal to the total contact force.

The equation for rotational motion is given by Eq. B.23 in terms of the reference system *s*. It is repeated here for particle *i*.

$$\begin{aligned}\overline{\mathbf{M}}^{s}_{(i)} = \dot{\overline{\mathbf{h}}}^{s}_{(i)} &= \underline{\overline{\mathbf{J}_{(i)}}}^{s}_{s}\,\dot{\overline{\boldsymbol{\omega}}}^{s}_{(i)} + \underline{\tilde{\overline{\boldsymbol{\omega}}}_{(i)}}^{s}_{s}\,\underline{\overline{\mathbf{J}_{(i)}}}^{s}_{s}\,\overline{\boldsymbol{\omega}}^{s}_{(i)} \\ &= \left[\underline{\overline{\mathbf{E}}}^{s}_{b}\,\underline{\overline{\mathbf{J}_{(i)}}}^{b}_{b}\,\underline{\overline{\mathbf{E}}}^{b}_{s}\right]\dot{\overline{\boldsymbol{\omega}}}^{s}_{(i)} + \underline{\tilde{\overline{\boldsymbol{\omega}}}_{(i)}}^{s}_{s}\left[\underline{\overline{\mathbf{E}}}^{s}_{b}\,\underline{\overline{\mathbf{J}_{(i)}}}^{b}_{b}\,\underline{\overline{\mathbf{E}}}^{b}_{s}\right]\overline{\boldsymbol{\omega}}^{s}_{(i)}\end{aligned} \tag{B.23}$$

During numeric integration it becomes necessary to do a transformation of the *inertia tensor*

$$\underline{\overline{\mathbf{J}}}^{s}_{s} = \underline{\overline{\mathbf{E}}}^{s}_{b}\,\underline{\overline{\mathbf{J}}}^{b}_{b}\,\underline{\overline{\mathbf{E}}}^{b}_{s} \tag{B.46}$$

since $\dot{\underline{\overline{\mathbf{J}}}}^{b}_{b} = \underline{\overline{\mathbf{0}}}$ and $\dot{\underline{\overline{\mathbf{J}}}}^{s}_{s} \neq \underline{\overline{\mathbf{0}}}$. The translational equation of motion, Eq. B.45 doesn't pose this problem.

An alternative way is to solve the rotational equation of motion in terms of reference system *b*. Working in reference system *b* eliminates the transformation of the *inertia tensor* (Eq. B.46) but, in the general three-dimensional case, the rotations obtained from integrating the rotational equation does not correspond to any physical angles which might be used to give the orientation of the body.

Stellenbosch University http://scholar.sun.ac.za

In terms of the body fixed system b, the rotational equation of motion then becomes

$$\overline{\mathbf{M}}^{b}_{(i)} = \dot{\overline{\mathbf{h}}}^{b}_{(i)} = \underline{\overline{\mathbf{J}_{(i)}}}^{b}_{b}\,\dot{\overline{\boldsymbol{\omega}}}^{b}_{(i)} + \underline{\tilde{\overline{\boldsymbol{\omega}}}_{(i)}}^{b}_{b}\,\underline{\overline{\mathbf{J}_{(i)}}}^{b}_{b}\,\overline{\boldsymbol{\omega}}^{b}_{(i)} \tag{B.47}$$

Expanding this equation into matrix notation and writing down each component gives:

$$\begin{aligned}
M^{b}_{(i)1} &= J^{b}_{(i)11}\dot{\omega}^{b}_{(i)1} + J^{b}_{(i)12}\left(\dot{\omega}^{b}_{(i)2} - \omega^{b}_{(i)1}\omega^{b}_{(i)3}\right) + J^{b}_{(i)13}\left(\dot{\omega}^{b}_{(i)3} - \omega^{b}_{(i)1}\omega^{b}_{(i)2}\right) \\
&\quad + \left(J^{b}_{(i)33} - J^{b}_{(i)22}\right)\omega^{b}_{(i)2}\omega^{b}_{(i)3} + J^{b}_{(i)23}\left[(\omega^{b}_{(i)2})^2 - (\omega^{b}_{(i)3})^2\right] \\
M^{b}_{(i)2} &= J^{b}_{(i)12}\left(\dot{\omega}^{b}_{(i)1} + \omega^{b}_{(i)2}\omega^{b}_{(i)3}\right) + J^{b}_{(i)22}\dot{\omega}^{b}_{(i)2} + J^{b}_{(i)23}\left(\dot{\omega}^{b}_{(i)3} - \omega^{b}_{(i)1}\omega^{b}_{(i)2}\right) \\
&\quad + \left(J^{b}_{(i)11} - J^{b}_{(i)33}\right)\omega^{b}_{(i)1}\omega^{b}_{(i)3} + J^{b}_{(i)13}\left[(\omega^{b}_{(i)3})^2 - (\omega^{b}_{(i)1})^2\right] \\
M^{b}_{(i)3} &= J^{b}_{(i)13}\left(\dot{\omega}^{b}_{(i)1} - \omega^{b}_{(i)2}\omega^{b}_{(i)3}\right) + J^{b}_{(i)23}\left(\dot{\omega}^{b}_{(i)2} + \omega^{b}_{(i)1}\omega^{b}_{(i)3}\right) + J^{b}_{(i)33}\dot{\omega}^{b}_{(i)3} \\
&\quad + \left(J^{b}_{(i)22} - J^{b}_{(i)11}\right)\omega^{b}_{(i)1}\omega^{b}_{(i)2} + J_{12}\left[(\omega^{b}_{(i)1})^2 - (\omega^{b}_{(i)2})^2\right]
\end{aligned} \tag{B.48}$$

Note that $J_{ij} = J_{ji}$. A considerable simplification can be made if the reference system b is chosen such that they are principal axes at the centre of mass. All the products of inertia vanish and Eq. B.48 reduce to:

$$\begin{aligned}
M^{b}_{(i)1} &= J^{b}_{(i)11}\dot{\omega}^{b}_{(i)1} + \left(J^{b}_{(i)33} - J^{b}_{(i)22}\right)\omega^{b}_{(i)2}\omega^{b}_{(i)3} \\
M^{b}_{(i)2} &= J^{b}_{(i)22}\dot{\omega}^{b}_{(i)2} + \left(J^{b}_{(i)11} - J^{b}_{(i)33}\right)\omega^{b}_{(i)1}\omega^{b}_{(i)3} \\
M^{b}_{(i)3} &= J^{b}_{(i)33}\dot{\omega}^{b}_{(i)3} + \left(J^{b}_{(i)22} - J^{b}_{(i)11}\right)\omega^{b}_{(i)1}\omega^{b}_{(i)2}
\end{aligned} \tag{B.49}$$

Assuming a two-dimensional environment, $M^{b}_{(i)1} = M^{b}_{(i)2} = 0$ and only the last equation in Eq. B.49 remains. For spheres and disks, the centre of mass coincides with the sphere or disk centre. For a spherical particle, any local reference system attached to the particle's centre of mass is a principal-axis system and the three principal moments of inertia are equal to one another. For a disk-shaped particle whose axis remains in the out-of-plane direction (in this case, direction s_3), $\omega^{b}_{(i)1} = \omega^{b}_{(i)2} = 0$. Thus by using either

Stellenbosch University http://scholar.sun.ac.za

a sphere or a disk, the term $\left(J^b_{(i)22} - J^b_{(i)11}\right)\omega^b_{(i)1}\omega^b_{(i)2}$ in the remaining Eq. B.49 vanishes, leading to $M^b_{(i)3} = J^b_{(i)33}\dot{\omega}^b_{(i)3}$.

The transformation matrix between the s and b reference systems, for the two-dimensional case, is

$$\underline{\overline{\mathbf{E}}}^s_b = \begin{bmatrix} \cos(\theta) & -\sin(\theta) & 0 \\ \sin(\theta) & \cos(\theta) & 0 \\ 0 & 0 & 1 \end{bmatrix}$$

Using this transformation matrix, it can easily be shown that $\omega^s_{(i)3} = \omega^b_{(i)3}$ and $M^s_{(i)3} = M^b_{(i)3}$. Using these two relations the final rotational equation of motion can be written as

$$M^s_{(i)3} = J^b_{(i)33}\dot{\omega}^s_{(i)3} \tag{B.50}$$

where $J^b_{(i)33}$ is constant and $M^s_{(i)3}$ and $\dot{\omega}^s_{(i)3}$ can easily be interpreted.

B.2.5 The Integration Scheme

The equations of motion, given by Eqs. B.45 and B.50, are both in terms of the global-axis system s and can be integrated using a centred finite-difference procedure involving a time step of $\triangle t$. This integration scheme can be shown to have an accuracy of order $O(\triangle t)^2$. The quantities $\dot{\vec{\mathbf{r}}}_{(i)}$ and ω_3 (applicable to every particle) are computed at the mid-intervals of $t \pm n\Delta t/2$ while the quantities $\vec{\mathbf{r}}_{(i)}, \ddot{\vec{\mathbf{r}}}_{(i)}, \dot{\omega}_{(i)3}, \vec{\mathbf{F}}_{(i)}$ and $\mathbf{M}_{(i)3}$ are computed at the primary intervals of $t \pm n\Delta t$.

Stellenbosch University http://scholar.sun.ac.za

The accelerations are calculated as

$$\ddot{\vec{\mathbf{r}}}_{(i)}(t) = \frac{1}{\Delta t}\left[\dot{\vec{\mathbf{r}}}_{(i)}(t + \Delta t/2) - \dot{\vec{\mathbf{r}}}_{(i)}(t - \Delta t/2)\right] \tag{B.51}$$

$$\dot{\omega}_{(i)_3}(t) = \frac{1}{\Delta t}\left[\omega_{(i)_3}(t + \Delta t/2) - \omega_{(i)_3}(t - \Delta t/2)\right] \tag{B.52}$$

Inserting these expressions into Eq. B.45 and Eq. B.50 and solving for the velocities at time $(t + \Delta t/2)$ results in

$$\dot{\vec{\mathbf{r}}}_{(i)}(t + \Delta t/2) = \dot{\vec{\mathbf{r}}}_{(i)}(t - \Delta t/2) + \left(\frac{\vec{\mathbf{F}}_{(i)}(t)}{m_{(i)}} + \vec{\mathbf{g}}\right)\Delta t \tag{B.53}$$

$$\omega_{(i)_3}(t + \Delta t/2) = \omega_{(i)_3}(t - \Delta t/2) + \left(\frac{M_{(i)_3}(t)}{J_{(i)_{33}}}\right)\Delta t \tag{B.54}$$

The position of each particle centre is updated using Eq. B.53.

$$\vec{\mathbf{r}}_{(i)}(t + \Delta t) = \vec{\mathbf{r}}_{(i)}(t) + \dot{\vec{\mathbf{r}}}_{(i)}(t + \Delta t/2)\Delta t \tag{B.55}$$

In summary, the calculation cycle for the law of motion is as follows. Given the values of $\dot{\vec{\mathbf{r}}}_{(i)}(t - \Delta t/2)$, $\omega_{(i)_3}(t - \Delta t/2)$, $\vec{\mathbf{r}}_{(i)}(t)$, $\vec{\mathbf{F}}_{(i)}(t)$ and $M_{(i)_3}(t)$, Eq. B.53 and Eq. B.54 are used to obtain $\dot{\vec{\mathbf{r}}}_{(i)}(t + \Delta t/2)$ and $\omega_{(i)_3}(t + \Delta t/2)$. Then Eq. B.55 is used to obtain $\vec{\mathbf{r}}_{(i)}(t + \Delta t)$. The values of $\vec{\mathbf{F}}_{(i)}(t + \Delta t)$ and $M_{(i)_3}(t + \Delta t)$, to be used in the next cycle, are obtained by application of the force-displacement law. Note that with $\dot{\vec{\mathbf{r}}}_{(i)}$ only known at $t \pm \Delta t/2$, makes it impossible to use viscous damping without decreasing the order of accuracy.

The solution of these equations will only be stable if the time step does not exceed a critical time step that is related to the minimum eigenperiod of the total system.

Stellenbosch University http://scholar.sun.ac.za

However, it is impractical to apply an eigenvalue analysis to a large, constantly changing system. The following simplified method can be employed.

First consider a one-dimensional single mass-spring system as in Fig. B.6.

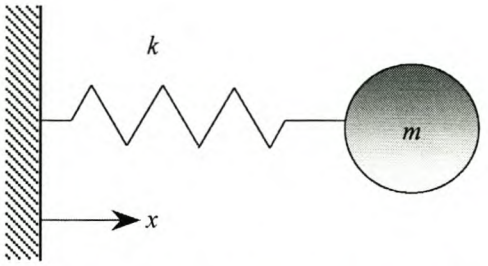

Figure B.6 - *Single Mass-Spring System*

The governing differential equation for the motion of the mass is given by

$$-k\,x = m\,\ddot{x} \tag{B.56}$$

where k is the spring stiffness and m the body's mass. The critical time step corresponding to a second-order finite-difference scheme for this equation is given by Bathe (1976):

$$t_{crit} = \frac{T}{\pi} = \frac{2\pi\sqrt{\left(m/k\right)}}{\pi} = 2\sqrt{\left(m/k\right)} \tag{B.57}$$

where T is the period of the system. For a series of masses and springs, as in Fig. B.7(a), the smallest period occurs when the masses are moving in synchronised opposing motion such that there is no motion at the centre of each spring. The motion of one of the masses can be described by the two equivalent systems shown in Fig. B.7(b) and B.7(c). The critical time step for this system is found to be

$$t_{crit} = 2\sqrt{m/(4k)} = \sqrt{m/(k)} \tag{B.58}$$

This can be used to determine the critical timesep for a DEM model. For a generalised multi mass-spring system it can be expressed as follows.

Stellenbosch University http://scholar.sun.ac.za

$$t_{crit} = \sqrt{m/k^{tran}} \quad \text{for translational motion and}$$

$$t_{crit} = \sqrt{J/k^{rot}} \quad \text{for rotational motion} \tag{B.59}$$

where k^{tran} and k^{rot} are the translational and rotational stiffness respectively and J is the moment of inertia of the particle.

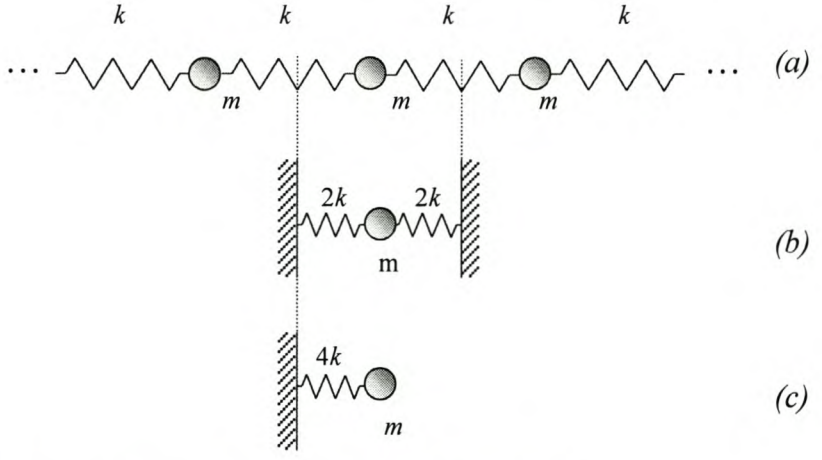

Figure B.7 - *Multiple Mass-Spring System*

A critical time step is found for each particle by applying Eq. B.59 separately to each degree-of-freedom and assuming that the degrees-of-freedom are uncoupled. The stiffness is estimated by summing the contribution from all contacts. The final critical time step is taken to be the minimum of all timesteps. The relation between force and displacement for a two-dimensional DEM system can be written as:

$$\begin{bmatrix} \Delta F_1 \\ \Delta F_2 \\ \Delta M_3 \end{bmatrix} = \begin{bmatrix} k_{11} & k_{12} & 0 \\ k_{21} & k_{22} & 0 \\ 0 & 0 & k_{33} \end{bmatrix} \begin{bmatrix} \Delta U_1 \\ \Delta U_2 \\ \Delta \theta_3 \end{bmatrix} \tag{B.60}$$

The elements of this stiffness matrix can be expressed for a particular contact in terms of the particle radius R, the contact normal vector $\vec{\mathbf{n}}$ and the contact stiffness K_n and K_s. The translational stiffness terms can be found by writing the contact force as the sum of its normal and shear components.

Stellenbosch University http://scholar.sun.ac.za

$$\begin{aligned}\Delta\vec{\mathbf{F}}_{(c)} &= \Delta\vec{\mathbf{F}}^{n}_{(c)} + \Delta\vec{\mathbf{F}}^{s}_{(c)} \\ &= K_n \Delta\vec{\mathbf{U}}^{n} + K_s \Delta\vec{\mathbf{U}}^{s} \\ &= K_n \left(\Delta U^{n}\vec{\mathbf{n}}\right) + K_s \left(\Delta\vec{\mathbf{U}} - \Delta U^{n}\vec{\mathbf{n}}\right) \\ &= \left(K_n - K_s\right)\vec{\mathbf{n}}\,\Delta U^{n} + K_s \Delta\vec{\mathbf{U}} \\ &= \left(K_n - K_s\right)\vec{\mathbf{n}}\left(\Delta\vec{\mathbf{U}}\cdot\vec{\mathbf{n}}\right) + K_s \Delta\vec{\mathbf{U}}\end{aligned} \tag{B.61}$$

Note that the subscript *(c)* refers to the fact that the force is acting at a contact and $\vec{\mathbf{n}}$ is again the contact normal vector. The rotational stiffness term is found by writing the moment-increment as a cross product of the radius vector $R\vec{\mathbf{n}}$ with the shear component of the contact force.

$$\begin{aligned}\Delta\vec{\mathbf{M}} &= R\vec{\mathbf{n}} \times \Delta\vec{\mathbf{F}}^{s} \\ &= R\vec{\mathbf{n}} \times \left(K_s \Delta\vec{\mathbf{U}}^{s}\right)\end{aligned} \tag{B.62}$$

The shear increment can be written as:

$$\Delta\vec{\mathbf{U}}^{s} = \Delta\vec{\theta} \times \left(R\vec{\mathbf{n}}\right) \tag{B.63}$$

Substituting Eq. B.63 into Eq. B.62 yields the final result.

$$\Delta\vec{\mathbf{M}} = R^2 K_s \Delta\vec{\theta} \tag{B.64}$$

The stiffness in Eq. B.59 is approximated by the diagonal terms of Eq. B.60. By comparing Eqs. B.61 and B.64 to Eq. B.60, the translational and rotational stiffness terms are found to be

$$\begin{aligned}k_{11} &= \left(K_n - K_s\right)n_1^2 + K_s \\ k_{22} &= \left(K_n - K_s\right)n_2^2 + K_s \\ k_{33} &= R^2 K_s\end{aligned} \tag{B.65}$$

where n_1 and n_2 are the two components of the contact normal vector $\vec{\mathbf{n}}$.

Stellenbosch University http://scholar.sun.ac.za

B.2.6 Mechanical Damping

Energy supplied to the system is dissipated through frictional sliding. However, frictional sliding may not be active in a given model or may not be sufficient to arrive at a steady-state solution in a reasonable number of cycles. The PFC^{2D} model has non-viscous damping available to dissipate energy by damping the equations of motion.

A damping-force term is added to the equations of motion, given by Eq. B.44 and Eq. B.47. The damped equations of motion can be written for particle i (in the general three-dimensional case).

$$\vec{\mathbf{F}}_{(i)} + m\vec{\mathbf{g}} + \vec{\mathbf{F}}_{(i)}^{damp} = m_{(i)}\ddot{\vec{\mathbf{r}}}_{(i)} \tag{B.66}$$

$$\vec{\mathbf{M}}_{(i)} + \vec{\mathbf{M}}_{(i)}^{damp} = \dot{\vec{\mathbf{h}}}_{(i)} = \underrightarrow{\mathbf{J}}_{(i)}\dot{\vec{\omega}}_{(i)} + \vec{\omega}_{(i)} \times \underrightarrow{\mathbf{J}}_{(i)}\vec{\omega}_{(i)} \tag{B.67}$$

The damping force and moment are defined as:

$$\vec{\mathbf{F}}_{(i)}^{damp} = -\alpha \begin{bmatrix} \left|F_{(i)_1} + m_{(i)}g_1\right| sign\left(\dot{r}_{(i)_1}\right) \\ \left|F_{(i)_2} + m_{(i)}g_2\right| sign\left(\dot{r}_{(i)_2}\right) \end{bmatrix} \tag{B.68}$$

$$M_{(i)_3}^{damp} = -\alpha \left|M_{(i)_3}\right| sign\left(\omega_{(i)_3}\right) \tag{B.69}$$

where $sign(y) = \begin{cases} +1 & \text{for} \quad y > 0 \\ -1 & \text{for} \quad y < 0 \\ 0 & \text{for} \quad y = 0 \end{cases}$

This form of damping has the following advantages.

1. Only accelerating motion is damped.
2. The damping constant α is non-dimensional
3. Since the damping is frequency-independent, regions of the assembly with different natural periods are all damped equally.

Stellenbosch University http://scholar.sun.ac.za

The purpose of damping is to reach a steady state initial condition. Damping is also needed during the physical contacts of particles to account for inelasticity of the collision. In this instance the standard damping of PFC^{2D} can not be used and additional damping terms must be added to the existing constitutive law. The standard method can, however, be used with caution.

B.3 PFC^{2D} Contact Constitutive Models

The overall constitutive behaviour of a material is simulated by associating a simple constitutive model with each contact. In general, a constitutive model can be divided into three parts: a stiffness model, a slip model and a bonding model. The stiffness model provides an elastic relation between the contact force and the relative displacement. The slip model allows the particles to slip relative to each other and the bonding model serves to limit the total normal and shear forces that the contact can handle by enforcing bond-strength limits.

First we look at the two stiffness models used in PFC^{2D} (Itasca 1999): a simple linear model and the Hertz-Mindlin model.

B.3.1 The Linear Contact Model

The contact stiffness relates the contact force and the relative displacement. The normal stiffness is a secant stiffness since it relates the total normal force to the total normal displacement. The shear stiffness is a tangent stiffness since it relates the increment in shear force to the increment in shear displacement. The force-displacement relations are given by Eq. B.30 and Eq. B.34, which is repeated here.

$$\vec{\mathbf{F}}^{n}_{(c)} = K_n U^n \vec{\mathbf{n}} \tag{B.70}$$

$$\Delta\vec{\mathbf{F}}^{s}_{(c)} = -K_s \Delta\vec{\mathbf{U}}^{s} \tag{B.71}$$

Stellenbosch University http://scholar.sun.ac.za

The linear contact model is shown in Fig. B.8 and is defined by the normal and shear stiffness k_n and k_s for the two contacting entities i and j.

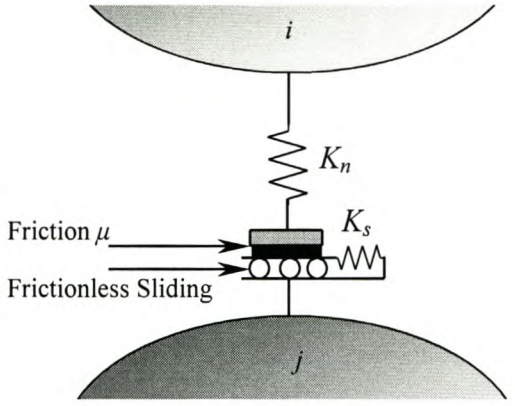

Figure B.8 - *Linear Contact Model*

The contact stiffness is computed assuming that the stiffness of the two entities acts in series. The contact normal stiffness is given by

$$K_n = \frac{k_{n(i)} k_{n(j)}}{k_{n(i)} + k_{n(j)}} \tag{B.72}$$

and the contact shear stiffness is given by

$$K_s = \frac{k_{s(i)} k_{s(j)}}{k_{s(i)} + k_{s(j)}} \tag{B.73}$$

Note that the secant and tangent stiffness is the same in a linear model.

B.3.2 The Hertz-Mindlin Contact Model

The classical theory of impact between frictionless elastic bodies is due to Hertz and follows directly from his static theory of elastic contact. Elastic wave motion in the bodies is ignored and the total mass of each body is assumed to be moving at any instant with the velocity of its centre of mass.

Stellenbosch University http://scholar.sun.ac.za

The Hertz-Mindlin model makes use of normal and shear stiffness and is defined by the following two parameters: shear modulus G and Poisson's ratio v of the two contacting spheres. The secant normal stiffness is given by

$$K_n = \left(\frac{2\widetilde{G}\sqrt{2\widetilde{R}}}{3(1-\widetilde{v})} \right) \sqrt{U^n} \tag{B.74}$$

and the shear tangent stiffness is given by

$$K_s = \left(\frac{2\left(\widetilde{G}^2 3(1-\widetilde{v})\widetilde{R}\right)^{1/3}}{2-\widetilde{v}} \right) \left| \vec{\mathbf{F}}^n_{(c)} \right|^{1/3} \tag{B.75}$$

where U^n is the sphere overlap and $\left|\vec{\mathbf{F}}^n_{(c)}\right|$ is the magnitude of the contact normal force. For a particle-particle contact we have the following relations

$$\widetilde{R} = \frac{2R_{(i)}R_{(j)}}{R_{(i)} + R_{(j)}}$$

$$\widetilde{G} = \tfrac{1}{2}\left(G_{(i)} + G_{(j)}\right) \qquad \text{(particle-particle)} \tag{B.76}$$

$$\widetilde{v} = \tfrac{1}{2}\left(v_{(i)} + v_{(j)}\right)$$

where the indices i and j indicate particle i and j respectively and R is the radius of the sphere. For a particle-wall contact PFC^{2D} assumes (Itasca 1999)

$$\widetilde{R} = R_{(i)}$$

$$\widetilde{G} = G_{(i)} \tag{B.77}$$

$$\widetilde{v} = v_{(i)}$$

where the index i refers to the particle as in Fig. B.4.

Stellenbosch University http://scholar.sun.ac.za

For a detail description of the Hertz model see Johnson (1987) and for the application of this model see Falcon (1998) and Schafer (1995).

B.3.3 The Slip Model

This model allows slip to occur between two entities in contact by limiting the shear force and is defined by the friction coefficient at the contact μ, where μ is taken to be the minimum friction coefficient of the two contacting entities. The contact is checked for slip conditions by calculating the maximum allowable shear contact force.

$$F_{slip}^{s} = \mu \left| \vec{\mathbf{F}}_{(c)}^{n} \right| \tag{B.78}$$

If $\left| \vec{\mathbf{F}}_{(c)}^{s} \right| > F_{slip}^{s}$, slip is allowed to occur by setting the magnitude of $\vec{\mathbf{F}}_{(c)}^{s}$ equal to F_{slip}^{s}.

B.3.4 The Bonding Models

PFC^{2D} allows particles to be bonded together at contacts. A contact-bond and a parallel-bond model are available. Both models can be visualised as if the particles are "glued" together. The contact-bond glue is of vanishingly small size that acts only at the contact point, while the parallel-bond glue is of a finite size that acts over either a circular or rectangular cross-section lying between the particles. The contact bond can only transmit a force, while the parallel bond can transmit both a force and a moment.

B.3.4.1 The Contact-Bond Model

A contact bond is defined by the following two parameters: normal contact bond strength F_{con}^{n} and a shear contact bond strength F_{con}^{s}.

The existence of a contact bond precludes the possibility of slip; i.e. the magnitude of the shear contact force is not adjusted to remain less than the allowable maximum of Eq. B.78. Instead, the magnitude of the shear contact force is limited by the shear

Stellenbosch University http://scholar.sun.ac.za

contact bond strength and bonds also allow tensile forces to develop at a contact. If the magnitude of the tensile normal contact force equals or exceeds the normal contact bond strength, the bond breaks, and both the normal and shear contact forces are set to zero. If the magnitude of the shear contact force equals or exceeds the shear contact bond strength, the bond breaks, but the contact forces are not altered, provided that the shear force does not exceed the friction (slip) limit.

Figure B.9 shows the constitutive behaviour in both the normal and shear contact directions. Note that either the contact-bond or the slip model is active. The figure shows $F^s_{con} > F^s_{slip}$, so if the bond breaks due to the fact that the shear contact bond strength has been exceeded, the value of the contact shear force will be changed to the value of the friction limit F^s_{slip}. If, however, $F^s_{con} < F^s_{slip}$ the value of the contact shear force will not be changed when the bond breaks.

Stellenbosch University http://scholar.sun.ac.za

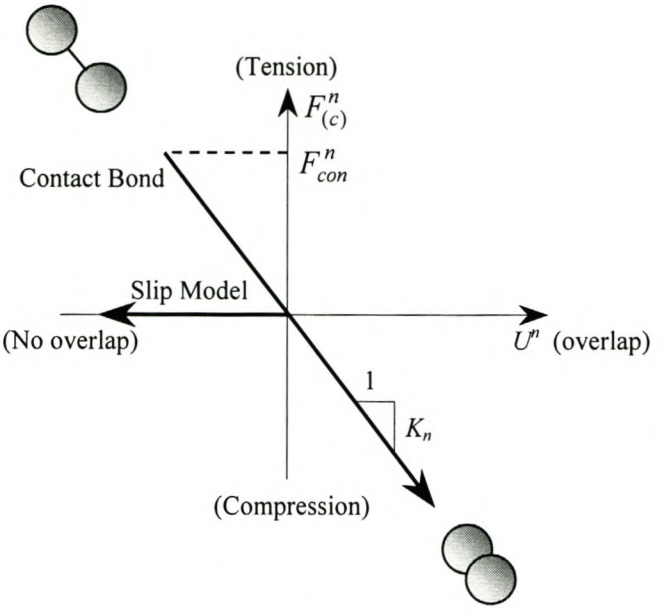

Normal Contact Force

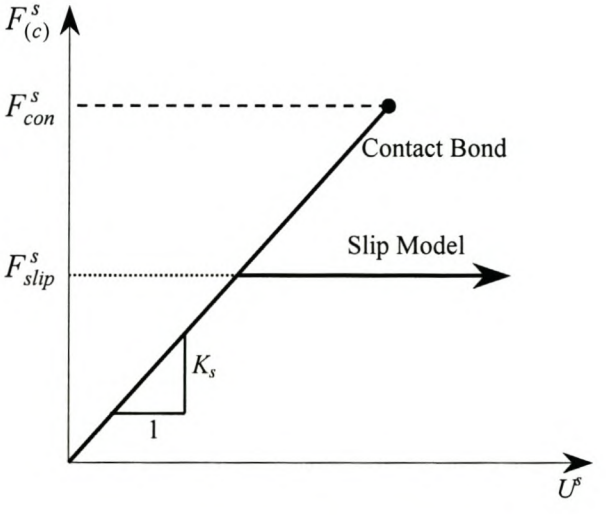

Shear Contact Force

Figure B.9 - *The Contact-Bond Model*

B.3.4.2 The Parallel-Bond Model

A parallel bond can be envisioned as a set of elastic springs with constant normal and shear stiffness, uniformly distributed over either a circular or rectangular cross-section lying on the contact plane and centred at the contact point. Relative motion at the contact causes a force and moment to develop within the bond material. This force and

Stellenbosch University http://scholar.sun.ac.za

moment act on the two bonded particles and can be related to maximum normal and shear stresses acting within the bond material at the bond periphery. If either of these maximum stresses exceeds its corresponding bond strength, the parallel bond breaks.

A parallel bond is defined by the following five parameters: normal and shear stiffness $k^n_{(p)}$ and $k^s_{(p)}$ (where the subscript p refers to the parallel bond), normal and shear strength $\sigma_{(p)}$ and $\tau_{(p)}$, and bond radius $R_{(p)}$.

The total force and moment associated with the parallel bond are denoted by $\vec{\mathbf{F}}_{(p)}$ and $M_{(p)3}$, with the convention that this force and moment represent the action of the bond on particle j in Fig. B.10. Note that the moment is not a vector, but only the component of the moment vector in the out-of-plane direction.

The force vector can be resolved into a normal and shear component.

$$\vec{\mathbf{F}}_{(p)} = \vec{\mathbf{F}}^n_{(p)} + \vec{\mathbf{F}}^s_{(p)} \tag{B.79}$$

These vectors and the moment are shown in the figure, where the bond is depicted as a finite-sized piece of elastic material. The normal force component vector can be expressed in terms of the scalar value $F^n_{(p)}$

$$\vec{\mathbf{F}}^n_{(p)} = F^n_{(p)}\vec{\mathbf{n}} \tag{B.80}$$

Stellenbosch University http://scholar.sun.ac.za

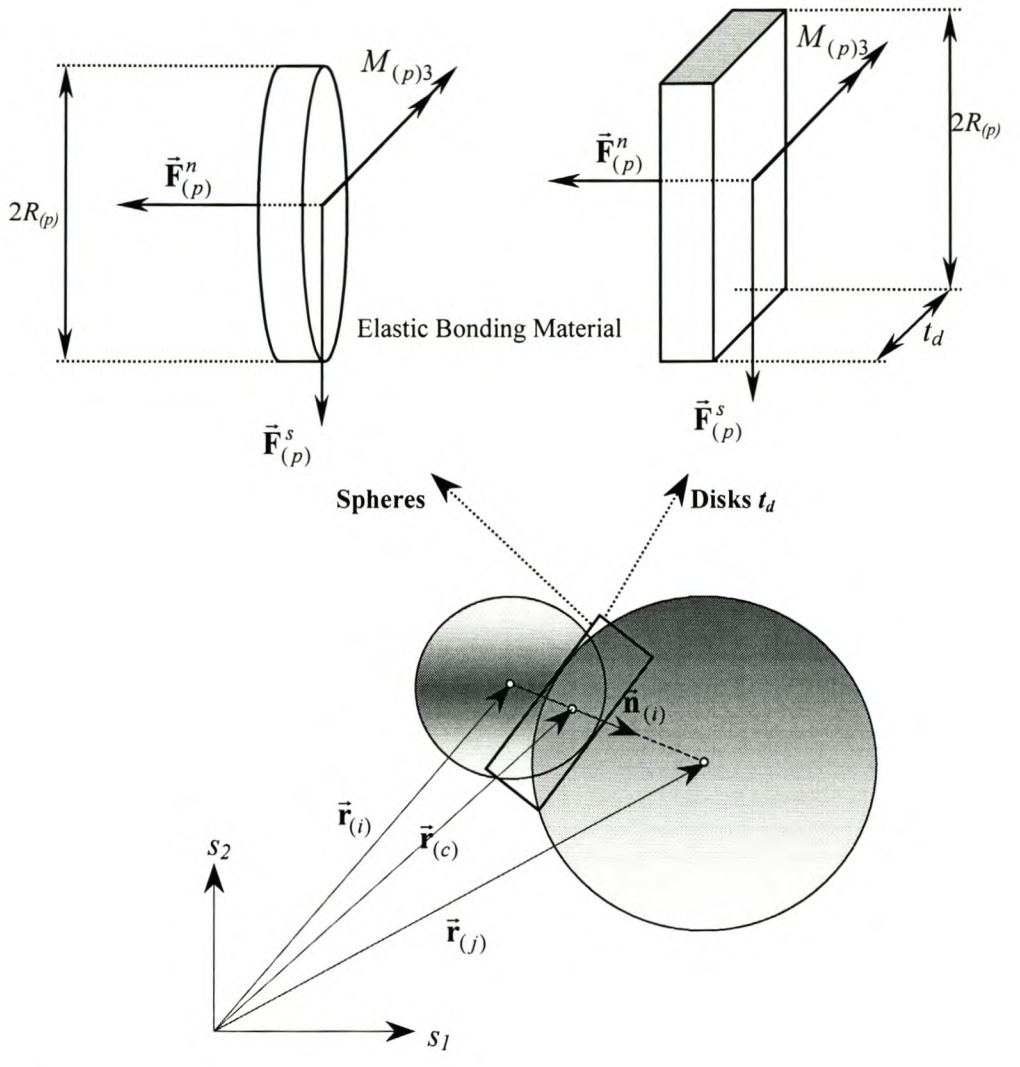

Figure B.10 – *The Parallel-Bond Model*

When the bond is formed, both the parallel bond force and moment are initialized to zero. Each subsequent relative displacement- and rotation-increment at the contact results in an increment of elastic force and moment that is added to the current values. The elastic force-increment occuring over a time step of Δt are calculated by

$$\Delta\vec{\mathbf{F}}^n_{(p)} = \left(-k^n_{(p)} A \Delta U^n\right)\vec{\mathbf{n}}$$
$$\Delta\vec{\mathbf{F}}^s_{(p)} = -k^s_{(p)} A \Delta\vec{\mathbf{U}}^s \tag{B.81}$$

with $\Delta\vec{\mathbf{U}} = \vec{\mathbf{V}}_{(c)}\Delta t$ and the elastic moment-increment by

$$\Delta M_{(p)3} = -k^n_{(p)} J_{(p)} \Delta\theta_3 \tag{B.82}$$

Stellenbosch University http://scholar.sun.ac.za

with $\Delta\theta_3 = (\omega_{(j)3} - \omega_{(i)3})\Delta t$. The contact velocity $\vec{\mathbf{V}}_{(c)}$ is given by Eq. B.31, A is the area of the bond cross-section and $J_{(p)}$ is the moment of inertia of the bond cross-section about an axis through the contact point and in the direction of $\Delta\theta_3$. These quantities are given by

$$A = \pi\left(R_{(p)}\right)^2 \quad \text{for spheres and } 2R_{(p)}t_d \text{ for a disk of thickness } t_d$$

$$J_{(p)} = \tfrac{1}{4}\pi\left(R_{(p)}\right)^4 \text{ for spheres and } \tfrac{2}{3}\left(R_{(p)}\right)^3 t_d \text{ for disks.} \tag{B.83}$$

The new force and moment vectors associated with the parallel bond are found by summing the old values existing at the start of the time step with the elastic force- and moment-increment vectors. The maximum tensile and shear stresses acting on the bond periphery are calculated, using beam theory, to be

$$\sigma_{(p)\max} = \frac{-F^n_{(p)}}{A} + \frac{\left|M_{(p)3}\right|}{J_{(p)}} R_{(p)}$$

$$\tau_{(p)\max} = \frac{\left|\vec{\mathbf{F}}^s_{(p)}\right|}{A} \tag{B.84}$$

If the maximum tensile stress exceeds the normal strength $\left(\sigma_{(p)\max} > \sigma_{(p)}\right)$ or the maximum shear stress exceeds the shear strength $\left(\tau_{(p)\max} > \tau_{(p)}\right)$, the parallel bond breaks. If the bond remains intact, the final force and moment vectors due to the bond are added to the contact forces and moments given by Eqs. B.40 to B.43.

Stellenbosch University http://scholar.sun.ac.za

B.4 Other Contact Constitutive Models

The above-described contact constitutive model is employed in PFC^{2D}. For a stiffness model either the linear or Hertz-Mindlin model is used. The slip model is always active and one of the contact-bond or parallel-bond models can be added. Other contact constitutive models have also been proposed by researchers and the remainder of this section will provide a brief introduction to these models.

Cundall (1979) proposed the model depicted in Fig. B.11. It looks very similar to the linear PFC^{2D} model (Fig. B.8), but there are some major differences. In both the contact normal and shear directions a damper has been added. These viscous dampers or dashpots contribute to the normal and shear contact force. Damping forces act only on the particles at contacts; this is very much different from the PFC^{2D} model where there is always a damping force acting on the particle as long as the resultant force on the particle is different from zero and the damping constant $\alpha \neq 0$.

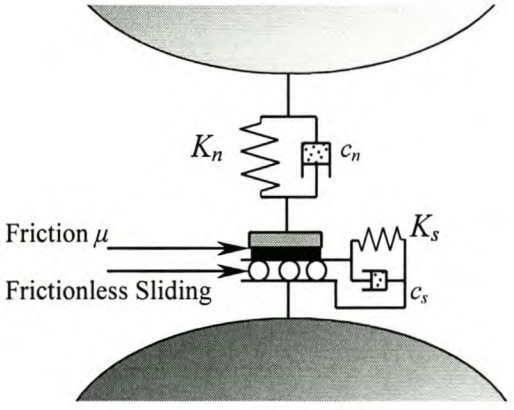

Figure B.11 - *Linear Contact Model with Dampers*

This way of viscous damping does, however, have two problems. It is possible for the resultant spring-dashpot force to be a tensile force at the end of the collision cycle. Usually this happens when the relative contact velocity (Eq. B.31) is so high that the magnitude of the viscous damping force is higher than the magnitude of the linear spring force. This has the effect that there is a tensile force between the two entities in

Stellenbosch University http://scholar.sun.ac.za

contact, which is physically not realistic for a cohesionless system. This problem can be overcome by simply breaking the contact if the normal contact force becomes tensile.

This damping model also has the effect that particle "softening" occurs when the two contacting entities moves away from each other while still in contact (unloading cycle). Experimental evidence, however, shows that the contact stiffness increases, so-called "hardening".

The slip part described in section B.3.3 is also applicable to this model. Although Cundall (1979) did not add any bond models to this proposed model, it will be possible to add the bond models from section B.3.4 to this model.

The next model, depicted in Fig. B.12, has been proposed by Walton (1986). The model makes use of a partially-latching-spring mechanism in the contact normal direction. The magnitude of the normal force is given by

$$F_{(c)}^{n} = K_1 U^{n} \qquad \text{for loading}$$

$$F_{(c)}^{n} = K_2 \left(U^{n} - U_0^{n} \right) \quad \text{for unloading} \tag{B.85}$$

where U^n is the overlap in the contact normal direction and U_0^n the value of U^n where the unloading curve goes to zero. This model corresponds to permanent or plastic deformation during a typical collision. Figure B.13 shows the contact constitutive model in the normal direction.

Stellenbosch University http://scholar.sun.ac.za

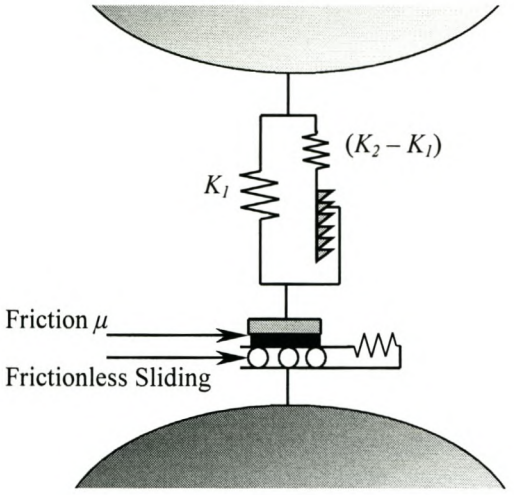

Figure B.12 – *Walton-Braun Model*

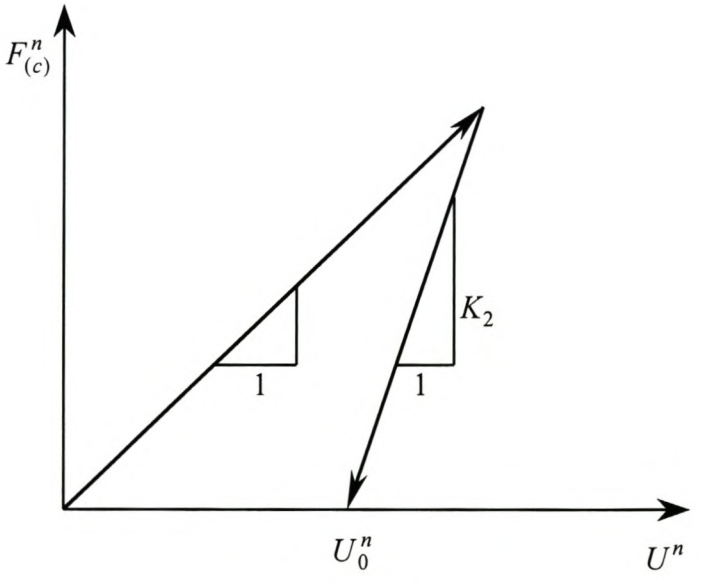

Figure B.13 - *Walton-Braun Constitutive Model*

A tangential spring stiffness K_T acts in the tangential direction. The model can be employed in two modes. In the constant coefficient of restitution mode, all the unloading lines have the same slope K_2. The restitution coefficient can be shown to be

$$e = \sqrt{\frac{K_1}{K_2}} \tag{B.86}$$

Stellenbosch University http://scholar.sun.ac.za

In the variable coefficient of restitution mode, the unloading slope K_2 is taken to be a linear function of the magnitude of the maximum normal force achieved before unloading.

$$K_2 = K_1 + SF^n_{(c)\max} \tag{B.87}$$

The corresponding restitution coefficient is

$$e = \left[\frac{\omega_0}{\left(SV^n_{(c)0} + \omega_0\right)}\right]^{\frac{1}{2}} \tag{B.88}$$

where $\omega_0 = \sqrt{\frac{K_1}{m_{red}}}$, $m_{red} = \frac{m_{(i)}m_{(j)}}{m_{(i)} + m_{(j)}}$ and $V^n_{(c)0}$ is the magnitude of the initial relative contact velocity (velocity of approach). The fact that the restitution coefficient is a function of the approach velocity has been experimentally confirmed by Walton (1986). This normal model gives the best description of elastic collisions as well as collisions where plastic deformation occurs.

Stellenbosch University http://scholar.sun.ac.za

APPENDIX C

SOIL MECHANICS SOLUTIONS

The plasticity theory is given in detail. The numeric solution procedure is discussed and an analytical solution of what is known as the Rankine state is given.

C.1 Solutions in Cartesian Coordinates

This formulation is based on Cartesian coordinates and follows the outline given in Chapter 2.

C.1.1 Stress Components at a Point

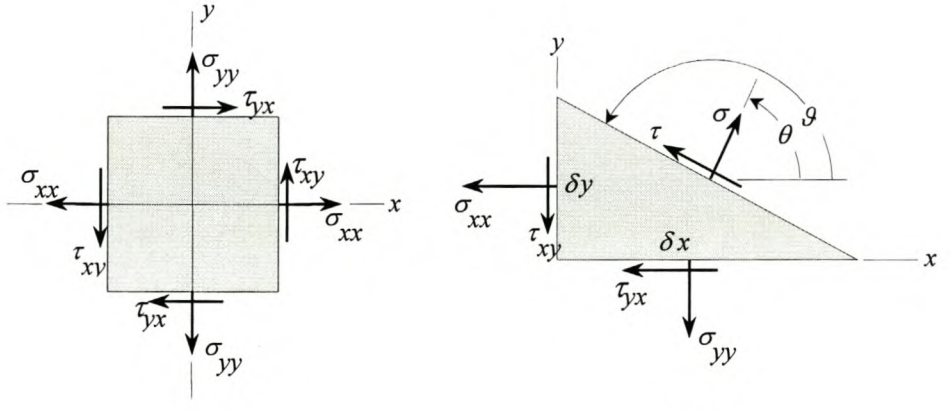

Figure C.1 – *Biaxial or plane stress*

Figure C.1(a) illustrates a state of biaxial or plane stress at a point. The outwardly directed normal or tensile stresses σ_{xx} and σ_{yy} on the element are defined as positive. The shear stresses τ_{xy} and τ_{yx} are defined positive on a face of an element if they act in the positive direction of the reference axis. Since the element is in static equilibrium, the negative faces will have shear stresses acting in the opposite direction, which are

Stellenbosch University http://scholar.sun.ac.za

also defined as positive. Because of static equilibrium, it follows for the shear stresses that

$$\tau_{xy} = \tau_{yx} \tag{C.1}$$

Consider the oblique plane in Fig. C.1(b) that cuts the stress element at an angle ϑ to the x-axis. Let θ be the angle from the x-axis to the normal to the plane. The relationship between the angles is

$$\vartheta = \theta + \frac{\pi}{2} \tag{C.2}$$

The normal and shear stresses on the oblique plane are obtained from equilibrium of forces. In terms of θ and ϑ ,these stresses follow as

$$\begin{aligned} \sigma &= \frac{\sigma_{xx}+\sigma_{yy}}{2} + \frac{\sigma_{xx}-\sigma_{yy}}{2}\cos(2\theta) + \tau_{xy}\sin(2\theta) \\ &= \frac{\sigma_{xx}+\sigma_{yy}}{2} - \frac{\sigma_{xx}-\sigma_{yy}}{2}\cos(2\vartheta) - \tau_{xy}\sin(2\vartheta) \end{aligned} \tag{C.3}$$

$$\begin{aligned} \tau &= -\frac{\sigma_{xx}-\sigma_{yy}}{2}\sin(2\theta) + \tau_{xy}\cos(2\theta) \\ &= \frac{\sigma_{xx}-\sigma_{yy}}{2}\sin(2\vartheta) - \tau_{xy}\cos(2\vartheta) \end{aligned}$$

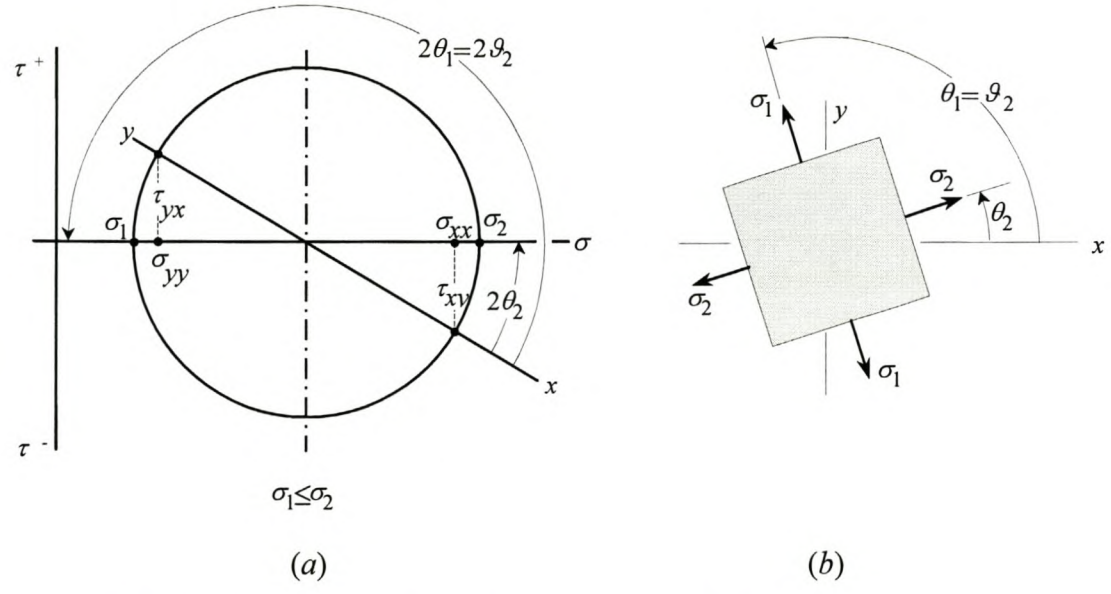

(*a*) (*b*)

Figure C.2 – *Mohr's stress circle diagram and stress element*

Stellenbosch University http://scholar.sun.ac.za

It is convenient to express the relationship of Eq. C.3 in a graphical format, called a Mohr's circle diagram. In Fig. C.2(a) a coordinate system is shown with normal stresses along the abscissa and shear stresses as the ordinates. The tensile or positive normal stresses are plotted to the right and the compressive stresses to the left on the abscissa. If the shear stress couple in Fig. C.1(a) is clockwise, the shear stresses are plotted upward, (τ^+). Counter-clockwise shear stresses are plotted downwards, (τ^-), irrespective if they are positive or negative on the physical element in Fig. C.1(a). It can be shown that Eq. C.3 represents a circle in the σ-τ space as depicted in Fig. C.2(a). The angles 2θ and 2ϑ are defined positive in the counter-clockwise direction and are measured from the x-axis as reference axis.

The extreme value of the normal stress in Eq. C.3 is obtained by differentiating σ with respect to θ and equating the result to zero. Two angles are found that satisfy this condition, θ_2 for the maximum normal stress and θ_1 for the minimum normal stress

$$\begin{aligned} \tan(2\theta_2) &= \frac{2\tau_{xy}}{\sigma_{xx}-\sigma_{yy}} & \theta_1 &= \theta_2 + \frac{\pi}{2} \\ \vartheta_2 &= \theta_2 + \frac{\pi}{2} = \theta_1 & \vartheta_1 &= \theta_1 + \frac{\pi}{2} = \theta_2 + \pi \end{aligned} \tag{C.4}$$

It is also clear that no shear stress exists on the two respective planes. The normal stresses on these planes are the principal stresses. The principle stresses are arranged in ascending order, $\sigma_1 \le \sigma_2$, and are given by

$$\begin{aligned} \sigma_1 &= \tfrac{1}{2}(\sigma_{xx}+\sigma_{yy}) - \tfrac{1}{2}\sqrt{(\sigma_{xx}-\sigma_{yy})^2 + 4\tau_{xy}^2} \\ \sigma_2 &= \tfrac{1}{2}(\sigma_{xx}+\sigma_{yy}) + \tfrac{1}{2}\sqrt{(\sigma_{xx}-\sigma_{yy})^2 + 4\tau_{xy}^2} \end{aligned} \tag{C.5}$$

The average stress or pressure is defined as

$$p = \tfrac{1}{2}(\sigma_2+\sigma_1) = \tfrac{1}{2}(\sigma_{xx}+\sigma_{yy}) \tag{C.6}$$

The stresses in the x-y plane can also be given in terms of the principal stresses and angles, θ_2 and ϑ_2, associated with the major principle stress σ_2.

Stellenbosch University http://scholar.sun.ac.za

$$\begin{aligned} \sigma_{xx} &= p+\tfrac{1}{2}(\sigma_2-\sigma_1)\cos(2\theta_2) &&= p-\tfrac{1}{2}(\sigma_2-\sigma_1)\cos(2\vartheta_2) \\ \sigma_{yy} &= p-\tfrac{1}{2}(\sigma_2-\sigma_1)\cos(2\theta_2) &&= p+\tfrac{1}{2}(\sigma_2-\sigma_1)\cos(2\vartheta_2) \\ \tau_{xy} &= \tfrac{1}{2}(\sigma_2-\sigma_1)\sin(2\theta_2) &&= -\tfrac{1}{2}(\sigma_2-\sigma_1)\sin(2\vartheta_2) \end{aligned} \tag{C.7}$$

C.1.2 Conditions of Critical State and Differential Equation of Equilibrium

Referring to Fig. C.1(b), consider a point in a granular material with a plane passing through it. Of interest for this study is the critical state of maximum shear stress without any slip occurring. Coulomb's law states that

$$|\tau_c| = c_o - \sigma_c \tan(\phi) \tag{C.8}$$

with σ_c and τ_c the critical stress components in that state.

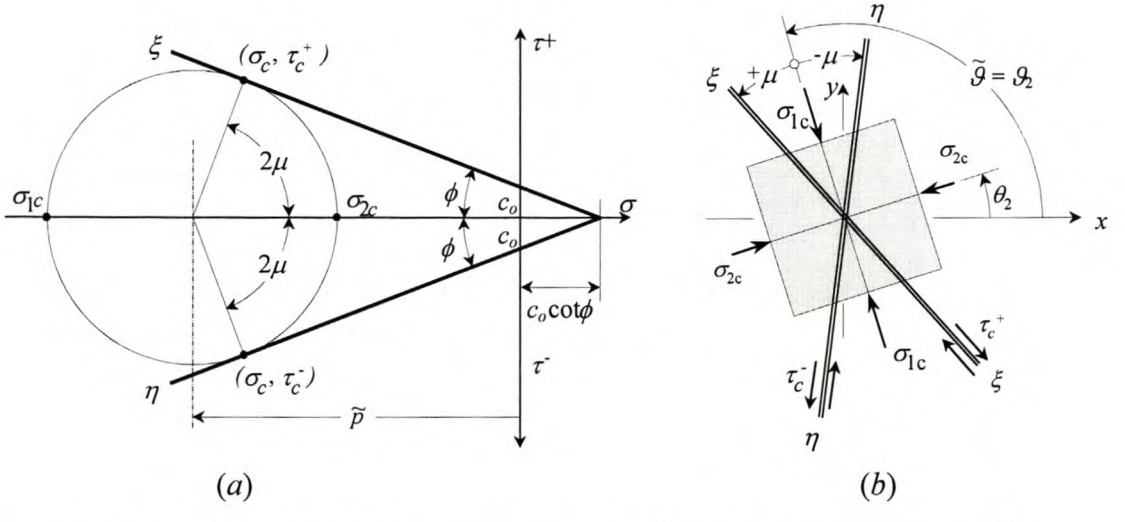

Figure C.3 – *(a) Critical state according to Mohr-Coulomb strength criterion*
(b) Directions of yield planes for critical state

This critical condition is depicted on the Mohr circle in Fig. C.3(a) with the two critical lines ξ and η for clockwise and counter-clockwise shear stresses respectively. It is clear from the Mohr circle that the angles of the two critical planes with respect to the x-axis are given by $\theta_2 \pm \mu + \pi/2$, which is equal to $\vartheta_2 \pm \mu$. The angle μ is given by

$$2\mu = \frac{\pi}{2} - \phi \tag{C.9}$$

Stellenbosch University http://scholar.sun.ac.za

In the critical state, the principal stresses are constrained because of the strength criterion of Eq. C.8. If σ_{ic} is the constrained principal stresses when the material is in the critical state, then it follows from the Mohr diagram in Fig. C.3(a) that

$$\sin(\phi) = \frac{\frac{1}{2}(\sigma_{2c} - \sigma_{1c})}{c_o \cot(\phi) - \frac{1}{2}(\sigma_{2c} + \sigma_{1c})} = \frac{\frac{1}{2}(\sigma_{2c} - \sigma_{1c})}{c_o \cot(\phi) - \tilde{p}} \tag{C.10}$$

with $\tilde{p}$ the average stress for the critical state.

$$\tilde{p} = \frac{\sigma_{2c} + \sigma_{1c}}{2} = \frac{\sigma_{1c} + c_o \cos(\phi)}{1 + \sin(\phi)} = \frac{\sigma_{2c} - c_o \cos(\phi)}{1 - \sin(\phi)} \tag{C.11}$$

The relationship between the stress components in the critical state follows from Eqs. (C.5), (C.6) and (C.10)

$$(\sigma_{xx} - \sigma_{yy})^2 + 4\tau_{xy}^2 = \sin^2\phi\,(2c_o \cot(\phi) - \sigma_{xx} - \sigma_{yy}) \tag{C.12}$$

Equation C.10 can also be written as

$$\sigma_{1c} = \sigma_{2c} N_\phi - 2c_o \sqrt{N_\phi} \quad \text{with} \quad N_\phi = (1 + \sin(\phi))/(1 - \sin(\phi)) = \tan^2(\mu) \tag{C.13}$$

Define the angle $\tilde{\vartheta} = \vartheta_2$ as the angle of the plane associated with the major principal stress σ_2. It follows from Eq. C.7 and Eq. C.10 for the stresses in the critical state in the x- and y-directions that

$$\begin{aligned}
\sigma_{xx} &= \tilde{p}\,(1 + \sin(\phi)\cos(2\tilde{\vartheta})) - c_o \cos(\phi)\cos(2\tilde{\vartheta}) \\
\sigma_{yy} &= \tilde{p}\,(1 - \sin(\phi)\cos(2\tilde{\vartheta})) + c_o \cos(\phi)\cos(2\tilde{\vartheta}) \\
\tau_{xy} &= \tilde{p}\sin(\phi)\sin(2\tilde{\vartheta}) \qquad - c_o \cos(\phi)\sin(2\tilde{\vartheta})
\end{aligned} \tag{C.14}$$

Next, the conditions for equilibrium in a changing stress field are investigated.

Stellenbosch University http://scholar.sun.ac.za

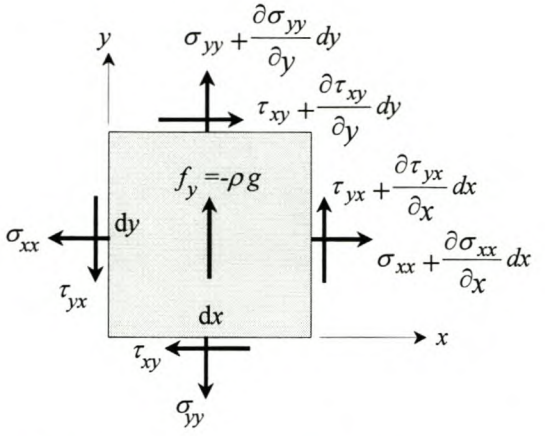

Figure C.4 – *Equilibrium condition on a differential element*

Consider the differential element in a varying stress field depicted in Fig. C.4. Assume the only body force is gravitation in the negative y-direction. The equilibrium conditions for forces in the x- and y-directions are then

$$\frac{\partial\sigma_{xx}}{\partial x}+\frac{\partial\tau_{xy}}{\partial y}=0, \qquad \frac{\partial\tau_{xy}}{\partial x}+\frac{\partial\sigma_{yy}}{\partial y}=\rho\, g \tag{C.15}$$

with ρ the bulk density of the material and g the gravitation acceleration. For plane critical equilibrium it follows from the substitution of Eq. C.14 into Eq. C.15

$$\begin{aligned}&\left(1+\sin(\phi)\cos(2\tilde{\vartheta})\right)\frac{\partial\tilde{p}}{\partial x}+\sin(\phi)\sin(2\tilde{\vartheta})\frac{\partial\tilde{p}}{\partial y}+\\&\qquad 2\sin(\phi)\left(c_o\cot(\phi)-\tilde{p}\right)\left(\sin(2\tilde{\vartheta})\frac{\partial\tilde{\vartheta}}{\partial x}-\cos(2\tilde{\vartheta})\frac{\partial\tilde{\vartheta}}{\partial y}\right)=0\\&\sin(\phi)\sin(2\tilde{\vartheta})\frac{\partial\tilde{p}}{\partial x}+\left(1-\sin(\phi)\cos(2\tilde{\vartheta})\right)\frac{\partial\tilde{p}}{\partial y}-\\&\qquad 2\sin(\phi)\left(c_o\cot(\phi)-\tilde{p}\right)\left(\cos(2\tilde{\vartheta})\frac{\partial\tilde{\vartheta}}{\partial x}+\sin(\tilde{2}\tilde{\vartheta})\frac{\partial\tilde{\vartheta}}{\partial y}\right)=\rho\, g\end{aligned} \tag{C.16}$$

Exchange $\phi=\pi/2-2\mu$ in the equations and add them after multiplying the first with $\sin(\tilde{\vartheta}-\mu)$ and the second with $-\cos(\tilde{\vartheta}-\mu)$. Repeat the procedure by multiplying the

Stellenbosch University http://scholar.sun.ac.za

first with $\sin(\tilde{\vartheta}+\mu)$ and the second with $-\cos(\tilde{\vartheta}+\mu)$. After considerable algebra, the critical equilibrium equations lead to

$$\begin{aligned}\left[\frac{\partial \tilde{p}}{\partial x}+\tan\left(\tilde{\vartheta}+\mu\right)\frac{\partial \tilde{p}}{\partial y}\right]-2\tan(\phi)(c_o\cot(\phi)-\tilde{p})\left[\frac{\partial \tilde{\vartheta}}{\partial x}+\tan\left(\tilde{\vartheta}+\mu\right)\frac{\partial \tilde{\vartheta}}{\partial y}\right]\\ =\rho\, g\left[\tan\left(\tilde{\vartheta}+\mu\right)+\tan(\phi)\right]\\ \left[\frac{\partial \tilde{p}}{\partial x}+\tan\left(\tilde{\vartheta}-\mu\right)\frac{\partial \tilde{p}}{\partial y}\right]+2\tan(\phi)(c_o\cot(\phi)-\tilde{p})\left[\frac{\partial \tilde{\vartheta}}{\partial x}+\tan\left(\tilde{\vartheta}-\mu\right)\frac{\partial \tilde{\vartheta}}{\partial y}\right]\\ =\rho\, g\left[\tan\left(\tilde{\vartheta}-\mu\right)-\tan(\phi)\right]\end{aligned} \tag{C.17}$$

The total derivatives are taken as

$$d\tilde{p}=\frac{\partial \tilde{p}}{\partial x}dx+\frac{\partial \tilde{p}}{\partial y}dy \qquad d\tilde{\vartheta}=\frac{\partial \tilde{\vartheta}}{\partial x}dx+\frac{\partial \tilde{\vartheta}}{\partial y}dy \tag{C.18}$$

The equilibrium equations (Eq. C.17) and the total derivatives (Eq.C.18) are a system of equations which can be solved simultaneously for the partial derivatives $\partial\tilde{p}/\partial x$, $\partial\tilde{p}/\partial y$, $\partial\tilde{\vartheta}/\partial x$ and $\partial\tilde{\vartheta}/\partial y$. The result is of the form

$$\frac{\partial \tilde{p}}{\partial x}=\frac{N_1}{D}, \qquad \frac{\partial \tilde{p}}{\partial y}=\frac{N_2}{D}, \qquad \frac{\partial \tilde{\vartheta}}{\partial x}=\frac{N_3}{D}, \qquad \frac{\partial \tilde{\vartheta}}{\partial y}=\frac{N_4}{D} \tag{C.19}$$

with

$$D=\left[dy-\tan\left(\tilde{\vartheta}+\mu\right)dx\right]\left[dy-\tan\left(\tilde{\vartheta}-\mu\right)dx\right] \tag{C.20}$$

If on the denominator D the right-hand side of the equations in Eq. C.19 is not equal to zero, then the values of the derivatives may be determined uniquely. However, if we select $D = 0$, then the partial derivatives in Eq. C.19 are not defined, but we can stipulate that they are at least finite, for example, $0\cdot\partial\tilde{p}/\partial x = N_1 = 0$. The denominator D has two real roots, implying that Eq. C.16 is a set of hyperbolic equations. If we select $N_i/D = 0/0$, the differential equations of the *characteristics curves* are obtained. It can be shown that a characteristic is the path of propagation of a physical disturbance, in this instance a slip line or shear plane in the material. It has the property that the

Stellenbosch University http://scholar.sun.ac.za

governing partial differential equations can be manipulated into total differential equations along, and only along, these lines. A characteristic is also a curve across which the derivatives of a physical property may be discontinuous, while the property itself remains continuous. Therefore $D = 0$ and $N_1 = N_2 = N_3 = N_4 = 0$ give two families of characteristics, $\xi(x,y)$ and $\eta(x,y)$, for the two roots of D,

$$\left.\frac{dy}{dx}\right|_{\xi} = \tan\left(\tilde{\vartheta} + \mu\right)$$

$$d\tilde{p} - 2\tan(\phi)\left(c_o \cot(\phi) - \tilde{p}\right) d\tilde{\vartheta} - \rho g \tan(\phi)\, dx - \rho g\, dy = 0 \tag{C.21}$$

and

$$\left.\frac{dy}{dx}\right|_{\eta} = \tan\left(\tilde{\vartheta} - \mu\right)$$

$$d\tilde{p} + 2\tan(\phi)\left(c_o \cot(\phi) - \tilde{p}\right) d\tilde{\vartheta} + \rho g \tan(\phi)\, dx - \rho g\, dy = 0 \tag{C.22}$$

Note that the first equation of each family gives the slope of the characteristic lines $\xi(x,y)$ or $\eta(x,y)$, while the second gives the change of the two unknown properties $\tilde{p}(x, y)$ and $\tilde{\vartheta}(x, y)$ along the specific lines.

These equations can only be solved if sufficient material properties and boundary conditions are known. Analytical solutions are only possible for some simple cases, such as a perfect smooth blade and weightless material. This is a valid assumption only if the material strength characteristics are dominated by the cohesion and not the internal friction.

Stellenbosch University http://scholar.sun.ac.za

C.1.3 Numerical Solution

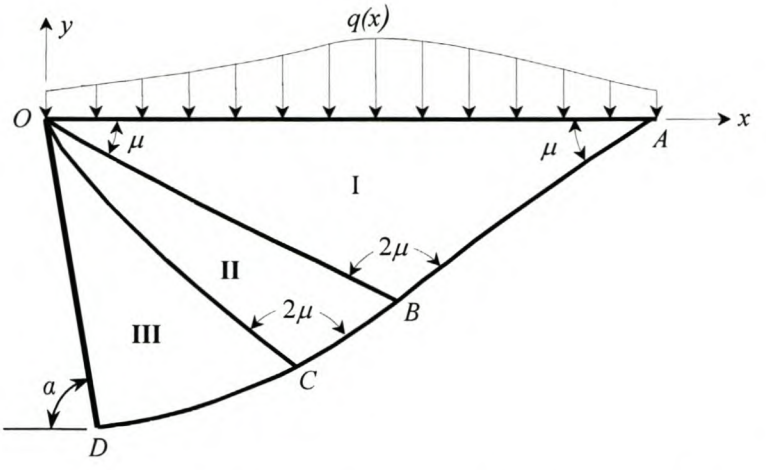

Figure C.5 – *Earthmoving / Passive earth retaining wall problem*

The analysis of the forces on the blade of an earthmoving apparatus is the classic analysis of the passive earth forces on a retaining wall. Figure C.5 depicts a configuration with a blade with rake angle a. Along the free surface $0A$ a normal pressure $q(x)$ is applied. Assume there are no shear stresses along $0A$. Inside OAD the stresses are in the critical state and continuous everywhere, except at point 0. Below the lowest critical line $ABCD$ the material is in an elastic state and the derivatives of the stresses are discontinuous across it. For large angles of a, three distinctive regions can be identified.

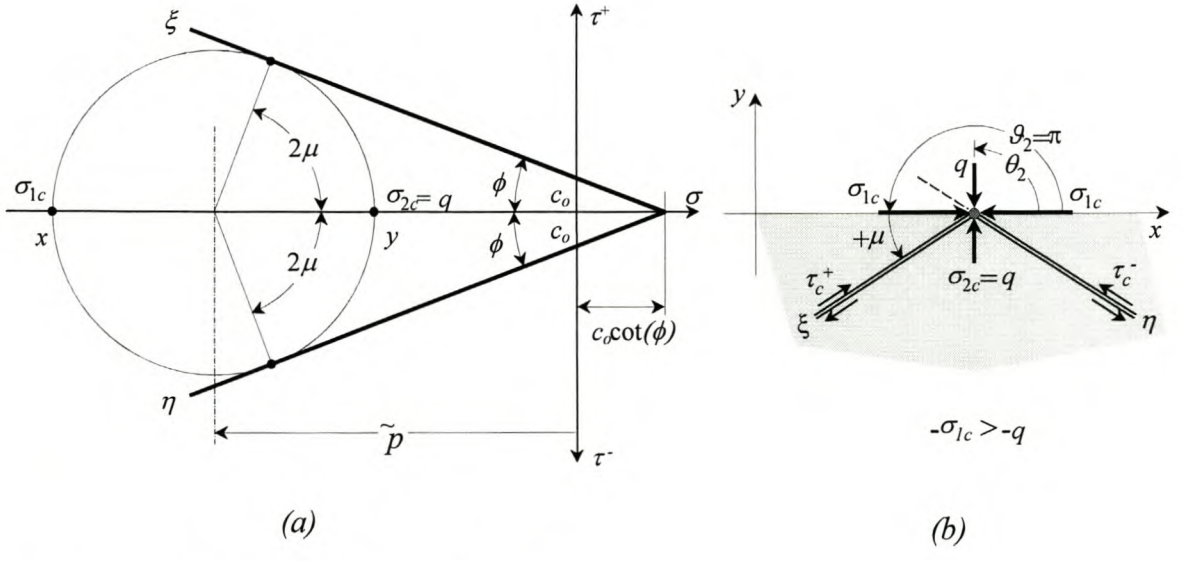

Figure C.6 – *Stress state on free surface*

Stellenbosch University http://scholar.sun.ac.za

In the passive earth pressure state we assume that the blade causes upward heaving of the material. On the surface we therefore found that $|\sigma_x| \geq |\sigma_y|$. If there are no shear stresses then σ_x and σ_y are the principle stresses and $\sigma_{2c}=q(x)$. From Fig. C.6 it is clear that on the free surface the following parameters are known

$$y = 0 \qquad \tilde{p} = \frac{q(x) - c_o \cos(\phi)}{1 - \sin(\phi)} \qquad \tilde{\vartheta} = \pi \tag{C.23}$$

It is advisable for numeric purposes to make Eq. C.21 and Eq. C.22 dimensionless. Define a characteristic length L, for example, the blade length, then for a medium with weight $\rho \neq 0$, we can define the following dimensionless parameters

$$x' = \frac{x}{L} \qquad y' = \frac{y}{L} \qquad \tilde{p}' = \frac{\tilde{p}}{\rho g L} \qquad c_o' = \frac{c_o}{\rho g L} \tag{C.24}$$

Eqs. (C.21) and (C.22) then become

$$\left.\frac{dy'}{dx'}\right|_{\xi} = \tan\left(\tilde{\vartheta} + \mu\right), \qquad d\tilde{p}' - 2\tan\phi\,(c_o' \cot(\phi) - \tilde{p}')d\tilde{\vartheta} - \tan(\phi)\,dx' - dy' = 0 \tag{C.25}$$

$$\left.\frac{dy'}{dx'}\right|_{\eta} = \tan\left(\tilde{\vartheta} - \mu\right), \qquad d\tilde{p}' + 2\tan(\phi)\,(c_o' \cot(\phi) - \tilde{p}')d\tilde{\vartheta} + \tan(\phi)\,dx' - dy' = 0 \tag{C.26}$$

In region I Eq. C.25 and Eq. C.26 can be solved numerically with finite differences with initial values at the free surface.

Stellenbosch University http://scholar.sun.ac.za

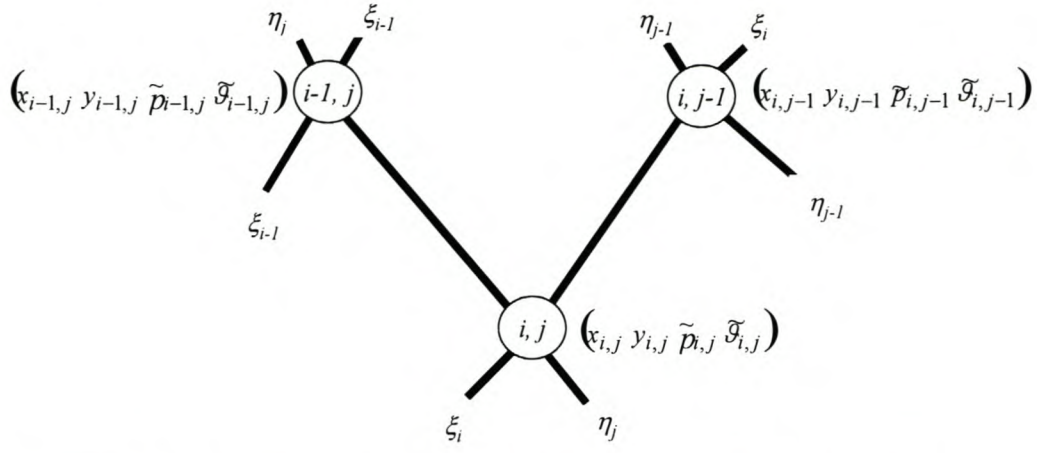

Figure C.7 – *Determination of a third point from two known points in the interior of the material*

Consider the points *(i-1,j)* and *(i,j-1)* in Fig. C.7. We assume that all the parameters are known from boundary values or from calculations from previous points. A new point *(i,j)* can be calculated at the intersection of the two characteristic lines ξ_i and η_j. The numerical value of the parameters at point *(i,j)* can be approximated with a finite difference descritisation of Eq. C.25 and Eq. C.26. It was found that the best results where obtained when the averages of the slopes were taken. The average values of $\tilde{p}'$ and $\tilde{\vartheta}$ along the characteristic lines are taken otherwise.

$$f_1 = \left(y'_{i,j} - y'_{i,j-1}\right) - \tfrac{1}{2}\left(x'_{i,j} - x'_{i,j-1}\right)\left[\tan\left(\tilde{\vartheta}_{i,j} + \mu\right) + \tan\left(\tilde{\vartheta}_{i,j-1} + \mu\right)\right] = 0$$
$$f_2 = \left(y'_{i,j} - y'_{i-1,j}\right) - \tfrac{1}{2}\left(x'_{i,j} - x'_{i-1,j}\right)\left[\tan\left(\tilde{\vartheta}_{i,j} + \mu\right) + \tan\left(\tilde{\vartheta}_{i-1,j} + \mu\right)\right] = 0 \tag{C.27}$$

and

$$f_3 = \left(\tilde{p}'_{i,j} - \tilde{p}'_{i,j-1}\right) - 2\left[c'_o - \tfrac{1}{2}\tan(\phi)\left(\tilde{p}'_{i,j} + \tilde{p}'_{i,j-1}\right)\right]\left(\tilde{\vartheta}_{i,j} - \tilde{\vartheta}_{i,j-1}\right) - \tan(\phi)\left(x'_{i,j} - x'_{i,j-1}\right) - \left(y'_{i,j} - y'_{i,j-1}\right) = 0$$
$$f_4 = \left(\tilde{p}'_{i,j} - \tilde{p}'_{i-1,j}\right) + 2\left[c'_o - \tfrac{1}{2}\tan(\phi)\left(\tilde{p}'_{i,j} + \tilde{p}'_{i-1,j}\right)\right]\left(\tilde{\vartheta}_{i,j} - \tilde{\vartheta}_{i-1,j}\right) + \tan(\phi)\left(x'_{i,j} - x'_{i-1,j}\right) - \left(y'_{i,j} - y'_{i-1,j}\right) = 0 \tag{C.28}$$

Stellenbosch University http://scholar.sun.ac.za

From Eqs. C.27 and C.28 one can solve for the unknown variables $x'_{i,j}$, $y'_{i,j}$, $\tilde{p}'_{i,j}$ and $\tilde{\vartheta}_{i,j}$. Note that the equations are non-linear with respect to $\tilde{\vartheta}_{i,j}$. Define the following vector and vector function

$$\overline{\mathbf{X}} = \begin{bmatrix} x'_{i,j} & y'_{i,j} & \tilde{p}'_{i,j} & \tilde{\vartheta}_{i,j} \end{bmatrix}^T \qquad \mathbf{F}(\overline{\mathbf{X}}) = \begin{bmatrix} f_1 & f_2 & f_3 & f_4 \end{bmatrix}^T \tag{C.29}$$

Use Newton's method to find the numerical values of the variables $\overline{\mathbf{X}}$ when $\mathbf{F}(\overline{\mathbf{X}}) = \mathbf{0}$.

$$\overline{\mathbf{X}}^{(p+1)} = \overline{\mathbf{X}}^{(p)} - \left[\mathbf{J}(\overline{\mathbf{X}}^{(p)})\right]^{-1} \mathbf{F}(\overline{\mathbf{X}}^{(p)}), \qquad p = 0,1,\cdots \tag{C.30}$$

with

$$\mathbf{J}(\overline{\mathbf{X}}) = \frac{\partial \mathbf{F}(\overline{\mathbf{X}})}{\partial \overline{\mathbf{X}}} = \begin{bmatrix} \partial f_1/\partial x'_{i,j} & \partial f_1/\partial y'_{i,j} & \partial f_1/\partial \tilde{p}'_{i,j} & \partial f_1/\partial \tilde{\vartheta}_{i,j} \\ \partial f_2/\partial x'_{i,j} & \partial f_2/\partial y'_{i,j} & \partial f_2/\partial \tilde{p}'_{i,j} & \partial f_2/\partial \tilde{\vartheta}_{i,j} \\ \partial f_3/\partial x'_{i,j} & \partial f_3/\partial y'_{i,j} & \partial f_3/\partial \tilde{p}'_{i,j} & \partial f_3/\partial \tilde{\vartheta}_{i,j} \\ \partial f_4/\partial x'_{i,j} & \partial f_4/\partial y'_{i,j} & \partial f_4/\partial \tilde{p}'_{i,j} & \partial f_4/\partial \tilde{\vartheta}_{i,j} \end{bmatrix} \tag{C.31}$$

For the first iteration, we can use a simple forward difference by setting $\tilde{\vartheta}_{i,j} = \tilde{\vartheta}_{i,j-1}$ *or* $\tilde{\vartheta}_{i-1,j}$ and do the same for $\tilde{p}_{i,j}$.

$$\begin{aligned} x'^{(0)}_{i,j} &= \frac{\left[x'_{i,j-1}\tan\left(\tilde{\vartheta}_{i,j-1}+\mu\right) - x'_{i-1,j}\tan\left(\tilde{\vartheta}_{i-1,j}-\mu\right)\right] - \left(y'_{i,j-1} - y'_{i-1,j}\right)}{\tan\left(\tilde{\vartheta}_{i,j-1}-\mu\right) - \tan\left(\tilde{\vartheta}_{i-1,j}-\mu\right)} \\ y'^{(0)}_{i,j} &= y'_{i,j-1} + \left(x'^{(0)}_{i,j} - x'_{i,j-1}\right)\tan\left(\tilde{\vartheta}_{i,j-1}+\mu\right) \\ \tilde{p}'^{(0)}_{i,j} &= \tilde{p}'_{i,j-1} \\ \tilde{\vartheta}^{(0)}_{i,j} &= \tilde{\vartheta}_{i,j-1} \end{aligned} \tag{C.32}$$

Before continuing with the calculations in region II, we first investigate the conditions along the blade.

Stellenbosch University http://scholar.sun.ac.za

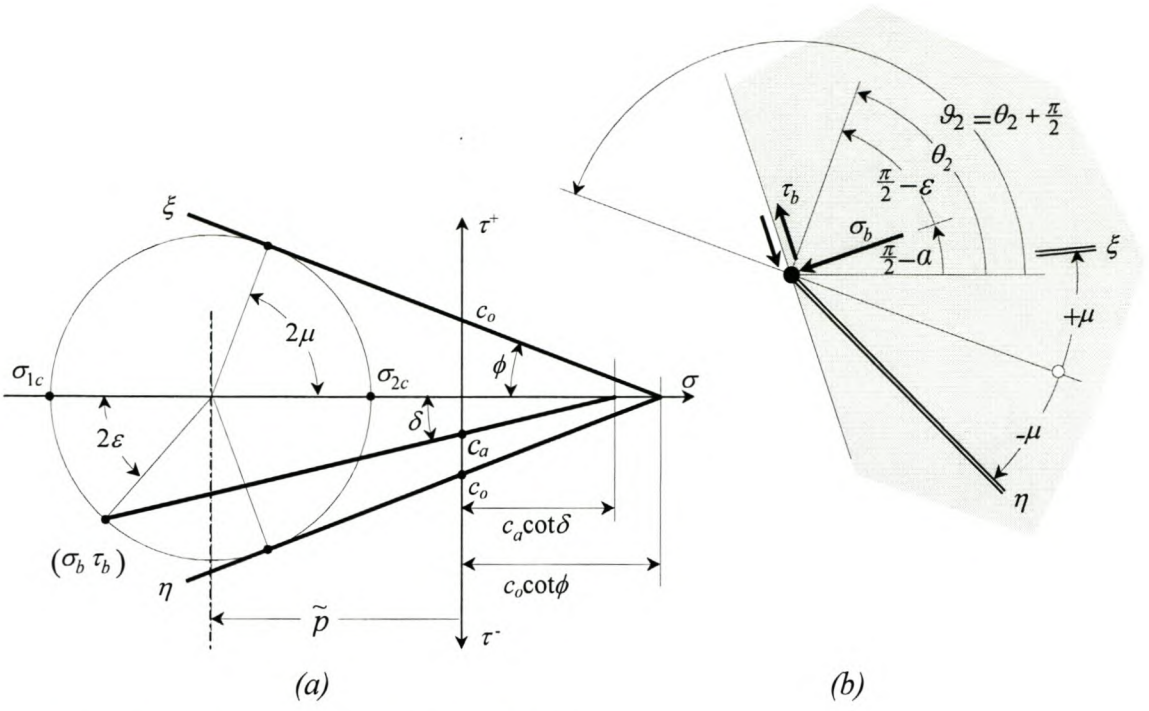

Figure C.8 – *Stress state against the blade*

When the rake angle is large, the distribution of stress in critical equilibrium can be continuous everywhere except at point *0*. Assume that the following equality holds along the blade

$$|\tau_b| = c_a - \sigma_b \tan\delta \qquad \delta \le \phi \tag{C.33}$$

with c_a the adhesion coefficient and δ the friction angle between the blade and the material. From the Mohr circle diagram in Fig. C.8(a) we find the angle ε

$$\varepsilon = \frac{1}{2}\left\{\delta + \sin^{-1}\left[\frac{\sin(\delta)}{\sin(\phi)}\left(1 + \frac{c_a\cot(\delta) - c_o\cot(\phi)}{c_o\cot(\phi) - \tilde{p}}\right)\right]\right\} \tag{C.34}$$

Note that for two special instances, Eq. C.34 can be simplified as

$$\varepsilon = \frac{1}{2}\left[\delta + \sin^{-1}\left(\frac{\sin(\delta)}{\sin(\phi)}\right)\right] \tag{C.35}$$

Stellenbosch University http://scholar.sun.ac.za

The first is for an ideal granular material when $c_o = c_a = 0$ and the second is when $c_a \cot(\delta) = c_o \cot(\phi)$. In other instances ε is dependant on $\tilde{p}$ and must be solved numerically. The first case is often called the "constraint adhesion" case. The direction of the plane of the major principle stress against the blade follows from Fig. C.8(b) for the passive state as

$$\tilde{\vartheta}_b = \frac{3\pi}{2} - \alpha - \varepsilon \tag{C.36}$$

In region III we can solve from a point in the interior to a point on the blade along a ξ characteristic.

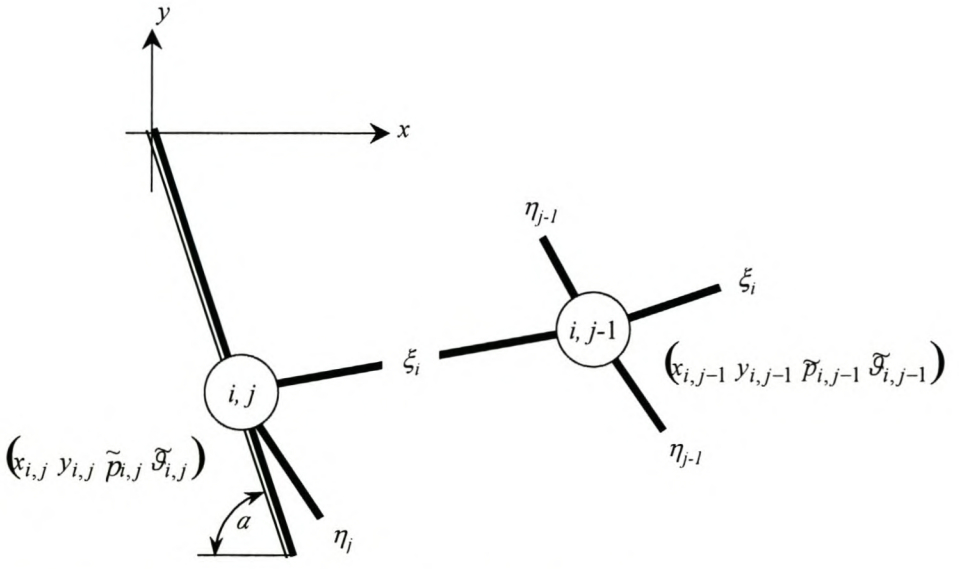

Figure C.9 – *Determination of a point on the blade*

We assume that all the parameters are known at an interior point (*i,j*-1). Along the blade, the *x*- and *y*-coordinates are constrained in terms of each other and the angle of the plane of the major principle stress is known.

Stellenbosch University http://scholar.sun.ac.za

$$\tilde{\vartheta}_{i,j} = \frac{3\pi}{2} - \alpha - \varepsilon$$
$$y'_{i,j} = \frac{y'_{i,j-1} - \frac{1}{2}x'_{i,j-1}\left[\tan\left(\tilde{\vartheta}_{i,j} + \mu\right) + \tan\left(\tilde{\vartheta}_{i,j-1} + \mu\right)\right]}{1 + \frac{1}{2}\tan(\beta)\left[\tan\left(\tilde{\vartheta}_{i,j} + \mu\right) + \tan\left(\tilde{\vartheta}_{i,j-1} + \mu\right)\right]} \tag{C.37}$$

$$x'_{i,j} = -y'_{i,j}\tan(\beta)$$

$$\tilde{p}'_{i,j} = \frac{2c'\left(\tilde{\vartheta}_{i,j} - \tilde{\vartheta}_{i,j-1}\right) + \tilde{p}'_{i,j-1}\left[1 - \left(\tilde{\vartheta}_{i,j} - \tilde{\vartheta}_{i,j-1}\right)\tan(\phi)\right] + \left(x'_{i,j} - x'_{i,j-1}\right) + \left(y'_{i,j} - y'_{i,j-1}\right)}{1 + \left(\tilde{\vartheta}_{i,j} - \tilde{\vartheta}_{i,j-1}\right)\tan(\phi)}$$

Note that in general $\varepsilon = \varepsilon\left(\tilde{p}_{i,j}\right)$ and Eq. C.36 must be solved iteratively. Equation C.35 can be used for the first guess. After the calculation of the parameter against the blade, the normal and tangential stresses against the blade can be calculated from Eq. C.3.

We can now return to the calculations in region II. First note that the values of $\tilde{\vartheta}$ change from its value along *0A* in Fig. C.5 to the value $\tilde{\vartheta}_b$ along the blade. This happens across the point of discontinuity at point *0*. Note that if $\tilde{\vartheta}_b$ is less than $\tilde{\vartheta}$ along *0A*, a series of η characteristics radiating from *0* can be introduced to account for the change in $\tilde{\vartheta}$. First, for $\tilde{\vartheta} = \pi$ along *0A*, the condition for region II to exist is then the definition of a large rake angle

$$\alpha > \frac{\pi}{2} - \varepsilon \tag{C.38}$$

A ξ characteristic (of zero length) can be constructed across point *0*. Equation C.21 can be integrated with $dx = dy = 0$. We can then construct a series of points on *0*

$$\begin{aligned} x'_k &= 0 \\ y'_k &= 0 \\ \tilde{\vartheta}_k &= \tilde{\vartheta}_0 + k\Delta\vartheta \\ \tilde{p}'_k &= \left(c'_o\cot(\phi) - \tilde{p}'_0\right)e^{-2\tan\phi\left(\tilde{\vartheta}_k - \tilde{\vartheta}_0\right)} \end{aligned} \tag{C.39}$$

Stellenbosch University http://scholar.sun.ac.za

with $\tilde{\vartheta}_0$ and $\tilde{p}_0$ the values on *0A* at point *0* and $\Delta\vartheta$ the increment in $\tilde{\vartheta}$. The interior points in region II can then be solved with the previous algorithms.

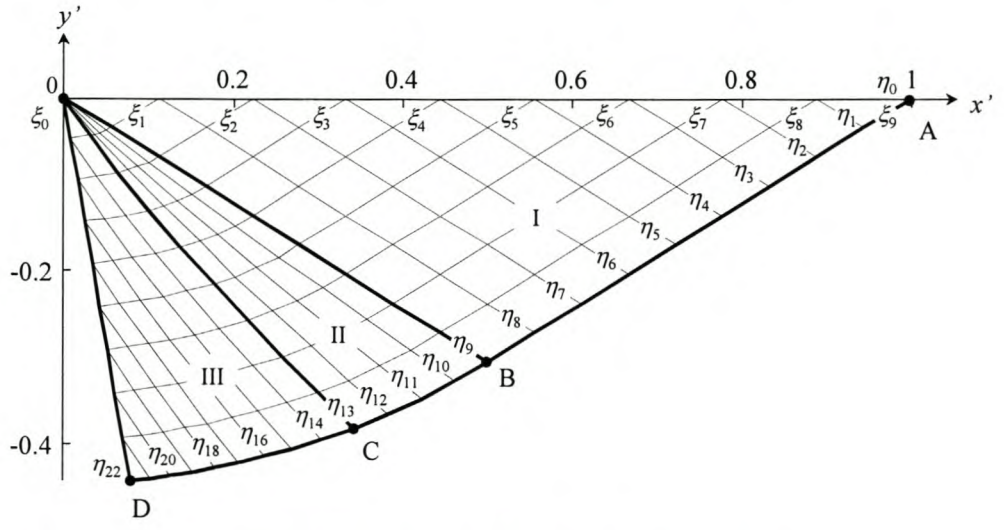

Figure C.10 – *Sample calculation with q(x) = constant.*

Figure C.10 shows the result from such an analysis for a straight blade. The outer characteristic line, ξ_9 in this case, is defined as the *rupture line*.

C.1.4 Analytical Solution

One case for which an analytical solution is possible is of special interest, the Rankine method. The blade is assumed to be perfectly smooth and vertical, i.e. $\alpha = 90°$ and $\delta = 0°$. The total blade force F acts perpendicular to the blade and it is incapable of supporting shear forces parallel to its surface. The stress from the blade to the material is therefore the major principle stress σ_1 and is horizontal all along the blade surface. The boundary conditions at the free surface are the same as in the previous section.

$$\tilde{p} = \frac{q(x) - c_o \cos(\phi)}{1 - \sin(\phi)} \qquad \tilde{\vartheta} = \pi \tag{C.40}$$

Since there is no reason for the angle $\tilde{\vartheta}$ to change over the entire region, it is constant everywhere and the characteristic lines have a constant angle of $\pm\mu$ to the horizontal.

Stellenbosch University http://scholar.sun.ac.za

Eqs. C.21 and C.22 can be simplified since there is no change in $\tilde{\vartheta}$ and $d\tilde{\vartheta} = 0$.

$$\left.\frac{dy}{dx}\right|_{\xi} = \tan(\mu) \qquad d\tilde{p} = \rho g \tan(\phi)\, dx + \rho g\, dy \tag{C.41}$$

$$\left.\frac{dy}{dx}\right|_{\eta} = -\tan(\mu) \qquad d\tilde{p} = -\rho g \tan(\phi)\, dx + \rho g\, dy \tag{C.42}$$

Dividing Eq. C.41 by dy

$$\frac{d\tilde{p}}{dy} = \rho g\left(1 + \frac{\tan(\phi)}{\tan(\mu)}\right) \tag{C.43}$$

The value of $\tilde{p}$ is known at the boundary (Eq. C.40), and to find the stresses at any position on the blade it is only necessary to integrate along a certain ξ line.

$$\begin{aligned}\tilde{p} &= \frac{q(x) - c_o \cos(\phi)}{1 - \sin(\phi)} + \int_0^y \frac{d\tilde{p}}{dy}\, dy \\ &= \frac{q(x) - c_o \cos(\phi)}{1 - \sin(\phi)} + \rho g y\left(1 + \frac{\tan(\phi)}{\tan(\mu)}\right)\end{aligned} \tag{C.44}$$

By using Eq. C.11, the major principle stress at the blade can be obtained.

$$\begin{aligned}\sigma_{1c} &= \tilde{p}(1 + \sin(\phi)) - c_o \cos(\phi) \\ &= (q(x) - c_o \cos(\phi))\frac{1 + \sin(\phi)}{1 - \sin(\phi)} + \rho g y\left(1 + \frac{\tan(\phi)}{\tan(\mu)}\right)(1 + \sin(\phi)) - c_o \cos(\phi)\end{aligned} \tag{C.45}$$

Thus, the total force F per unit width integrates to

Stellenbosch University http://scholar.sun.ac.za

$$F = \int_0^{-h} \sigma_{1c}\, dy$$

$$= \rho g h^2 N_\phi + c_o\, h \cot(\phi)\left(N_\phi - 1\right) - q(x)\, h\, N_\phi \tag{C.46}$$

where N_ϕ is given by Eq. C.13.

C.2 Solutions in Polar Coordinates

The computation procedure using Sokolovski's general solution in Cartesian coordinates becomes unstable for material numbers below 10^{-2} (Hettiaratchi and Reece, 1974). Applicable to this case is the surcharge number, q / (ρgh). To overcome this problem, polar coordinates r and θ can be employed.

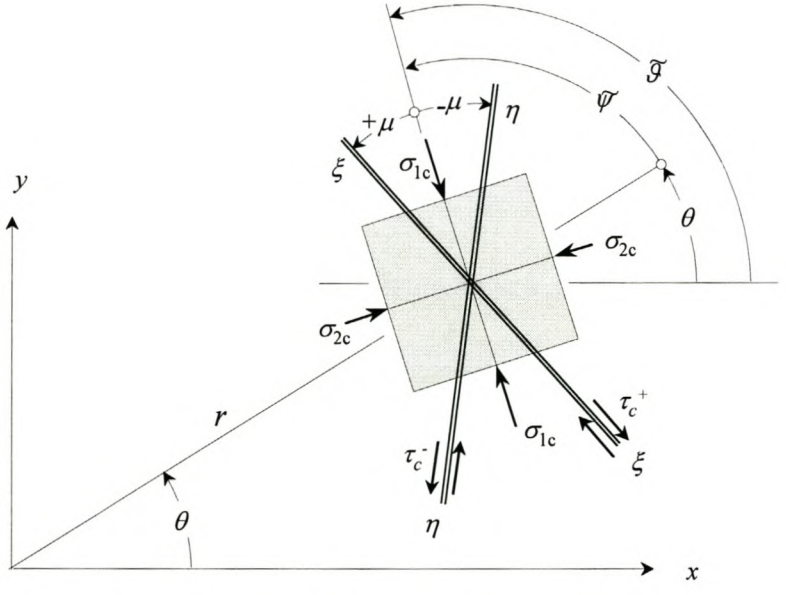

Figure C.11 – *Critical state in polar coordinates*

$$x = r\cos(\theta) \qquad y = r\sin(\theta) \tag{C.47}$$

$$r^2 = x^2 + y^2 \qquad \theta = \tan^{-1}\frac{y}{x} \tag{C.48}$$

The stress components at a point follow directly from the equilibrium in Fig. C.1 and Eq. C.3

Stellenbosch University http://scholar.sun.ac.za

$$\begin{bmatrix}\sigma_{rr}\\ \sigma_{\theta\theta}\\ \tau_{r\theta}\end{bmatrix}=\begin{bmatrix}\cos^2(\theta) & \sin^2(\theta) & 2\sin(\theta)\cos(\theta)\\ \sin^2(\theta) & \cos^2(\theta) & -2\sin(\theta)\cos(\theta)\\ -\sin(\theta)\cos(\theta) & \sin(\theta)\cos(\theta) & \cos^2(\theta)-\sin^2(\theta)\end{bmatrix}\begin{bmatrix}\sigma_{xx}\\ \sigma_{yy}\\ \tau_{xy}\end{bmatrix} \tag{C.49}$$

The principal stresses of Eq. C.5 in polar coordinates then become

$$\begin{aligned}\sigma_1 &= \tfrac{1}{2}(\sigma_{rr}+\sigma_{\theta\theta})-\tfrac{1}{2}\sqrt{(\sigma_{rr}-\sigma_{\theta\theta})^2+4\tau_{r\theta}}\\ \sigma_2 &= \tfrac{1}{2}(\sigma_{rr}+\sigma_{\theta\theta})+\tfrac{1}{2}\sqrt{(\sigma_{rr}-\sigma_{\theta\theta})^2+4\tau_{r\theta}}\end{aligned} \tag{C.50}$$

while the angles θ_2 and ϑ_2 associated with the major principal stress σ_2 lead to

$$\frac{2\tau_{r\theta}}{\sigma_{rr}-\sigma_{\theta\theta}}=\tan(2\theta_2-2\theta)=\tan(2\vartheta_2-2\theta-\pi) \tag{C.51}$$

The relationship between the stress components in the critical stress state (Eq. C.12) can be written as

$$(\sigma_{rr}-\sigma_{\theta\theta})^2+4\tau_{r\theta}^2=\sin^2(\phi)\,(2c_o\cot(\phi)-\sigma_{rr}-\sigma_{\theta\theta}) \tag{C.52}$$

After the introduction of $\tilde{p}=(\sigma_{rr}+\sigma_{\theta\theta})/2$ and $\tilde{\psi}$, the stress components in polar coordinates in the critical state are given by

$$\begin{aligned}\sigma_{rr} &= \tilde{p}\,(1+\sin(\phi)\cos(2\tilde{\psi}))-c_o\cos(\phi)\cos(2\tilde{\psi})\\ \sigma_{\theta\theta} &= \tilde{p}\,(1-\sin(\phi)\cos(2\tilde{\psi}))+c_o\cos(\phi)\cos(2\tilde{\psi})\\ \tau_{r\theta} &= \tilde{p}\sin(\phi)\sin(2\tilde{\psi})\qquad -c_o\cos(\phi)\sin(2\tilde{\psi})\end{aligned} \tag{C.53}$$

with

$$\tilde{\psi} \;=\; \tilde{\vartheta}-\theta \;=\; \vartheta_2-\theta \tag{C.54}$$

Stellenbosch University http://scholar.sun.ac.za

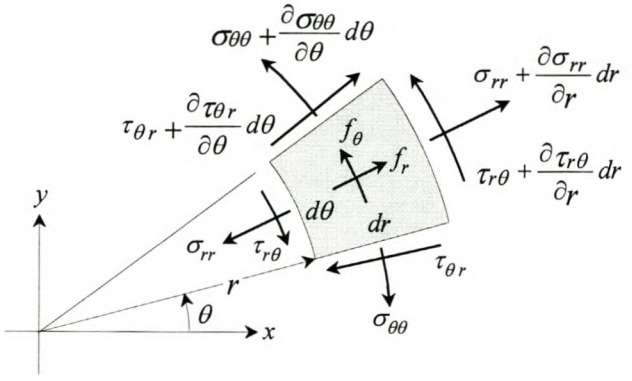

Figure C.12 – *Equilibrium condition on a differential element in polar coordinates*

Consider the differential element in a varying stress field depicted in Fig. C.12. The equilibrium conditions for forces are then

$$\begin{aligned} \frac{\partial \sigma_{rr}}{\partial r} + \frac{1}{r}\frac{\partial \tau_{r\theta}}{\partial \theta} + \frac{\sigma_{rr} - \sigma_{\theta\theta}}{r} + f_r = 0 \\ \frac{\partial \tau_{r\theta}}{\partial r} + \frac{1}{r}\frac{\partial \sigma_{\theta\theta}}{\partial \theta} + \frac{2\tau_{r\theta}}{r} + f_\theta = 0 \end{aligned} \tag{C.55}$$

Assume the only body force is gravitation in the y-direction, then the body forces are

$$f_r = -\rho\, g \sin(\theta) \qquad f_\theta = -\rho\, g \cos(\theta) \tag{C.56}$$

If Eq. C.53 is substituted into Eq. C.55

$$\begin{aligned} &\left(1 + \sin(\phi)\cos(2\tilde{\psi})\right)\frac{\partial \tilde{p}}{\partial r} + \sin(\phi)\sin(2\tilde{\psi})\frac{1}{r}\frac{\partial \tilde{p}}{\partial \theta} + \\ &\quad 2\sin(\phi)\left(c_o \cot(\phi) - \tilde{p}\right)\left[\sin(2\tilde{\psi})\frac{\partial \tilde{\psi}}{\partial r} - \cos(2\tilde{\psi})\frac{1}{r}\left(\frac{\partial \tilde{\psi}}{\partial \theta} + 1\right)\right] = \rho\, g \sin)\theta) \\ &\sin(\phi)\sin(2\tilde{\psi})\frac{\partial \tilde{p}}{\partial r} + \left(1 - \sin(\phi)\cos(2\psi)\right)\frac{1}{r}\frac{\partial \tilde{p}}{\partial \theta} - \\ &\quad 2\sin(\phi)\left(c_o \cot(\phi) - \tilde{p}\right)\left[\cos(2\tilde{\psi})\frac{\partial \tilde{\psi}}{\partial r} + \sin(2\tilde{\psi})\frac{1}{r}\left(\frac{\partial \tilde{\psi}}{\partial \theta} + 1\right)\right] = \rho\, g \cos(\theta) \end{aligned} \tag{C.57}$$

Stellenbosch University http://scholar.sun.ac.za

If the same procedure as in the previous section is repeated, Eq. C.58 is obtained. Note that Eq. C.17 can be transformed directly by employing the transformation for the two curve linear coordinate systems.

$$\left[\frac{\partial \tilde{p}}{\partial r}+\frac{1}{r}\tan(\tilde{\psi}+\mu)\frac{\partial \tilde{p}}{\partial \theta}\right]-2\tan(\phi)\,(c_o\cot\phi-\tilde{p})\left[\frac{\partial \tilde{\psi}}{\partial r}+\frac{1}{r}\tan(\tilde{\psi}+\mu)\left(\frac{\partial \tilde{\psi}}{\partial \theta}+1\right)\right]=$$
$$\frac{\rho\, g}{\cos(\phi)}[\sin(\theta+\phi)+\cos(\theta+\phi)\tan(\tilde{\psi}+\mu)]$$

$$\left[\frac{\partial \tilde{p}}{\partial r}+\frac{1}{r}\tan(\tilde{\psi}-\mu)\frac{\partial \tilde{p}}{\partial \theta}\right]+2\tan(\phi)\,(c_o\cot\phi-\tilde{p})\left[\frac{\partial \tilde{\psi}}{\partial r}+\frac{1}{r}\tan(\psi-\mu)\left(\frac{\partial \tilde{\psi}}{\partial \theta}+1\right)\right]=$$
$$\frac{\rho\, g}{\cos(\phi)}[\sin(\theta-\phi)+\cos(\theta-\phi)\tan(\psi-\mu)] \qquad \text{(C.58)}$$

The total derivatives are then

$$\frac{d\tilde{p}}{dr} = \frac{\partial \tilde{p}}{\partial r}+\frac{\partial \tilde{p}}{\partial \theta}\frac{d\theta}{dr}$$
$$\frac{d\tilde{\vartheta}}{dr} = \frac{\partial \tilde{\psi}}{\partial r}+\left(\frac{\partial \tilde{\psi}}{\partial \theta}+1\right)\frac{d\theta}{dr} = \frac{d\tilde{\psi}}{dr}+\frac{d\theta}{dr} \qquad \text{(C.59)}$$

The characteristics equations in polar coordinates then become

$$r\frac{d\theta}{dr}\bigg|_{\xi}=\tan(\psi+\mu)$$
$$d\tilde{p}-2\tan(\phi)\,(c_o\cot(\phi)-\tilde{p})(d\psi+d\theta)=\frac{\rho\, g}{\cos(\phi)}[\sin(\theta+\phi)dr+\cos(\theta+\phi)\,r\,d\theta] \qquad \text{(C.60)}$$

and

$$r\frac{d\theta}{dr}\bigg|_{\eta}=\tan(\tilde{\psi}-\mu)$$
$$d\tilde{p}+2\tan(\phi)\,(c_o\cot(\phi)-\tilde{p})(d\psi+d\theta)=\frac{\rho\, g}{\cos(\phi)}[\sin(\theta-\phi)dr+\cos(\theta-\phi)\,r\,d\theta] \qquad \text{(C.61)}$$

Stellenbosch University http://scholar.sun.ac.za

According to Sokolovski, a range of problems related to the equilibrium of wedges can be treated on the supposition that all the components of stress, σ_{rr}, $\sigma_{\theta\theta}$ and $\tau_{r\theta}$, are proportional to r, or that p is proportional to r, and that ϑ and ψ depend only on θ. Introduce a new function $\chi=\chi(\theta)$, and define

$$\tilde{p} = \rho g r \chi(\theta) \qquad \tilde{\psi} = \tilde{\psi}(\theta) \tag{C.62}$$

If we consider an ideal granular medium ($c_o = 0$), Eq. C.57 becomes

$$\begin{aligned} &\chi(1+\sin\phi\cos(2\tilde{\psi}))+\sin(\phi)\sin(2\tilde{\psi})\frac{d\chi}{d\theta}+2\chi\sin(\phi)\cos(2\tilde{\psi})\left(\frac{d\tilde{\psi}}{d\theta}+1\right)=\sin(\theta) \\ &\chi\sin(\phi)\sin(2\tilde{\psi})+(1-\sin(\phi)\cos(2\psi))\frac{d\chi}{d\theta}+2\chi\sin\phi\sin(2\tilde{\psi})\left(\frac{d\tilde{\psi}}{d\theta}+1\right)=\cos(\theta) \end{aligned} \tag{C.63}$$

Solve with respect to the derivatives

$$\frac{d\chi}{d\theta} = \frac{\cos(2\tilde{\psi}+\theta)+\chi\sin(2\tilde{\psi})}{\cos(2\tilde{\psi})-\sin(\phi)} \tag{C.64}$$

$$\frac{d\tilde{\psi}}{d\theta}+1 = \frac{\sin(\theta)-\sin(\phi)\sin(2\tilde{\psi}+\theta)-\chi\cos^2(\phi)}{2\chi\sin(\phi)(\cos(2\tilde{\psi})-\sin(\phi))} \tag{C.65}$$

It is clear from Eq. C.64 and Eq. C.65 that the denominators of the right-hand terms become zero if $\tilde{\psi}=\pm\mu$ or if $\theta=\tilde{\vartheta}\pm\mu$. The numerators may vanish simultaneously or it may be different from zero if the derivatives are infinite. Referring to Fig. C.11 it can be seen that the conditions when denominators are zero correspond with the directions of the characteristic lines at the point under consideration. The differential equation of the line can therefore be obtained from Eq. C.60 and Eq. C.61.

$$r\frac{d\theta}{dr} = \tan(\tilde{\psi}\pm\mu) \tag{C.66}$$

and the equations of the lines itself become

Stellenbosch University http://scholar.sun.ac.za

$$r = r_0 \exp\left(\int_{\theta_0}^{\theta} \cot(\tilde{\psi} \pm \mu) d\theta\right) \tag{C.67}$$

Another point of interest is in a simple state if $\tilde{\vartheta} = const$. This implies that Eq. C.65 becomes zero and

$$\chi = \frac{\sin(\theta) - \sin(\phi)\sin(2\tilde{\psi} + \theta)}{\cos^2(\phi)} \tag{C.68}$$

Although this formulation in polar coordinates has no instability, the equations are extremely stiff which poses problems for the numeric solution.

The formulation in Cartesian coordintes was found stable for values of $|q| \geq 0.02\,\rho\,g\,L$, where L is the reference length. The pressure against the blade also proved to be a linear function in y, the blade depth. Using these two observations, it is possible to obtain an accurate solution for the blade force by applying a surcharge pressure q. With the pressure against the blade linear, a simple offset method is used to calculate the total blade force, i.e. cancelling of the surcharge pressure. With the magnitude of q varying from $0.02\rho gL$ to $0.1\rho gL$ it had no significant effect (less than 1.5% difference) on the final blade forces.

Stellenbosch University http://scholar.sun.ac.za

APPENDIX D

BLADE RESULTS

Additional blade results are presented in this appendix. Figure D.1 shows the shock wave moving through the material with an average velocity of 6750 times the blade velocity. The wave front stays parallel to the blade for both $a = 90°$ and $60°$. During this simulation, the blade was not accelerated. Immediately after time step one, it had a velocity equal to the blade velocity. Other simulations were run where the blade was given an acceleration. This decreased the velocity of the shock wave, but it was still clearly visible.

Stellenbosch University http://scholar.sun.ac.za

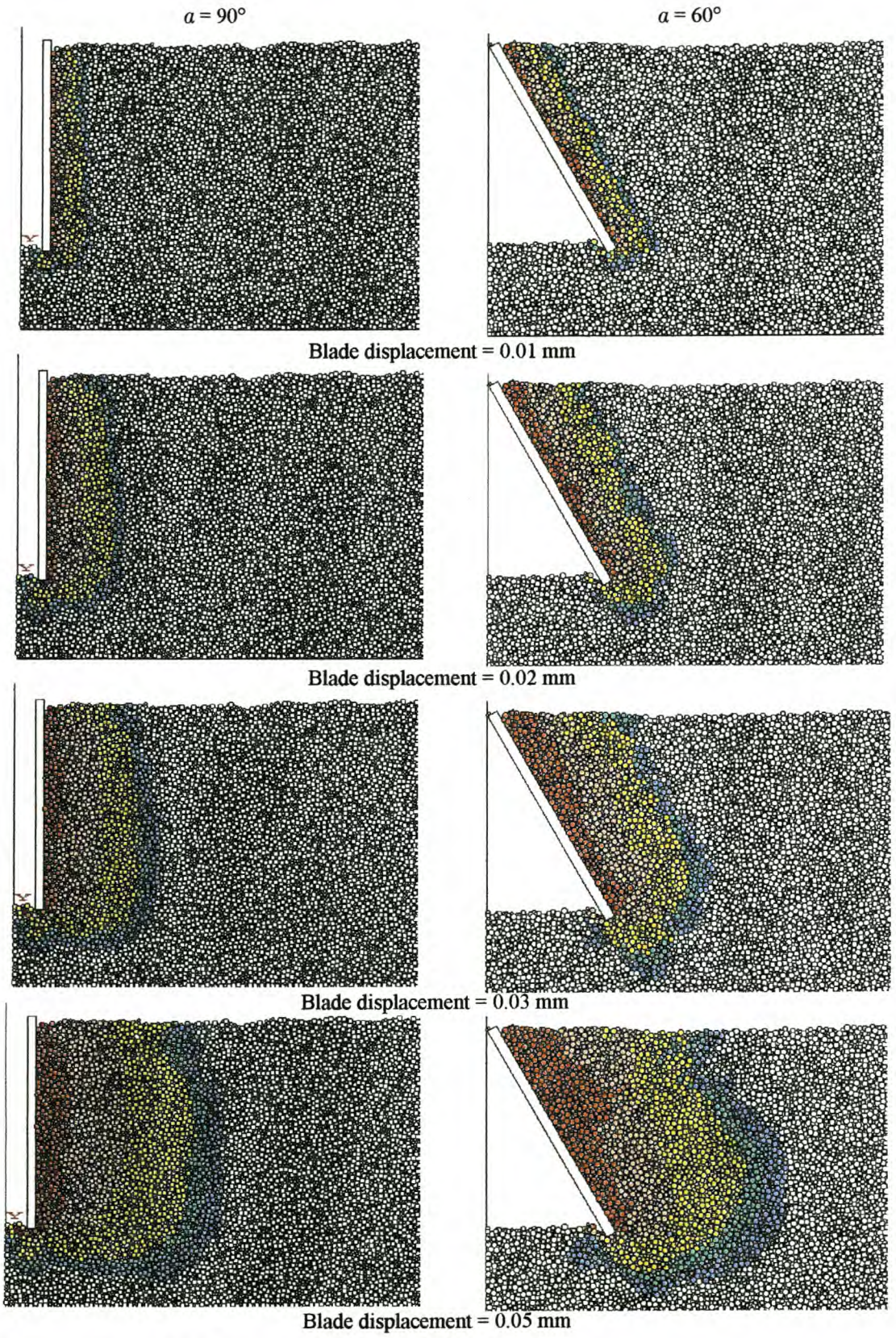

Figure D.1 – *Shock waves*

Stellenbosch University http://scholar.sun.ac.za

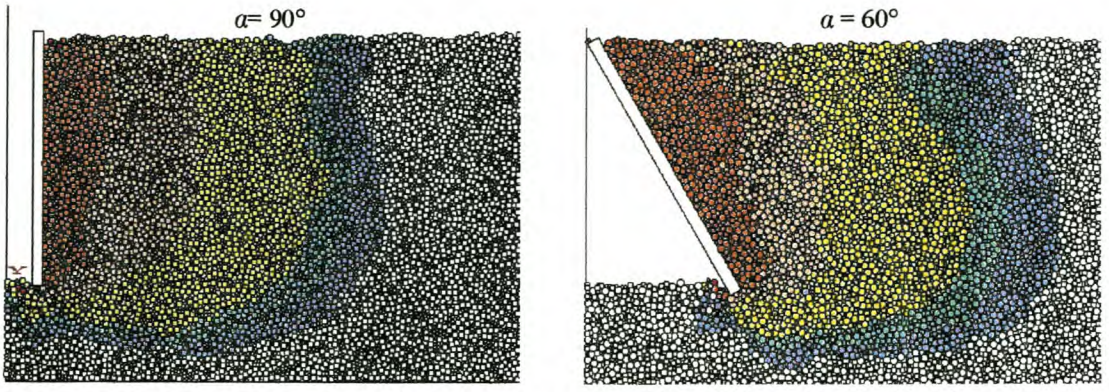

Blade displacement = 0.08 mm

$PDR \geq 1.0$ → Red	$0.80 \leq PDR < 1.0$ → Orange	$0.50 \leq PDR < 0.80$ → Light Orange
$0.25 \leq PDR < 0.50$ → Yellow	$0.10 \leq PDR < 0.25$ → Green	$0.05 \leq PDR < 0.10$ → Light Blue
$0.00 \leq PDR < 0.05$ → White	$PDR < -0.05$ → Dark Blue	

Figure D.1 (cont.) – *Shock waves*

Figures D.2 and D.3 show the rupture lines for wheat as created with a particle relative displacement ratio of 2% . The immersed depth h is 250 mm. The theoretical rupture zone is larger than the measured one. The numeric rupture line is not smooth at all, but most of the particles fall within the theoretical region.

Figures D.4 to D.11 show the draft force plotted against immersed depth h. Figures D.4 to D.7 show the corn results and the others the wheat results. The maximum, average and minimum experimental and simulation values are used. The accuracy of the soil mechanics models decreases with a decrease in rake angle.

Stellenbosch University http://scholar.sun.ac.za

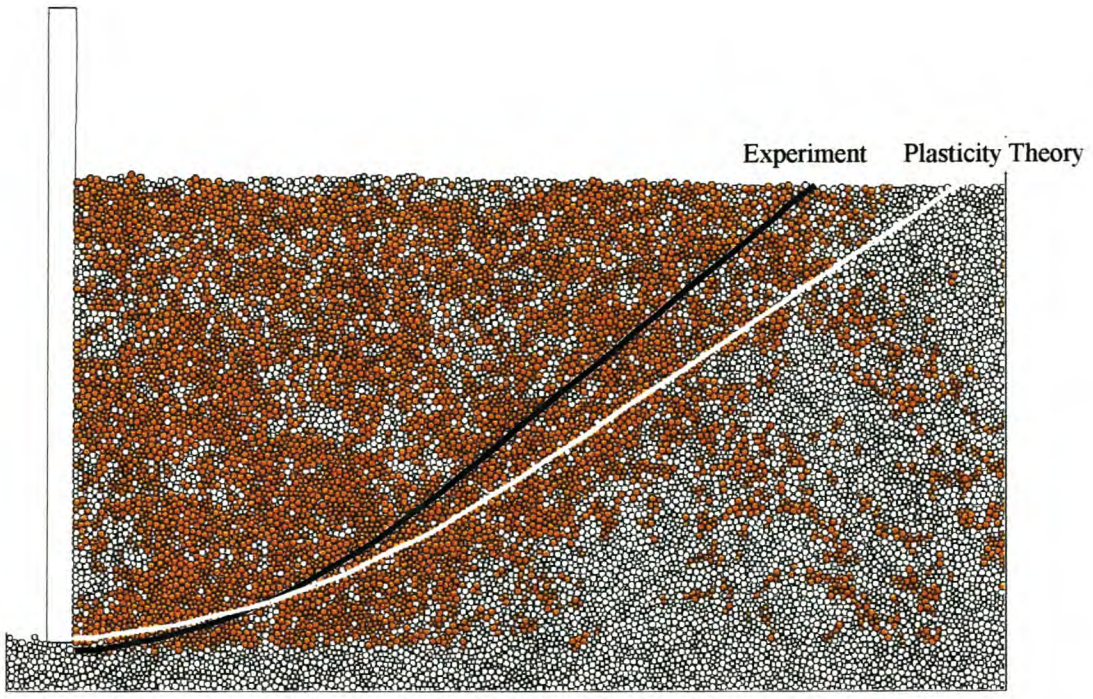

Figure D.2 – *Rupture lines for* $\beta = 90°$ *and* $h = 250$ *mm*

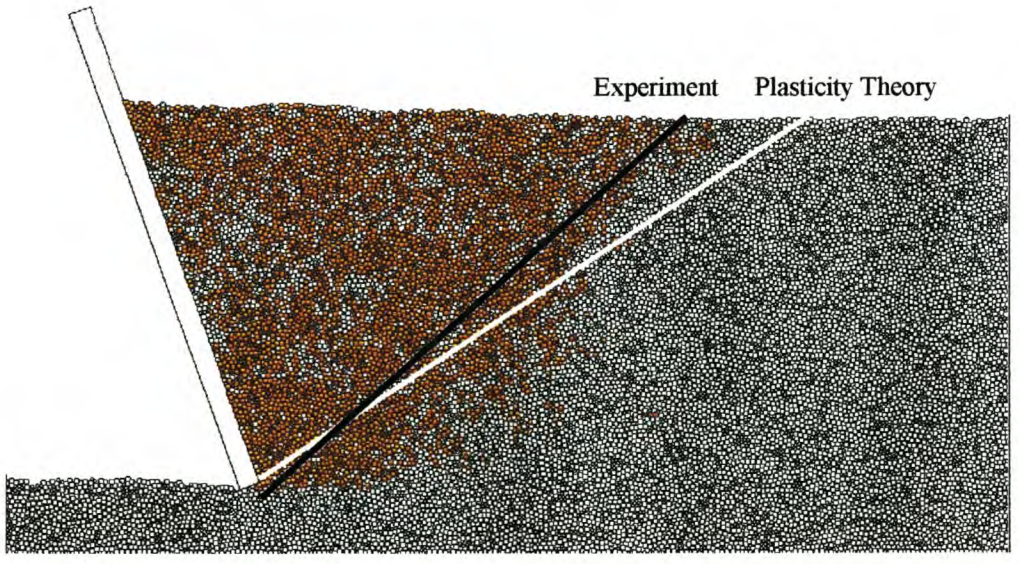

Figure D.3 – *Rupture lines for* $\beta = 70°$ *and* $h = 250$ *mm*

Stellenbosch University http://scholar.sun.ac.za

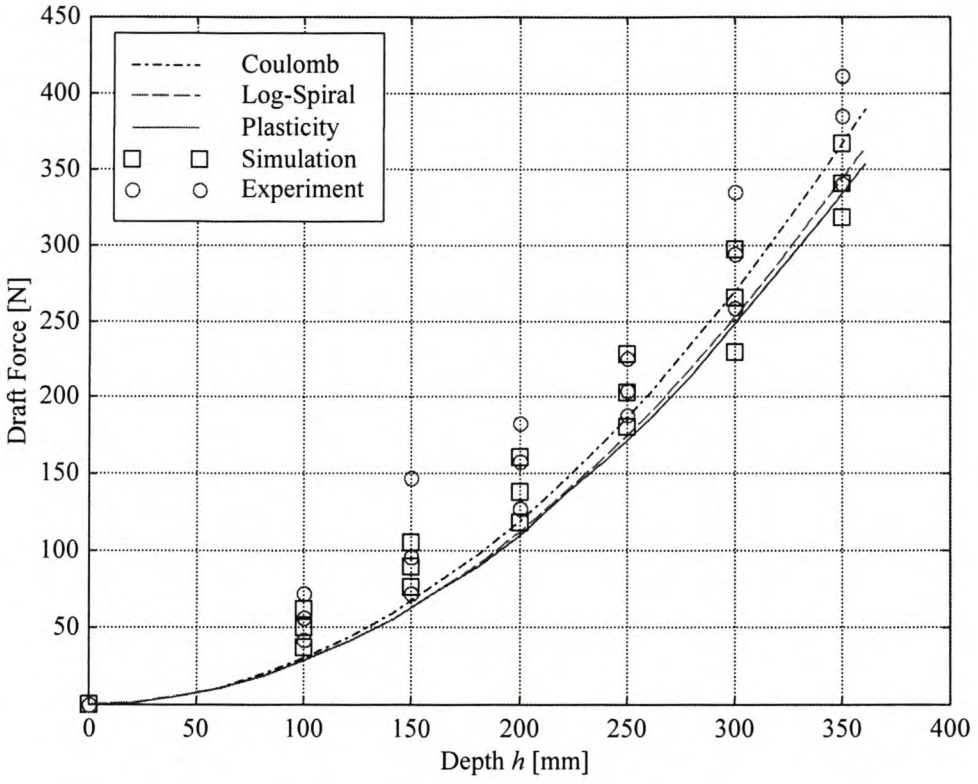

Figure D.4 – *Corn draft force: a = 90°*

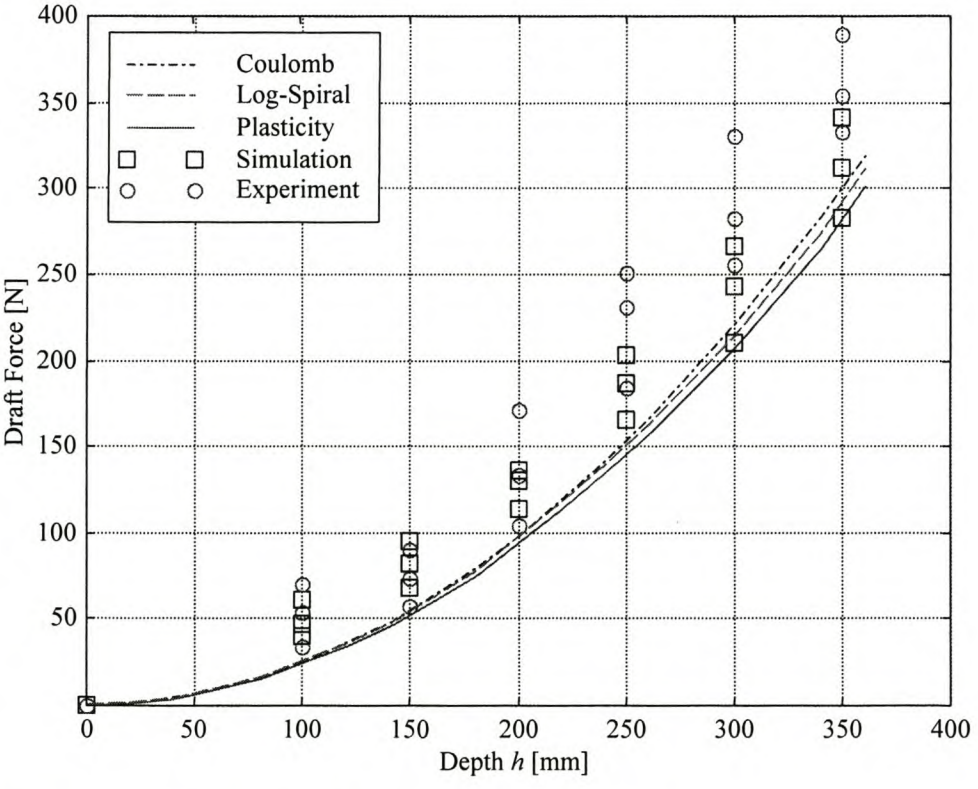

Figure D.5 – *Corn draft force: a = 80°*

Stellenbosch University http://scholar.sun.ac.za

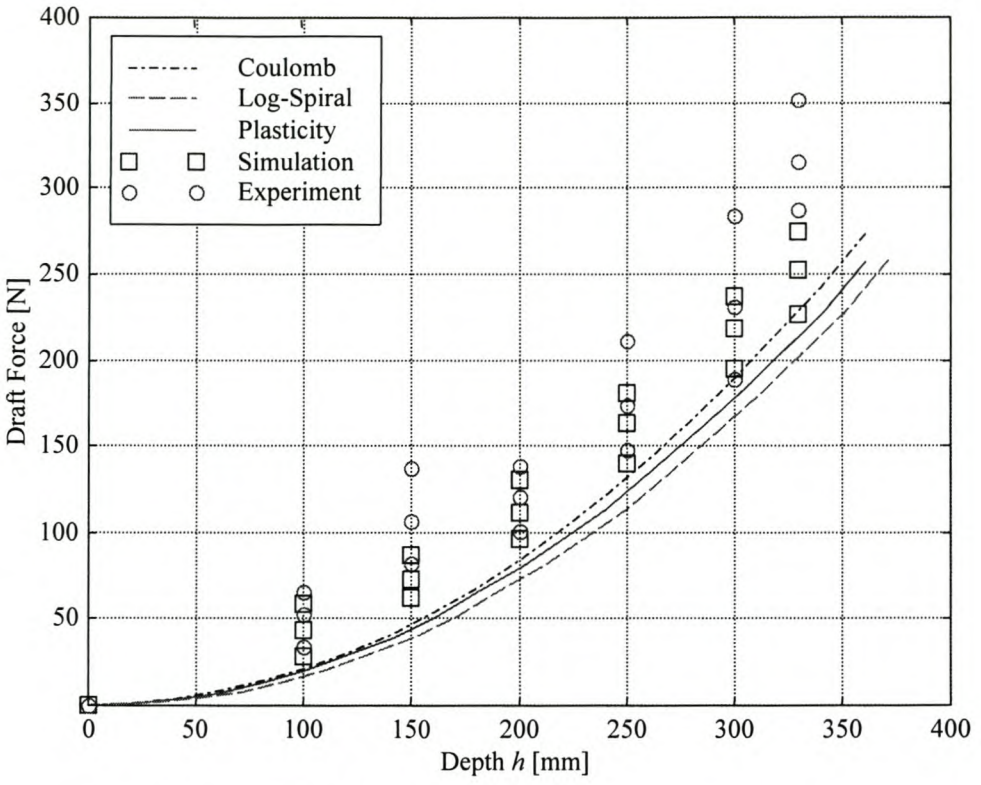

Figure D.6 – *Corn draft force: a = 70°*

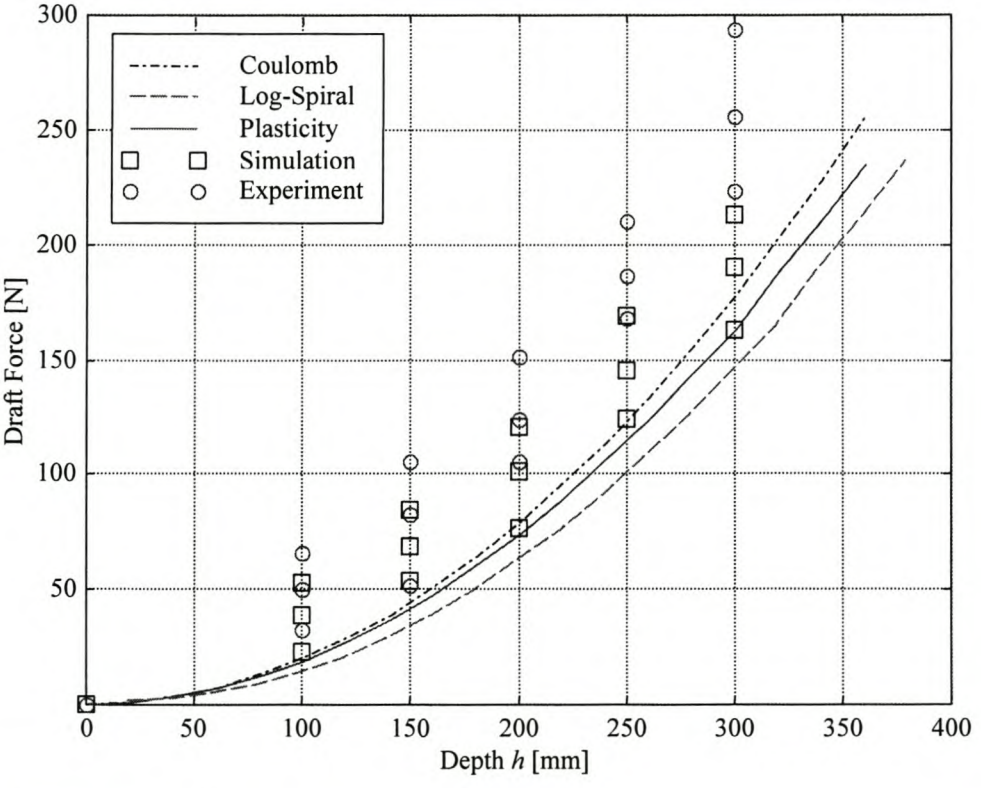

Figure D.7– *Corn draft force: a = 60°*

Stellenbosch University http://scholar.sun.ac.za

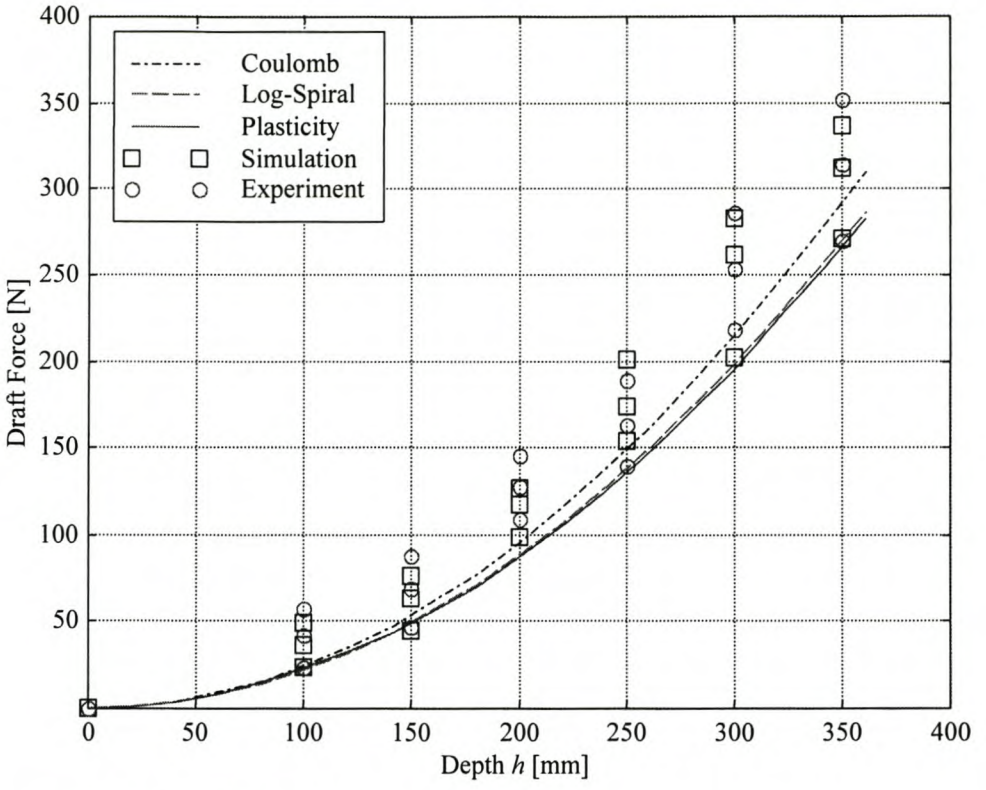

Figure D.8 – *Wheat draft force: α = 90°*

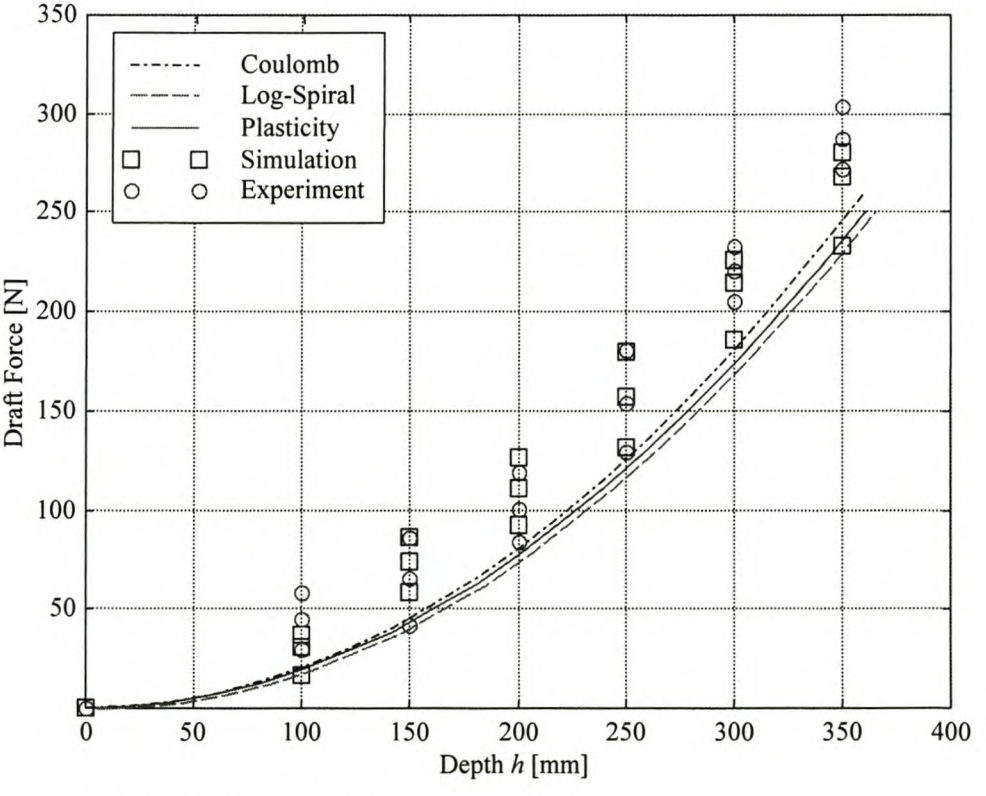

Figure D.9 – *Wheat draft force: α = 80°*

Stellenbosch University http://scholar.sun.ac.za

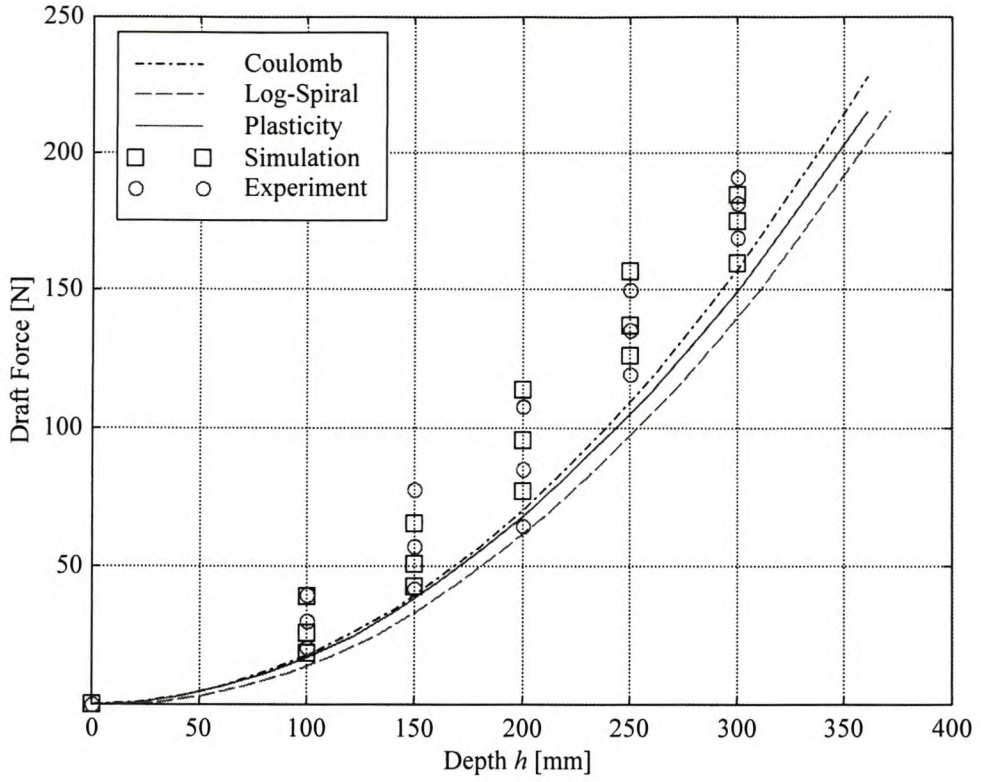

Figure D.10 – *Wheat draft force: α = 70°*

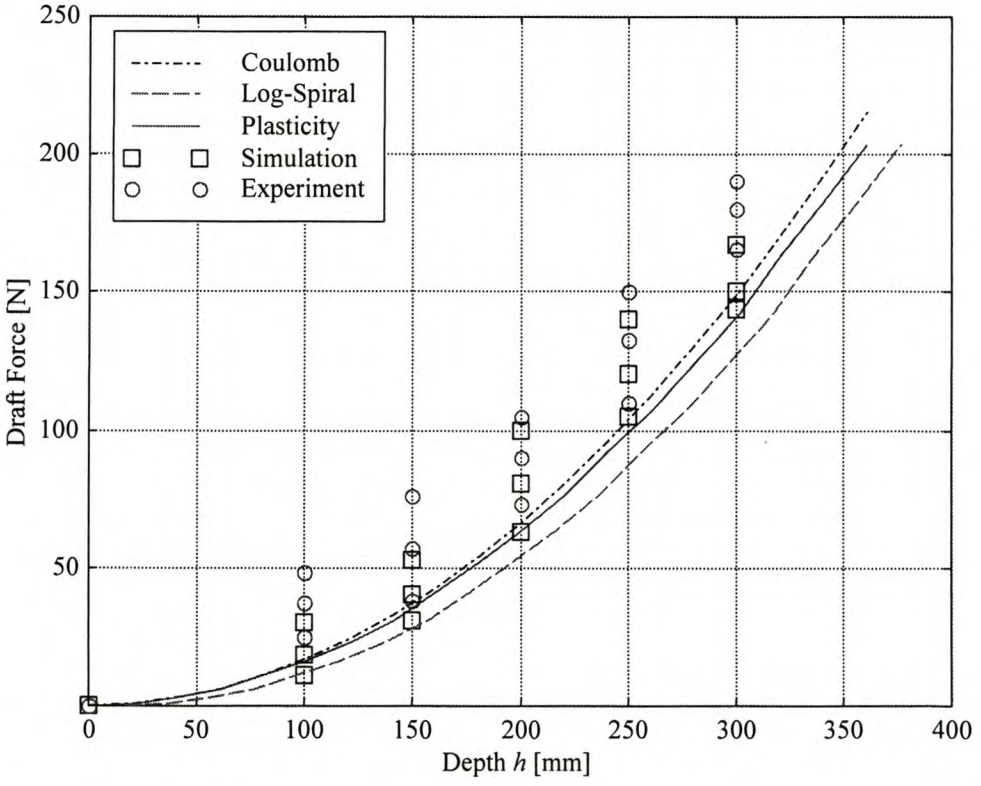

Figure D.11 – *Wheat draft force: α = 60°*

Stellenbosch University http://scholar.sun.ac.za

APPENDIX E

BLADE DYNAMIC MODEL

A simple dynamic model based on dynamic principles is given in Chapter 2.1.3. Bohatier and Nouguier (2000) proposed an elementary model for establishing the relative importance of the static and dynamic forces on a translating blade.

The considered domain is an isosceles triangular *ABC* as in Fig. E.1.

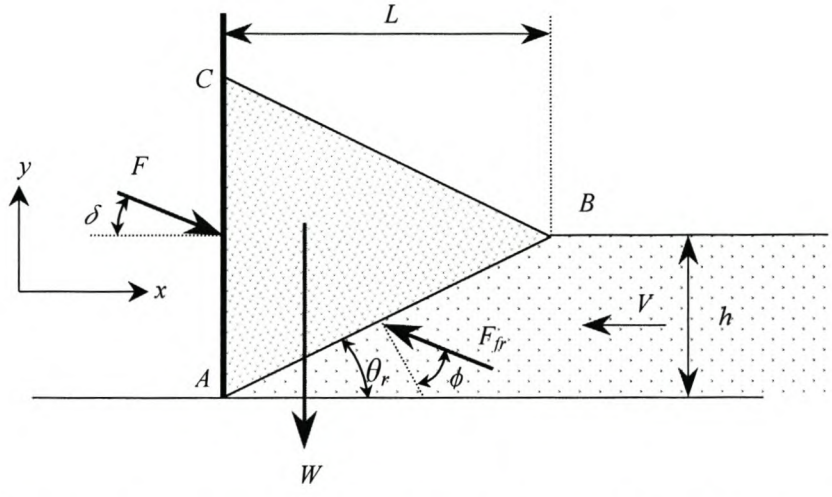

Figure E.1 – *Domain and boundary conditions for dynamic model*

The following assumptions are made:

- The relative deformation of the material is localised on the shear surface.
- The material is homogeneous, isotropic and incompressible.
- Mohr-Coulomb strength criterion is applicable.

The domain of interest is defined by three parts: the shear surface *AB*, the material-tool contact surface *AC* and the free surface *BC*.

Stellenbosch University http://scholar.sun.ac.za

The linear momentum equation for a deformable control volume (fluid mechanics) can be written as (White,1994, pp. 127)

$$\sum \overline{\mathbf{F}} = \frac{d}{dt}\left(\int_{CV} \overline{\mathbf{V}}\, \rho \, dv\right) + \int_{CS} \overline{\mathbf{V}}\, \rho\, (\underline{\mathbf{V}}_r \cdot \overline{\mathbf{n}})\, dA \tag{E.1}$$

where $\sum \overline{\mathbf{F}}$ is the vector sum of all forces acting on the control-volume material considered as a free body, $\overline{\mathbf{V}}$ is the material velocity vector relative to an inertial (non-accelerating) coordinate system, ρ the material density, $\overline{\mathbf{n}}$ the unit normal vector on the area being integrated, *CV* the control volume and *CS* the control surface. For a fixed control volume the relative velocity $\overline{\mathbf{V}}_r = \overline{\mathbf{V}}$ and Eq. E.1 becomes

$$\sum \overline{\mathbf{F}} = \frac{d}{dt}\left(\int_{CV} \overline{\mathbf{V}}\, \rho \, dv\right) + \int_{CS} \overline{\mathbf{V}}\, \rho\, (\underline{\mathbf{V}} \cdot \overline{\mathbf{n}})\, dA \tag{E.2}$$

The velocity components are $\overline{\mathbf{V}} = V_x \overline{\mathbf{e}}_{\mathbf{x}} + V_y \overline{\mathbf{e}}_{\mathbf{y}} + V_z \overline{\mathbf{e}}_{\mathbf{z}}$ in the general 3-D case. With the rate of change of momentum within the control volume $\left(\frac{d}{dt}\left(\int_{CV} \overline{\mathbf{V}}\, \rho \, dv\right)\right)$ constant, Eq. E.2 simplifies to

$$\sum \overline{\mathbf{F}} = \int_{CS} \overline{\mathbf{V}}\, \rho\, (\underline{\mathbf{V}} \cdot \overline{\mathbf{n}})\, dA \tag{E.3}$$

When the outcoming flow is perpendicular onto the view as in Fig. E.1, i.e. in the *z*-direction, Eq. E.3 yields

$$\overline{\mathbf{F}}_{fr} + \overline{\mathbf{F}} - \rho\, g\, h\, L\, \overline{\mathbf{e}}_{\mathbf{y}} = \rho\, h\, V_x (V_z \overline{\mathbf{e}}_{\mathbf{z}} + V_x \overline{\mathbf{e}}_{\mathbf{x}}) \tag{E.4}$$

The term ρghL is the weight per unit width of the material inside the triangle. The directions of the force vectors $\overline{\mathbf{F}}_{fr}$ and $\overline{\mathbf{F}}$ are known and for the two-dimensional case the forces can be resolved into *x*- and *y*-components.

Stellenbosch University http://scholar.sun.ac.za

$$\begin{bmatrix} -\sin(\theta_r + \phi) & \cos(\delta) \\ \cos(\theta_r + \phi) & -\sin(\delta) \end{bmatrix} \begin{bmatrix} F_{fr} \\ F \end{bmatrix} = \begin{bmatrix} \rho h V_x^2 \\ \rho g h L \end{bmatrix} \tag{E.5}$$

With $L = h/\tan(\theta_r)$ the two equations can be solved analytically to obtain the total force on the blade

$$F = \frac{\rho g h^2 \tan(\theta_r + \phi)}{\tan(\theta_r)[\cos(\delta) - \sin(\delta)\tan(\theta_r + \delta)]} \left[1 + \frac{V^2 \tan(\theta r_r)}{g h \tan(\theta_r + \phi)}\right] \tag{E.6}$$

The Froud number $Froud = \dfrac{V_x}{\sqrt{g h}}$ can be identified in Eq. E.6 that can now be written as

$$F = \frac{\rho g h^2 \tan(\theta_r + \phi)}{\tan(\theta_r)[\cos(\delta) - \sin(\delta)\tan(\theta_r + \delta)]} \left[1 + \frac{Froud^2 \tan(\theta_r)}{\tan(\theta_r + \phi)}\right] \tag{E.7}$$

Equation E.6 can be separated into a static and dynamic part.

$$F_{static} = \frac{\rho g h^2 \tan(\theta_r + \phi)}{\tan(\theta_r)[\cos(\delta) - \sin(\delta)\tan(\theta_r + \delta)]} \tag{E.8}$$

$$F_{dynamic} = \frac{\rho g h^2 \tan(\theta_r + \phi)}{\tan(\theta_r)[\cos(\delta) - \sin(\delta)\tan(\theta_r + \delta)]} \left[\frac{V_x^2 \tan(\theta_r)}{g h \tan(\theta_r + \phi)}\right] \tag{E.9}$$

The dynamic force differs from the static force by a factor

$$\varepsilon = \frac{V_x^2 \tan(\theta_r)}{g h \tan(\theta_r + \phi)} \tag{E.10}$$

Bohatier and Nouguier (2000) consider the flow as quasi-static for $\varepsilon < 0.1$, dynamic for $\varepsilon > 10$ and mixed in the intermediate case. In most practical cases of soil cutting, the flow will be the most of the time only quasi-static or in some cases mixed flow. It is, however, possible to get dynamic flow in special cases where h is small and the velocity

Stellenbosch University http://scholar.sun.ac.za

high. Note that all the forces are per unit width, i.e. Nm^{-1}. The value of θ_r must be determined using an upper-bound method, i.e. the final value of θ_r is the one which will give the minimum blade force F.

Stellenbosch University http://scholar.sun.ac.za

APPENDIX F

BUCKET RESULTS

The filling of the bucket with wheat is shown in Figs. F.1 and F.2 for $\beta = 0°$ and $10°$ respectively. Note that the pictures are all drawn horizontally.

The initial stages are very sensitive to the starting conditions and only a slight change in the position of the bucket or the material density can have a big influence on the first two to three pictures. Despite the differences in the free surface geometry, the fill percentages are still in close agreement with the experimental results.

The effect of the drag angle can also be seen on the *Initial Laminar Layer* where the material flows more easily into the bucket due to gravitational assistance. The numeric predictions are more accurate for lower drag angles.

Figure F.3 shows the force chains that develop at contacts. The width of the chains is an indication of the force magnitude. The force chains can be drawn by using only the contact normal force, the contact shear force or the total contact force. In this case, the total contact force has been used.

The force chains give an indication of where the forces are working in on the bucket and also give an indication of the stresses in the material. Up to 300 mm, most of the forces act on the bottom. From 300 mm onwards, high tooth forces develop. The contact forces in the payload are low during the initial part of filling but after 500 mm, when the material reaches the back of the bucket, they start to increase. The *Active dig Zone* in front of the tooth can be identified by the high material contact forces.

Stellenbosch University http://scholar.sun.ac.za

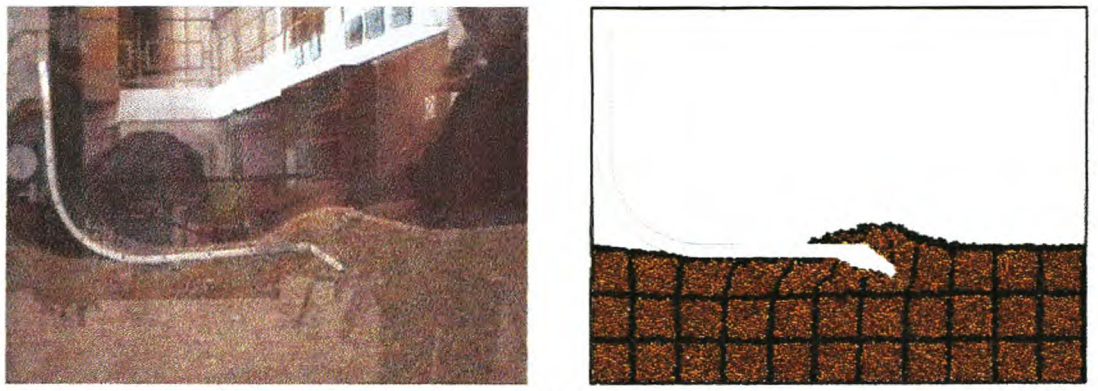

100 mm

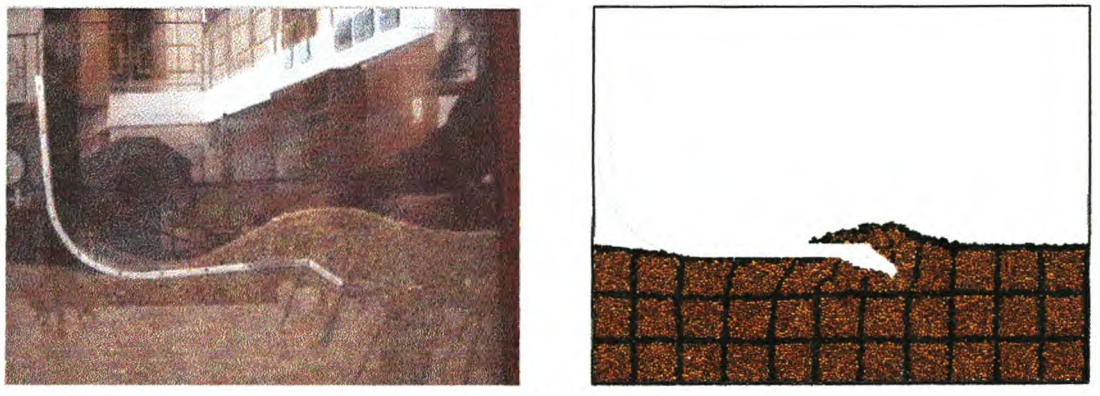

200 mm

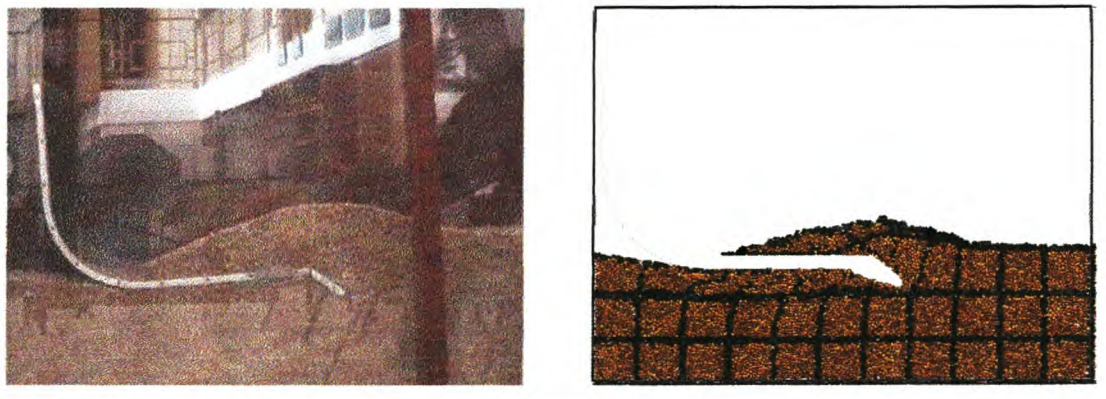

300 mm

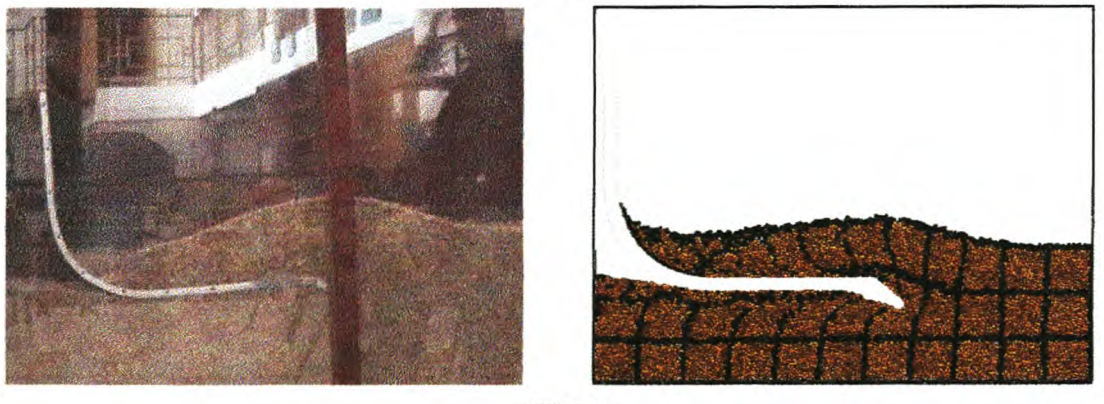

400 mm

Figure F.1a – *Bucket filling with wheat and* $\beta = 0°$

Stellenbosch University http://scholar.sun.ac.za

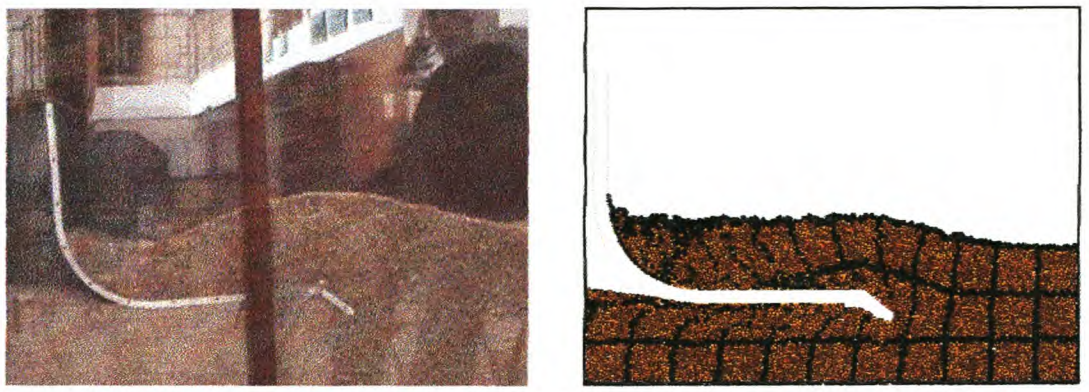

500 mm

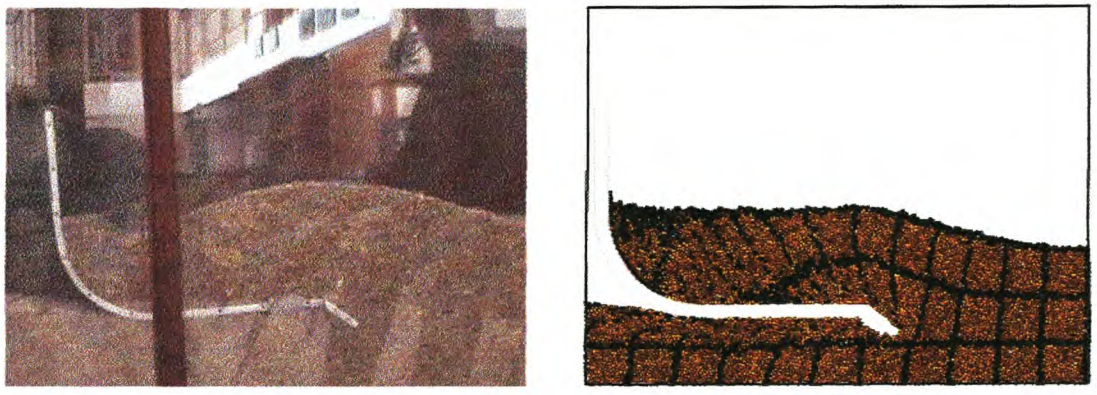

600 mm

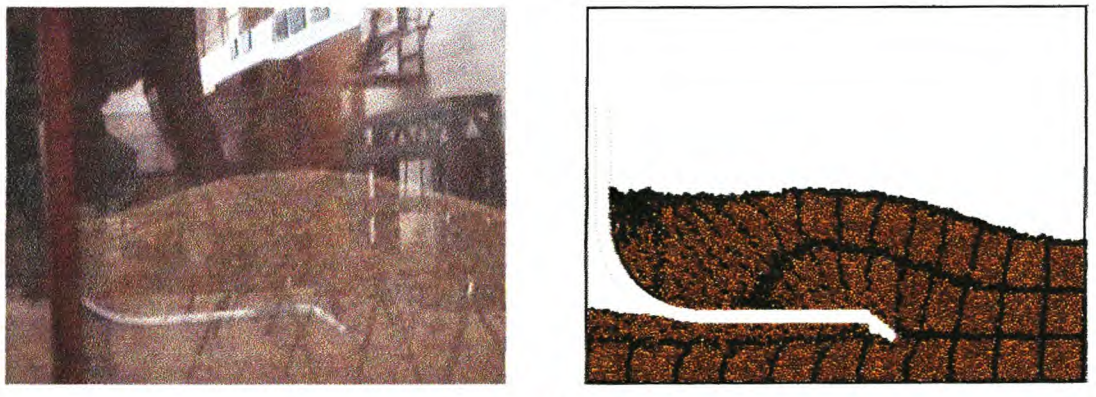

700 mm

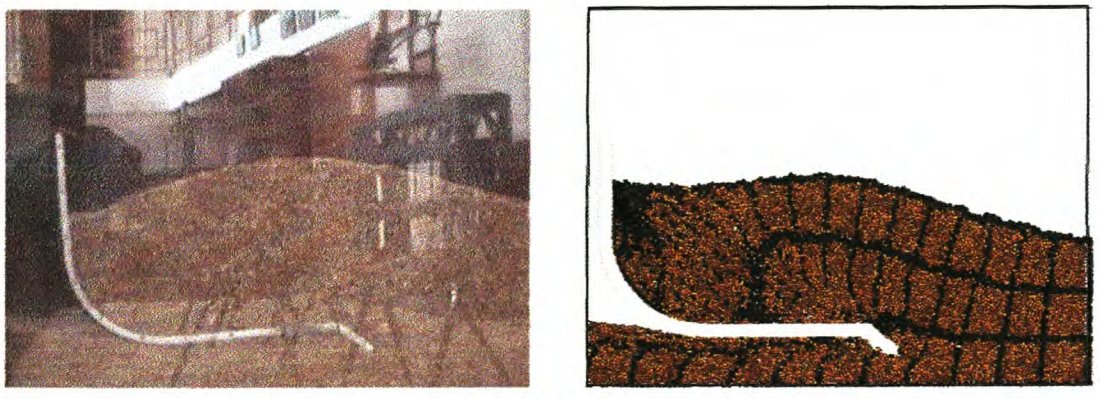

800 mm

Figure F.1b – *Bucket filling with wheat and* $\beta = 0°$

Stellenbosch University http://scholar.sun.ac.za

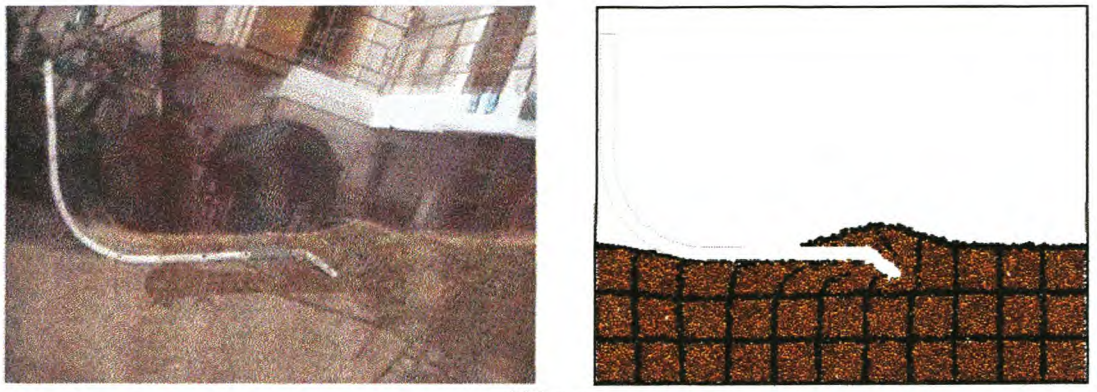

100 mm

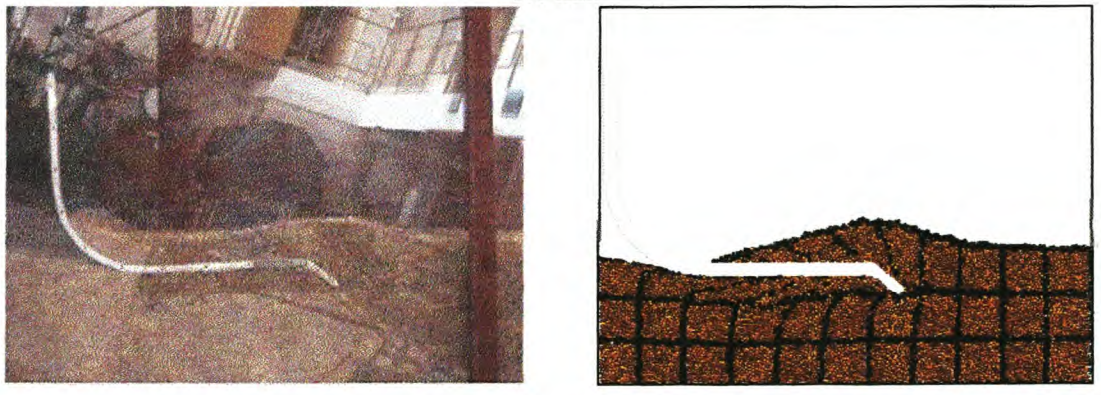

200 mm

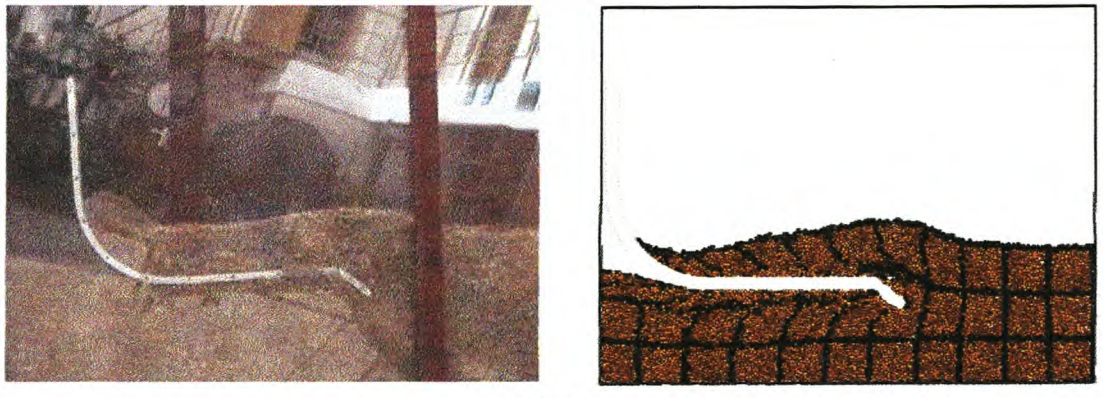

300 mm

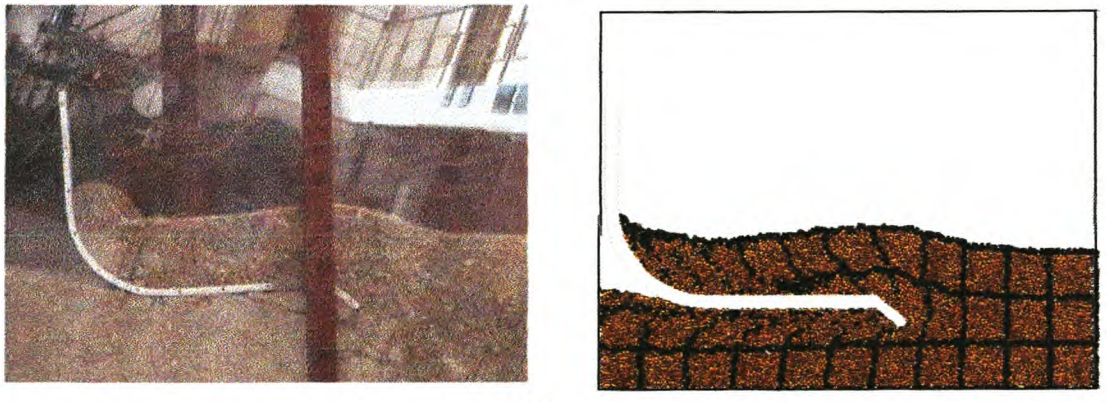

400 mm

Figure F.2a – *Bucket filling with wheat and β = 10°*

Stellenbosch University http://scholar.sun.ac.za

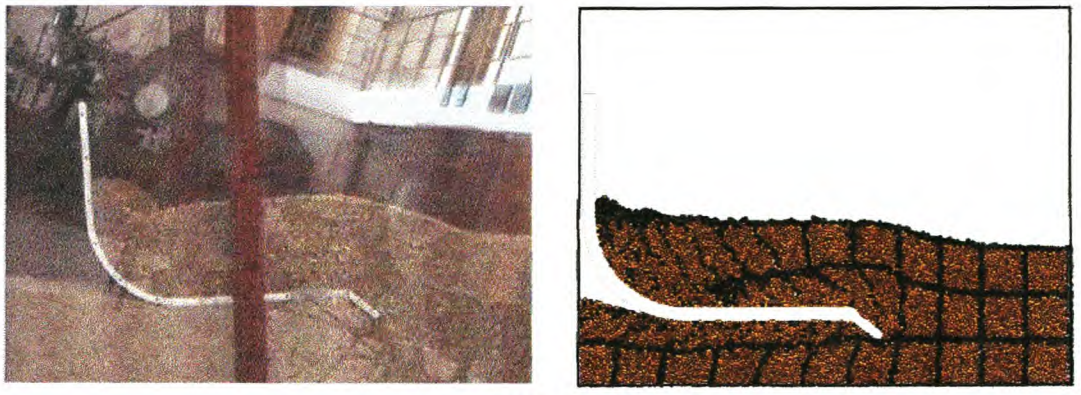

500 mm

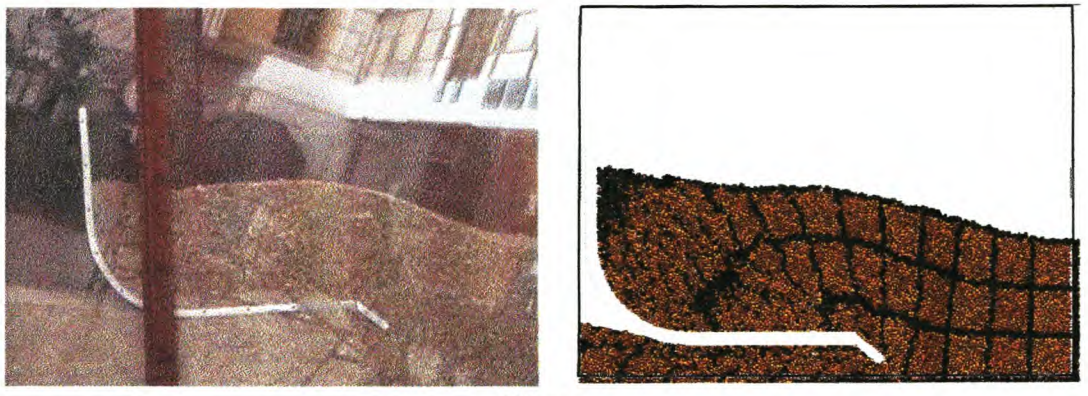

600 mm

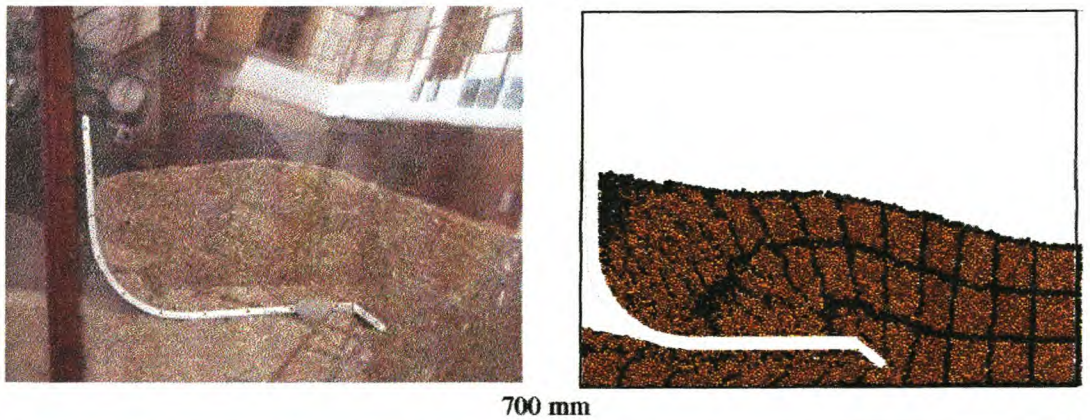

700 mm

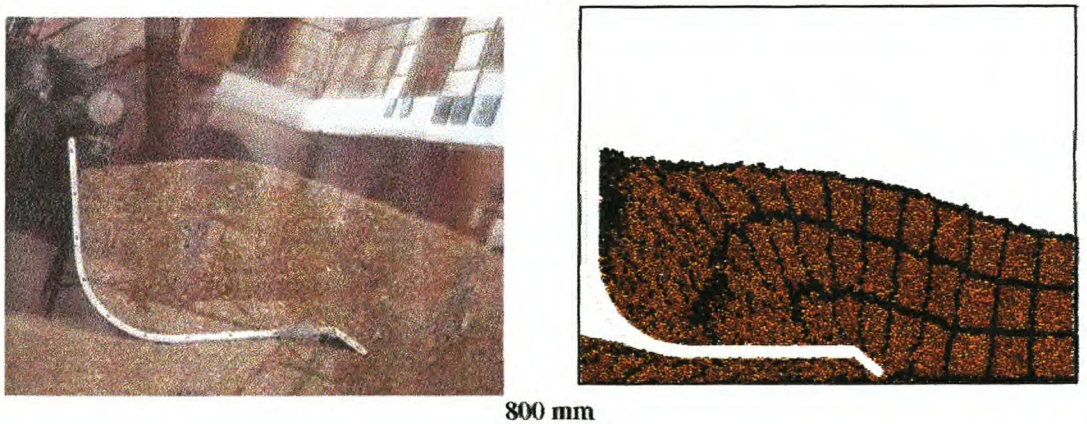

800 mm

Figure F.2b – *Bucket filling with wheat and $\beta = 10°$*

Stellenbosch University http://scholar.sun.ac.za

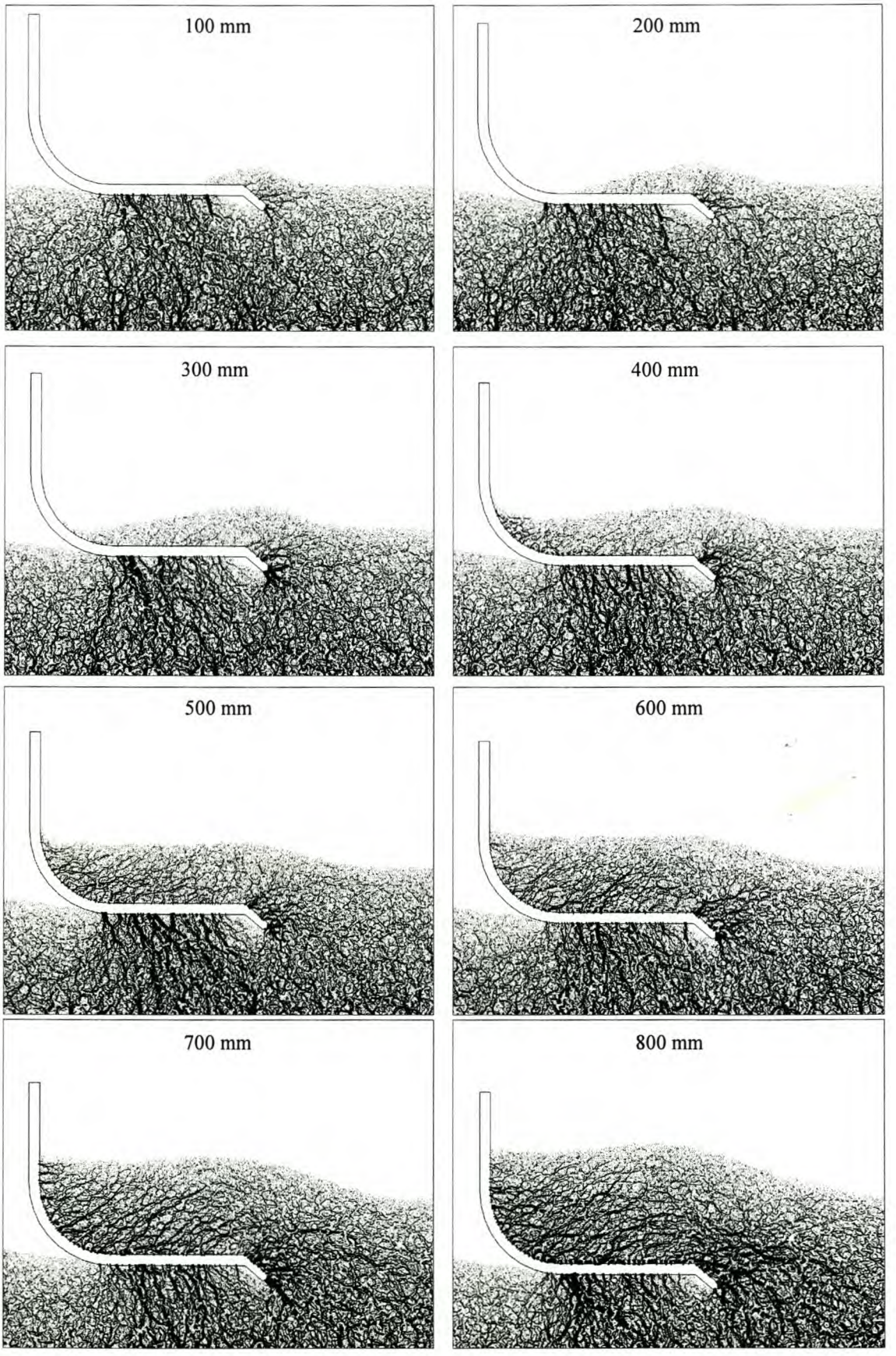

Figure F.3 – *Force chains, $\beta = 0°$*

Stellenbosch University http://scholar.sun.ac.za

Figure F.4 shows the flow regimes for $\beta = 0°$ and corn based on particle total relative displacement ratios. The flow regimes as stated in the *Shear Zone Theory* are clearly visible. The *Dead Load Rupture Line* starts to form after 500-600 mm.

After 600 mm, it is not possible to distinguish between the *Active Dig Zone*, the *Active Flow Zone* and the *Dead Load.* The material is being bulldozed and the original flow pattern changes. The angle of 34° that the *Dead Load Rupture Line* makes with the bucket's bottom is higher than the measured value of 26±4°. The ability of DEM to predict this phenomenon is encouraging.

Stellenbosch University http://scholar.sun.ac.za

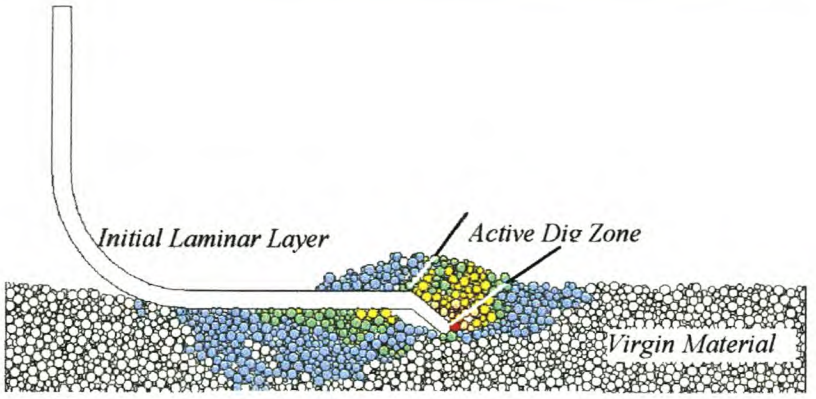

Bucket Displacement = 100 mm

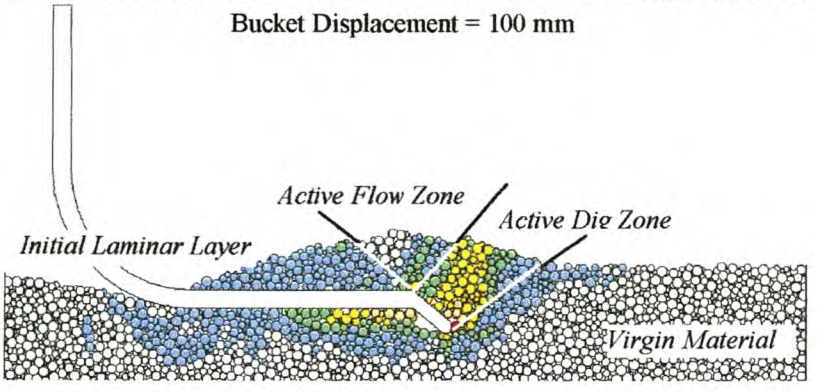

Bucket Displacement = 200 mm

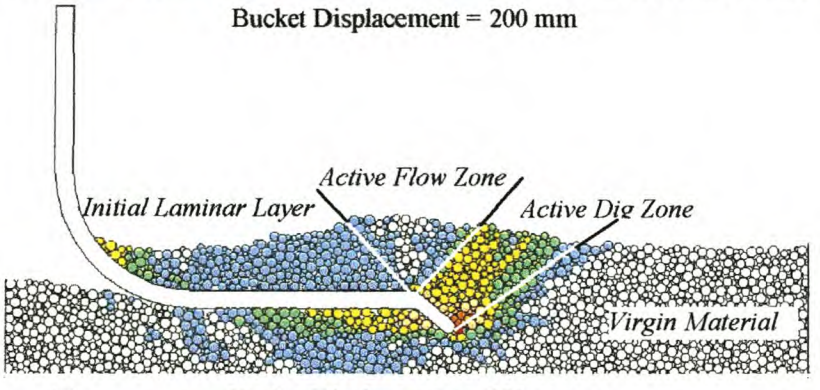

Bucket Displacement = 300 mm

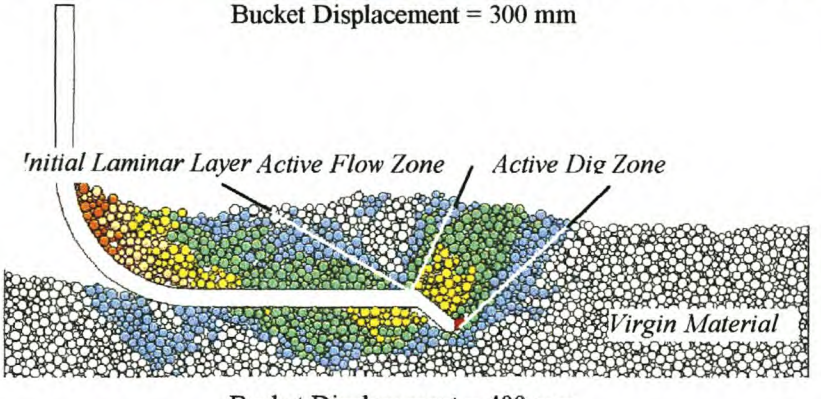

Bucket Displacement = 400 mm

$PDR \geq 0.95$ → Red	$0.80 \leq PDR < 0.95$ → Dark Orange
$0.65 \leq PDR < 0.80$ → Light Orange	$0.40 \leq PDR < 0.65$ → Yellow
$0.25 \leq PDR < 0.40$ → Green	$0.10 \leq PDR < 0.25$ → Blue
$PDR < 0.10$ → White	

Figure F.4a – *Flow regimes*

Stellenbosch University http://scholar.sun.ac.za

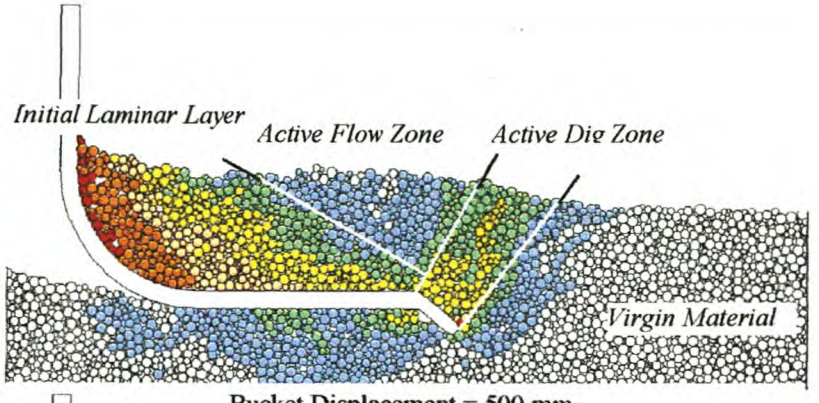

Bucket Displacement = 500 mm

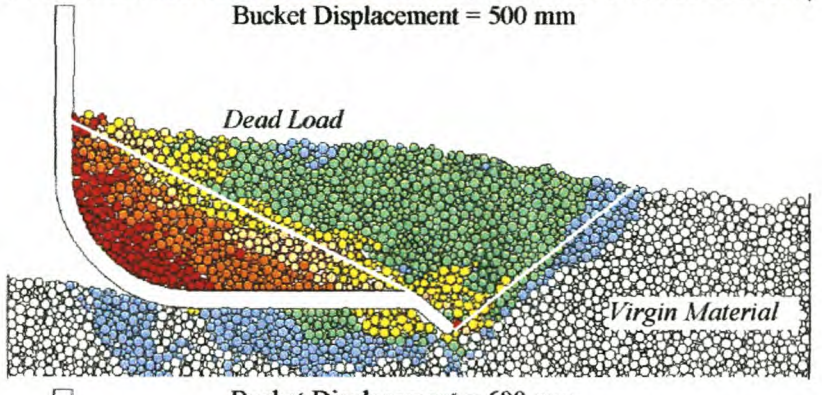

Bucket Displacement = 600 mm

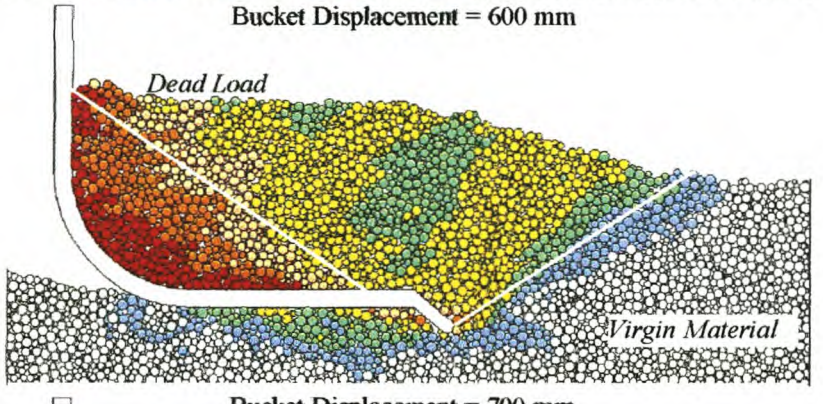

Bucket Displacement = 700 mm

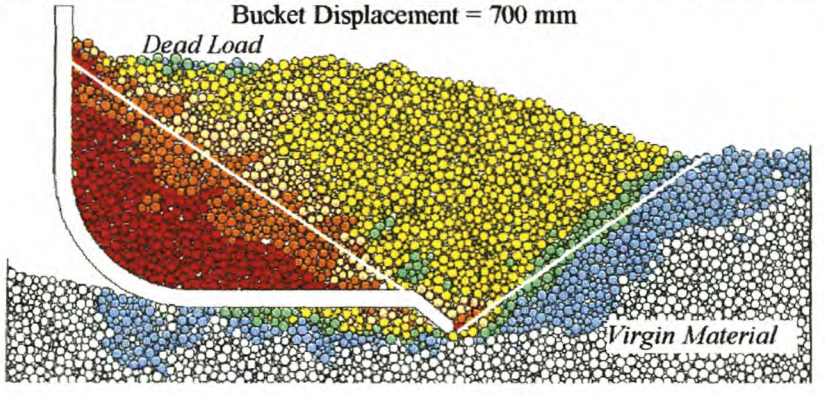

Bucket Displacement = 800 mm

$PDR \geq 0.95$ → Red	$0.80 \leq PDR < 0.95$ → Dark Orange
$0.65 \leq PDR < 0.80$ → Light Orange	$0.40 \leq PDR < 0.65$ → Yellow
$0.25 \leq PDR < 0.40$ → Green	$0.10 \leq PDR < 0.25$ → Blue
$PDR < 0.10$ → White	

Figure F.4b – *Flow regimes*

Stellenbosch University http://scholar.sun.ac.za

APPENDIX G

BUCKET ENERGY BREAKDOWN

The theoretical breakdown of the total dig energy involved in filling a bucket yields significant results (Rowlands, 1991). The emphasis of various components can be highlighted as well as their relative effects when comparing the behaviour due to different bucket and material types.

The following calculations are based on approximations and are not meant to represent the various processes exactly. The aim is to show trends in energy distribution and to make a comparison with the results obtained from numeric simulations. For this analysis the energy is assumed to be consumed in four major processes.

- Increasing the potential energy by raising the bucket and payload against gravity.
- Accelerating the bucket and the payload from rest up to full drag speed.
- Bucket-material friction, both inside and outside the bucket.
- Material-material friction.

Assume that the payload enters the bucket at a constant rate over the full drag. This assumption is made by Rowlands (1991) based on observations and measurements from video recordings. The material is assumed to be purely frictional, i.e. no cohesion or adhesion is present.

Potential Energy

The potential energy gained by the bucket and payload may be expressed in terms of vertical displacement as follows

Stellenbosch University http://scholar.sun.ac.za

$$E_p = \int_0^{y_{fill}} g\, m(y)\, dy \tag{G.1}$$

where E_p = potential energy, g = acceleration due to gravity, $m(y)$ = total mass (bucket and payload) in terms of height displacement and y_{fill} the height gained by the payload and bucket during the total fill procedure. Assuming that the payload enters at a constant rate

$$g\, m(y) = W_b + \frac{W_p}{y_{fill}}\, y \tag{G.2}$$

and

$$y_{fill} = x_{fill} \sin(\beta) \tag{G.3}$$

where x_{fill} is the total drag distance, β the drag angle and W_b and W_p the bucket weight and the maximum payload (i.e. the payload at the end of the drag distance) respectively.

Energy Due to Acceleration

From the standard dynamics formula $V^2 = V_o^2 + 2\,a\,s$ the constant acceleration required to attain full drag speed V_x over a distance x_a can be calculated as

$$a = \frac{V_x^2}{2\,x_a} \tag{G.4}$$

Since each unit of payload mass only has to accelerate once, the energy required to accelerate the total payload is simply the sum of its parts. Assuming that the bucket accelerates over the same distance x_a, the total energy required is

$$E_a = m(y_{fill})\, a\, x_a = m(y_{fill}) \frac{V_x^2}{2} \tag{G.5}$$

i.e. the total kinetic energy at the end of the drag.

Stellenbosch University http://scholar.sun.ac.za

Friction Energy: Material-Bucket

Quantifying the energy consumed by the friction between the bucket and the material is an extremely complex task. Various simplifications and assumptions must be made otherwise the exercise becomes impractical.

The total material-bucket friction energy can be broken into components corresponding to the bottom and the sides of the bucket, both inside and out. Friction associated with the inside rear of the bucket has been disregarded since very little evidence of material movement across this surface has been observed. The friction across the teeth and lip of the bucket will be considered separately. The energy consumed by friction can be expressed as

$$E_f = \int_0^{x_{fill}} \tan(\delta) N(x)\, dx \tag{G.6}$$

where E_f is the consumed energy due to friction, δ = angle of bucket-material friction and $N(x)$ is the normal load on the surface expressed in terms of drag displacement x.

For the outside bottom of the bucket, it can be assumed that the normal load increases at a constant rate, due to the payload. The magnitude of the normal force is the drag angle's cosine component of the payload and bucket weights. The normal force can be expressed in terms of the drag displacement

$$N(x) = \left(W_b + \frac{W_p}{x_{fill}} x \right) \cos(\beta) \tag{G.7}$$

Substitution of this equation into Eq. G.6 gives the total friction energy consumed associated with the outside bottom.

The friction energy associated with the inside-bottom of the bucket can be calculated in a similar fashion, with the elimination of the component of the normal force due to the bucket weight. However, since the inside surface is only in contact with the moving

Stellenbosch University http://scholar.sun.ac.za

material (*Initial Laminar Layer*) for the initial part of the drag, the total distance over which integration is performed must be reduced. Rowlands (1991) recommends that only half of the total drag distance should be used.

Determining the friction associated with the outer, side surfaces is more complex. Most of the following assumptions and calculations work on "worst case" scenarios. It is assumed that the bucket begins its drag completely free of the bank and ends completely submerged. It is also assumed that the rate at which the bucket enters the bank is constant over the full drag. The normal force due to the material against the side of the bucket will be determined by the calculations based on Coulomb's theory for retaining walls (Chapter 2). The passive force against the vertical bucket sides is given by

$$F = \tfrac{1}{2}\gamma L h^2 \left[\frac{\cos(\phi)}{\sqrt{\cos(\delta)} - \sqrt{\sin(\phi+\delta)\sin(\phi)}} \right]^2 \tag{G.8}$$

where h is the material depth, L the bucket length and γ the unit weight of the material. The normal load against the side can be expressed in terms of the drag displacement

$$N(x) = \tfrac{1}{2}\gamma L \left(\frac{H}{x_{fill}} x \right)^2 \left[\frac{\cos(\phi)}{\sqrt{\cos(\delta)} - \sqrt{\sin(\phi+\delta)\sin(\phi)}} \right]^2 \tag{G.9}$$

where H is the height of the bucket and Eq. G.6 is used again to calculate the energy consumed.

Similarly, values for the inner sides of the bucket can be calculated, but as with the bottom surface, certain limitations must be included. Firstly, the bucket length value must be reduced since for most of the drag, material movement is not occurring along the full length of the surface. Secondly, the maximum material height value must also be reduced to account for the large amount of "dead" load in the bucket. Based on observations, Rowlands (1991) estimates that both values should be halved.

Stellenbosch University http://scholar.sun.ac.za

The estimation of the friction across the teeth and bucket lip is even more complex. Rowland (1991) made use of an equation derived by Hettiaratchi and Reece (1974) for flat blades. This method is similar to that of Perumpral et al (1983) and McKeyes (1978) but is presented in an additive style where each term corresponds to a separate physical process. The result depends on four dimensionless factors ("K" factors), which represent the effects of soil weight, soil cohesion, soil/blade adhesion and surcharge pressure respectively. Their modelling does not precisely represent the geometry of dragline bucket teeth; however, to estimate a "worst case" value for the soil resistance force, certain assumptions can be made. The terms in the Hettiaratchi and Reece equation that relate to soil/blade cohesion, adhesion and surcharge have been eliminated. The resulting equation is

$$F = \gamma h^2 B K_\gamma \tag{G.10}$$

where F is the resistance force on the blade, B the total tooth and lip width and K_γ the factor due to gravity and the slip wedge and tooth geometry. Thus for the teeth, the normal force can be expressed as

$$N(x) = \gamma B K_\gamma \left(\frac{H}{x_{fill}} x \right)^2 \tag{G.11}$$

By substituting this expression into Eq. G.6, and by integrating and solving, the friction energy value can be obtained.

Friction Energy: Material-Material

It is not possible to calculate the energy dissipation in the material itself. To complete the analysis, the total boundary energy obtained from the numeric simulation is used and all the other components are subtracted from it to obtain the magnitude of the material-material friction energy.

Stellenbosch University http://scholar.sun.ac.za

Results

Table G.1 summarises the parameters used to determine the energy distribution. This corresponds to the numeric simulation with $\beta = 10°$ and corn as material.

Symbol	Value	Description
E_{total}	100 J	The total boundary energy obtained from simulation
x_{fill}	800 mm	The total drag (fill) distance
β	10°	The drag angle
W_b	0	The bucket weight
ρ	778 kg·m^{-3}	The material bulk density
Vol	13.1·10^{-3} m^3	The total bucket volume
V_x	10 mm·s^{-1}	Drag speed
δ	14.3°	The material (corn)-bucket friction angle
ϕ	23.6°	The material internal friction angle (numeric)
L	220 mm	Bucket length
B	200 mm	Bucket width
H	220 mm	Bucket height
L_t	42 mm	Tooth length
α_t	40°	Tooth rake (attack) angle

Table G.1 – *Parameters used for calculation of energy distribution*

The bucket is 100% filled after a displacement of 800 mm and the maximum payload is calculated as

$$W_p = \rho g \, \mathrm{Vol} = 100N \tag{G.12}$$

Table G.2 sets out the total digging (boundary) energy breakdown.

Stellenbosch University http://scholar.sun.ac.za

Component	Value [J]
Potential	6.9
Acceleration	0.0
Friction: Bucket-Material	40.1
Friction: Material-Material	53.0
Total	100.0

Table G.2 – *Energy breakdown*

It is significant that over half of the total energy is consumed in material-material friction. The acceleration (kinetic) energy component can be ignored.

Stellenbosch University http://scholar.sun.ac.za

REFERENCES

Albert, R., Albert, I., Hornbaker, D., Shiffer, P. and Barabasi, A., 1997, "The Maximum Angle of Stability in Wet and Dry Spherical Granular Media", *Physical Revue E,* 56, 6271.

Albert, R., Pfeifer, M.A., Shiffer, P. and Barabasi, A., 1998, "Drag Force in a Granular Medium", peter.schiffer.1@nd.edu.

Anderson, M.G. and Richards, K.S., 1989, *Slope Stability, Geotechnical Engineering and Geomorphology*, John Wiley & Sons.

Bagster, D.F. and Bridgwater, J., 1967, "The Measurement of the Force Needed to Move Blades Through a Bed of Cohesionless Granules", *Powder Technology*.

Barabasi, A., Albert, R. and Schiffer, P., 1999, "The Physics of Sandcastles: Maximum Angle of Stability in Wet and Dry Granular Media", *Physica A*, 266, pp. 340-345.

Barnard, J.L., 1999, *Die Ontwerp en Vervaardiging van 'n Twee Dimensionele Simulasie Toetsbank vir Grondverskuiwingstoerusting*, Final year project, University of Stellenbosch.

Belytshko, T., Lu, Y.Y. and Gu, L., 1994, "Element Free Galerkin Methods", *Int. Journal. Numer. Methods. Eng.,* Vol. 37, pp. 229-256.

Bohatier, C. and Nouguier, C., 2000, "Dynamic Soil-Tool Interaction Forces and Flow State", *Proceedings: International Conference on Applied Mechanics, SACAM* 2000, January 2000 Durban South Africa, pp. 294.

Bohatier, C. and Nouguier, C., 1999, "Numerical Modelling of Large Deformations in Soils: Continuum or Granular Medium", *Energy Sources Technology Conference & Exhibition, ETCE99-6713, ASME.*

Stellenbosch University http://scholar.sun.ac.za

Bromhead, E.N., 1992, *The Stability of Slopes*, 2nd Edition, Blackie Academic & Professional, London.

Buchholtz, V. and Poschel, T., 1993, "Numerical Investigation of the Evolution of Sandpiles", Preprint.

Chi, L. and Kushwaha, R.L., 1991, "Three-Dimensional, Finite Element Interaction Between Soil and Simple Tillage Tool", *Transactions of the ASAE*, Vol. 32(2), pp. 361-366.

Cleary, P.W., 2000, "DEM Simulation of Industrial Particle Flows: Case Studies of Dragline Excavators, Mixing in Tumblers and Centrifugal Mills, *Powder Technology*, Vol. 109, pp. 83-104.

Cleary, P.W., 1998, "The filling of Dragline Buckets", *Mathematical Engineering in Industry*, Vol. 7, No. 1, pp. 1-24.

Cleary, P.W., 1997, "Modelling Industrial Granular Flows for Draglines and Centrifugal Mills", *Australian Journal of Mining*, September 1997.

Cleary, P.W. and Sawley, M.L., 1999, "Three-Dimensional Modelling of Industrial Granular Flows, *Second International Conference on CFD in the Minerals and Process Industries, CSIRO, Melbourne, Australia, 6-8 December 1999.*

Coppersmith, S.N., Liu, C., Majumdar, S., Narayan, O. and Witten, T.A., 1996, "Model for Force Fluctuations in Bead Packs", *Physical Review E*, Vol. 53(5), pp. 4673-4685.

Corriveau, D., Savage, S.B. and Oger, L., 1996, "Internal Friction Angles: Characterization using Biaxial Test Simulations", *IUTAM Symposium on Mechanics of Granular and Porous Materials*, Kluwer Academic Publishers, Netherlands.

Crouch, S.L. and Starfield, A.M., 1983, *Boundary Element Methods in Solid Mechanics*, George Allen & Unwin, London.

Stellenbosch University http://scholar.sun.ac.za

Cundall, P.A. and Strack, D.L., (1979), "A Discrete Numerical Model for Granular Assemblies", *Geotechnique*, 29(1), pp. 47-65.

De Jong, J.A.H., Hoffman, A.C. and Finkers, H.J., 1999, "Properly Determine Powder Flowability to Maximize Plant Output", *Chemical Engineering Progress*, April 1999, pp. 25-34.

Desai, C.S. and Christian, J.T., 1977, *Numerical Methods in Geotechnical Engineering*, McGraw-Hill, Inc.

Duran, J., 1999, *Sands, Powders, and Grains: An Introduction to the Physics of Granular Materials*, Springer-Verlag New York, Inc.

Esterhuyse, S.W.P, 1997, *The Influence of Geometry on Dragline Bucket Filling Performance*, Masters Degree thesis, University of Stellenbosch.

Falcon, E., Laroche, C. and Coste, C., 1998, "Behavior of one inelastic ball bouncing repeatedly off the ground", *The European Physical Journal B*, 3, pp. 45-57.

Grisso, R.D., Yasin, M. and Kocher, M.F., 1996, "Tillage Implement Forces Operating in Silty Clay Loam", *Transactions of the ASAE*, Vol. 39, pp. 1977-1982.

Hansen, J.B., 1961, *Earth Pressure Calculation*, The Danish Technical Press, Copenhagen.

Hassenpflug, W.C., 1993, "Matrix Tensor Notation Part I: Rectilinear Orthogonal Coordinates", *Computers and Mathematics with Applications*, Vol. 26, No. 3, pp. 55-93.

Head, K.H., 1992, *Manual of Soil Laboratory Testing, Volume 1: Soil Classification and Compaction Tests, Second Edition*, Pentech Press, London.

Head, K.H., 1988, *Manual of Soil Laboratory Testing, Volume 2: Permeability, Shear Strength and Compressibility Tests*, Pentech Press, London.

Stellenbosch University http://scholar.sun.ac.za

Hettiaratchi, D.R.P. and Reece, A.R., 1974, "The Calculation of Passive Soil Resistance", *Geotechnique*, Vol. 26, No. 3, pp. 289-310.

Itasca *PFC*^{2D}, 1999, *Theory and Background, Version 2.0*, www.itascacg.com.

Johnson, K.L., 1987, *Contact Mechanics*, Cambridge University Press, Cambridge.

Koolen, A.J. and Kuipers, H., 1983, *Agricultural Soil Mechanics*, Springer-Verlag, Heidelberg.

Kun, F. and Herrmann H.J., 2000, "A Discrete Element Method for Fragmentation Processes", *International Symposium on Continuous and Discontinuous Modelling of Cohesive Frictional Materials (CDM)*, 27 – 28 April 2000, Stuttgart.

Kushwaha, R.L. and Shen, J., "Finite Element Analysis of the Dynamic Interaction Between Soil and Tillage Tool", *Transactions of the ASAE*, Vol. 37(5), pp. 1315-1319.

Lambe, T.W. and Whitman, R.V., 1969, *Soil Mechanics*, John Wiley & Sons, Inc., New York.

Look, B., 1994, *Spreadsheet Geomechanics an Introduction*, A.A. Balkema, Rotterdam.

Luding, S., Clement, E., Blumen, A., Rajchenbach, J. and Duran, J., 1994, "Models and Simulations of Granular Materials, *Physical Review E*, Vol. 49(2).

Luth, H.J. and Wismer, R.D., 1971, "Performance of Plane Soil Cutting Blades in Sand", *Transactions of the ASAE*, pp. 255.

McKyes, E., 1985, *Soil Cutting and Tillage*, Elsevier, Amsterdam.

McKyes, E., 1978, "The Calculation of Draft Forces and Soil Failure Boundaries of Narrow Cutting Blades", *Transactions of the ASAE*, pp. 20.

Stellenbosch University http://scholar.sun.ac.za

Merchant, M.E., 1945, "Mechanics of the Metal Cutting Process. I. Orthogonal Cutting and a Type 2 Chip", *Journal of Applied Physics*, Vol. 16, No. 5, pp. 267.

Mühlhaus, H.-B., 2000, "Discrete and Continuous Models for Cohesive Frictional Materials", *International Symposium on Continuous and Discontinuous Modelling of Cohesive Frictional Materials (CDM)*, 27 – 28 April 2000, Stuttgart.

Narayan, O. and Nagel, S.R., 1999, "Incipient Failure in Sandpile Models", Preprint.

Oda, M. and Iwashita, K., 1999, *An Introduction: Mechanics of Granular Materials*, A.A Balkema Publishers, Rotterdam Netherlands.

Osman, M.S., 1964, "The Mechanics of Soil Cutting Blades", *Journal of Agricultural Engineering Research*, Vol. 9, No. 4, pp. 313.

Perumpral, J.V., Chance, L.C., Woeste, F.E. and Desai, C.S., 1980, "A Matrix Method for Force and Moment Analysis on a Tillage Tool", *Transactions of the ASAE*, pp.1072.

Perumpral, J.V., Grisso, R.D. and Desai, C.S., 1983, "A Soil-Tool Model Based on Limit Equilibrium Analysis", *Transactions of the ASAE*, pp. 991.

Reimbert, M. L. and Reimbert, A. M., 1976, *Silos, Theory and Practice*, Trans Tech Publications, Clausthal, Germany.

Rhodes, M., 1998, *Introduction to Particle Technology*, John Wiley & Sons Ltd, Chichester, England.

Ros, V., Smith, R.J., Marley, S.J. and Erbach, D.C., 1995, "Mathematical Modelling and Computer-Aided Design of Passive Tillage Tools", *Transactions of the ASAE*, Vol. 38, pp. 675-683.

Rowlands, J.C., 1991, *Dragline Bucket Filling*, Phd Thesis, University of Queensland

Stellenbosch University http://scholar.sun.ac.za

Salencon, J. and Pecker, A., 1995, "Ultimate Bearing Capacity of Shallow Foundations under Inclined and Eccentric Loads. Part I: Purely Cohesive Soil", *European Journal of Mechanics, A/Solids*, 14, No. 3, pp. 349 – 375.

Schafer, J., Dippel, S. and Wolf, D.E., 1995, "Force schemes in simulations of granular materials", Preprint to *Journal de Physique I.*

Siemens, J.C., Weber, J.A. and Thornburn, T.H., 1965, "Mechanics of Soil as Influenced by Model Tillage Tools", *Transactions of the ASAE*, pp. 1.

Smith, I.M., 1982, *Programming the Finite Element Method with Applications to Geomechanics*, John Wiley & Sons.

Sokolovski, V. V., 1954, *Statics of Soil Media*, Butterworths Scientific Publications, London, (translated 1960).

Szabo, B., Barnes, F., Sture, S. and Ko, H.Y., 1998, "Effectiveness of Vibrating Bulldozer and Plow Blades on Draft Force Reduction", *Transactions of the ASAE*, Vol. 41(2), pp. 283-290.

Taylor, D.W., 1948, *Fundamentals of Soil Mechanics*, John Wiley & Sons, Inc., New York.

Terzaghi, K., 1947, *Theoretical Soil Mechanics*, John Wiley & Sons, Inc., New York.

Terzaghi, K. and Peck, R.B., 1962, *Soil Mechanics in Engineering Practice*, John Wiley & Sons, Inc., New York.

Walton, O.R. and Braun, R.L., 1986, "Viscosity, Granular-Temperature, and Stress Calculations for Shearing Assemblies of Inelastic, Frictional Disks", *Journal of Rheology*, 30(5) , John Wiley and Sons, Inc.

White, F.M., 1994, *Fluid Mechanics*, 3rd Edition, McGraw-Hill, Inc.

Stellenbosch University http://scholar.sun.ac.za